

University of Southern Queensland
School of Mechanical and Electrical Engineering

**USE OF FIBRE-OPTIC (FBG) SENSORS IN THE STRUCTURAL
HEALTH MONITORING OF A BATTLEFIELD HELICOPTER ROTOR
BLADE**

A dissertation submitted by

Michael S. Fairbanks-Smith

in the fulfilment of the requirements of

ENG4111 and ENG4112 Research Project

towards the degree of

Bachelor of Engineering (Mechanical)

Submitted: October, 2014

ABSTRACT

As the use of fibre composite materials and components become more widely accepted, so does the inherent risks of sudden and possibly catastrophic failure. This creates a distinct need for sound, structural health monitoring (SHM) methods to be employed to both warn of, and prevent impending failure.

For aviation related fibre composite components this is of paramount importance; however, a secondary but equally important consideration is that of service life. Any extension of a components service life is of great financial and operational benefit to both civil and military operators of aviation assets. This is particularly true of military helicopters which use fibre reinforced composite rotor blades, such as the Boeing CH-47 Chinook. Experience has shown that these highly exposed components are frequently damaged during combat operations and rapidly come into short supply as a result of often minor damage. This minor damage may necessitate blade replacement prior to the aircraft being authorised for further flight.

This project seeks to use finite element analysis (FEA) methods and physical blade testing via the use of optical fibre Bragg grating (FBG) sensors to evaluate typical battlefield, ballistic penetration damage by small arms fire projectiles to a composite Boeing CH-47 Chinook rotor blade test section.

Abaqus FEA software was used to create both a flat plate simulation and a Boeing-Vertol VR-7 Aerofoil assembly model. Physical testing was conducted on a blade by applying incremental load increases as well as incremental levels of simulated damage. Both FBG and strain gauge systems were used to assess the micro-strain levels at predetermined, critical locations. The data response from these systems was then validated as far as possible by FEA methods, with correlations able to be drawn between the strain systems and the FEA results.

This research demonstrated that the use of FBG sensors on the surface of a complex composite component is an appropriate method for determining strains in the vicinity of damage, which was validated in specific areas by FEA methods. It also concluded that FEA methods alone are very difficult to use in a practical sense when assessing the significant size, type and random nature of ballistic damage to a complex composite structure.

With further future development the possibility of the embedding FBG sensor systems at manufacture into a composite rotor blade for real time SHM or lifing assessment exists. This may in turn lead to enhanced service life management of such components by moving to an on-condition based lifing approach.

LIMITATIONS OF USE

The Council of the University of Southern Queensland, its Faculty of Health, Engineering & Sciences, and the staff of the University of Southern Queensland, do not accept any responsibility for the truth, accuracy or completeness of material contained within or associated with this dissertation.

Persons using all or any part of this material do so at their own risk, and not at the risk of the Council of the University of Southern Queensland, its Faculty of Health, Engineering & Sciences or the staff of the University of Southern Queensland.

This dissertation reports an educational exercise and has no purpose or validity beyond this exercise. The sole purpose of the course pair entitled “Research Project” is to contribute to the overall education within the student’s chosen degree program. This document, the associated hardware, software, drawings, and other material set out in the associated appendices should not be used for any other purpose: if they are so used, it is entirely at the risk of the user.

CERTIFICATION OF DISSERTATION

I certify that the ideas, designs and experimental work, results, analyses and conclusions set out in this dissertation are entirely my own effort, except where otherwise indicated and acknowledged.

I further certify that the work is original and has not been previously submitted for assessment in any other course or institution, except where specifically stated.

Michael Shane Fairbanks-Smith

Student Number: **w0030116**

ACKNOWLEDGEMENTS

This research project was carried out under the principle supervision of Dr Jayantha Epaarachchi. My sincerest thankyou is passed to Dr Epaarachchi for his support and guidance, but in particular for his patience.

I also wish to extend my thankyou to Mr Wayne Crowell for his expert advice and assistance during the testing phases.

Finally, I would also like to acknowledge the Centre of Excellence in Engineered Fibre Composites for allowing the use of their facilities and equipment, and the many USQ staff whom I have pestered for advice over the course of this research project.

Table of Contents

ABSTRACT	ii
LIMITATIONS OF USE	iii
CERTIFICATION OF DISSERTATION	iv
ACKNOWLEDGEMENTS	v
LIST OF FIGURES	xiii
LIST OF TABLES	xix
NOMENCLATURE AND ACRONYMS	xxi
CHAPTER 1 - INTRODUCTION	1
1.1 Project Aim & Objectives	1
1.11 Project Aim	1
1.12 Project Objectives	1
1.2 Project Significance & Benefits	2
1.21 Significance	2
1.22 Initial Benefits.....	2
1.23 Long Term Benefits	3
CHAPTER 2 - BACKGROUND & LITERATURE REVIEW.....	4
2.1 Introduction	4
2.11 Helicopter and Rotary Wing Evolution	5
2.12 The CH-47 Chinook Drive and Control System Overview.....	6
2.13 CH-47 Chinook Rotor Blade	11
2.14 Rotor Loads and Forces	17
2.2 Composite Materials.....	18
2.31 Glass Fibre-Reinforce Plastics (GFRP)	22
2.32 Glass Fibres.....	23
2.33 The Matrix	27

2.34	Thermoplastics	28
2.35	Thermosetting	28
2.36	Fibre Volume	28
2.37	Fibre Orientation	29
2.4	Methods of Manufacture of GFRP Components and Sections	30
2.41	Pultrusion	30
2.42	Compression / Preform Moulding	31
2.5	Rotor Blade and Composite Laminate Defects & Damage	32
2.6	Modes of Failure	35
2.7	FEA Simulation	40
2.8	Structural Health Monitoring (SHM)	41
2.9	Fibre-Bragg Grating (FBG) Sensors	45
2.91	Types of Gratings	49
CHAPTER 3 - METHODOLOGY		52
3.1	General Overview	52
3.2	Level of Analysis	54
CHAPTER 4 - CONSEQUENTIAL EFFECTS, ETHICAL RESPONSIBILITY & SUSTAINABILITY		56
4.1	General Overview	56
4.2	Considerations	56
4.3	Sustainability	57
CHAPTER 5 - RESOURCE ANALYSIS		58
5.1	General Overview	58
5.2	Key Project Risk	58
5.3	Required Resources	59
CHAPTER 6 - PROJECT TIMELINE		60
6.1	General Overview	60

6.2	Test Plan Phase Outline.....	60
6.3	Design & Manufacture of Equipment and Models	61
6.31	Design & Manufacture of Test Fixtures	61
6.32	FEA Model Development.....	61
6.4	Phase 1 - Destructive Testing of Blade Sub-Sections	61
6.5	Phase 2 Pre-Damage Application Testing.....	62
6.51	Testing Methodology: Pre-Damage.....	62
6.52	Strain Measurement	62
6.53	Cord-wise Distributed Load.....	62
6.54	FEA and Test Results Comparison.....	63
6.55	Testing Phase Time-Line Comments.....	63
6.6	Phase 3 - Testing Results and Model Verification	63
6.61	Results Consideration	63
6.62	Conclusions.....	63
6.63	Compilation and Completion of Test Documentation.....	63
6.7	Gantt Chart – Time Management.....	64
CHAPTER 7 - RISK MANAGEMENT & CONTROL		66
7.1	General Overview.....	66
7.2	Risk Rating	66
CHAPTER 8 - ROTOR TEST FIXTURE DESIGN & MANUFACTURE		67
8.1	General Overview.....	67
8.2	Design Process	67
8.3	Test Fixture Design Constraints	69
8.4	Fixture Conceptual Options.....	72
8.5	Testing Fixture Sub-components & Materials	73
8.6	Testing Fixture Manufacture	76
8.61	Root-End Clamp	76

8.62	Lower Adjustable Support	77
8.63	Upper Load Plate	78
8.7	Main Support & Test Fixture Assembly	79
CHAPTER 9 - DETERMINATION OF ROTOR BLADE MATERIAL PROPERTIES		86
9.1	General Overview	86
9.2	Relevant ISOs	86
9.3	FLEXURAL TESTING PROCEDURE AND RESULTS	91
9.31	Determination of Flexural Properties	91
9.32	Test Coupon Manufacture	91
9.33	Determination of Specimen Material Class	92
9.34	Determination of Test Coupon Size	92
9.35	Flexural Testing Procedure	94
9.36	Test Velocity	96
9.37	Loading Member and Support Dimensions	97
9.38	Manual Calculation of Results	97
9.39	Flexural Test Results	100
9.39.1	Failure Modes	102
9.4	TENSILE TESTING PROCEDURE AND RESULTS	104
9.41	Determination of Tensile Properties	104
9.42	Test Coupon Manufacture	104
9.43	Determination of Specimen Type	105
9.44	Determination of Test Coupon Size	105
9.45	Tensile Testing Procedure	107
9.46	Test Velocity	108
9.47	Grip Spacing	108
9.48	Tensile Test Results	108

9.49	Failure Modes	110
9.5	FIBRE-FRACTION TESTING PROCEDURE AND RESULTS	111
9.51	Determination of Fibre-Fraction	111
9.52	Calcination Sample Manufacture	111
9.53	Calcination Testing Procedure	112
9.54	Results – Glass Content	113
9.55	Calculation of Glass Content	114
9.56	Results - Ply Stacking Sequence	116
CHAPTER 10	- FEA MODELS	119
10.1	General Overview	119
10.2	Rotor Profile Co-ordinates	119
10.3	Sub-component Modelling	121
10.4	Rotor Skin	123
10.5	Rotor D-spar	124
10.6	Erosion Cap	125
10.7	Honeycomb Core	126
10.8	Meshed FEA Rotor Assembly	127
10.9	Strand 7	128
10.10	Abaqus Ply Stack Plot	131
CHAPTER 11	FBG SENSOR SYSTEM	133
11.1	General Overview	133
11.2	FBG / Optic Fibre Connection Process	134
11.3	FBG Position	138
11.4	FBG System Operation	140
11.5	FBG Confirmation Testing	142
CHAPTER 12	- ELECTRICAL STRAIN GAUGE SENSOR SYSTEM	143
12.1	General Overview	143

12.2	Strain Gauge Electrical Attachment	145
12.3	Strain System Components	146
12.4	Strain Gauge Location	148
12.5	Strain Gauge Channel & Position Number	150
12.6	Strain Gauge Attachment	150
12.7	Unplanned Damage Area Strain Gages	152
CHAPTER 13 - BALLISTIC TESTING TRIALS		155
13.1	General Overview	155
13.2	Ballistic Test Sample	155
13.3	Test Conditions	156
13.4	Test Results	156
CHAPTER 14 - BLADE SECTION TESTING		160
14.1	General Overview	160
14.2	Maximal Load	160
14.3	Quality Assurance Tests	162
14.4	Testing Conditions	163
14.5	Incremental Damage Application	165
14.6	Testing Cessation	167
CHAPTER 15 - RESULTS		168
15.1	General Overview	168
15.2	FBG System Results	168
15.3	FBG & Strain Gauge Results Comparison	172
15.4	Test 4 vs FBG Results	174
15.5	Test 9 vs FBG Results	176
15.6	Test 4-9 and FBG Results	177
15.7	Tests 1 – 9 Correlations	178
15.8	Blade Assembly FEA Results	181

15.9 Flat Plate FEA Results	184
CHAPTER 16 - DISCUSSION.....	190
16.1 Interpretation of Results	190
16.2 Comparison with the Project Aim	191
16.3 Limitations and Improvements.....	193
16.4 Recommendations	194
CHAPTER 17 – CONCLUSION & RECOMMENDATIONS FOR FUTURE RESEARCH.....	195
17.1 Conclusion.....	195
17.2 Further Work	196
LIST OF REFERENCES	197
APPENDICES	201
Appendix A: Project Specification.....	201
Appendix B: Risk Management and Hazard Reduction	203
Appendix C: Fibre Bragg Grating Data Sheet.....	210
Appendix D: Strain Gauge Data Sheet.....	211
Appendix E: USQ Glass Content Performa	212
Appendix H: Test Two Discussion	222
Appendix I: Test Three Discussion	227
Appendix J: Test Four Discussion.....	232
Appendix K: Test Five Discussion.....	238
Appendix L: Test Six Discussion.....	244
Appendix M: Test Seven Discussion	250
Appendix N: Test Eight Discussion	256
Appendix O: Test Nine Discussion	262

LIST OF FIGURES

Figure 1.	Paul Cornu's helicopter as constructed in mid-1907	5
Figure 2.	The MRH and ARH utilise fully composite fibre components.....	6
Figure 3.	The Boeing CH-47 Chinook Battlefield Helicopter.....	7
Figure 4.	CH-47 proportion overview.	7
Figure 5.	CH-47 drive system.....	8
Figure 6.	CH-47 rotor head assembly.....	9
Figure 7.	Forward rotor head blade attachment.....	10
Figure 8.	Overview of the CH-47 rotor blade.....	13
Figure 9.	Rotor blade detailed cross section.....	14
Figure 10.	Profile plot of the corrected data.....	16
Figure 11.	Blade cord-wise centreline and camber mean-line plot.....	16
Figure 12.	Fibre Composite cross sections.....	19
Figure 13.	Specific stiffness vs specific strength chart.....	21
Figure 14.	Material modulus vs density chart.....	22
Figure 15.	Material modulus vs cost per unit volume chart.....	24
Figure 16.	Material density vs fatigue strength.....	25
Figure 17.	Aligned, random and woven fibres.....	27
Figure 18.	Tensile strength vs fibre orientation and stress for E-glass fibres	29
Figure 19.	Unidirectional & multi-directional plies.....	30
Figure 20.	General pultrusion process.....	31
Figure 21.	Typical battle damage due to small arm fire.....	34
Figure 22.	RPG damage to a CH-47 aft rotor blade.....	34
Figure 23.	Composite Crack propagation.....	37
Figure 24.	Interlaminar stress concentrations.....	38
Figure 25.	Modes of laminate crack growth.....	39
Figure 26.	Optical micrograph of impact damage.....	40
Figure 27.	Boeing 787 Dreamliner composite materials.....	43
Figure 28.	Relationship between aircraft structures.....	44
Figure 29.	Optical fibre components & construction	46
Figure 30.	FBG principle of operation.....	47
Figure 31.	FBG spectral response.....	48

Figure 32.	FBG signal forms.	50
Figure 33.	Project methodology outline.	53
Figure 34.	Levels and types of analysis.....	54
Figure 35.	Test fixture design approach.	68
Figure 36.	CEEFC 200 Tonne hydraulic test press.	70
Figure 37.	Hydraulic press cross beam.....	71
Figure 38.	Initial root end clamp concept.....	73
Figure 39.	Root-end clamp sub-component.	77
Figure 40.	Lower adjustable support.	78
Figure 41.	The upper load plate.....	79
Figure 42.	Blade test fixture assembly un-welded.	80
Figure 43.	Root-end clamp weld locations.....	81
Figure 44.	Test fixture with blade installed.....	82
Figure 45.	Lower adjustable support axis.....	83
Figure 46.	Test fixture deflection and load orientation.	84
Figure 47.	Movement trials of the assembled test fixture.	85
Figure 48.	Sectioned blade for test samples.	88
Figure 49.	D-spar sample sections.....	89
Figure 50.	Final tensile (long) and flexural (short) testing coupons.	89
Figure 51.	Final skin calcination test samples.....	90
Figure 52.	Three-point test diagram.	91
Figure 53.	Flexural test coupons and testing machine.....	95
Figure 54.	Flexural test close up view.....	96
Figure 55.	Flexural test stress vs strain plot.	101
Figure 56.	Three point bending test failure modes.....	102
Figure 57.	Flexural test coupon observed modes of failure.	103
Figure 58.	Summary of Type 2 tensile specimen dimensions.....	106
Figure 59.	D-spar tensile test coupons.....	107
Figure 60.	MTS Insight tensile testing machine.....	108
Figure 61.	Tensile test computer screen shot plots and data.	109
Figure 62.	Failed tensile test sample.	110
Figure 63.	D-spar calcination samples and crucibles.	111
Figure 64.	Calcination skin samples.....	112
Figure 65.	CEEFC electronic scale and temperature controlled furnace.	113

Figure 66.	Three D-spar samples post calcination.	114
Figure 67.	Skin samples pre and post calcination.	115
Figure 68.	D-spar plies post separation demonstrating fragility.	115
Figure 69.	D-spar plie orientation magnified view.....	116
Figure 70.	Skin sample with plies separated following calcination.	116
Figure 71.	MS Excel data point confirmation plot.	121
Figure 72.	Graphical layout of FEA part creation order.....	122
Figure 73.	FEA skin model and datum.....	123
Figure 74.	FEA Skin model mesh grid with 11500 elements.....	124
Figure 75.	FEA rotor spar model.....	124
Figure 76.	FEA D-spar model mesh grid of 23550 elements.....	125
Figure 77.	FEA titanium erosion nose cap.	125
Figure 78.	FEA titanium erosion nose cap mesh grid of 2400 elements.....	126
Figure 79.	FEA Nomex honeycomb core model.....	126
Figure 80.	FEA Nomex core section initial mesh grid of 950 elements.	127
Figure 81.	FEA model of skin and erosion cap meshed assembly.....	128
Figure 82.	FEA model of D-spar, skin and erosion cap meshed assembly.	128
Figure 83.	FEA model of D-spar, skin, erosion cap and core final assembly.	128
Figure 84.	Ply properties entered into Strand 7.....	129
Figure 85.	Strand 7 D-spar laminate model detailing the results for E , ν and G . 130	
Figure 86.	Strand 7 skin laminate model detailing the results for E , ν and G	130
Figure 87.	Abaqus D-spar plie stack plot.	132
Figure 88.	Overview of major FGB system components.....	134
Figure 89.	Typical optic fibre strippers.	135
Figure 90.	The Vitel high precision fibre cleaver.....	135
Figure 91.	The Vitel v. 2000 s175 fusion splicing machine.....	137
Figure 92.	Internal to D-spar FBG location (mm).....	138
Figure 93.	Location of the FBG sensor.	139
Figure 94.	Micron Optics sm125 four channel optical sensing interrogator.	140
Figure 95.	Micron Optics, Enlight software was used for the FBG analysis.	141
Figure 96.	Upper surface strain gauges.	143
Figure 97.	Typical pre-wired foil type strain gauge.	144
Figure 98.	Nine pin plug modification.	145
Figure 99.	Modification of the 9 pin connector plugs.	146

Figure 100.	StrainSmart System 5000 (5100B) data acquisition system.	147
Figure 101.	Hydraulic cylinder, lines, LVDT and load cell with FBG.	148
Figure 102.	Upper test surface strain gauge positions (mm).	149
Figure 103.	Lower test surface strain gauge positions (mm).	149
Figure 104.	Internal D-spar strain gauges.	151
Figure 105.	Blade test section ‘accidental’ damage.	152
Figure 106.	Impact damage location with strain gauges.	153
Figure 107.	Accidental damage strain gauge orientation.	154
Figure 108.	Resultant ballistic damage (external).	158
Figure 109.	Top view of internal ballistic damage.	159
Figure 110.	Mid-span load testing (Test 3).	164
Figure 111.	Blade deflection at the maximal 2500N cantilever load.	165
Figure 112.	Location, axis and order of damage holes relative to the D-spar. .	165
Figure 113.	Hole 1 at 3.0 mm depth and full thickness.	166
Figure 114.	Blade surface with three completed damage holes post testing. ...	167
Figure 115.	Micron Optics – ENLIGHT software screen shot.	169
Figure 116.	MatLab plot of FBG Test 9 results.	169
Figure 117.	MatLab plot of Test 9 FBG peak shift indicating tensile strain. ...	170
Figure 118.	Micro Optics ENLIGHT response data file extract.	171
Figure 119.	MatLab plot of FBG peaks (zoom view).	172
Figure 120.	Test 4 load vs Micro-strain plot.	174
Figure 121.	Test 4 – Load & strain gauge / FBG comparison plot.	175
Figure 122.	Test 3 – Load & strain gauge plot (1000N) FBG comparison.	175
Figure 123.	Test 9 – Load & strain gauge / FBG comparison plot.	176
Figure 124.	Test 9 – Load & strain gauge / FBG comparison plot.	177
Figure 125.	Test 1 – 9 Comparison plot of FBG & strain gauge #1.	178
Figure 126.	FBG and strain gauge trend.	179
Figure 127.	Test 1 – 9 Comparison plot of FBG & strain gauges #1 & #3.	180
Figure 128.	Abaqus D-spar FBG and Strain gauge #1 micro-strain.	182
Figure 129.	Abaqus Skin FEA strain gauge position #3 micro-strain.	183
Figure 130.	Flat plate simulation composite layup.	184
Figure 131.	Flat plate verification fine model mesh (two through holes).	185
Figure 132.	Test 7 FEA simulation results overview.	185
Figure 133.	Test 7 FEA simulation micro-strain values.	186

Figure 134.	Test 8 FEA simulation results overview.	186
Figure 135.	Test 8 FEA simulation micro-strain values.	187
Figure 136.	Test 9 FEA simulation results overview.	187
Figure 137.	Test 9 FEA simulation micro-strain values.	188
Figure 138.	Test 1 plot of wavelength vs power.	217
Figure 139.	Test 1 plot of peak wavelength vs power.	217
Figure 140.	FBG data acquisition system display.	218
Figure 141.	Strain gauge (SmartStrain) data acquisition system screen.	218
Figure 142.	Test 1 – Load & strain gauge micro-strain ($\mu\epsilon$) plot.	219
Figure 143.	Test 1 – Load & strain gauge plot including load removal.	220
Figure 144.	Test 2 – Load & strain gauge plot including load removal.	223
Figure 145.	Test 2 – Load & strain gauge micro-strain ($\mu\epsilon$) plot.	223
Figure 146.	Test 2 - FBG wavelength vs power complete plot.	224
Figure 147.	Test 2 - FBG wavelength vs power reduced scale plot.	224
Figure 148.	Test 2 - FBG wavelength vs power peak plot with chirping.	225
Figure 149.	Test 3 – Load & strain gauge plot including load removal.	228
Figure 150.	Test 3 – Load & strain gauge plot held at 1000N.	228
Figure 151.	Test 3 – Load & strain gauge plot (1000N) FBG comparison.	229
Figure 152.	Test 3 - FBG wavelength vs power complete plot.	229
Figure 153.	Test 3 - FBG wavelength vs power reduced scale plot.	230
Figure 154.	Test 3 - FBG wavelength vs power peak with massed response.	230
Figure 155.	Test 4 – Load & strain gauge plot including load removal.	233
Figure 156.	Test 4 – Load & strain gauge plot.	233
Figure 157.	Test 4 – Load & strain gauge / FBG comparison plot.	234
Figure 158.	Test 4 - FBG and strain gauge #1 comparison.	234
Figure 159.	Test 4 - FBG wavelength vs power complete plot.	235
Figure 160.	Test 4 - FBG wavelength vs power reduced scale plot.	235
Figure 161.	Test 4 - FBG wavelength vs power peak with massed response.	236
Figure 162.	Test 5 – Load & strain gauge plot including load removal.	239
Figure 163.	Test 5 – Load & strain gauge plot.	239
Figure 164.	Test 5 – Load & strain gauge / FBG comparison plot.	240
Figure 165.	Test 5 - FBG and strain gauge #1 comparison.	240
Figure 166.	Test 5 - FBG wavelength vs power complete plot.	241
Figure 167.	Test 5 - FBG wavelength vs power reduced scale plot.	241

Figure 168.	Test 5 - FBG wavelength vs power peak with chirping.	242
Figure 169.	Test 6 – Load & strain gauge plot including load removal.	245
Figure 170.	Test 6 – Load & strain gauge plot.	245
Figure 171.	Test 6 – Load & strain gauge / FBG comparison plot.....	246
Figure 172.	Test 6 - FBG and strain gauge #1 comparison.	246
Figure 173.	Test 6 - FBG wavelength vs power complete plot.	247
Figure 174.	Test 6 - FBG wavelength vs power reduced scale plot.	247
Figure 175.	Test 6 - FBG wavelength vs power peak with chirping.	248
Figure 176.	Test 7 – Load & strain gauge plot including load removal.	251
Figure 177.	Test 7 – Load & strain gauge plot.	251
Figure 178.	Test 7 – Load & strain gauge / FBG comparison plot.....	252
Figure 179.	Test 7 - FBG and strain gauge #1 comparison.	252
Figure 180.	Test 7 - FBG wavelength vs power complete plot.	253
Figure 181.	Test 7 - FBG wavelength vs power reduced scale plot.	253
Figure 182.	Test 7 - FBG wavelength vs power peak with chirping.	254
Figure 183.	Test 8 – Load & strain gauge plot including load removal.	257
Figure 184.	Test 8 – Load & strain gauge plot.	257
Figure 185.	Test 8 – Load & strain gauge / FBG comparison plot.....	258
Figure 186.	Test 8 - FBG and strain gauge #1 comparison.	258
Figure 187.	Test 8 - FBG wavelength vs power complete plot.	259
Figure 188.	Test 8 - FBG wavelength vs power reduced scale plot.	259
Figure 189.	Test 8 - FBG wavelength vs power peak with chirping.	260
Figure 190.	Test 9 – Load & strain gauge plot including load removal.	263
Figure 191.	Test 9 – Load & strain gauge plot.	263
Figure 192.	Test 9 – Load & strain gauge / FBG comparison plot.....	264
Figure 193.	Test 9 - FBG and strain gauge #1 comparison.	264
Figure 194.	Test 9 - FBG wavelength vs power complete plot.	265
Figure 195.	Test 9 - FBG wavelength vs power reduced scale plot.	265
Figure 196.	Test 9 - FBG wavelength vs power peak with chirping.	266

LIST OF TABLES

Table 1.	CH-47 Rotor blade tabulated data.....	11
Table 2.	VR-7 Aerofoil with tab (vr7b-il) (Aerospace.illinois.edu, 2014).	15
Table 3.	Project resource requirements.....	59
Table 4.	Test fixture constraints.....	69
Table 5.	Test fixture decision matrix.....	72
Table 6.	General description of fixture components.....	74
Table 7.	General properties of fixture materials.....	76
Table 8.	Main Support dimensions and mass.....	79
Table 9.	Flexural test specimen requirements.....	92
Table 10.	Flexural test specimen length.....	93
Table 11.	Flexural test specimen width.....	93
Table 12.	Specimen dimensional tolerance.....	94
Table 13.	Final test sample preferred dimensions.....	94
Table 14.	Load and support member radius as derived from ISO 14125	97
Table 15.	Data obtained from the MTS Alliance RT/10 test machine.....	100
Table 16.	Flexural testing manually entered data.....	100
Table 17.	Flexural test primary failure modes.....	103
Table 18.	Tensile test specimen dimensions summary.....	106
Table 19.	Tensile test summary of results.....	109
Table 20.	Glass content test results & data.....	113
Table 21.	D-spar plie orientation.....	117
Table 22.	Skin laminate plie stacking sequence.....	118
Table 23.	Blade profile coordinates.....	120
Table 24.	Summary of Strand 7 calculated results and actual tested modulus. .	131
Table 25.	FBG specification data.....	133
Table 26.	Strain gauge data.....	144
Table 27.	Data acquisition input channel and position number.....	150
Table 28.	Ballistic test sample specifications.....	155
Table 29.	Ballistic test data.....	156
Table 30.	Ballistic test damage data.....	157
Table 31.	Identified testing faults and corrective action.....	162

Table 32.	Test Conditions.	163
Table 33.	FBG & Strain Gauge (# 1) Results Comparison.....	173
Table 34.	Table of comparison for Tests 4 and 9.....	177
Table 35.	Lower surface strain comparison ($\mu\epsilon$).	180
Table 36.	Un-planned damage area surface strain comparison ($\mu\epsilon$).....	181
Table 37.	Test 4 FEA / testing results comparison.	183
Table 38.	FBG and flat plate FEA results comparison.	189
Table 39.	Test 1 - General Conditions	214
Table 40.	Test 1 - data summary table.	221
Table 41.	Test 2 - General Conditions	222
Table 42.	Test 2 - data summary table.	225
Table 43.	Test 3 - General Conditions	227
Table 44.	Test 3 - data summary table.	231
Table 45.	Test 4 - General Conditions	232
Table 46.	Test 4 - data summary table.	236
Table 47.	Test 5 - General conditions with damage.....	238
Table 48.	Test 5 - data summary table.	242
Table 49.	Test 6 - General conditions with damage.....	244
Table 50.	Test 6 - data summary table.	248
Table 51.	Test 7 - General conditions with damage.....	250
Table 52.	Test 7 - data summary table.	254
Table 53.	Test 8 - General conditions with damage.....	256
Table 54.	Test 8 - data summary table.	260
Table 55.	Test 9 - General conditions with damage.....	262
Table 56.	Test 9 - data summary table.	266

NOMENCLATURE AND ACRONYMS

The following list details the nomenclature and acronyms used in the following text.

A	Appendix
ACT	Australian Capital Territory
AK-47	Avtomat Kalashnikova 47 (Assault Rifle)
ARH	Armed Reconnaissance Helicopter
BTL	Blade Test Loading
CEEFC	Centre of Excellence in Engineered Fibre Composites
CF	Centrifugal Force
CFT	Composite Fibre Technologies
CH-47	Cargo Helicopter 'Chinook' 47
dBm	Decibel-milliwatts
DA	Disk Area
DL	Disk Loading
<i>E</i>	Modulus of Elasticity
FBG	Fibre Bragg Grating
FEA	Finite Element Analysis
FRP	Fibre Reinforce Plastic
<i>g</i>	Gravity
GFR	Glass Fibre Reinforced
GFRP	Glass Fibre Reinforced Plastic
$G_{i,j}$	Shear Modulus in <i>i,j</i> Direction
IEAust	Institute of Engineers Australia
ISO	International Organization for Standardization
LVDT	Linear Variable Differential Transformer
MANPADS	Man-portable Air-defence Systems

MRH	Multi Role Helicopter
NACA	National Advisory Committee for Aeronautics
NATO	North Atlantic Treaty Organisation
n_{eff}	Effective Refractive Index
NH90	Naval Helicopter 90
NHI	NATO Helicopter Industries
Nm	Nanometre
OHS	Occupational Health and Safety
PPE	Personal Protective Equipment
QLD	Queensland
R	Reflectivity
RCWL	Response Centre Wavelength
SAM	Surface to Air Missile
SG	Strain gauge
SHM	Structural Health Monitoring
SI	International System of Units
S_u	Ultimate Tensile Strength
S_y	Yield Strength
TP	Test Plan
US	United States
USQ	University of Southern Queensland
ν	Poisson Ratio
Wk	Week
WS	Wavelength Start
Δ	Change in/of
ΔW	Wavelength Delta
ϵ	Ultimate Strain

λ	Wavelength
Λ	Grating Period
λ_B	Bragg Wavelength
ν	Poisson's Ratio
$\sigma_{i,j}$	Stress in i,j Direction
3D	Three Dimensional

CHAPTER 1 - INTRODUCTION

‘Unlike for the automobile driver, there are no repair stations in the sky for the pilot’ (common aviation saying)

1.1 Project Aim & Objectives

Following are the project aims and objectives as detailed within the project specification located at Appendix A.

1.11 Project Aim

This project seeks to investigate the use of fibre-optic sensors (FBG) in the structural health monitoring of a fully FRP constructed, battlefield helicopter rotor blade (CH-47 Chinook) via the use of FEA modelling and performing static strain and vibration testing for both pre and post simulated battlefield damage.

1.12 Project Objectives

1. Research helicopter rotor blade construction, maintenance, loading, fatigue, stresses and strains.
2. In particular, research CH47 Chinook helicopter mission profiles and loads, typical battlefield damage and damage criteria.
3. Create an appropriate FEA model using CREO 2.0 and Abaqus software via physical measurement, profiling and physical testing of a rotor blade test section.
4. Manufacture appropriate rotor blade testing clamp and jigs and fixtures.
5. Conduct testing to validate FEA model using FBG & electrical strain sensors.

6. Apply simulated battlefield damage to rotor blade (physical) and modify FEA model to reflect this damage.
7. Re-conduct structural testing.
8. Verification of FEA Model.

1.2 Project Significance & Benefits

The following section describes the significance and benefits of this research project.

1.21 Significance

Catastrophic failure of helicopter rotor blades has been the cause of loss of life and aircraft and whilst not common, is of significant concern. As such rotor blade serviceability is closely managed by operators. Additionally, helicopter rotor blades have a 'throw away' life applied to them that must not be exceeded. Any improvement in the SHM of rotor blades has the potential to extend the useable life of the blade, reduce maintenance and improve safety. Conversely, use of these components outside of the design usage spectrum for extended periods may introduce unsafe conditions. Improved SHM of rotor blades may lead to a reduction in service life; however, may provide significantly enhanced safety, in turn avoiding the resultant financial and personal cost in the event of component failure. The outcomes of this project will provide firsthand knowledge and make contributions towards the development of SHM systems.

1.22 Initial Benefits

1. Provide a better understanding of the structural response of a helicopter blade by validated FE methods.
2. Preliminary application of FBG sensors in helicopter rotor SHM.
3. Investigation of the effects and consequently the remaining life of a damaged helicopter blade.

1.23 Long Term Benefits

1. Further future development may result in these investigations enabling the evaluation of damaged rotor blades by military engineers.
2. Is a step in the potential use of FBG sensors within helicopter rotor blade structures, leading towards the development of embedded FBG sensor networks during the manufacture of rotor blades.

CHAPTER 2 - BACKGROUND & LITERATURE REVIEW

2.1 Introduction

This chapter will present some background information and the material reviewed as part of the literature review. In particular, it will establish the need for structural health monitoring (SHM) of fibre composite structures, specifically helicopter rotor blades, types of defects, modes of failure and current methods of analysis, to include finite element analysis (FEA) and SHM monitoring. Academic works, text books, technical journals, relevant helicopter manufacture publications (where able) and various credible internet sources have been accessed as part of this review.

Subsequent chapters will further consider the implications of this review in the compilation, design and conduct of the experimentation and methodologies employed within this research project.

In addition, this chapter will investigate currently available literature in the areas of fully helicopter composite blade design, common defects and types of battlefield damage and other relevant areas.

Investigation into FBG and other alternate methods of failure detection of composite structures will be conducted with respect to the application on battlefield helicopter rotor blades.

2.11 Helicopter and Rotary Wing Evolution

‘On December 17, 1903, Wilbur and Orville Wright made four brief flights at Kitty Hawk with their first powered aircraft. The Wright brothers had invented the first successful airplane’ (Smithsonian National Air and Space Museum 2014). It would be another four years before the first serious claim of manned flight in a helicopter was made. Paul Cornu (1881–1944), a Frenchman, with his father Jules and brother Jacques, pioneered the development of three rotating-wing aircraft concepts from 1906 to 1908. Paul Cornu claimed that he flew a twin-rotor helicopter concept for the first time in November of 1907; however, a more recent engineering analysis of this claim has proven this as unlikely to be true (Leishman & Johnson 2007), thus pushing the initial helicopter flight sometime farther back into the 20th Century.



Figure 1. Paul Cornu's helicopter as constructed in mid-1907 (*Source: Leishman & Johnson 2007*)

From this early concept, momentum grew as it was recognised that a vehicle with the ability to both vertically take off and land would have significant advantage over the traditional fixed wing aircraft. The period between 1907 through 1940 saw limited investment as the technology and designs were limited at best.

The advent of the Auto-gyro allowed for the development of the lift mechanism in isolation of the power and propulsion systems. This resulted in rapid gains in rotor lift, stability and control systems technology.

With the advent of World War II in the early 1940's the potential for vertical take-off and landing was truly recognised, none-more-so than the militaries of the day whom provided significant funding in a race to perfect this technology for the upcoming conflict.

Following market ups and downs, the development of gas turbine engines was the catalyst for the rapid development of the helicopter for both combat and civil employment. This, in combination with subsequent conflicts has provided the current generation of highly specialised helicopters from retro-fitted previous designs such as the Boeing CH-47 medium lift cargo helicopter to the largely fibre composite constructed Eurocopter, Armed Reconnaissance Helicopter (ARH) and the NATO Helicopter Industries (NHI), Multi-Role Helicopter (MRH). In these aircraft fibre composites are utilised in the construction of structural, load carrying external panels, frame members and bulk-heads.



Figure 2. The MRH and ARH utilise fully composite fibre components.

The more recent and rapid improvement in helicopter performance and reliability is in part at least due to the significant redesign, design improvements and advanced materials used to manufacture one of the most critical components of the aircraft; the rotor blade.

2.12 The CH-47 Chinook Drive and Control System Overview

Given the number of differing rotor blade designs, materials and methods used to manufacture them this research will focus on the Boeing CH-47 (Cargo Helicopter) medium lift helicopter, and in particular one of its six rotor blades.



Figure 3. The Boeing CH-47 Chinook battlefield helicopter.

The CH-47 has six counter rotating rotor blades with the aft blades rotating clockwise and the forward blades rotating in counter-clockwise direction. Each of the six rotor blades is approximately 8.4 meters in length not including the hub assembly, and 9.14 m from the centre of the rotor hub assembly. The CH-47 rotor blade is a predominately FRP composite constructed blade.

Following is an indicative guide to give the reader a context for the aircraft size and proportionality of the rotor blades. US imperial units have been used (Boeing 2014).

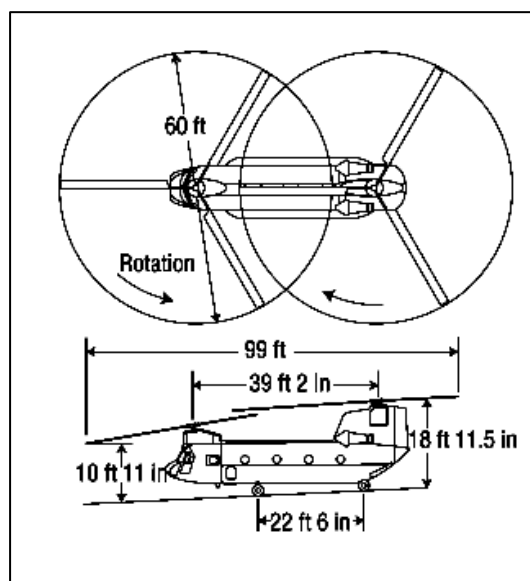


Figure 4. CH-47 proportion overview (Source: Boeing 2013).

Lift is produced by the rotor system which consists of two fully articulated, counter-rotating rotor heads. Each rotor head has three FRP blades. The forward rotor is driven by the forward transmission through a vertical rotor drive shaft. The aft rotor is driven by the aft transmission through a second, much larger, vertical drive shaft. The rotor heads consists of a hub connected to three pitch-varying links by three horizontal hinge pins which permit blade flapping in an up and down motion. Static mechanical stops on the top and the bottom of the hub limit the blade flapping motion. The aft rotor head is equipped with centrifugal droop stops which provide an increase in blade flapping angle for ground and flight operation.

Fig. 5 details the CH-47 drive system components with the rotor heads and blades removed.

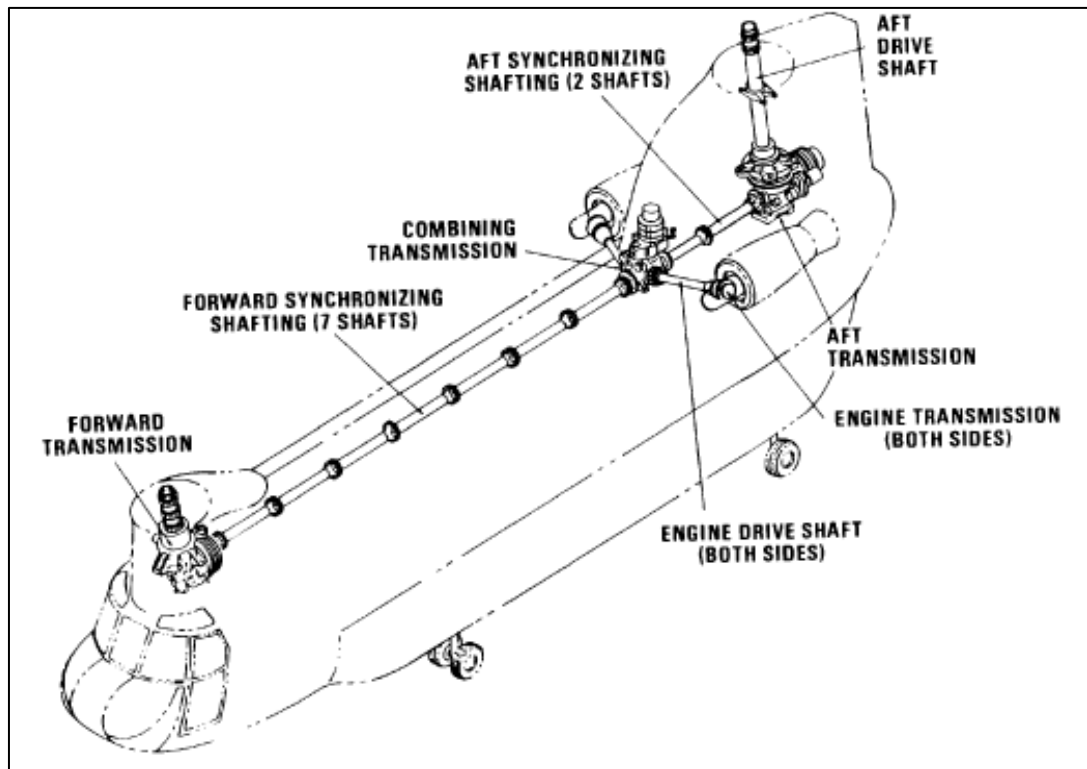


Figure 5. CH-47 drive system (Source: US Army 2002).

Following is a diagram depicting the CH-47 rotor head assembly. It details the blade roots ends attached to the pitch varying housing. NOTE: For brevity not all components in this figure have been discussed in the preceding text.

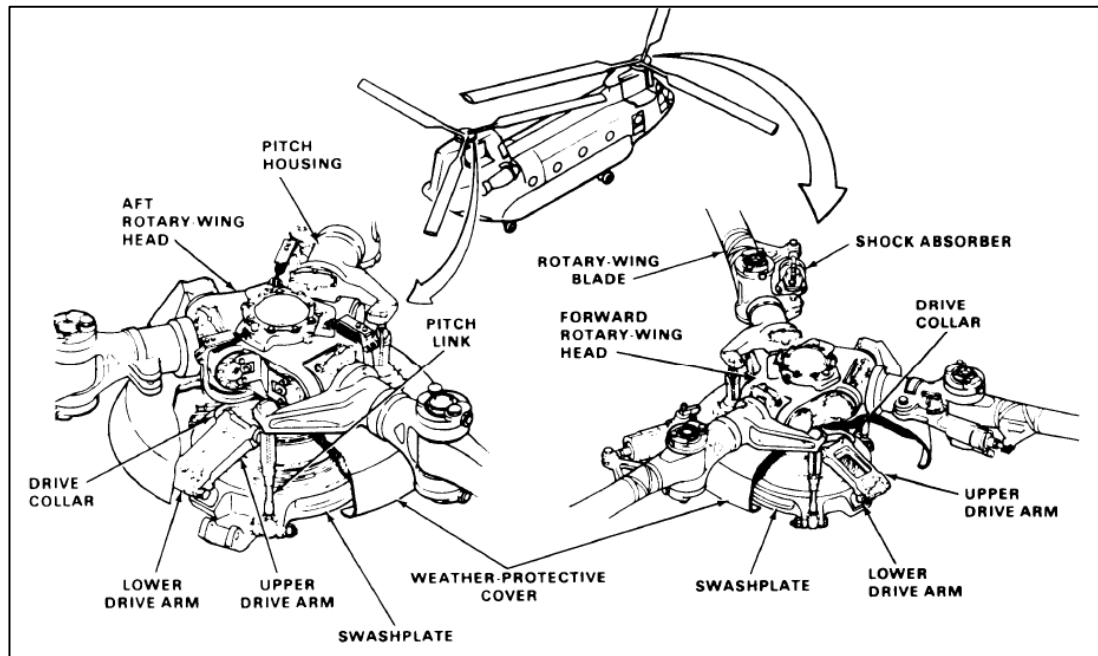


Figure 6. CH-47 rotor head assembly (Source: US Army 2002).

Mounted coaxially over the pitch-varying shafts are pitch-varying housings to which the lead / lag dampener is attached. This direct action shock absorber is attached to the blade and to the pitch-varying housing to control the rate of fore / aft movement of the blade. Each pitch-varying shaft is connected to the pitch-varying housing via a laminated, tie bar assembly. The high tensile strength and low torsional stiffness of the tie bar retains the blade against centrifugal force and allows the blade pitch to change about the pitch axis. Blade pitch changes are accomplished by three pitch-varying links connected from the rotating ring of the swash plate to the pitch-varying housing on each rotor blade (U.S. Army 2002).

The following diagram details a forward rotor head depicting the pitch, flap and lead / lag axis. The rotor blade is attached to the rotor head at the vertical pin which also allows for the lead / lag movement.

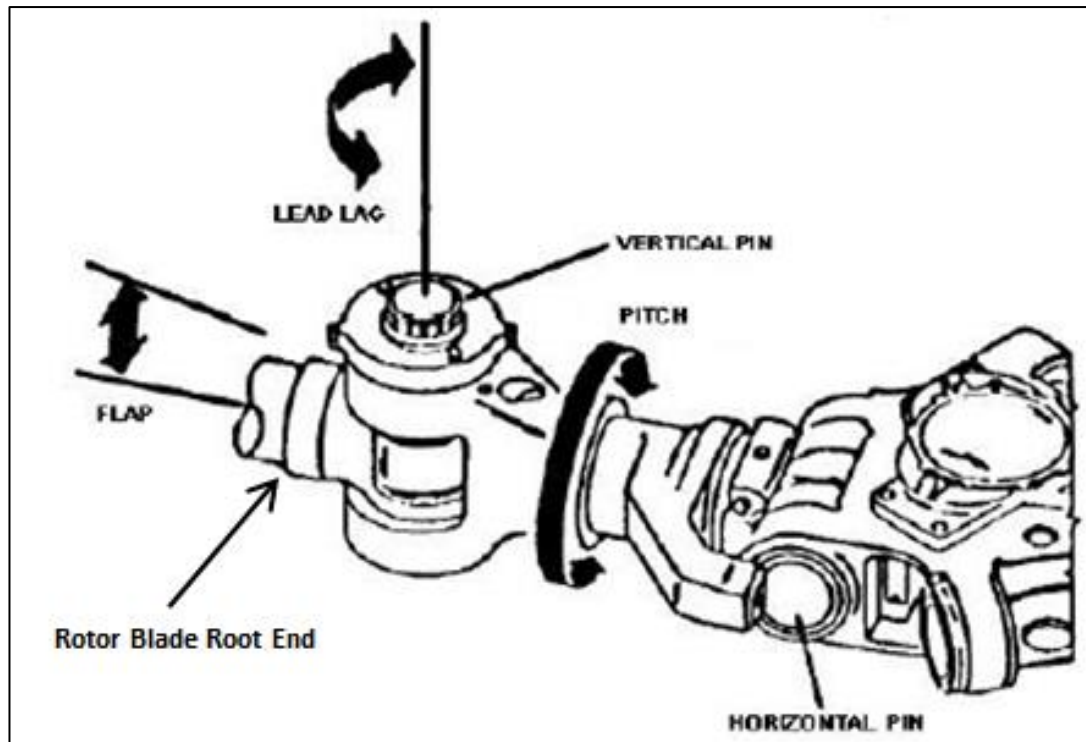


Figure 7. Forward rotor head blade attachment (Source: US Army 2002).

Cyclic pitch changes (the change of blade attitude independently of one another pending the position of rotation) are accomplished by tilting the swash plate. Collective pitch changes (alteration of all the blade attitudes simultaneously) are achieved by vertical movement of the swash plate. Combined collective and cyclic pitch changes result from combined control inputs by the pilot.

This system provides lift (thrust) to the airframe via two 4,777 maximum shaft horsepower Honeywell T55-GA-714A (Honeywell Aerospace 2005), turbo-shaft gas turbine engines. This is through a series of five transmissions and nine synchronising drive shafts to the two vertical drive shafts driving the two fully articulated rotor heads and blades. Cockpit induced flight control inputs will change blade incidence to enable varying flight attitude and direction changes (U.S. Army 2002).

These systems and control methods are utilised by the pilot to fly the rotor blades as required for directional flight control.

2.13 CH-47 Chinook Rotor Blade

The CH-47 rotor blade studied in this project is one of the largest helicopter rotor blades currently in both civil and military service (US Army 2002).

The CH-47 rotor blade external tabulated dimensions, weight and radius of rotation inclusive of rotor head assembly diameter are presented in Table 1 below. Load share and velocity are also detailed.

Table 1. CH-47 Rotor blade tabulated data.

	Imperial	Metric	Notes
Length	330.5 inches	8.395 m	From centre of Blade Attachment Pin to Blade Tip Cap.
Cord	32.0 inches	0.813 m	From Nose Cap to Trailing Edge, not inclusive of Trim Tab.
Thickness	6.0 inches	0.153 m	At thickest point.
Weight	357.0 lbs	161.0 kg	158 – 163 kg range.
Radius of Rotation	360.0 inches	9.144 m	Inclusive of Rotor Head Diameter.
RPM	225 RPM	225 RPM	Flight Idle RPM
Load Share	18371.12 lbs	8333 kg	Average per blade at maximum all up weight.
Linear Blade Tip Velocity	482 mph	775 km/h	Relative to fuselage.

The term ‘flight ideal’ mentioned in the above table refers to the rotor RPM for sustained, steady state flight such as at altitude cruise.

The CH-47 rotor blade is constructed largely of glass fibre-reinforced plastic (GFRP); however, has several metallic components due to the specific requirements of the application. These and rotor blade construction will be discussed further in the following paragraphs.

During the blade design process the US Army and Boeing agreed that a GFRP rotor blade was a superior choice to that of a fully metallic, primarily alloy constructed blade due to the following considerations:

1. Glass fibre is non-corrosive,
2. Crack propagation is considerably slower due to the characteristics of the fibreglass composition, and
3. Represented a significant improvement in mitigating ballistic damage (U.S. Army CH-47 Helicopter repairer supervisor hand-out, 2002).

In the available literature, the US Army which is an Authorised Engineering Organisation for the Chinook, describes the CH-47 rotor blade as being constructed of Fibreglass (U.S. Army 2002). Whilst this is in the most part true, although very general, there are several metallic components used within the blade to include a titanium erosion nose cap, stainless steel nose weights (partial blade length), bronze-alloy damper attachment bushings and the blade tip balance weight assembly consisting of various metallic materials to include stainless steel and Inconel alloy.

The rotor blade flight surface comprises of a composite fiberglass, titanium and Nomex core assembly, with the main structural component being a torsion tube, or as it is commonly known a D-spar due to its physical form. The D-spar is manufactured using what is believed to be an E-glass and epoxy resin.

A breakdown of the rotor blade sub-components is presented as follows.

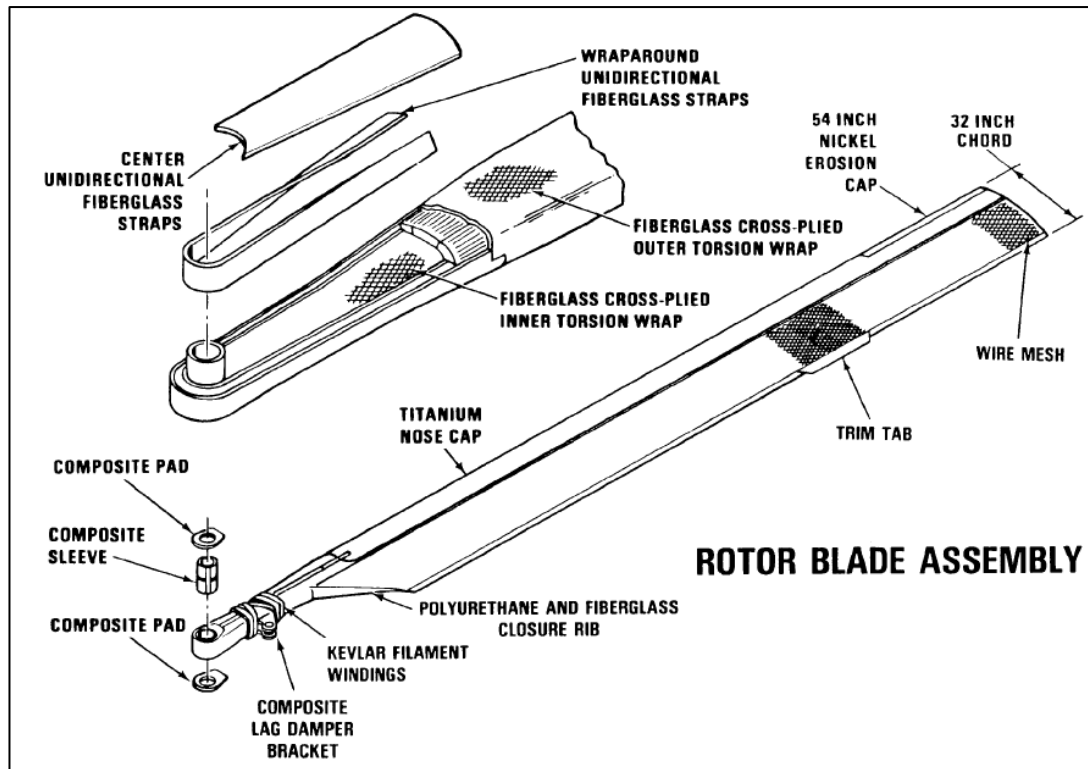


Figure 8. Overview of the CH-47 rotor blade (*Source: US Army 2002*).

Many of the above components are not within the scope of this project as they would overly complicate the modelling and physical testing results. In particular, the blade root-end has been avoided due to the complexity and difficulty in physical test results interpretation. As a result, the outboard section of the blade has been selected for the testing and modelling, and is used to depict the internal components of the blade in Fig. 9 below.

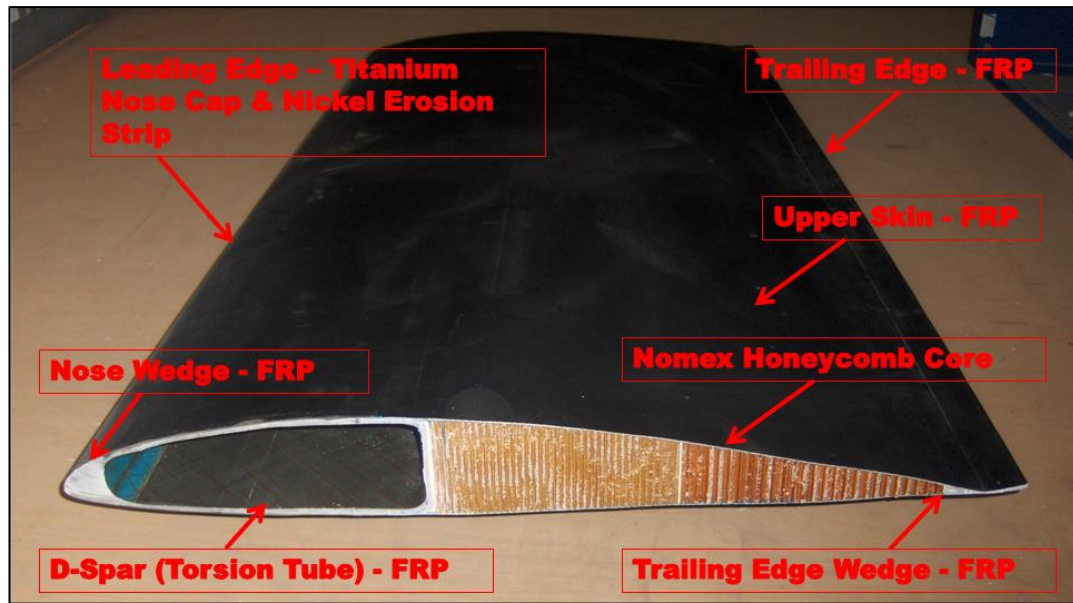


Figure 9. Rotor blade detailed cross section.

Above is a detailed cross-sectional projection of the CH-47 composite blade (flight surface) and the sub-components used in its manufacture. This is the actual blade section modelled and used in physical testing and FEA model validation.

It can be seen from the above figure that the internal sub-components of the blade are few; however, they are in some cases difficult to delineate from one another such as the skin and the adjoining sub-components to which it is bonded. Of additional note is the nose wedge and D-spar interface where the actual surfaces are very closely bonded giving the appearance of a single structure.

The Boeing-Vertol VR-7 Airfoil with tab (vr7b-il) is a National Advisory Committee for Aeronautics (NACA) recognised aerofoil for the use on the CH-47. With many hundreds of registered NACA aerofoils, this project will solely focus on the Boeing-Vertol VR-7 aerofoil; however, the research and testing methodology will be such that it may be applied to additional composite rotor blades.

Adding to the complexity of this research is the lack of detailed information for the Boeing-Vertol VR-7 Airfoil with tab (vr7b-il). It is believed this is a result of the component being enlarge used for military applications and therefor attracts a level of security over and above that of a similar civil component.

This resulted in the necessity for flexural, tensile and calcination testing of the major sub-components such as the D-spar and skin in order to create an adequate FEA model.

Additionally, the blade external profile required physical measurement in order to validate and correct the publically available NACA profile data. This was achieved with the use of Vernier callipers and a precision engineers steel rule.

The following table details the verified and corrected NACA profile data, where the blade cord wise span is equal to 1.0 unit (814.4 mm = 1 unit).

Table 2. VR-7 Aerofoil with tab (vr7b-il) (Aerospace.illinois.edu, 2014).

Upper Surface Profile		Lower Surface Profile	
X - Axis	Y - Axis	X-Axis	Y-Axis
0.00	0.00	0.00	0.00
0.005	0.0165	0.005	-0.00575
0.01	0.0218	0.01	-0.0081
0.02	0.0298	0.02	-0.0109
0.03	0.03615	0.03	-0.0129
0.04	0.0415	0.04	-0.01445
0.05	0.04605	0.05	-0.01585
0.06	0.05025	0.06	-0.01710
0.07	0.0541	0.07	-0.01805
0.085	0.0593	0.085	-0.01985
0.102	0.0645	0.102	-0.02145
0.12	0.0691	0.12	-0.02285
0.14	0.0737	0.14	-0.0241
0.16	0.0775	0.16	-0.0251
0.18	0.0808	0.18	-0.0260
0.20	0.0838	0.20	-0.0266
0.225	0.0867	0.225	-0.0273
0.255	0.0892	0.255	-0.0280
0.29	0.0909	0.29	-0.0285
0.33	0.0914	0.33	-0.0289
0.37	0.0905	0.37	-0.0290
0.41	0.0887	0.41	-0.0285
0.45	0.0856	0.45	-0.0275
0.49	0.0816	0.49	-0.0260
0.53	0.0767	0.53	-0.0240
0.57	0.0710	0.57	-0.0220
0.61	0.0646	0.61	-0.0199
0.65	0.0580	0.65	-0.0179
0.69	0.0514	0.69	-0.0158
0.73	0.0447	0.73	-0.0138
0.77	0.0374	0.77	-0.01075
0.81	0.0301	0.81	-0.00845
0.845	0.0235	0.845	-0.0064
0.88	0.0167	0.88	-0.00425
0.91	0.0105	0.91	-0.00235
0.935	0.0062	0.935	-0.0006
0.96	0.0050	0.96	0.00
1.0		1.0	0.00

A computer plot of the above data produces the profile required for FEA modelling and was manually entered into the modelling programs such as MS Excel, Abaqus and Creo 2.0 as required.

The following figures are plots of the profile data which depicts both the external profile and the cord-wise centreline and camber mean-line in blue and brown respectively.

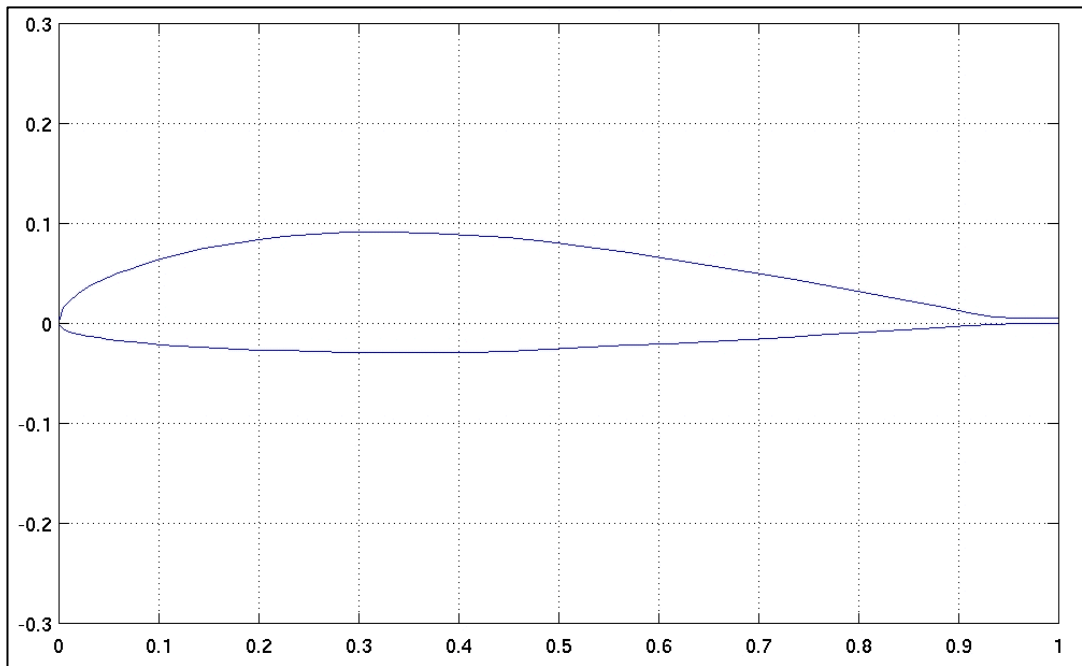


Figure 10. Profile plot of the corrected data.

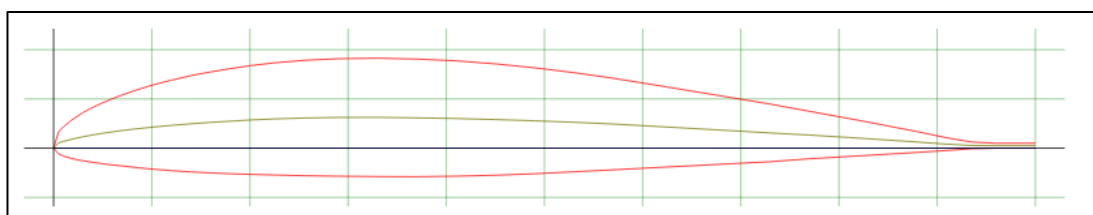


Figure 11. Blade cord-wise centreline and camber mean-line plot.

The large surface area, profile and dynamic nature of the rotors whilst in operation exposes them to several differing types of damage and may exacerbate existing defects leading to partial or complete failure. These, along with rotor loads and forces are discussed further in the following section.

2.14 Rotor Loads and Forces

The primary loads encountered by a helicopter rotor blade in both hover and flight are the centrifugal force (CF) and flap and chord wise bending moments. Combinations of these forces result in a complex and dynamic loading environment to include elastic flap bending, lag bending, elastic twist, and axial deflections. Previously, Fig. 7 described flapping and lead/ lag orientations. In addition, whilst in flight the helicopter fuselage may be assumed to be a rigid body undergoing six degrees of freedom (Kim 2004).

Kim (2004, p.1-2) had the following to say about the calculation of flight loads in his paper ‘Analytical calculation of helicopter main rotor blade flight loads in hover and forward flight’:

The calculation of rotor loads is a difficult task because of the complex interactions of structural, inertial, and aerodynamic forces acting on the rotary wing. Basically, it is necessary to calculate the periodic aerodynamic and inertial forces of the blade, and thus the resulting motion of structural components. Since the higher harmonic blade loading is the principal source of high loads, an accurate analysis of the rotor aerodynamics is required, including the effects of the rotor wake, stall, and compressibility. The high frequencies involved and the importance of resonance excitation also require good inertial and structural models.

As presented by Kim, this is a very complicated task made even more so due to the lack of publically available information and data for military components such as the CH-47 rotor blade. In addition, to apply accurate test conditions capable of replicating these forces would not be possible, or be within the scope of this research.

As a result, a simplified load methodology was required. As stated by Prouty (1990, p. 4), ‘rotor thrust divided by the disk area (DA) gives the disk loading (DL)’.

The disk area is defined by the area swept by the blades of a rotor systems lift producing surfaces. In the case of a tandem-rotor helicopter such as the CH-47, where one rotor over-laps the other, only the projected area should be used (Prouty 1990, p. 6).

Making the assumption that the rotor thrust is equal to the aircraft gross weight a simplified loading calculation may be performed which in turn may be mathematically reduced to a per-blade load.

This loading, whilst a pressure load, was calculated and used in the testing; however, was applied as a bending load resembling that of the flapping / coning bending moments as mentioned by Kim (2004, p. 1). These calculations are further presented in paragraph 14.2.

2.2 Composite Materials.

Hodgkinson (2000, p.1) stated that ‘in the mind of the general public the term ‘composite materials’ is largely either misunderstood or not understood at all’.

Composites are produced when two or more materials or phases are used together in order to provide a combination of properties that could not be achieved via the use of a single material (Askeland & Phule 2008). Composite materials can be used where unusual or differing properties are required in differing directions, axis or planes. These may include combinations of stiffness, corrosion resistance, hardness, temperature resistance, torsional strength or strength to weight (Askeland & Phule 2008).

At the macro-level, steel reinforced concrete is an example whilst at the micro-level, glass-fibre reinforce plastic, such as that used in the subject rotor blade, is an example. In both cases the fibres, or steel reinforcing bars, provided the strength in tension whilst the resin matrix, or concrete, serves the purpose to bind the reinforcement fibres into a single structural system.

The resin must hold the reinforcement in place and act as a load path for transfer between the fibres. Through a combination of adhesive and cohesive characteristics, the resin enables the development of a single material system which provides not only tensile capacity but compressive and shear capacity as well (USQ Mechanics and Technology of Fibre Composites 2013).

The following figure provides a photomicrograph of actual composite cross section (left) and idealized representations of fibre packing: hexagonal (centre) and square (right).

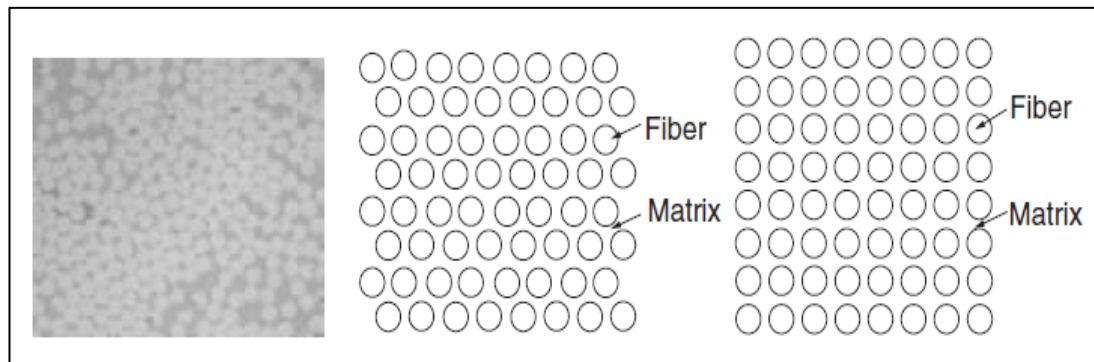


Figure 12. Fibre Composite cross sections (*Source: Marks' 2008*).

In a relatively short period of time, modern composites as we know them today have progressed significantly in both quality and performance which is largely due to the US Military and space agencies. While not being the largest consumer of composite materials in terms of volume, military development has been the major driving force behind material and production method development with early experimentation beginning in 1941 (USQ Mechanics and Technology of Fibre Composites 2013).

This experimentation continues today with many modern, and leading edge military weapon platforms, such as aircraft and maritime vessels utilising composite materials in many applications thought not possible only a few decades ago, such as stressed panels on aircraft (Hugh, J 2008).

The NHI MRH helicopter is an example of an aircraft employing several fibre reinforced panels comprising of Kevlar, boron & carbon fibres in load carry applications.

Applications such as the fuselage and tail boom sections utilise Kevlar, boron & carbon fibres whilst the rotor blades use carbon/ glass Nomex honeycomb and Rohacell foam in their construction (Augusta-Westland 2013).

In addition to military and aviation applications, composites have been used in the automotive industries and in more recent times are becoming more widely accepted in the field of civil engineering.

Applications such as road bridges, walk ways and reinforcing bars are becoming readily available by specialised companies (Wagners' CFT 2014).

Askeland & Phule (2008) have said that 'most fibre-reinforced composites provide improved strength, fatigue resistance, Young's modulus and strength to weight ratio by incorporating strong, stiff, but brittle fibres into a softer, more ductile matrix'.

The strength vs stiffness properties of composites materials are a key consideration in structural applications (Hollman 1998) and are presented below when compared to other engineering materials in a comparison of material specific stiffness vs specific strength.

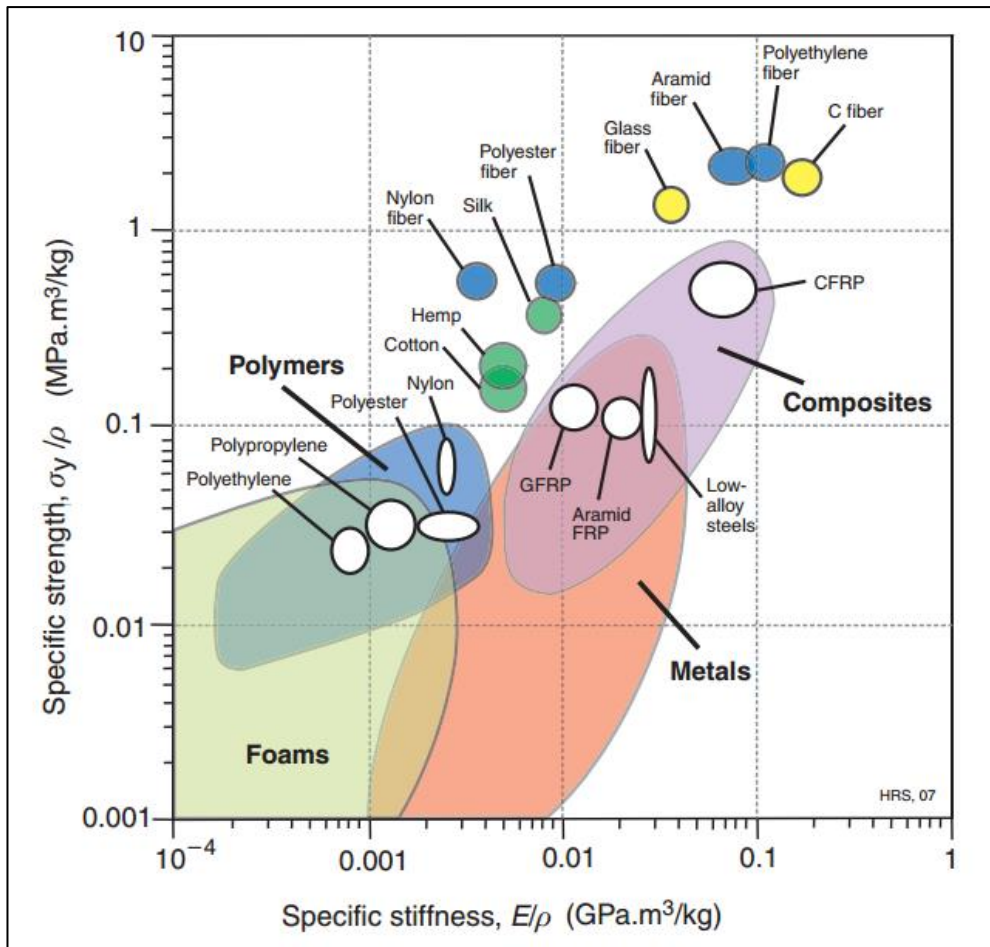


Figure 13. Specific stiffness vs specific strength chart (Source: Ashby, M et al 2007).

The Young's modulus to density ratio is another key area for consideration, in particular within aviation applications, and is presented in the following comparison of material modulus vs density with GFRP underscored in red.

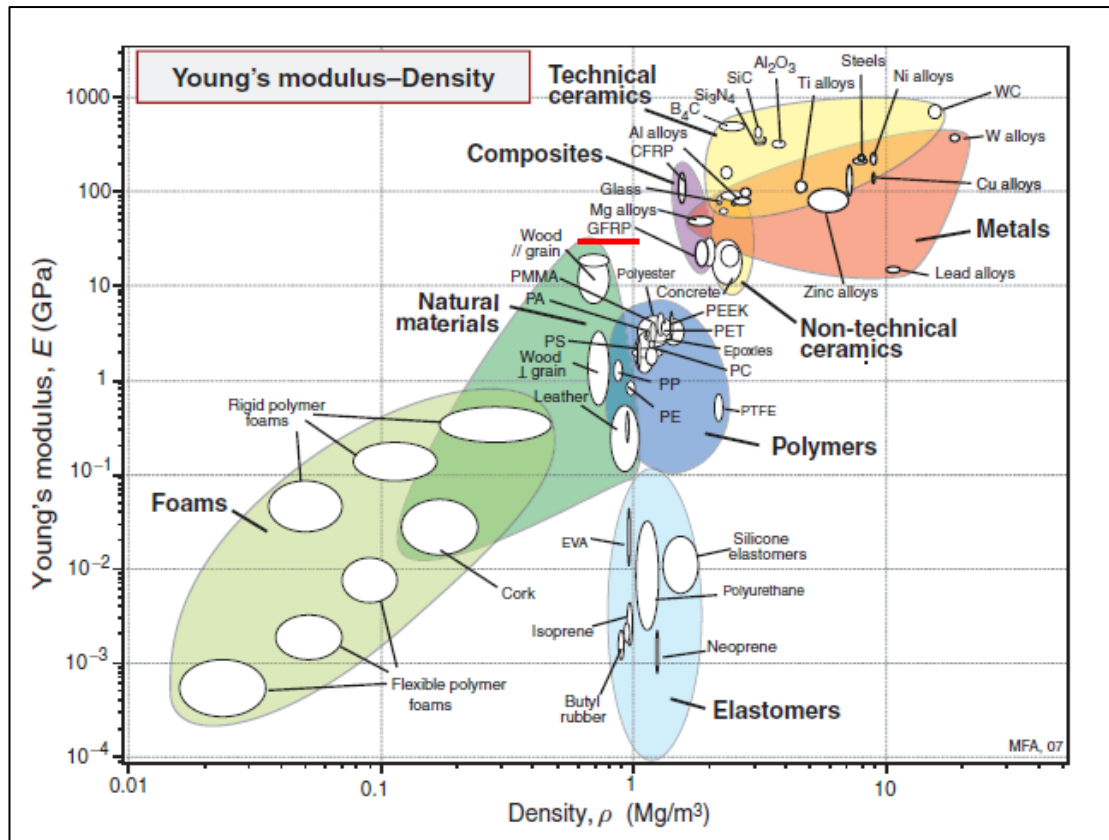


Figure 14. Material modulus vs density chart (Source: Ashby, M et al 2007).

The Young's modulus to density ratio for glass fibre reinforced plastics (GFRP) with a polymer or epoxy matrix which is currently one of the most commonly used FRPs can be seen.

2.31 Glass Fibre-Reinforce Plastics (GFRP)

Glass fibre reinforced plastics (GFRPs) are composite materials composed of a matrix, often polymer, reinforced with glass fibres.

GFRPs are a commonly used substitute for more traditional structural materials, such as steel. This is largely due to the improvement of GFRP mechanical properties in more recent times.

A more recent, and extreme example of GFRP being used to replace a longstanding and conventional steel product, is the work being performed by Deshmukh & Jaju (2011) in their research titled, *Design and Analysis of Glass Fibre Reinforced Polymer (GFRP) Leaf Spring*.

In this work Deshmukh & Jaju conducted experimental testing with the assistance FEA software showing stresses and deflections which were validated with analytical and experimental results. Compared to the steel spring, the composite spring has stresses that are lower and the composite spring weight was approximately 74% lower. From this, it is easily concluded why GFRP is being used in applications where a good strength to weight ratio is required such as rotor blades.

This is particularly true within the aviation industry where small amounts of additional weight represent potentially severe penalties, such as economic losses due to extra fuel consumption or loss of passenger / load capacity. It is for this reason that this industry is a pioneer of fibre composite development and use along with the US Military (USQ Mechanics and Technology of Fibre Composites 2013).

2.32 Glass Fibres

Glass fibres are broken down into the four primary categories of E, S2, A and C glass of which E-glass is the most common (USQ Mechanics and Technology of Fibre Composites 2013). The general properties and advantages of glass fibres which make them a common choice are:

1. High tensile strength,
2. Heat resistance,
3. Thermal stability,
4. Chemical resistance,
5. Moisture resistance,
6. Fire resistance,
7. Electrical properties: non-conductive,
8. Readily available, and
9. Low comparative cost, as seen below.

As presented above, relative low cost to performance ratio has been a key factor in the employment of GFRP in industry. Whilst pricing of other fibres are reducing as consumption levels increase GFRP remains an economical choice, particularly within the civil construction sector.

The following figure provides a comparison of material modulus vs cost per unit volume chart with GFRP achieving a good balance between cost and performance when overall weight of the material is also considered.

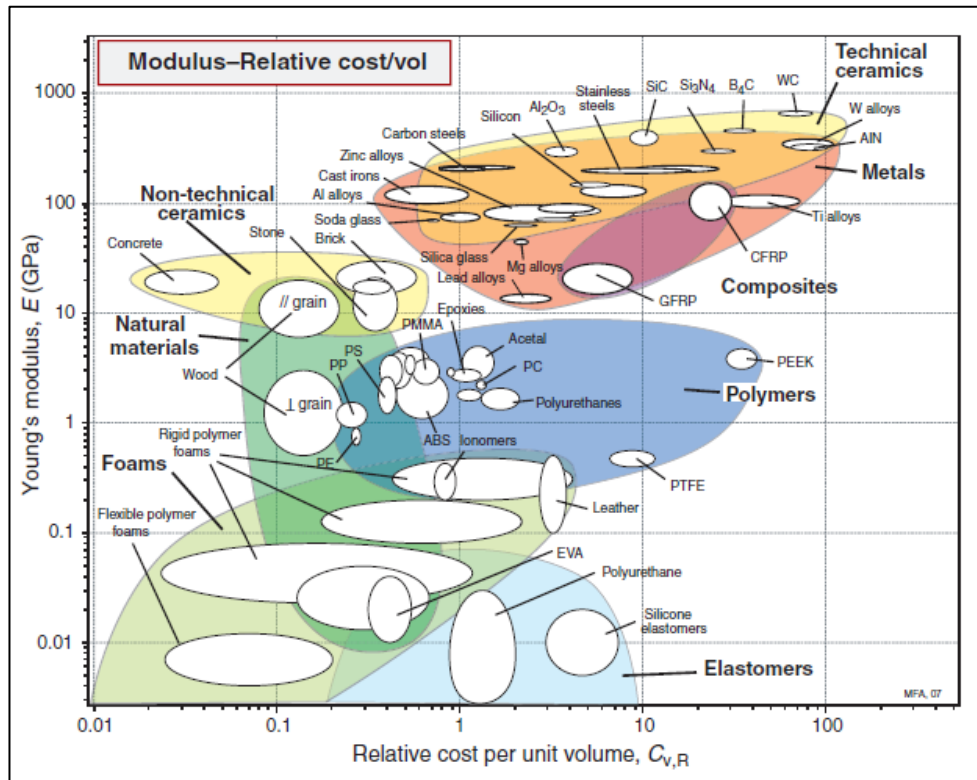


Figure 15. Material modulus vs cost per unit volume chart (Source: Ashby, M et al 2007).

Possibly the greatest advantage of composite structures is the reduction in weight for comparable strength. This reduction in weight was presented by Karbhari, Steenkamer and Wilkins (1997) as three main benefits in civil engineering structures; however, these weight advantages are also, if not more so applicable to other industries, such as aviation as they:

1. Provide a reduced dead weight enabling a higher live load capacity for the same supporting structure as in the case of replacement structures.
2. Provide a reduced dead weight enabling the use of lighter and smaller supporting structures in new structures.

3. Provide a reduced dead weight enabling greater ease of placement without the heavy equipment or machines or additional personnel.

There are however several disadvantages of glass fibres, of concern are the (USQ Mechanics and Technology of Fibre Composites 2013):

1. Low modulus of elasticity (≈ 70 GPa), and
2. Long term performance and service life.

A significant drawback for glass fibres is their long term behaviour as they are known to provide considerably less fatigue resistance when compared to other fibres such as carbon. This is further illustrated in the Fig. 16 below which presents a comparison of material density vs fatigue strength, again with GFRP underscored in red.

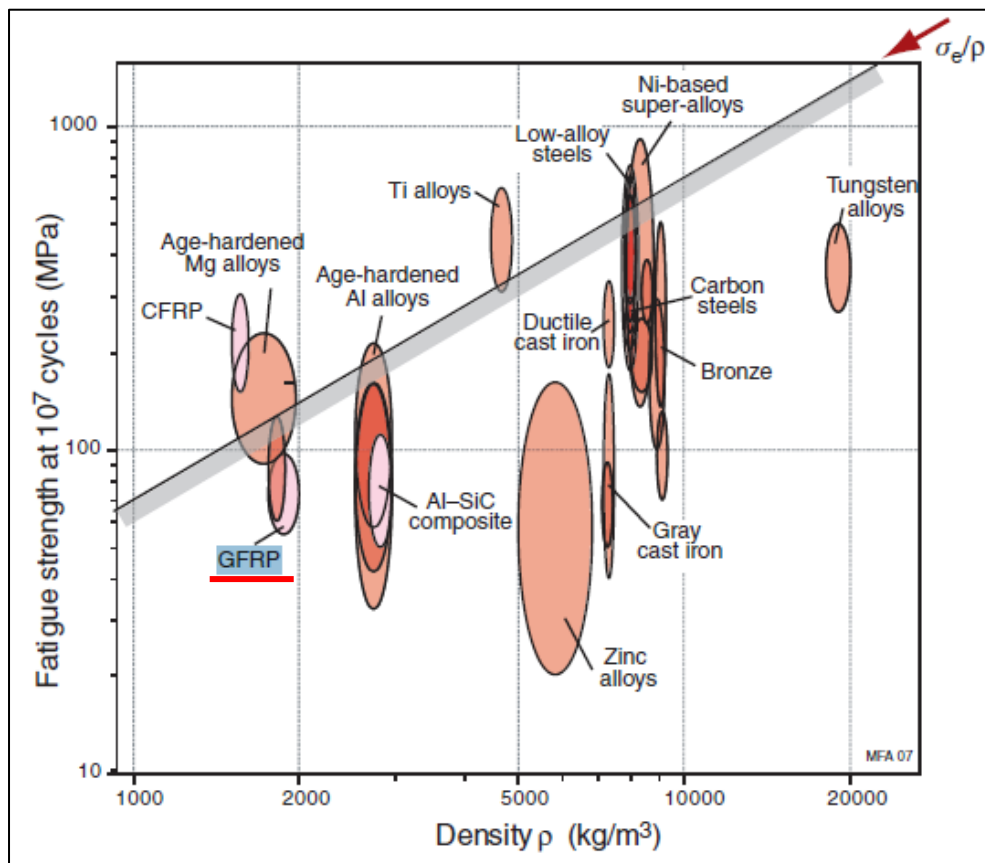


Figure 16. Material density vs fatigue strength (Source: Ashby, M et al 2007).

Additionally, glass fibres suffer from creep, stress rupture and have raised concerns over the performance of the fibre / matrix adhesion in moist or salt water environments (USQ Mechanics and Technology of Fibre Composites 2013).

Despite a move away from GFRP towards lighter FRPs in more recent times, and the above drawbacks, it is the advantages that have driven the aviation industry to accept GFR composites as an effective material in applications such as the CH4-7 rotor blade.

These fibres are contained within a matrix which may be aligned in a particular orientation for a particular load application, may be random or chopped or in the form of a woven mat.

Aligned GRFs are used in the CH-47 rotor blade in order to carry loads along a particular pre-determined load path such as the longitudinal or axial direction due to the centrifugal load.

As was determined during the calcination testing (discussed later) a significant amount of fibre volume was orientated in 0° axis, or length wise to the blade. This is intuitive given the loads experienced by the blade when in motion.

The following figure provides an indicative illustration of aligned, random and woven fibres.

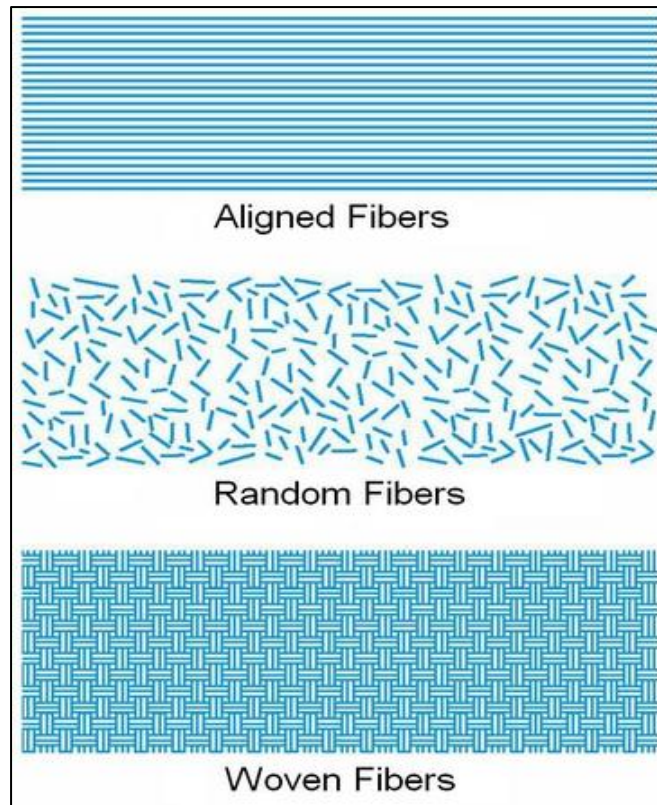


Figure 17. Aligned, random and woven fibres (Source: City college of San Francisco 2014).

The alignment of the fibres is achieved, amongst other functions, by the use of a matrix

2.33 The Matrix

To achieve a high level composite performance, correct selection of both the fibre reinforcement and the matrix (resin) which binds the material together into a cohesive structural unit must occur.

Whilst the fibres possess strength and stiffness properties of approximately two or three orders of magnitude above that of the resin, they are essentially a cable capable of good tensile loading, but little or no compressive or shear capacity the matrix to support them (Ganguli & Prashant 2006).

Therefore the primary function of the matrix is to transmit the force to the fibres which carry the majority of the load, and to carry compressive forces and shear forces tangential to the fibres.

Additionally the matrix protects and separates the fibres and minimises the effects of moisture, oxygen, corrosive environmental factors and damaging light sources such as UV (Askeland & Phule 2008). In turn the matrix may have a protective layer applied such as paint, to protect the matrix itself.

GFRP commonly use two differing matrix materials to include polymer and epoxy resins. Polymer resins may then again be broken down into Thermo-set and Thermoplastics.

2.34 Thermoplastics

Thermoplastics are a polymeric material which is comprised of long chain molecules having no covalent bond between the molecules. This allows the material to behave like a solid at lower temperatures; however, when heat becomes plastic and may be reformed. Once reformed and allowed to cool the material will retain its new shape. This process of reforming may be repeated many times over, or until a breakdown in the materials properties occurs to prevent further reforming.

2.35 Thermosetting

Thermoset polymers are materials have reactive, low molecular weight compounds are cross-linked with covalent bonds to create a single three-dimensional network. Once cured these materials form one network which behaves like one large molecule. As such thermoset polymers cannot be reformed with heat.

Thermosetting polymers are by far the most widely used form of polymeric matrix materials in GFRP composites (USQ 2013).

2.36 Fibre Volume

The larger the volume of fibre with respect to the matrix volume will increase the strength and stiffness of the composite. This is true up to approximately 80% of the volume fraction as the fibres may not be completely contained within the matrix (Askeland & Phule 2008).

2.37 Fibre Orientation

The orientation of the fibres plays a crucial role in effective load carry capacity of the composite. Long unidirectional orientation of the fibres provides anisotropic properties with very good strength and stiffness in the direction of the fibres (Blanc R et al 2006).

Tensile strength vs fibre orientation and stress for E-glass fibres reinforced with an epoxy matrix are presented below. It is easily seen that the maximal condition is achieved when the fibre is parallel to the load path.

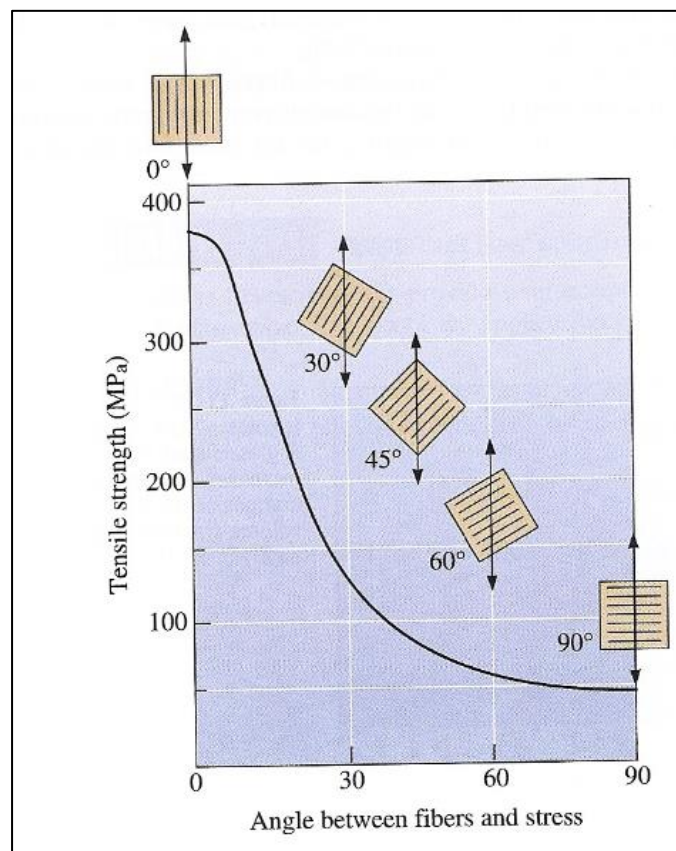


Figure 18. Tensile strength vs fibre orientation and stress for E-glass fibres (Source: Askeland, P & Phule, P 2008).

Layering of these fibres, as plies, allows tailoring of the material to meet very specific load conditions whilst minimising excessive material in others where it is not required.

Fibre orientation of each individual layer is specified via an angle of either a positive or negative sense, from the primary fibre direction which is denoted as 0° . The following figure presents unidirectional plies (a) with aligned fibres which can be used to create multi-layered composite structures resulting in good strength in a unidirectional sense (0°). Whilst more complicated lay-ups (b) may provide strength in differing directions ($0^\circ/\pm 45^\circ/90^\circ$) depending on the fibre orientation, as in the case of the Ch47 D-spar and skin.

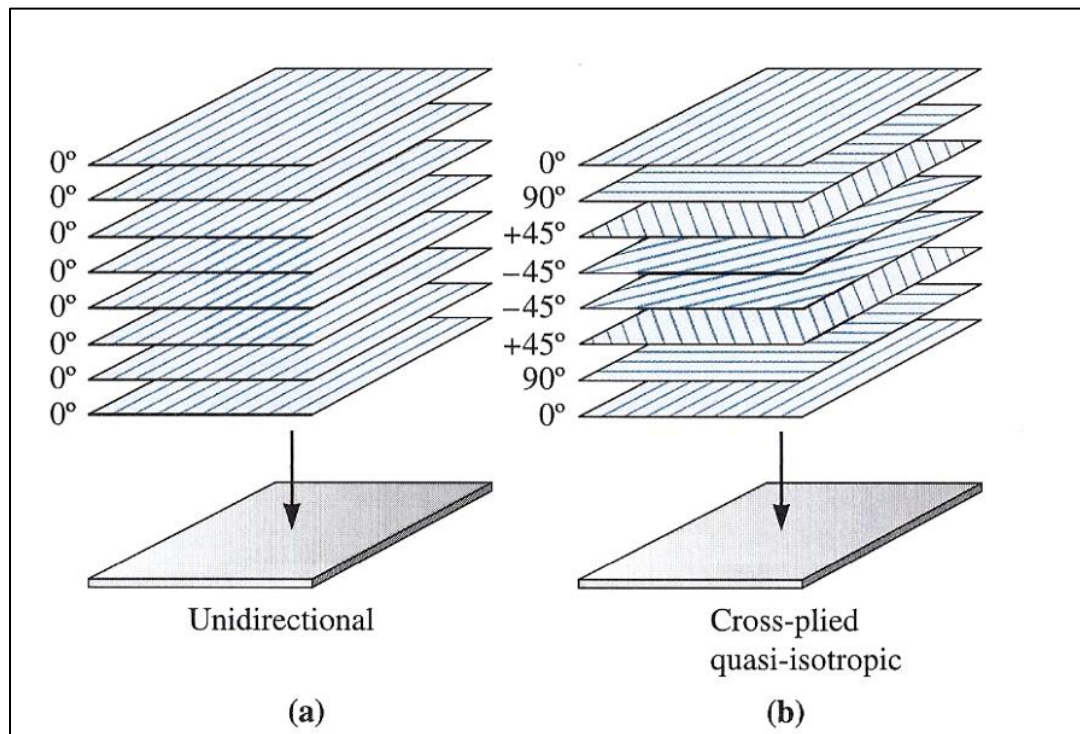


Figure 19. Unidirectional & multi-directional plies (Source: Askeland, P & Phule, P 2008).

2.4 Methods of Manufacture of GFRP Components and Sections

The following section details some common methods of manufacture for GFRP components and structures such as the rotor blade D-spar and skin.

2.41 Pultrusion

Pultrusion is a process where continuous fibres are drawn through a resin bath and into a die to both form and cure the fibre-resin composite into the desired shape.

Generally speaking the process consists of five steps (Groover 2007):

1. Fibre feeding,
2. Resined impregnation,
3. Pre-die forming,
4. Shaping and curing, and
5. Cutting to length.

The following diagram outlines the general pultrusion process in which the fibre path flow is from left to right.

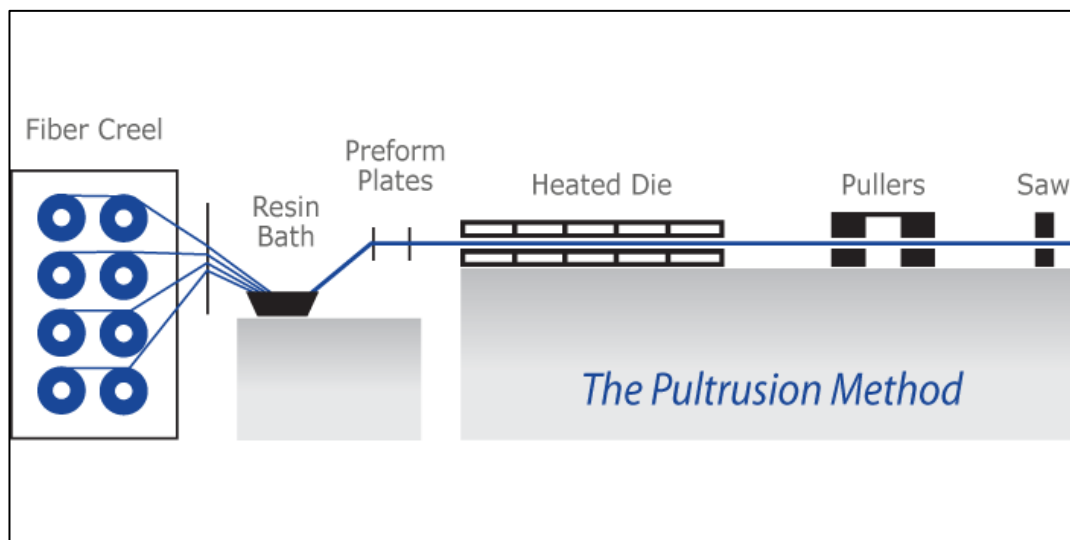


Figure 20. General pultrusion process (Source: Universal pultrusion 2013).

Whilst no documentary evidence is able to be obtained, it is believed by the author that this process may be used to manufacture components such as a rotor D-spar.

2.42 Compression / Pre-form Moulding

This process involves the placement of pre-cut fibre matting and additional components into a mould section.

The mould section is then charged with resin, required adhesives and placed under elevated temperatures and pressures (Groover 2007) to impregnate the matting and tightly bond component into a pre-determined form.

It is believed by the author that this process may have been used to manufacture the CH-47 rotor blade along with filament winding techniques for the addition of external components such as the skin and dampener bracket.

2.5 Rotor Blade and Composite Laminate Defects & Damage

Aircraft are designed and constructed to accepted airworthiness standards. It is expected that these standards provide an acceptable risk of structural failure when operated within the design limitations. However, aircraft structures deteriorate from the 'as manufactured' condition throughout their service life. This deterioration is caused by fatigue, environmental factors and accidental or battle damage.

There are several common damage types experienced by helicopter rotor blades whilst in service. These are generally exacerbated by high-intensity operational tempo and environmental influences (such as humidity or particulate exposure) of a combat aircraft.

Some of the more common damage types include, but are not limited to:

1. Leading edge erosion; particularly in fine and sandy particulate environments such as the Middle-East or central Australia. It should be noted that erosion damage may occur on all blade surfaces; however, is more prominent on the leading edge.
2. Inter-laminate delamination; which is usually due to the presence of a manufacturing defect such as voiding or porosity, or some other form of initiating damage.
3. Moisture ingress; may be experienced in wet and humid environments and can lead to composite performance reductions or an out of balance condition of the rotor blade.

4. Debris-impact damage; may be caused by larger foreign objects such as stones or birds and as the name suggest may result in blade damage such as skin penetration or deformation types of damage.
5. Outer skin compression damage; is a result of localised pressure on the skin surface in the vicinity of the trailing edge skin and Nomex core. This type of damage appears like a very shallow indentation and may be large in width when compared to depth.
6. Battle Damage; is the focus of this research, however the principles and methodology used maybe applied to other forms of damage. Whilst there are many forms of battle damage, in general, it can be described as a forceful impacting and penetrative damage. It is usually inflicted via small arms fire, rocket propelled grenade or by more sophisticated methods, such as Man-portable air-defence systems (MANPADS) which are shoulder-launched, surface-to-air missiles (SAMs). These are typically guided weapons and are a threat to low-flying aircraft, especially helicopters. During this project a focus will be placed on small arms fire battle damage, primarily the 7.62 mm round as used by the AK-47 Kalashnikov assault rifle given its prevalence within current global conflict.

Of the above types of damage, most are detectable with careful visual examination such as those conducted during a pre-flight inspection or a periodic maintenance inspection. Exceptions may lie in the areas of delamination and moister ingress; however, these are also often detected via visual examination or in-flight vibration noticed by the crew prior to the fault reaching a critical point or complete failure.

In particular, battle damage is easily observable by the eye as it almost always results in partial or full thickness, penetration damage.

This is demonstrated by the following examples, in which it is observable that the projectile entry and exit of small arm fire may result in significantly differing damage profiles. This damage is to the D-spar of a CH-47 rotor blade, a critical area which traditionally would result in the discarding of the entire rotor blade. The differing nature of the damage between the point of entry and exit is also depicted.



Figure 21. Typical battle damage due to small arm fire (Cline C et al. 2011).

Typically, projectile entry is round and relatively uniform in comparison to the projectile exit which may be very un-uniform and irregular in shape introducing differing modes of failure to the composite component affected. The reason for this discontinuity in damage profile is due to projectile design. Modern military ballistic projectiles are designed to plastically deform or fragment on impact thus inflicting as severe a damage pattern as possible to the target, which in the case of small arms fire are usually opposing combatant personnel. As can be seen, this exit damage complexity poses significant challenges in modelling battle damage due to small arms fire in composite structures.

The following indicative picture is of the resultant battle damage from an RPG on a CH-47 Chinook aft rotor blade. Again, the irregular nature of the damage is easily observable and is at least in part a result of the composition of the material itself.



Figure 22. RPG damage to a CH-47 aft rotor blade.

Cline et al (2011, p. 56) had the following to say about damage assessment of composite rotor blades:

Despite known damage tolerance, the assessment of damage for composite rotor blade spars (thick-walled composite laminates) that have been subjected to small arms fire is analytically challenging. The resulting damage site is irregular, characterized by ragged edged holes, as well as a zone of severe matrix damage and delamination that are also random in nature.

The helicopter rotor system operates in a highly dynamic and unstable aerodynamic environment leading to severe vibratory loads (Pawar 2006). Repeated exposure of composite rotor blades to this severe loading condition can both induce damage in the blade and/ or accelerate pre-existing or imparted damage secondary effects. In effect, these flight conditions may cause small arms fire battle damage to continue to grow and accelerate to a point of complete blade failure. For this reason many damaged rotor blades are discarded without any formal assessment of damage other than visual, in particular to the spar or blade root region.

Although advanced helicopter rotor systems are generally made of composite materials (Ganguli 2006), Pawar (2006, p. 410) stated that ‘very little work has been done on the modelling of damage in the composite rotor system’. Since 2006, studies in this area have increased such as those performed by Ganguli and Pawar; however, few are investigating ballistic imparted damage, such as small arms fire, in critical areas of the rotor blade or the modes of failure.

2.6 Modes of Failure

As stated by Ganguli (2006, p. 410) and is widely accepted ‘matrix cracking is the first failure mode observed in fibre reinforced composite laminates and occurs in both monotonic loading and fatigue loading leading to more serious damage such as delamination or fibre fracture’.

In their paper Ganguli and Pawar (2006) modelled the composite rotor blade as a thin walled composite beam which effectively represented the D-spar or torsion tube of a composite rotor blade.

Several methods of modelling composite rotor blade matrix cracking, resulting in delamination, have been used. Of these approaches classical plate theory, first-order shear deformation plate theory, shear lag techniques and 2-D and 3-D finite element analysis are the most common.

Ganguli and Pawar claim to have completed the first work studying the effect of key damage modes on the structural behaviour of a composite helicopter rotor blade in their 2006 paper, *On the effect of progressive damage on composite helicopter rotor system behaviour*. To the best of the author's knowledge this appears to be the case, therefor indicating the relatively new nature of studies in this field.

It is noted however that since 2006 there has been a significant increase in interest in the area of SHM for composite aero-structures in general. However, rotor blades are still the poor cousin to other components such as stressed fuselage panels and fixed wing flight surfaces.

As far back as 1992, Chandra and Chopra had modelled the structural behaviour of thin wall composite beams and validated their model with experimental results.

Ganguli and Pawar (2006, p. 417) stated that '...matrix cracking is rarely the cause of blade failure'.

As matrix cracking density increases to high levels, these cracks may induce dis-bonding and delamination between individual lamina; however, the progression from these failure modes to fibre breakage depends largely on the specific loading conditions (Ganguli 2006).

The following figure presents crack propagation through the matrix (a) evolving into a micro-delamination between the matrix and fibre (b) and eventual fibre fracture through multiply fibres (c).

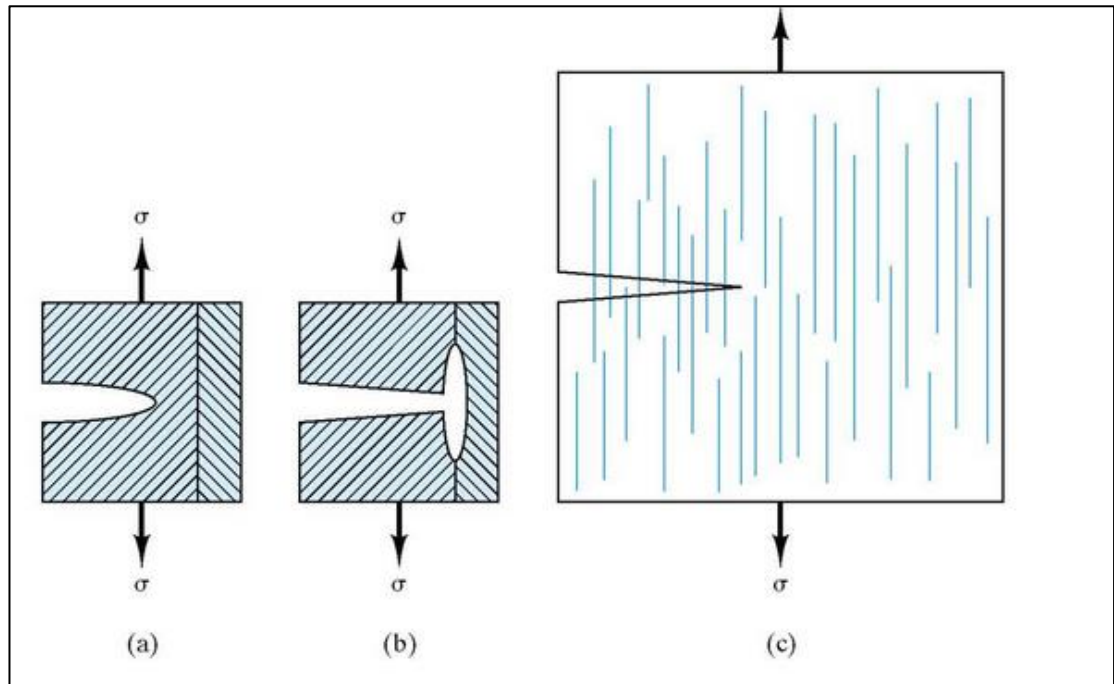


Figure 23. Composite Crack propagation (Source: City college of San Francisco 2014).

The most severe form of damage in composites is fibre fracture or breakage. This is due to the fibres being the principle load carrying element of FRP. Hence fibre failure is linked directly to the final failure of composites; however, it must be noted that sparse breaks of individual fibres may not result in total failure of the composite (Ganguli 2006).

This is almost certainly going to occur in small arms battle damage conditions. As can be expected, a reduction in rotor blade stiffness properties due to the damage will adversely affect the behaviour of the rotor blade response in flight (Ganguli 2006).

When discussing fibre breakage in a composite rotor blade Ganguli and Pawar state:

The main function of the matrix in composite materials is to provide a means of distributing load to transmitting fibres. However, due to matrix cracking and debonding / delamination damage modes, the matrix fails to transmit loads to the neighbouring fibres when some fibres break. Therefore, the broken fibres are simply separated from the intact ones as far as load sharing is concerned and the composite behaves like dry bundles of fibres.

Fibre breakage, as a result of battle damage, may be exacerbated by the specific geometry or structural elements of the blade area affected. This in turn may increase the rate of crack propagation or delamination progress.

Structural elements which create interlaminar stress concentrations applicable to composite rotor blades include any irregular or rapid change in profile such as free edges, notches or mechanically fastened areas. Of particular interest to composite rotor blades are bonded joints and rapid changes in ply geometry such as drops or steps. Structural elements which create interlaminar stress concentrations applicable to composite rotor blades are detailed below.

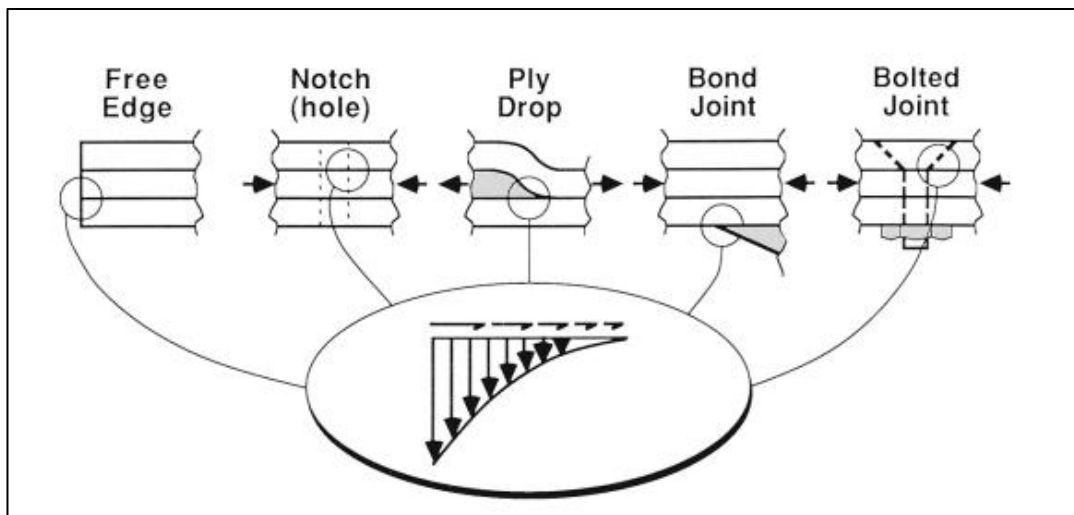


Figure 24. Interlaminar stress concentrations (*Source: Mandell et al 2003*).

As presented by Mandell (2003) there are three primary modes of laminate failure which include:

1. Mode I: Opening mode,
2. Mode II: In-plane sliding mode, and
3. Mode III: Tearing / shearing mode.

The three modes of laminate crack growth in composite structures, Mode I - opening, Mode II - sliding and Mode III – tearing are presented below. It should be noted that mixed-mode cracks are also common in many geometries.

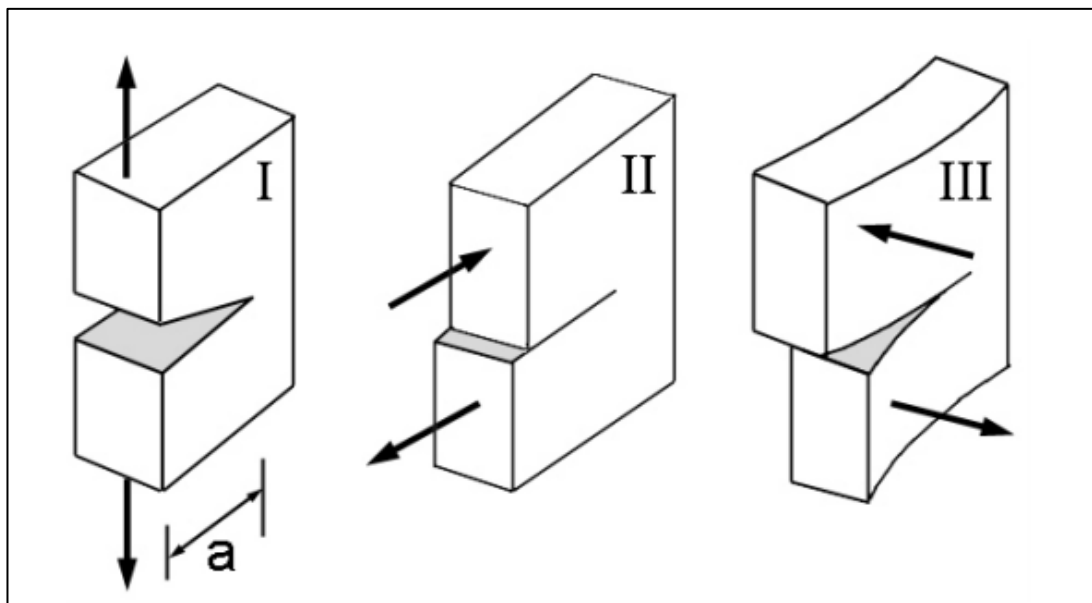


Figure 25. Modes of laminate crack growth (Source: Mandell et al 2003).

By its very nature, battle damage of a composite structure, or penetrative impact damage can reasonably be expected to be a combination of the above modes, in combination with severe matrix cracking and non-uniform, random delamination.

In addition, damages caused by impact are often insidious and may be small in extent, however, these microscopic damages can lead to deterioration of mechanical properties (Chow-Shing Shin 2014).

It is highly probable that such microscopic damages would be present in both limited and severe small arms fire battle damage. Chow-Shing Shin (2014) stated that ‘In particular, on subsequent cyclic service loading, these microstructural defects may grow and eventually lead to catastrophic failures’.

The following diagram illustrates the extent of post-impact damage to a matrix. It is an optical micrograph of a section of FRP detailing the positions of imbedded fibre sensors and the extent of post-impact damage matrix and delamination (a) immediately following impact, and (b) after 200,000 cycles have been applied.

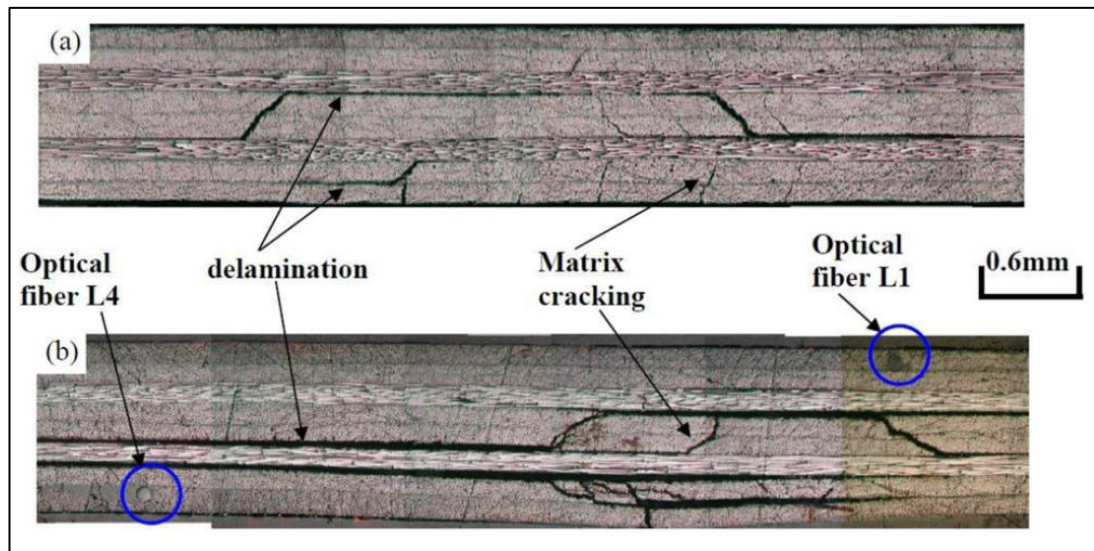


Figure 26. Optical micrograph of impact damage (Source: Chow-Shing Shin 2014).

2.7 FEA Simulation

As stated by Epaarachchi et al (2012) ‘finite element analysis techniques are being widely used to identify stress concentrations and hence to locate FBG sensors’.

The finite element method is a numerical approach to engineering problems (Logan 2012). Generally speaking the FE method results in a system of simultaneous algebraic equations, as opposed to differential equations, resulting in approximate values at a number of locations. This process segments a component into a system of smaller units (finite elements) which are interconnected at point (nodes) or boundaries is called discretization.

This results in a method that solves for each element, as opposed to the entire body, by formulating equations and combining them to gain a solution for the body (Seshu 2003).

Some typical areas in which FEA is utilised include stress analysis, vibration analysis, heat transfer, fluid flow and impact analysis.

There are many FEA software packages available on the market today, each with their own benefits and specialisations. ANSYS, CREO, Strand 7 and Abaqus are some of the more commonly used packages.

For this research Abaqus was selected as the primary FEA software package due to its advanced composite modelling capability and the ability to model and predict ballistic impact damage and failure. However, the complex material behaviour of composites makes analysis of these structures a significant challenge (Simular 2007).

As a result of the complexity of the rotors structure and resultant complexity of any FEA model, methods of modelling simplification were considered necessary as a contingency plan. Simplification of the structure may be considered as an option which was explored by Pawar and Ganguli (2006) whom stated that ‘helicopter rotor blades are typically modelled as 1-D beam...’. Another more significantly simplified variation is that of a flat plate model of the D-spar surface.

With respect to composite structures Pawar and Ganguli (2006) added that Strains are useful local indicators of damage. Physical strains readings are able to be readily obtained by FBG systems, and are able to be predicted by FEA methods providing a basis for comparison and verification of results.

2.8 Structural Health Monitoring (SHM)

The process of implementing a damage identification strategy for aerospace, civil and mechanical engineering infrastructure is referred to as structural health monitoring. For this purpose, damage may be defined as changes to the material and/or geometric properties of these systems, including changes to the boundary conditions and system connectivity, which adversely affect the current or future performance of these systems (Farrar & Warden 2006).

In essence SHM is a process aimed at providing accurate and in-time information concerning structural health condition and performance (Princeton University 2014).

Damage identification is typically conducted with five closely related disciplines that include SHM, condition monitoring, non-destructive evaluation / testing, statistical process control and damage prognosis (Farrar & Warden 2006).

Almost all governmental and private industrial enterprises have a willingness to detect damage or defects in their products as soon as possible to avoid potentially expensive repair, retrofit and/ or replacement costs or, in the worst case potential injury or loss of human life. With the advent of composite fibre components becoming more common within civil engineering applications and being a mainstay material within the aviation manufacturing sector, SHM of these components is an intrinsic and important component of such industries products.

Epaarachchi et al (2012, p203 - 204) had the following to say about the monitoring of FRP composites:

The main disadvantages of using FRP composites in the aircraft industry are their difficulty for repair, anisotropic behaviour, degradation of strength with time, high initial setup cost, and most importantly the complex failure criteria. Because of these undesirable properties, the FRP composite structures in the aircraft need to be closely monitored to prevent unexpected failure.

The monitoring of aeronautical FRP structures may be conducted utilising many methods depending on the application and role of the FRP structure to be monitored.

Some examples include:

1. Non-destructive testing methods such as radiography, ultrasound and Infrared Thermography,
2. Visual inspection,
3. Acoustic inspection,
4. The use of electrical strain gages, and more recently
5. Experimentation into the use of optical sensors such as Fibre Bragg Grating (FBG) sensors.

The advancing aviation industry has ever increasing requirements for advanced composite SHM techniques, in particular to primary and critical structure components manufactured from FRP.

As can be seen in Fig 27 the Boeing 787 Dreamliner is comprised of $\approx 50\%$ composite materials by weight necessitating advanced SHM techniques.

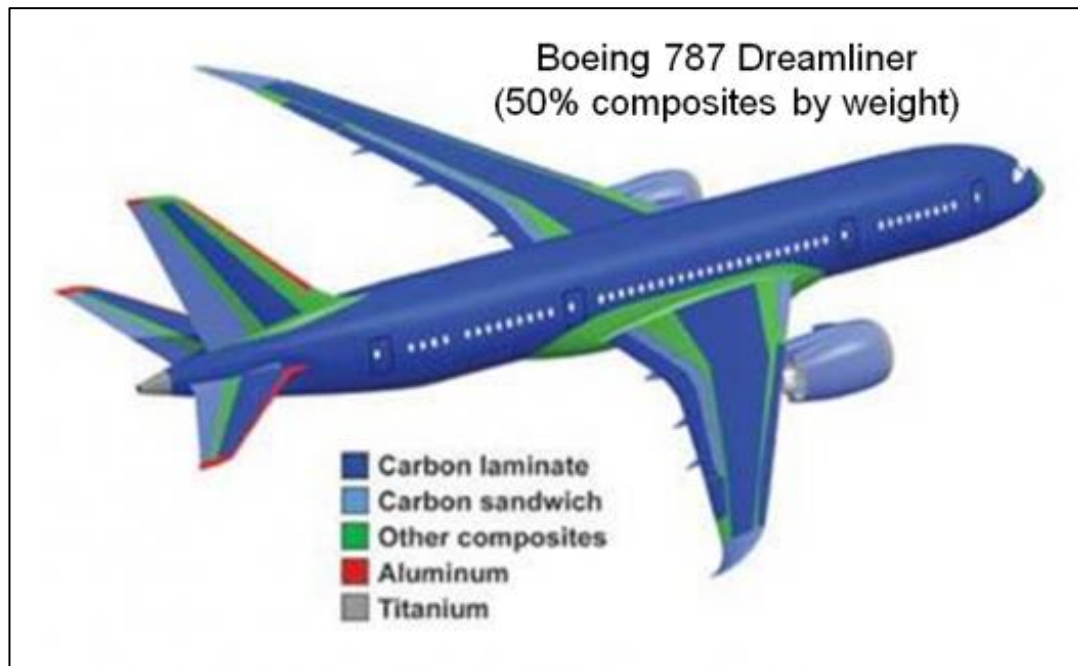


Figure 27. Boeing 787 Dreamliner composite materials.

The CH-47 rotor blade is considered a critical structure based on the consequence of failure, regardless of the likelihood of such an event.

The relationship between aircraft structures, dynamic components and critical structures, which the rotor blade is classified, is presented in the following figure.

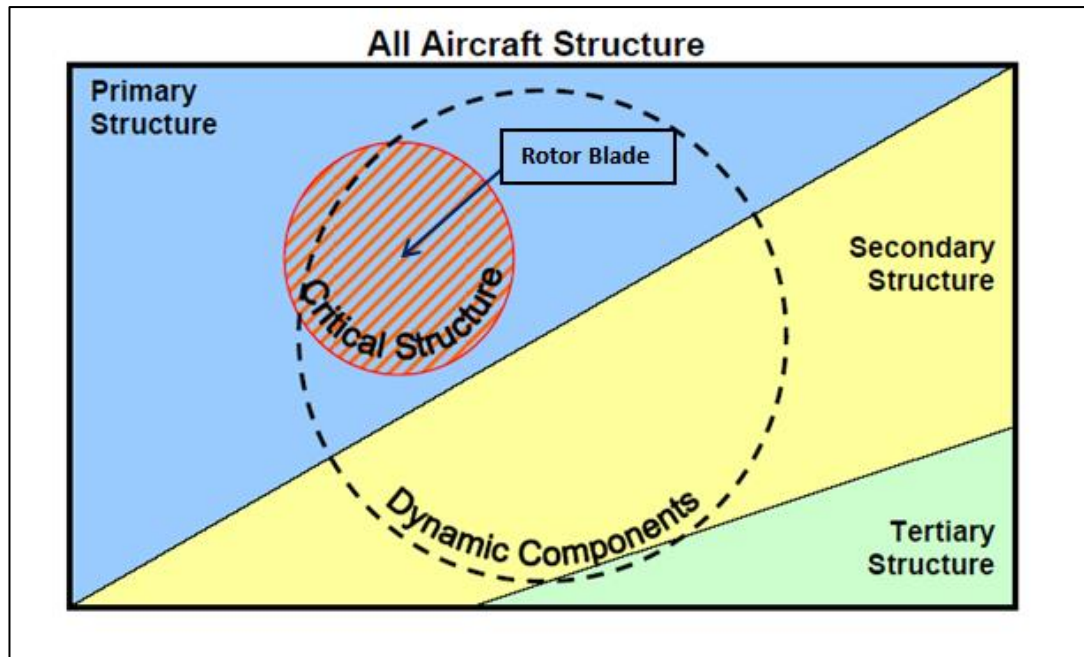


Figure 28. Relationship between aircraft structures.

It is for this reason that a composite rotor blade is a prime candidate for the trail of new and evolving SHM techniques such as optical sensors.

As stated by Dragan (2011) of the Polish Air Force 'Fibre Bragg Grating (FBG) optic sensor is one of the most promising...'

Additionally, helicopter rotor blades generally have a finite critical retirement life that once reached, mandates the disposal of the components. They may also be discarded as a result of relatively minor damage which may pose little to no threat of continued failure or reduction in performance. As such the use of strain sensor such as FBG may extend the useable life of FRP components beyond those currently mandated by component manufactures.

Strains are useful local indicators of damage (Ganguli & Pawar 2006) and quantifiers of damage effects for a give region. As can be reasonably expected, the change in strain is will occur at locations where damage is situated with the change in strain increasing as damage levels increase (Ganguli & Pawar 2006).

As a result it is foreseeable that with further development and research in the area, FRP structural components could achieve an 'on-condition' lifing policy with FBG sensors monitoring the strain in critical areas.

It is also important to note that an 'on-condition' lifing policy may well reduce the service life of an individual component based on its in-service and operating environment. Whilst this is a reduced service period, in the case of a rotor blade a greater level of safety would have been achieved.

The diminutive FBG sensors may provide an opportunity of imbedding sensors into FRP structures, such as rotor blades, at manufacture to monitor critical locations (Epaarachchi et al 2012) as part of an advanced SHM approach.

2.9 Fibre-Bragg Grating (FBG) Sensors

Fibre-Bragg Grating (FBG) sensors have been used for the SHM of FRP composites for more than two decades with advances in FBG sensor technology providing the opportunity to develop more sophisticated SHM systems (Epaarachchi et al 2012).

A FBG may be defined as 'a periodic or aperiodic perturbation of the effective refractive index in the core of an optical fibre' (Paschotta 2013). With the basic principle of FBG analysis is the scanning of returned wave lengths (Epaarachchi et al 2012).

FBG sensors are a passive fibre optic component, which have the attributes of reflection and filtering of light. They display the following attributes:

1. Used to measure strain via physical deformation,
2. Are non-conductive,
3. Are electrically passive,
4. Are not susceptible to EMI, and
5. Are small in length (≈ 5.0 mm) with the Core $\approx 5-9$ microns and the Cladding ≈ 125 microns in diameter.

FBG sensors are manufactured using UV light which is capable of breaking down the inherently stable silicon-oxygen bonds of the fibre core.

The overlap of two UV beams, or via a mask placed over the fibre, allows the required periodic change in the refractive index of the fibre core to be achieved (Smart Fibres 2014).

A schematic of optical fibre components and FBG sensor manufacture follows.

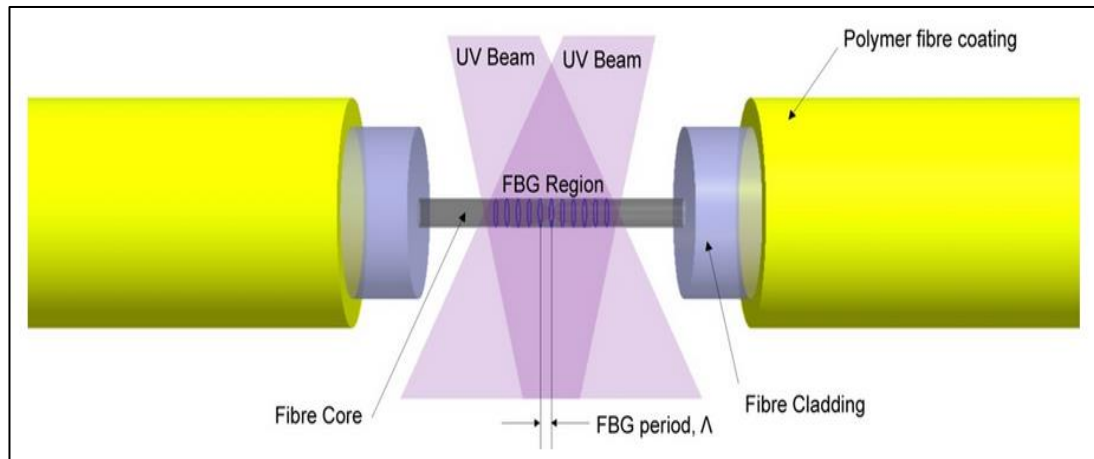


Figure 29. Optical fibre components & construction (Source: Smart Fibres 2014).

As can be seen from the above figure FBG sensors have three components, being an inner core, fibre cladding and a polymer fibre protective coating. The optimal material for the core and cladding is glass (SiO_2). The inner core can range from 5 - 9 μm and has a higher refractive index than the cladding. The difference in the refractive index between the core and cladding allows light to propagate in the core only (Ashby 2007).

Smart Fibres Ltd. UK (2014) says the following about FBG operation:

The grating formed at this modified region of fibre becomes a wavelength selective mirror where light travelling down the fibre is partially reflected at each of the tiny index variations, but these reflections interfere destructively at most wavelengths and the light continues to propagate down the fibre uninterrupted. However, at one particular narrow range of wavelengths, constructive interference occurs and light is returned down the fibre.

The following diagram is a representation of this process and the principle of FBG operation.

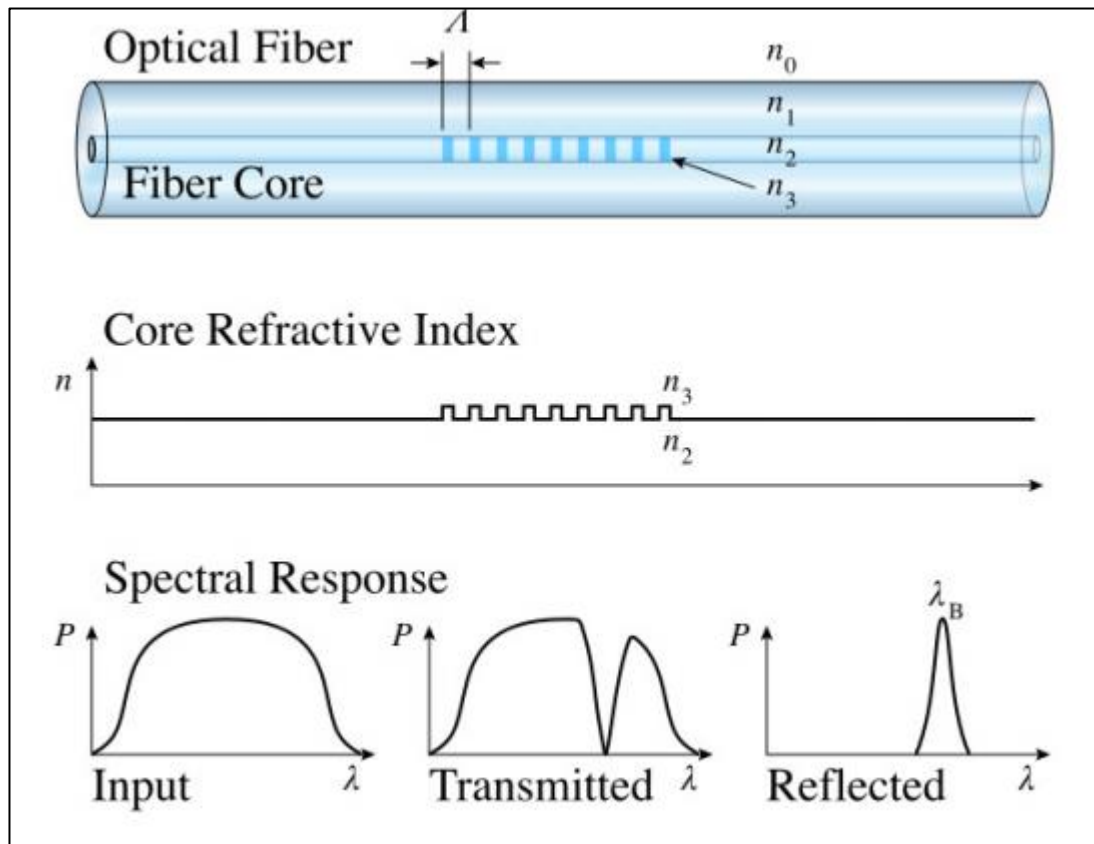


Figure 30. FBG principle of operation (Source: Sao D et al 2009).

The maximum reflectivity occurs at the Bragg wavelength (λ_B), which is determined by:

$$\lambda_B = 2 n_{\text{eff}} \Lambda \quad (2.1)$$

Where:

Λ = Grating Period

n_{eff} = Effective Refractive Index

λ = Bragg Wavelength

This shift in Bragg wavelength is a result of the physical deformation of the FBG and is equitable to the strain experienced by the sensor, which represents a change in reflected spectral response due to this physical deformation (lengthening or compressing) of the FBG. This is depicted in the following diagram.

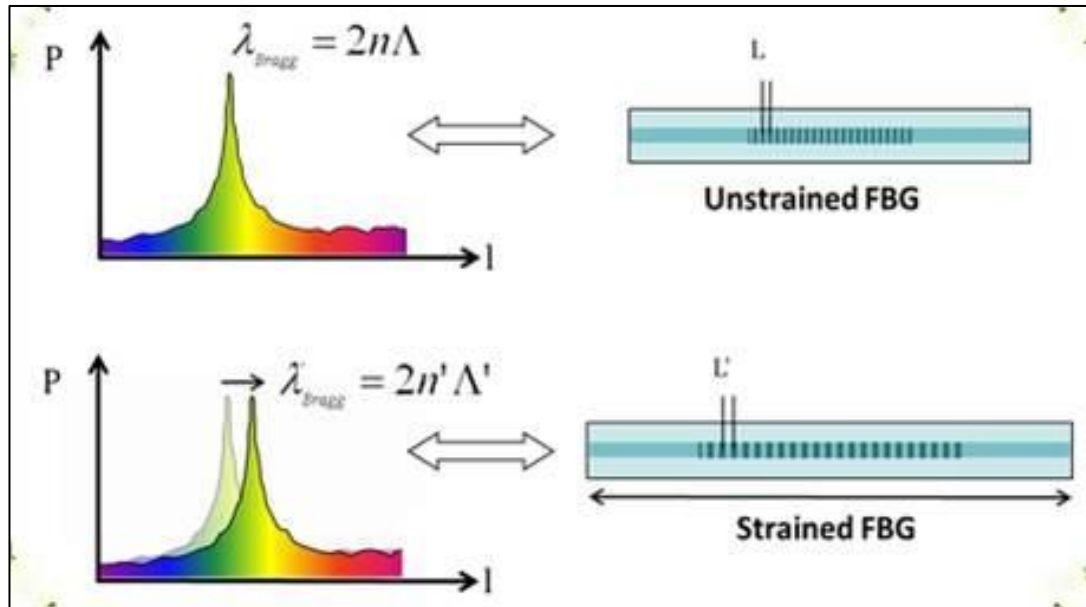


Figure 31. FBG spectral response.(Wang 2005).

Importantly, it must be noted that FBGs are affected by changes in temperature and are influenced by thermal expansion or contraction. This condition is given by:

$$\Delta\lambda_B = \lambda_B(1-\rho_\alpha)\Delta\varepsilon + \lambda_B(\alpha+\xi)\Delta T \quad (2.2)$$

Where:

ρ_α = photoelastic coefficient of the fibre,

α = thermal expansion coefficient of the fibre,

ξ = thermo-optic coefficient of the fibre,

$\Delta\varepsilon$ = change of strain, and

ΔT = change in temperature.

Given that FBG sensors are very long in comparison to their diameter it is reasonable to assume that the load is in a single plane, and that an FBG measuring principle axial strain will represent the principle in-plane strain experienced by the fibre.

In addition to temperature and strain measurement, FBG sensors may be used in pressure, displacement and acceleration application (Smart Fibres 2014).

2.91 Types of Gratings

There are several types of grating commercially available which include:

1. Uniform positive-only index change,
2. Gaussian apodized,
3. Raised-cosine apodized,
4. Chirped,
5. Discrete phase shift, and
6. Superstructure.

The respective signal from each of the common types of fibre gratings is detailed below with: (a) uniform with positive-only index change, (b) Gaussian-apodized, (c) raised-cosine-apodized, (d) chirped, (e) discrete phase shift, and (f) superstructure.

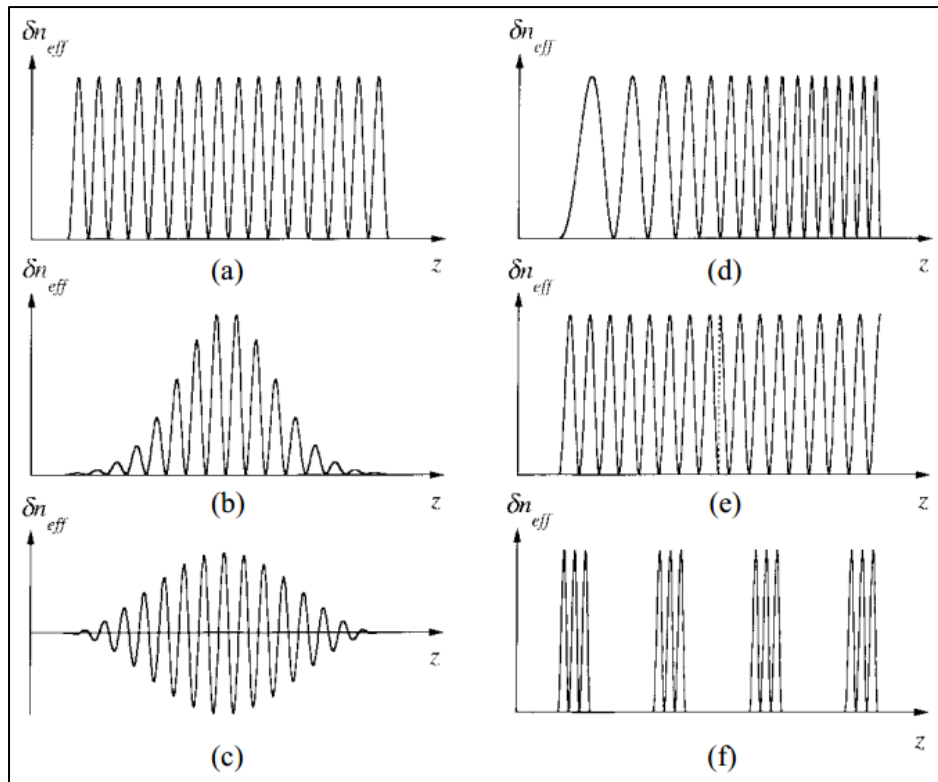


Figure 32. FBG signal forms (Source: Erdogan, T 1997).

Of the six common FBG sensors, the Gaussian-apodized sensor (b) was selected for this research. This selection was based primarily on the sensors apodization, which refers to the sensors refractive index approaching zero at each end of the grating. The apodized return signal, allows for the filtering out and removal of the Airy pattern which may, if left, reduce focus and clarity of the return intensity peak signals.

Khalid et al (2012, p. 80) stated the following with respect to the advantage of Gaussian-apodized FBG sensors:

The spectral response of a grating with a uniform index modulation along the fiber length has harmonics on the sides of the main lobe which are undesirable and may be suppressed by the procedure called apodization. Apodization is a variation of the modulation depth along the grating length. The apodized fiber Bragg grating plays an important role in order to suppress the side lobes while maintaining the reflectivity and narrow bandwidth. The side lobes are due to multiple reflections at the grating ends.

The return spectral response as depicted in Fig. 32 (b) and by Khalid is the same form as those returned during the physical testing phases of this project as detailed in Chapter 15 - Results.

An additional yet important consideration is that these FBGs are relatively common and are readily available from various manufacturers, such as Technica SA, with a minimal lead time.

The FBG, data collection system and methodology used are discussed further in the following chapters.

CHAPTER 3 - METHODOLOGY

3.1 General Overview

The following chapter discusses the methodology adopted during this project and outlines the major task groups to be completed. Following is the methodology and the overview diagram, initially constructed as a form of project guidance. This diagram breaks the project down into the major task groups which are all discussed, in detail, in subsequent chapters.

Following are the key areas identified for consideration as part of the methodology development:

1. Research / Literary review.
2. Design blade test fixture using FEA and manual calculations as required.
3. Manufacture blade test fixture and perform trial installation.
4. Create FEA model of the blade test section.
5. Conduct destructive blade testing to determine skin and D-spar sub-component properties (flexural, tensile and ply composition / orientation).
6. Create FEA model using Abacus, Strand 7 and Creo 2.0 as required.
7. Perform physical testing of the blade test section.
8. Measure strain in 10 most critical areas.
9. Simulate battlefield damage (Small Arms $\approx 7.62\text{mm}$) incrementally (depth and quantity) throughout the testing process.
10. Modify FEA model to include damage.
11. Compare / verify FEA model results with testing results.
12. Verify use of FEA model and FBG sensor use in this application.

Fig. 33 below is the general concept which was followed throughout the development and conduct of this research in order to achieve an accurate and validated result. This is followed by a description of the level of analysis determination.

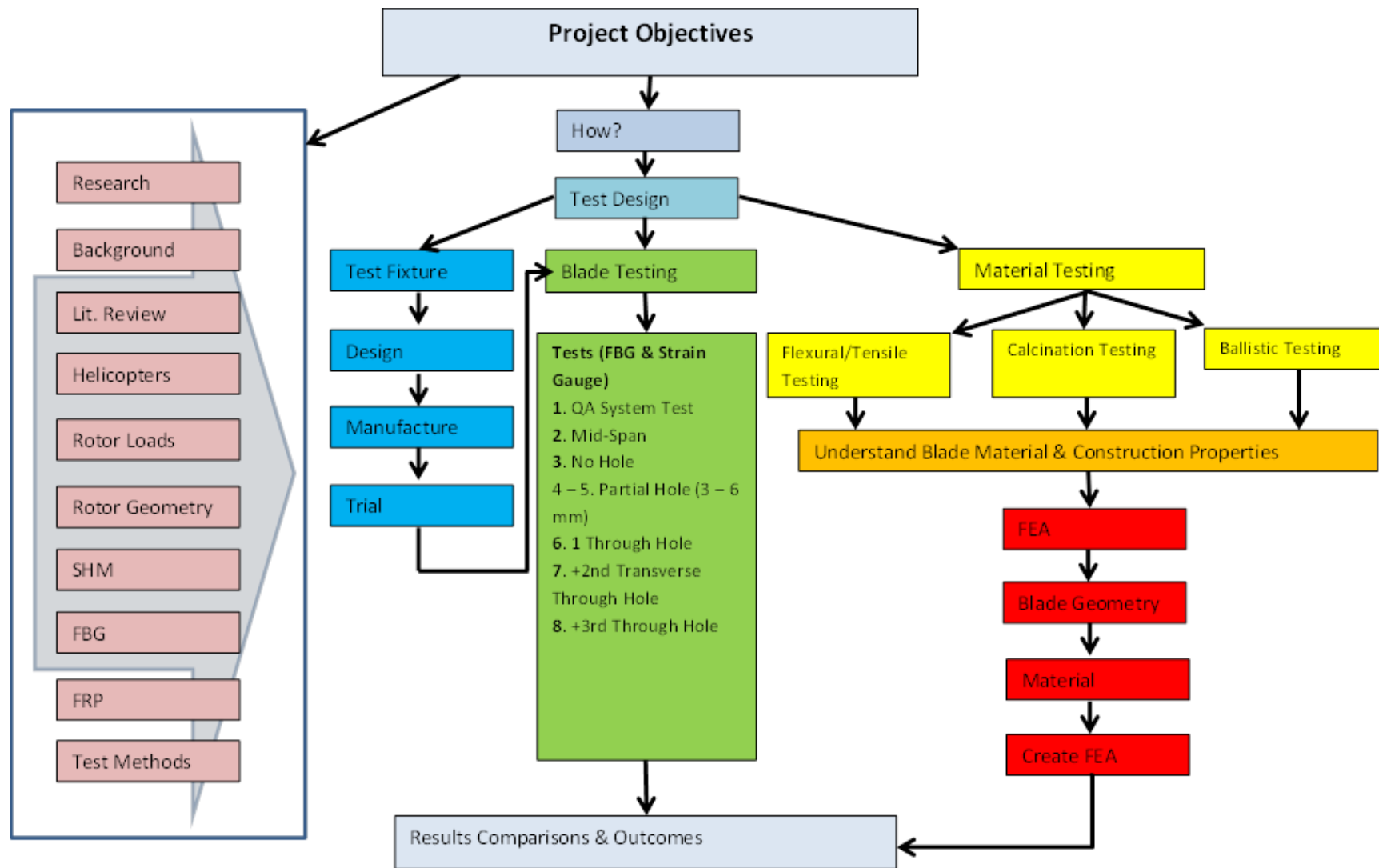


Figure 33. Project methodology outline.

3.2 Level of Analysis

Differing levels of analysis may be performed on composite materials and components. Daniel and Ishai (2006, p. 27) state that ‘composite materials can be analysed at different levels and on different scales, depending on the particular characteristics and behaviour under consideration’. These areas of analysis include:

1. Constituent Level – Micromechanics,
2. Lamina (Plie) Level – Macromechanics,
3. Laminate Level – Macromechanics, and
4. Component / Structure Level - Structural Analysis.

The following figure demonstrates these levels of analysis further.

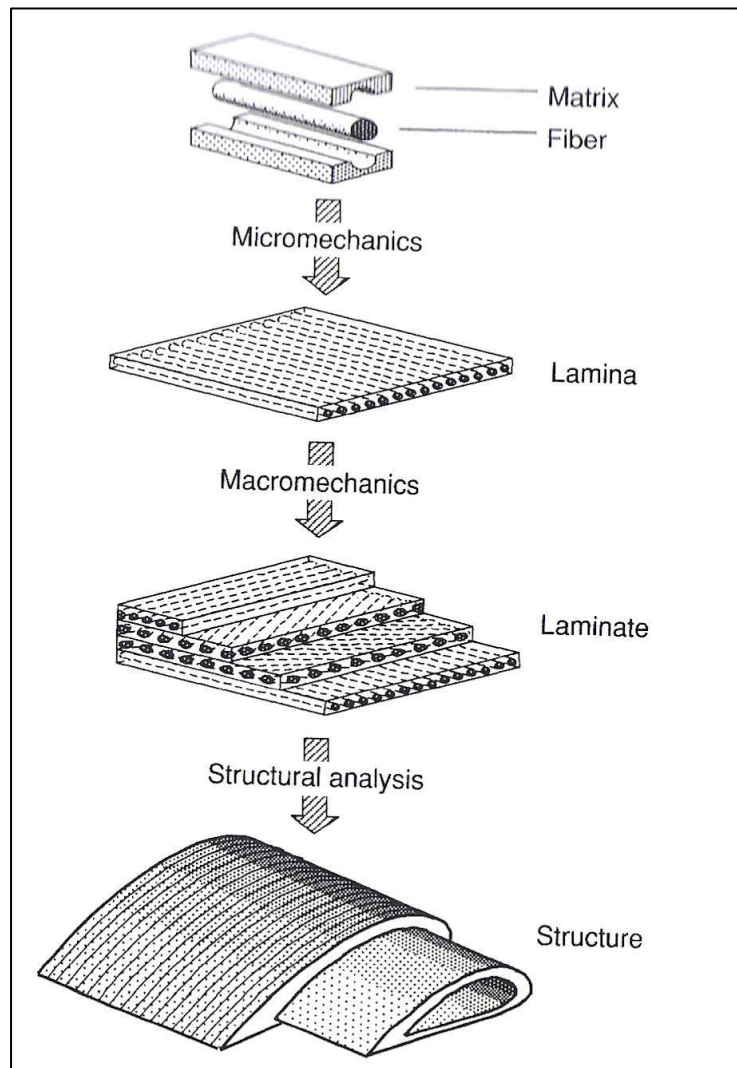


Figure 34. Levels and types of analysis (Source: Daniel et al 2006).

Whilst consideration was given to the laminate level of analysis, primary testing for rotor blade sub-component composite properties was conducted at the laminate and structural levels. It was performed on the blade skin and D-spar in order to determine the flexural modulus and tensile strength. In addition, a calcination test was conducted to determine the fibre-fraction and plie orientation of these sub-components.

Final testing was conducted at the structural level with the measurement of strain present at pre-determined locations on the complete rotor blade structure.

As presented by Daniel and Ishai (2006, p. 28) ‘...at the structural level, methods such as finite element analysis coupled with lamination theory may predict the overall behaviour of the structure...’.

This approach will be further combined, and compared, with the FBG and electrical strain sensor measuring methods to both determine the structures current behaviour under test conditions and validate the prediction of behaviour within the FEA model.

In order to gain a reasonably accurate comparison between the FEA and physical testing results a testing fixture was required to be developed that, as closely as possible, replicated some of the loads experienced by the blade in flight. This was to be achieved whilst minimising any severe local stress concentrations in the vicinity of any sensors as a result of restraining and clamping of the blade test section. It was also important that the load not be applied as a point and was rather a distributed load as far as possible given the testing equipment and limitations.

CHAPTER 4 - CONSEQUENTIAL EFFECTS, ETHICAL RESPONSIBILITY & SUSTAINABILITY

4.1 General Overview

The Institution of Engineers Australia (IEAust) holds the correct application of sustainability methods and consideration along with consequential effects of engineering practice in very high regard.

As a result IEAust has set out ten aspects of sustainability that should be considered, as a minimum, during the course of engineering works. Of these, as stated by IEAust (1997) *'Warfare is inherently destructive of sustainability, and, in contrast, peace, development and environmental protection are interdependent and indivisible'* may be the most applicable to this research project.

4.2 Considerations

Whilst there is no doubt about the validity and truth of the statement, it is also important to note that warfare, in particular by modern militaries has become a significantly more precise practice thus reducing many of the effects on both the environment and developed infrastructure of warring nations. It is also important to recognise that warfare between nations is a condition that is a result of many factors that often, unavoidably, led to conflict. Therefore, any reduction in the operational phase and duration for which combative actions occur will lesson any negative impact in an environmental and material manner. This is certainly not to say that the negative impact on human factors is to be reduced.

As a result, it is believed by the author that a means of passively expediting the finalisation of conflict is a result worthy of pursuit. Therefore, any improved availability rate of the CH-47 cargo helicopter possibly as a result of this project may well, in some small manner, contribute to this.

The CH-47 has on many occasions been utilised both during and post conflict to distribute humanitarian aid, to restore civic function and repair infrastructure to affected areas. Again, an improved availability rate of aircraft is often crucial in this function.

4.3 Sustainability

In addition, this research project (with further future development) may lead to the prolonging of composite rotor blade service life thus reducing the requirement for manufacture of replacement components whilst reducing the rate discarded blades. The inclusion of advanced technologies such as in-bedded FBG sensors into composite rotor blades is considered as presenting little increase in adverse effects to the environment or sustainability over those currently experienced within industry.

CHAPTER 5 - RESOURCE ANALYSIS

5.1 General Overview

All resources required for this research project were available at the University of Southern Queensland, the Centre for Engineering Excellence in Fibre Composites or were able to be achieved at personal residence.

Access to Creo 2.0, Strand 7 and Abaqus 12 was made available at the P2 laboratory and a personal computer in the case of Creo 2.0 and Abaqus. All other required software was installed on a personal computer.

The author liaised with relevant USQ and CEEFC staff and the project supervisor for the allocation of materials or components such as FBGs and testing equipment. Additional relevant supervision was coordinated by the author as required. All other equipment, materials and tools were supplied by the author as required.

There were no anticipated hard-ware delivery delays as all resources were available at USQ or freely within the Toowoomba region from multiple suppliers.

5.2 Key Project Risk

The key risk to this project with respect to resources lies with the functionality and availability of USQ and CEEFC testing equipment. Should these resources have become unserviceable for an extended period the variability of the project would have been threatened. As a redundancy measure, an alternate hydraulic press for applying loads was made available, if required, by a local machine shop.

There was no redundancy measure in place for specialised FBG and electrical strain data collection equipment should it become unavailable or unserviceable.

5.3 Required Resources

The following table is an overview of the required resources; however, it is general in nature and where specifics are required the relevant section of this document should be consulted. Whilst all resources are of importance, the key risk areas to project completion have been highlighted in red.

Table 3. Project resource requirements.

Resource	Location	Supplied by	Remarks
Computer	Private / USQ Z-Block & P9	Private / USQ	
Creo 2.0 software	Private / USQ Z-Block & P9	USQ	Loaded to Private PC
Abaqus 12	USQ P9	USQ	USQ & Loaded to Private PC
Rotor Blade Test Section	USQ CEEFC	Private	Obtained
Power Tools	Private	Private	General cutting, welding and wood-working power tools.
Hand Tools	Private	Private	General cutting and wood-working hand tools.
Blade test jig/ fixture materials	Private / USQ CEEFC	Private / USQ CEEFC	Hardwood, C-section steel & 3.0 mm high density rubber matting.
Blade Test Tabs	Private	Private	Removed from blade section & used for tensile, flexural & calcination testing. Obtained
Testing Equipment	USQ CEEFC	USQ CEEFC	
FBG and electrical strain sensors and associated fibre-optic cables, connectors and adhesives.	USQ CEEFC	USQ CEEFC Private	
Test data acquisition equipment	USQ CEEFC	USQ CEEFC Z9	
Blade section strain testing equipment	USQ CEEFC	USQ CEEFC Z9	Hydraulic press, steel mounting sections and required hardware.
Vibration analysis equipment (time permitting)	USQ CEEFC	USQ CEEFC Z9	Accelerometers, cables and data analyser.

CHAPTER 6 - PROJECT TIMELINE

6.1 General Overview

The following chapter details the project timeline, referred to as the Test Plan (TP), and in particular the broad method and sequence of events to include physical testing. It was noted that this TP, whilst as accurate as reasonably possible may have required alteration due to issues such as availability of testing machinery and equipment, unexpected delays in FEA modelling, complications in both physical testing and model verification and jig fixture manufacture.

All care was taken to address unforeseen delays, and as such a built in additional time factor of approximately 15% was added to each phase.

Drafting of this report occurred simultaneously with the testing and research activities over the duration of the research project period minimising the reporting burden in the final stages.

6.2 Test Plan Phase Outline

The TP was broken down into three primary phases to include:

1. Phase 1: Destructive testing of blade sub-sections & determination of material properties,
2. Phase 2: Pre-damage application testing, and
3. Phase 3: Testing results & FEA verification activities.

The above phases are discussed in greater detail in following paragraphs; however, prior to the testing phase initial design and development of both test fixtures and FEA models was considered.

6.3 Design & Manufacture of Equipment and Models

The following section discusses the design and manufacture of the testing fixtures and FEA models.

6.31 Design & Manufacture of Test Fixtures

There was a requirement for the design and manufacture of a suitable blade clamping system for the blade test section root end. This was required to provide an adequately ridged interface with the test apparatus and to resist the loads applied to the blade in testing. It was envisaged that it would consist of two hardwood sections which will clamp around the blade profile and support the blade end as a downward force was applied.

This was a major task which had three weeks allocated to its completion.

6.32 FEA Model Development

An appropriate pre-damage FEA model of the blade test section was to be developed within Abaqus from the available known data and physical properties determined during the literature review and testing. However, it was very difficult to gain such information on the blade construction and materials due to it being a military item and propriety limitations. This in turn led to the necessity for physical testing of individual sub-components in order to gain such information.

This was a significant task and was allocated six weeks for completion.

6.4 Phase 1 - Destructive Testing of Blade Sub-Sections

Blade GFRP skin plies and larger sections such as the D-spar required individual testing to determine the characteristics of each. This data was then assigned within the FEA model for each respective sub-component. A cord-wise blade section (50 - 100 mm wide) was disassembled into the major sub-sections (Skin, D-spar) in order to determine each respective characteristic via mechanical testing.

The characterisation parameters for the multi-directional laminates sought include the Modulus of Elasticity (E), Ultimate Tensile Strength (S_u) both longitudinal and transvers, Poisson Ratio (ν), Ultimate Strain (ϵ) and Yield Strength (S_y).

This was a medium level task, and as such has had one week allocated.

6.5 Phase 2 - Pre-Damage Application Testing

The following section discusses the pre-damage testing general methodology.

6.51 Testing Methodology: Pre-Damage

Using the previously developed blade section FEA model and engineering judgment, the ten most critical areas displaying the largest stress and strain concentrations were selected and their coordinates recorded. At each of these ten locations strain sensors were adhered to the prepared surface. The FBG sensor was located at a high strain intensity location on the D-spar internal surface with electronic strain sensors being used in all other locations.

Only one FBG was utilised as a cost saving measure due to FBG sensors costing approximately \$200.00 - \$300.00 each and being significantly more expensive than electrical sensors at approximately \$20.00 per item.

6.52 Strain Measurement

Physical testing of the blade test section was conducted using the large hydraulic press located at the USQ CEEFC to place a downward force on the blade test section commensurate with that experienced in straight and level flight. The strain at each of the ten locations was then be recorded.

6.53 Cord-wise Distributed Load

A distributed load was applied in order to achieve a loading profile more closely resembling that experienced by a rotor blade in normal, straight and level flight. This was achieved by loading the blade tip at approximately 1500 mm from the clamped root end. This replicated the most severe bending moment and greatest flexure of the blade test specimen prior to the application of incremental simulated ballistic damage.

6.54 FEA and Test Results Comparison

The results obtained from the above testing regime and the FEA model were compared in order to validate the FEA model and the test procedure.

Should modification to the FEA model have been required for results accuracy and/ consistency, this would have occurred at this juncture. Once successful validation had occurred the next phase of testing commenced.

6.55 Testing Phase Time-Line Comments

Approximately three weeks was allocated to the testing phase and it was considered as the highest risk activity to the project time line.

6.6 Phase 3 - Testing Results and Model Verification

The testing results and verification with respect to the project time line are discussed in the following sections.

6.61 Results Consideration

A careful and considered approach towards understanding the results was required during this during this phase as the results were from three differing sources which all had to be considered and correlated.

6.62 Conclusions

Following careful consideration of the results, conclusions were drawn with respect to the overall project and its aims and objectives, in conjunction with the Project Specification.

6.63 Compilation and Completion of Test Documentation

The results and verification documentation was correlated and drafted as it occurred. This process commenced on initiation of the TP.

Given the nature of this project, the following program was created to ensure adequate time was allocated to each phase, whilst allowing a significant factor of safety with respect to time allocations to task.

6.7 Gantt Chart – Time Management

The following Gantt chart is a mid-project ‘example only’ of the expected project timeline at that point and indicates how the project time was managed. It should be noted that this was a live document which was regularly updated for major milestones with an additional time allocation to allow for testing equipment availability and/ or otherwise unforeseen delaying circumstances.

Table 4. Testing program timeline example.

	15 - 30 May 14		01 – 30 June 14				01 – 31 July 14				01 – 30 August 14			
Approx. Week #	20	22	23	24	25	26	27	28	29	30	31	32	33	34
Pre-Testing Phase	Design & Manufacture of Test Fixtures (Wk 1 -2) 100% Complete													
	FEA Model Development (Wk 1-3) 20% Complete													
Phase 1			Sample Collection / Destructive Testing of Blade Sub-Sections (Wk 3-6) 65% Complete											
Phase 2							Pre / Post- Ballistic Battle Damage Testing (Wk 5 - 9)							
											FEA and Test Results Comparison (Wk 8 – 10)			
Phase 3	Compilation and Completion of Documentation: 15 May – 15 October 14 65% Complete													

	= Completed
	= In-Progress
	= Awaiting Commencement

CHAPTER 7 - RISK MANAGEMENT & CONTROL

7.1 General Overview

The nature of this project and research was very 'hands on' involving the manufacture of jigs and fixtures, mechanical testing in a laboratory environment and the use of power tools and machines in the preparation of test samples. In addition, a significant component of the project is conducted within an office environment.

7.2 Risk Rating

Whilst the highest risk rating attained during the risk assessment process was Medium, all care was taken to reduce hazards during the completion of this project, to include any work that was required to be conducted remotely to the University of Southern QLD and the CEEFC.

At Appendix B is the completed ACT Work Safety and Risk Control Form and OHS Risk Rating Form chosen for assessment of this project.

CHAPTER 8 - ROTOR TEST FIXTURE DESIGN & MANUFACTURE

8.1 General Overview

This section details the design and manufacture of the blade section testing fixtures.

It was identified early in the planning phase that a significantly robust blade retaining system for the physical testing of the blade section was required, and that significant effort and time allocation was going to be absorbed during its conception, design and manufacture. As a result it was approached in isolation and as a single engineering design task.

8.2 Design Process

As conveyed by Ertas and Jones (1996) it is critical that a design process be followed for all but the simplest of engineering designs. As a result the following general design approach was adopted.

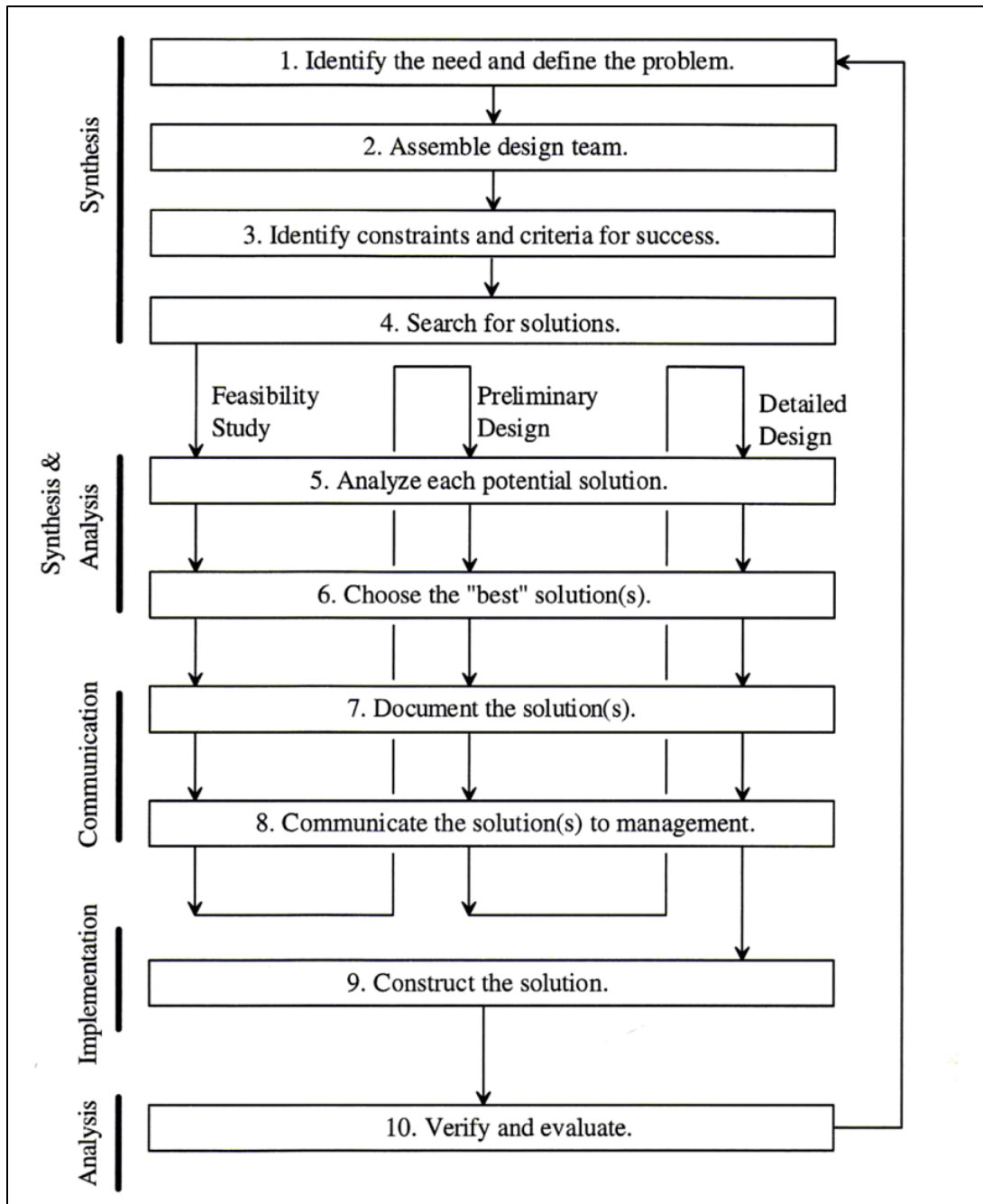


Figure 35. Test fixture design approach (Holtzapfel, M 2000).

During the synthesis phase, in particular point three of the design approach, the following ten major constraints were identified and considered as critical.

8.3 Test Fixture Design Constraints

The following constraints were applied to the design process and are presented in the below table.

Table 4. Test fixture constraints.

Serial	Constraint	Remarks
1	Safe for Use	The test fixture must not present any unacceptable risk to health or safety either during its manufacture or use.
2	Non-Damaging	Must not damage blade section or test equipment.
3	Blade Orientation	Must orientate blade with the lower surface facing upper most for correct load application as in flight.
4	Clear Upper-most Blade Surface	Must provide significant, unobstructed upper surface area for the application of FBG and Elect. Strain sensors and associated hard-ware.
5	Minimum Downward Deflection	Measurement of the hydraulic press cylinder determined a travel of 80 mm. Therefor a minimum of 80 mm downward deflection must be available to the blade in the test fixture design.
6	Transportable	As the test hydraulic press is utilised by the university, the test fixture must be able to be removed and accurately repositioned should it be required.
7	Ease of Manufacture/ Availability of Materials	The test fixture must be able to be easily manufactured with limited equipment and resources. Materials must be readily available.
8	Adequate Strength to resist testing loads	The test fixture must possess adequate strength and rigidity to resist applied testing loads.
9	Simplicity	The final design must be as simple as possible.
10	Minimal Cost	The test fixture must total cost must be keep to a minimum (not to exceed \$100.00).

In addition to the above constraints, the complete test fixture including the test blade section was required to fit within the CEEFC 200 tonne hydraulic press, depicted below.

As can be seen this is a large testing press capable of applying significant downward force, as such the width and height constraints were determined as critical; however, low in risk given the physical internal dimensions of the testing press.



Figure 36. CEEFC 200 Tonne hydraulic test press (USQ CEEFC 2014).

The hydraulic actuator was used to apply down ward force to the blade test section.

It has an 80 mm travel limitation; however, bulk height adjustment may be achieved by moving the cross beam up or down as required by removing the bolts restraining the cross beam. A chain block was then used to adjust the beam height. The cross beam is depicted below.



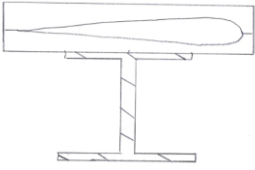
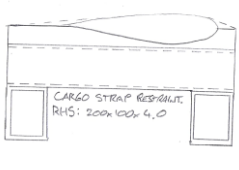
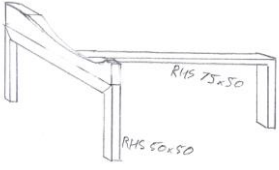
Figure 37. Hydraulic press cross beam (USQ CEEFC 2014).

Adhering to the top ten critical constraints, several conceptual design sketches were produced and a decision matrix applied to assist in the final conceptual design selection. The decision matrix is presented as follows, with simplified conceptual hand sketches inserted for clarification.

8.4 Fixture Conceptual Options

Table 5 details the testing fixture conceptual options and general determination decision matrix.

Table 5. Test fixture decision matrix.

Decision Matrix – Test Fixture Broad Concept Selection Process					
Concept		Universal-Beam	Welded Dual RHS	Three-Point Support	
Critical Constraint # From Table 4	Weighting				
		1	3	2	1
		2	3	1	2
		3	3	3	3
		4	2	3	1
		5	1	2	1
		6	1	3	2
		7	1	3	1
		8	3	3	2
		9	2	3	1
		10	1	3	1
Total:		59	39	33	

As can be seen from the conceptual sketches the universal beam concept is the only design which does not have a larger width than that of the test blade section's cord-wise width. This was identified as a potential stability risk around the beam's longitudinal axis. Whilst tipping was considered as very unlikely due to the applied load being normal to the blade cord-wise axis, a risk management strategy was developed should it be required. This involved the use of a second I-beam to be placed under the fixture, parallel to the first I-beam in order to essentially double the main support beam width.

Two identical universal beams were available for use at the USQ CEEFC and were reserved for this task.

Additionally, in order to resist the large moment forces involved ($> 3750\text{N}$) it was recognised that a steel strap was required to reinforce and resist the separation of the two halves whilst providing adequate rigidity. An initial conceptual drawing is presented in Fig. 38 below.

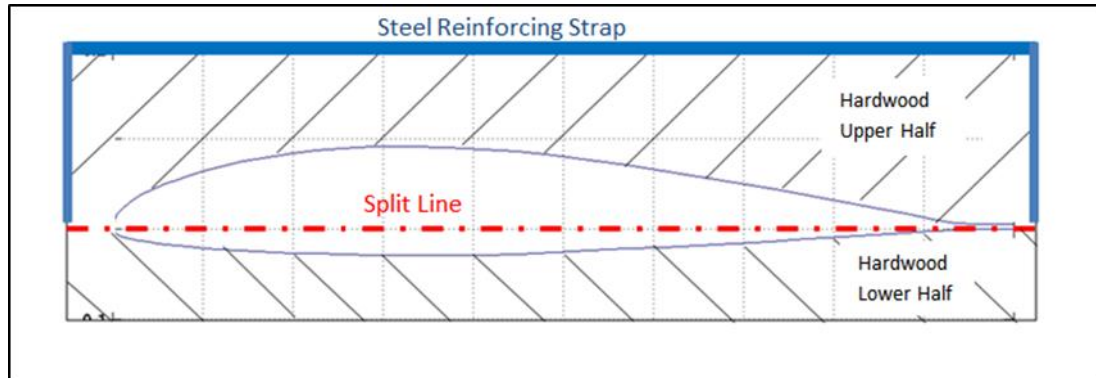


Figure 38. Initial root end clamp concept.

The selected universal beam test fixture and subsequent material selection and design process is presented in the following paragraphs.

8.5 Testing Fixture Sub-components & Materials

For design purposes the test fixture was broken down into four main sub-components, they are:

1. Root-end clamp,
2. Lower adjustable support,
3. Upper load plate, and
4. Main support.

In addition to these sub-components there was a requirement for various connecting hardware. These sub-components and hardware are detailed in the following table which additionally explains the primary role and materials selected for each.

Table 6. General description of fixture components.

Nomenclature	Role	Material/s	Remarks
Root-End Clamp	Provide a secure fixed blade end capable of resisting all applied testing loads to include torsion.	1. Hard Wood (200 x 50 mm). 2. Channel – Structural Steel (75 x 45 x 5.0 mm).	Attached to I-Beam with tack welds to the lower channel edges at eight points. Manufactured and supplied by M. Fairbanks-Smith.
Lower Adjustable Support	Provide a lower support mechanism about which the moment will act.	1. Cypress Pine (75 x 45 mm). 2. RHS – Steel (75 x 150 x 3.0 mm)	Not permanently attached to I-Beam. Will remain free floating to allow for longitudinal and vertical adjustment as required during testing. Manufactured and supplied by M. Fairbanks-Smith.
Upper Load Plate	Provide a contoured surface for load application to include torsion.	1. Cypress Pine (75 x 45 mm). 2. Channel – Structural Steel (75 x 45 x 5.0 mm)	May not be utilised for testing; however, was manufactured as a redundancy for load application. Manufactured and supplied by M. Fairbanks-Smith.
Main Support	Provide adequate support and rigidity to the other test fixtures.	1. I-Beam – Structural Steel	Two I-Beam sections are available should one prove inadequate to resist torsional loading conditions. In this event the Root-End Clamp and Lower Support will span the two I-Beams. Supplied by USQ CEEFC.
Hardware	Assemble sub-components and fixture.	1. M10 High-Tensile Threaded Rod (2.0 m) 2. M10 High-Tensile Nuts 3. 40 x 40 x 2.5 mm Zinc Plated Washers 4. M10 x 75 mm Coach Screws	Manufactured and supplied by M. Fairbanks-Smith.

As stated by Ertas & Jones (1996, p. 125) 'Selecting proper materials and understanding the fabrication processes associated are two of the most important responsibilities...'

This was considered in the material selection process; however, only a minor material investigation was required due to the relatively low associated loads, low frequency of the applied loads and limited duration of testing. The following primary areas, as presented by Ertas & Jones (1996), were considered in the selection process:

1. Static Characteristics:
 - a. Ultimate & yield strength,
 - b. Young's modulus, and
 - c. Hardness.
2. Fracture Characteristics:
 - a. Toughness,
 - b. Mode of failure – not sudden, and
 - c. Flaw growth.
3. Manufacturing:
 - a. Availability,
 - b. Weldability,
 - c. Machinability, and
 - d. Quality.

Areas which were considered to a lesser extent included:

1. Fatigue Characteristics - due to low cyclic frequency of testing regime,
2. Thermal Properties – no extreme temperature or fluctuations are expected, and
3. Corrosion Characteristics – testing is to be conducted in-doors in a noncorrosive environment. Steel materials are not dissimilar and compatible.

As the testing was conducted completely indoors, within a noncorrosive environment, the effects of corrosion on the fixture could be discounted; however, importantly the interface between the blade and the timber contact point must be considered.

Whilst no specific data could be identified, it was assumed that corrosive damage to the blade as a result of contact with the fixture timber is very unlikely given the relative corrosion resistance of E-glass and the relatively inert nature of timber.

The general properties for the selected test fixture materials are as follows.

Table 7. General properties of fixture materials.

Nomenclature	Modulus of Elasticity	Compressive Strength	Stress Grade (Timber) / Yield Strength (Steel)
Cypress Pine	9.0 GPa	53.0 MPa	F11
Spotted Gum	23.0 GPa	75.0 MPa	F22
Channel Structural Steel	220 GPa	400 MPa	250 MPa
RHS - Steel	220 GPa	400 MPa	250 MPa

8.6 Testing Fixture Manufacture

Following is a description of the process of manufacture for the four sub-components.

8.6.1 Root-End Clamp

The root-end clamp's primary purpose is to restrain and limit cord-wise / horizontal movement, torque around the longitudinal axis and provide a rigid end capable of resisting the applied test loads without inducing damaging stresses into the blade section. It consists of a clamping arrangement into which the blade section was inserted with its upper flight surface orientated such that it is facing downwards. Threaded rods are lightly tensioned via the M10 hex nuts so as to adequately restrain the blade without causing crushing damage.

The root-end clamp comprises of two steel channel sections which provide rigidity and resist deformation under loaded conditions. Inserted in the channel sections is a hardwood profile section which is manufactured by slitting to create two halves and accurately band-sawing the blade outer profile removing the unwanted material. This profile was then sanded with a barrel sander to obtain a smooth, consistent profile free from stress raisers or appreciable, sudden changes in form. The assembly is connected with the two sections of M10 threaded rod and nuts.

The secondary function of the steel channel section is to allow for welding of the root-end clamp in a perpendicular orientation to the main support beam longitudinal axis.

The root-end clamp in both the open and closed position is depicted below.



Figure 39. Root-end clamp sub-component.

8.62 Lower Adjustable Support

The lower adjustable support's primary purpose is to allow for an adjustable support mechanism between the blade and the main support beam.

This sub-component is not permanently fixed to the main support and is adjustable to allow for positional changes during testing. It may be adjusted along the length of the blade section to provide a point around which a bending moment will occur as the test load is applied.

The support consists of an RHS section which supports and resists deflection of a cypress pine section profiled matched to that of the blades upper flight surface. This surface is orientated so it is facing downwards. The timber is attached to the RHS by two sections of M10 threaded rod and nuts, and 40 x 40 x 2.0 mm flat washers.

The cypress profile section, selected as it is softer than hardwood, was manufactured by accurately band-sawing the blade outer profile removing the unwanted material. This profile was then sanded with a barrel sander to obtain a smooth, consistent profile free from stress raisers or appreciable, sudden changes in form as depicted below.



Figure 40. Lower adjustable support.

8.63 Upper Load Plate

The upper load plate's primary purpose is to allow for an adjustable load application method to the upper surface of the blade section. It is fixed to the hydraulic press actuating cylinder at varying depths via the use of shim plates. This in turn can impart a lengthwise 'bending' load to the blade.

The plate consists of a channel section which supports and resists deflection of a cypress pine section profiled to that of the blade's lower flight surface, which is orientated so it is facing uppermost. The timber is attached to the channel by two M10 x 75 mm coach bolts whilst the load plate may be bolted or welded to the press cylinder.

The cypress profile section, selected as it is softer than hardwood yet still has an appropriate compressive strength, was manufactured by accurately band-sawing the blade outer profile and removing the unwanted material.

This profile was then sanded with a barrel sander to obtain a smooth, consistent profile free from stress raisers or appreciable, sudden changes in form as depicted below.



Figure 41. The upper load plate.

8.7 Main Support & Test Fixture Assembly

The primary function of the main support is the transfer the testing loads to the concrete floor. Additionally, it acts as an attachment point for the root-end clamp and supports the lower adjustable support whilst raising the test from the floor and providing longitudinal and axial stability during testing. It also allows for movement of the entire test specimen without disturbance relative to the fixture should it be required.

The main support is a universal beam of the following dimensions:

Table 8. Main Support dimensions and mass.

Main Support Dimensions	
Dimension	(mm)
Length	1600
Depth of Section	330
Flange Width	310
Flange Thickness	25
Web Thickness	15
Mass	260 kg

The following figure is the complete blade test fixture assembly without the blade section installed and the upper load plate lying on the floor next to the main support. The main support (blue beam) has a mass of ≈ 260 kg and is approximately 1700 mm in length. The four galvanised RHS positioned perpendicular to the universal beam section are welded in place to allow for movement of the fixture which is further discussed later.

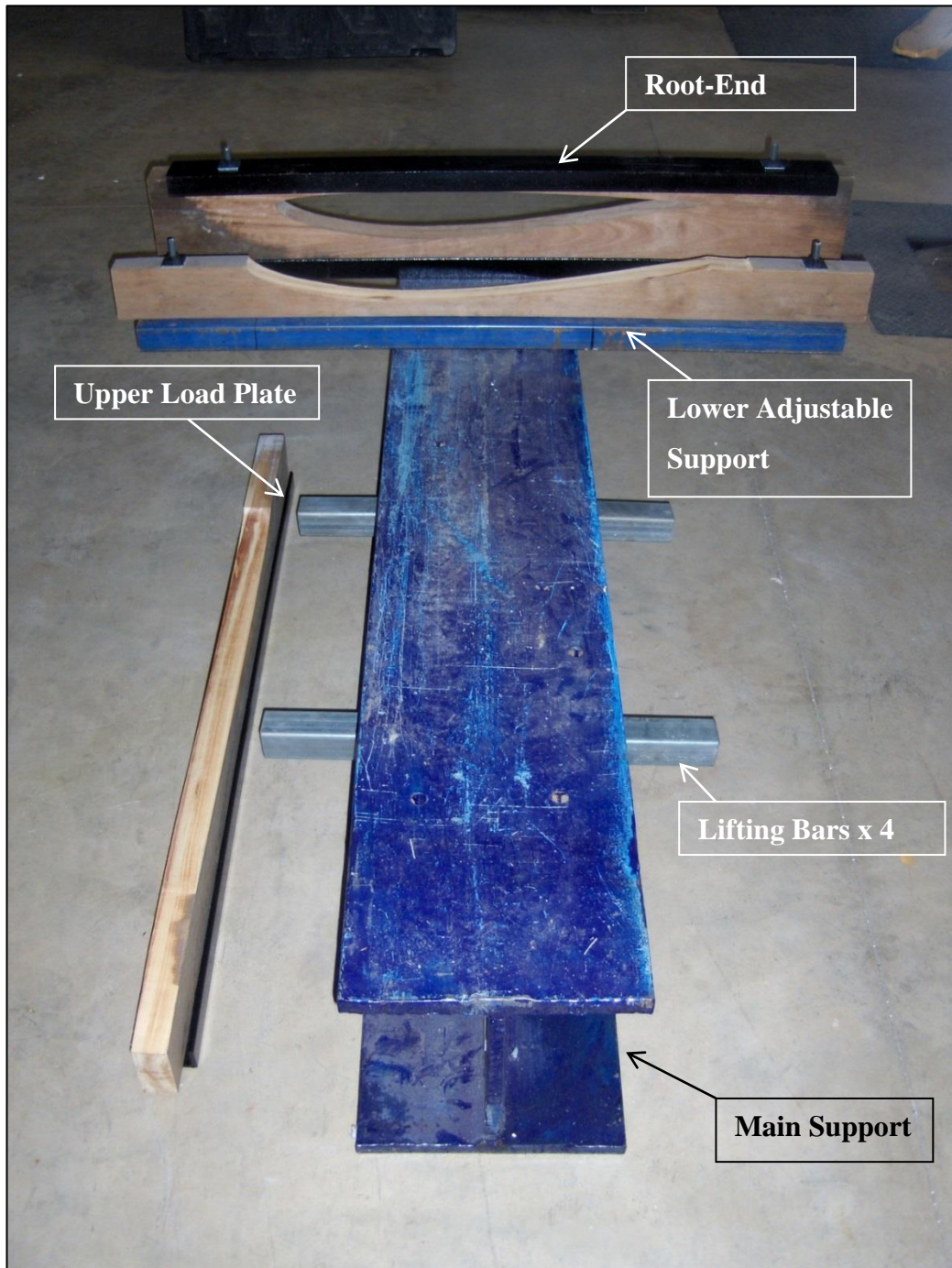


Figure 42. Blade test fixture assembly un-welded.

The following figure is an oblique view of the main support, lower support and root-end clamp (closed) and fillet weld locations (in red). It should be noted that the fillet welds are duplicated on the non-visible side of the root-end clamp requiring four welds in total.

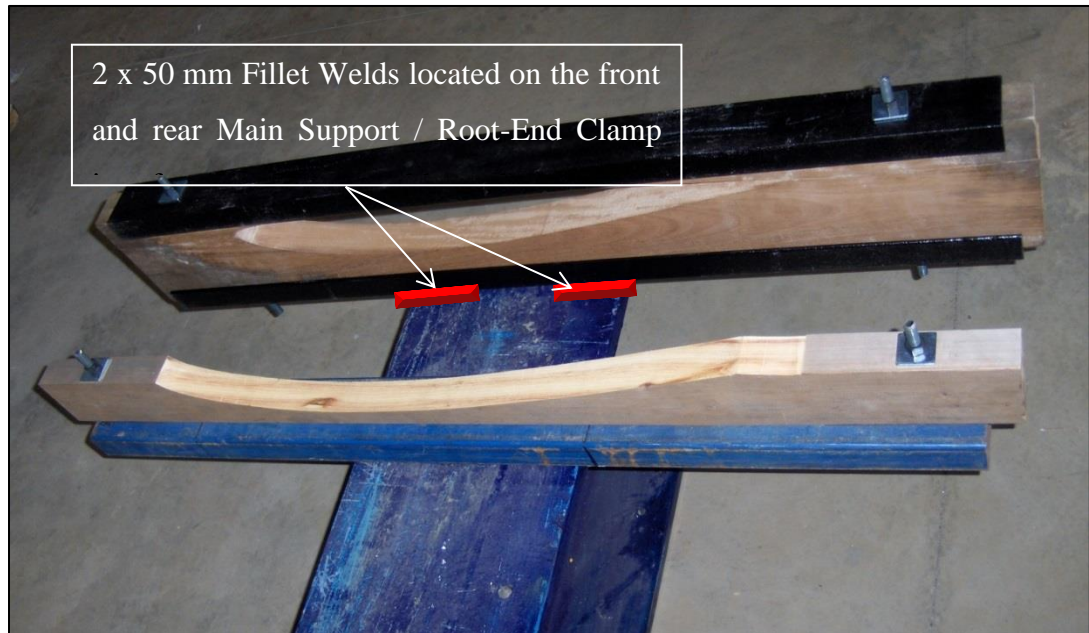


Figure 43. Root-end clamp weld locations.

The following figures detail the test fixture with the blade test section installed along with the position of all sub-components relevant to one another. It should be noted however that for the purpose of the set-up trial the lower adjustable support was arbitrarily positioned away from the root-end clamp for clarity purposes and it is not in the actual testing location.

The assembled blade test fixture is viewed from the fixed end.

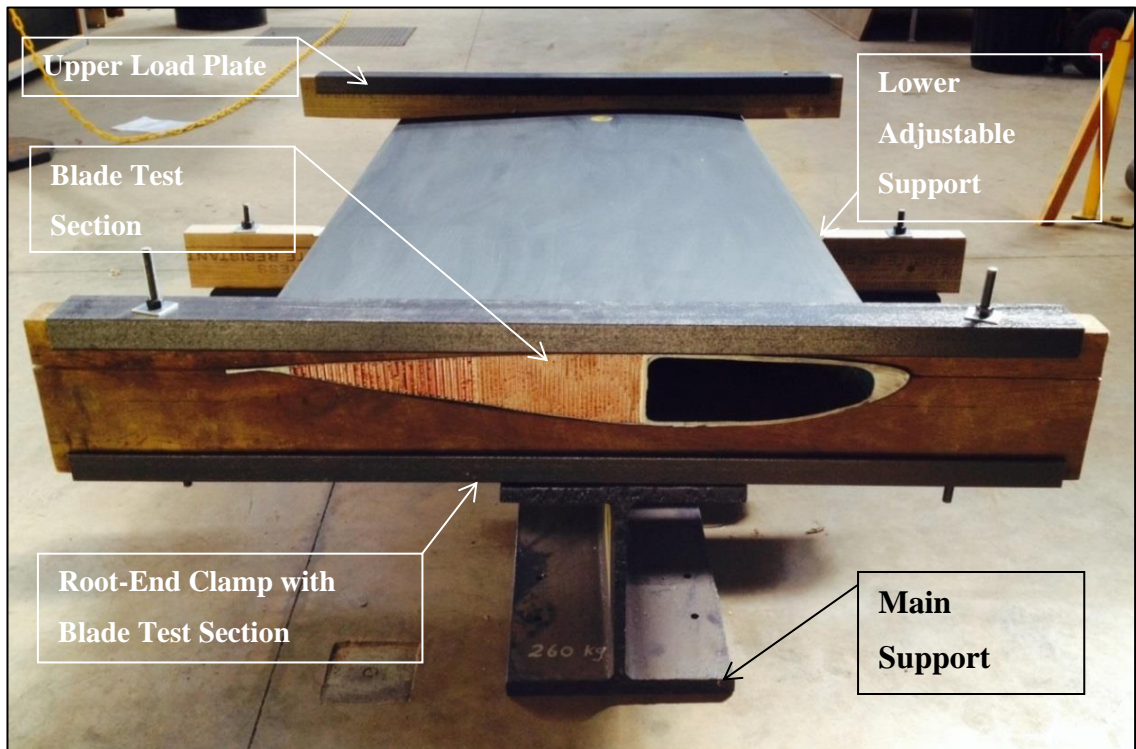


Figure 44. Test fixture with blade installed.

Following is the assembled blade test fixture with the blade section installed detailing the adjustable support plane of adjustment. **NOTE:** The lower adjustable support is not located in the final testing position.



Figure 45. Lower adjustable support axis.

Fig. 46 following is the assembled test fixture with the blade test section installed as viewed from the free end displaying the 80.0 mm range of deflection and load orientation.

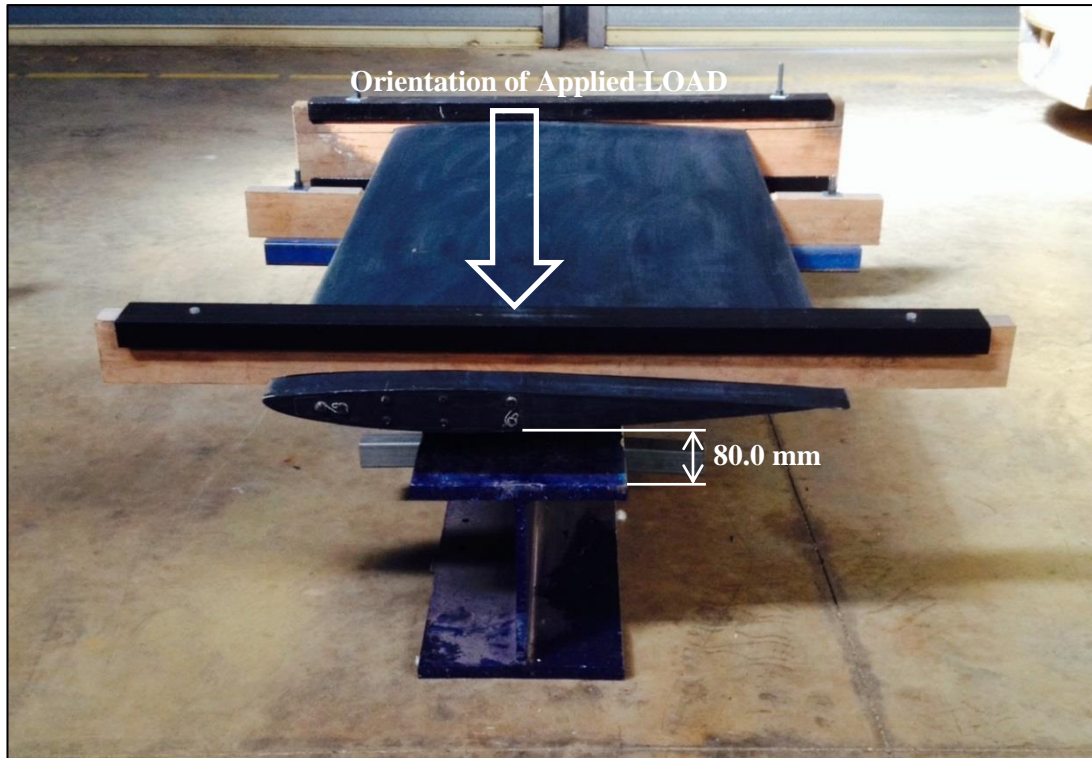


Figure 46. Test fixture deflection and load orientation.

Lifting and movement of the complete test fixture, to include the blade test section, to and from the hydraulic press was achieved via a pallet jack.

Given the weight of the fixture with the blade installed being approximately 300 kg a movement trail was required. This was trialled during the manufacture of the fixture, and prior to final fixture welding, which was successful. There was no concern of toppling or load run away within the testing facility at the CEEFC.

The pallet jack is installed and lifting the test fixture in Fig. 47 below.



Figure 47. Movement trials of the assembled test fixture.

Location markings (not depicted), were accurately positioned on the concrete floor beneath the hydraulic press and were used for accurate fixture re-positioning should movement be required mid-testing.

CHAPTER 9 - DETERMINATION OF ROTOR BLADE MATERIAL PROPERTIES

The following chapter discusses the requirement for and determination of the rotor blade material properties.

9.1 General Overview

Given the little information publically available with respect to the physical properties of the CH-47 composite rotor blade, testing of major blade sub-components was required.

These sub-components include the main load carrying D-spar and the outer skin. It was determined that as a minimum requirement for the establishment of an accurate FEA model was the flexural and tensile properties of both sub-components along with their respective fibre-fractions and orientations.

Hodgkinson (2005) stated that ‘...composites are generally required to function as load-bearing structures’ and that ‘...elastic modulus, strength, ductility and fracture toughness are particularly important properties’. These properties are required in order to create an accurate FEA model of the blade section, primarily the tensile and flexural properties and the fibre-fraction as a percentage.

9.2 Relevant ISOs

The following testing procedures were developed with particular reference to the following ISOs:

1. **ISO 14125**, Fibre-reinforce plastic composites – Determination of flexural properties,

2. **ISO 527-1**, Plastics – Determination of tensile properties - Part 1: General Principles,
3. **ISO 527-4**, Plastics – Determination of tensile properties - Part 4: Test conditions for isotropic and orthotropic fibre-reinforced plastic composites, and
4. **ISO 1172**, Textile-glass-reinforced plastics - Prepregs, moulding compounds and laminates — Determination of the textile-glass and mineral-filler content - calcination methods.

Whilst these ISOs were adhered to as closely as possible, some requirements were unable to be achieved. In particular, adhering to the mandated test specimen quantity and size was not possible in all cases as it was greatly influenced and constrained by the rotor blade geometry and the limited quantity available for sectioning. This is further detailed in the following paragraphs.

As can be seen by the following figures there was a finite limit to the amount of rotor blade available for disassembly and use as test coupons which limited to number of test coupons able to be manufactured. Added to this is the complex geometry of the component and additional bonded sub-components such as the titanium nose cap. The nose cap and the D-spar's inherent curvature ruled out the opportunity to create spar coupons from the majority of the spar, leaving only the rear-most surface for use. This surface enabled five test coupons and three fibre-fraction test pieces to be manufactured.

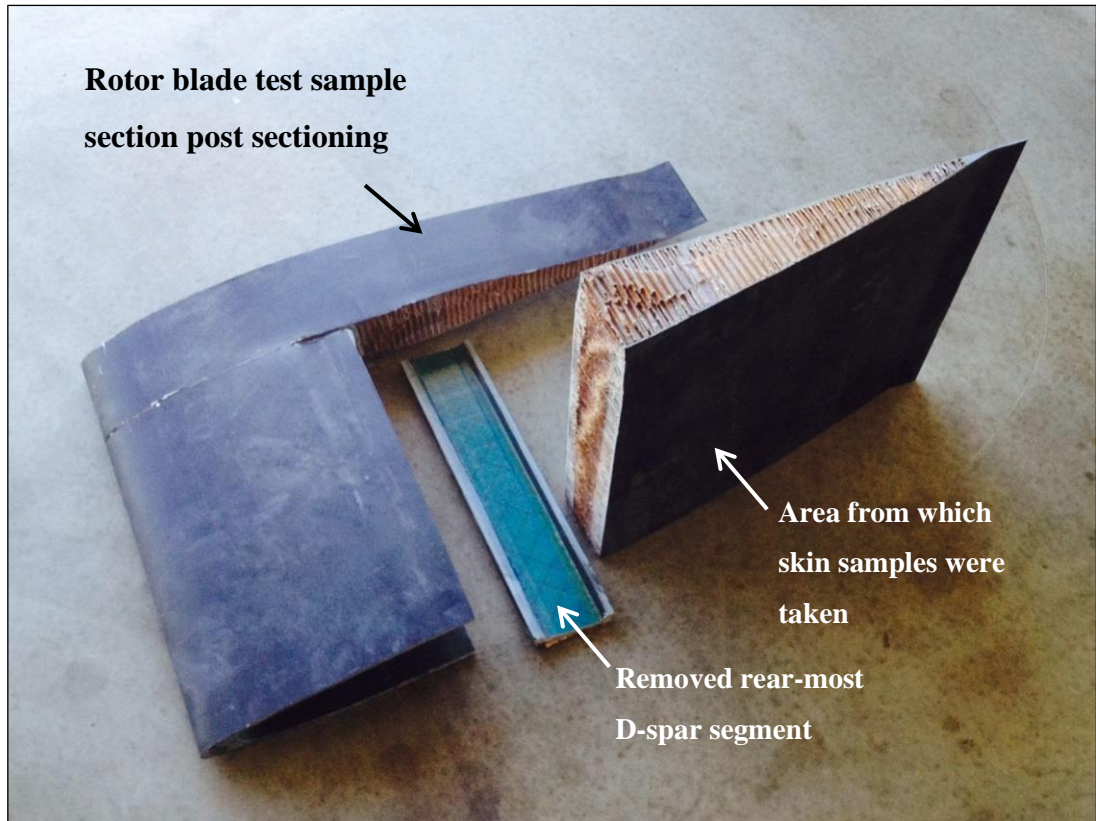


Figure 48. Sectioned blade for test samples.

From the above D-spar and skin sections all required test coupons and fibre-fraction samples were to be obtained. Two sections were able to be removed that were useable from which to create the five test coupons. The D-spar section with unsuitable portions removed prior to flexural/ tensile test coupon and fibre-fraction sample manufacture is pictured below.

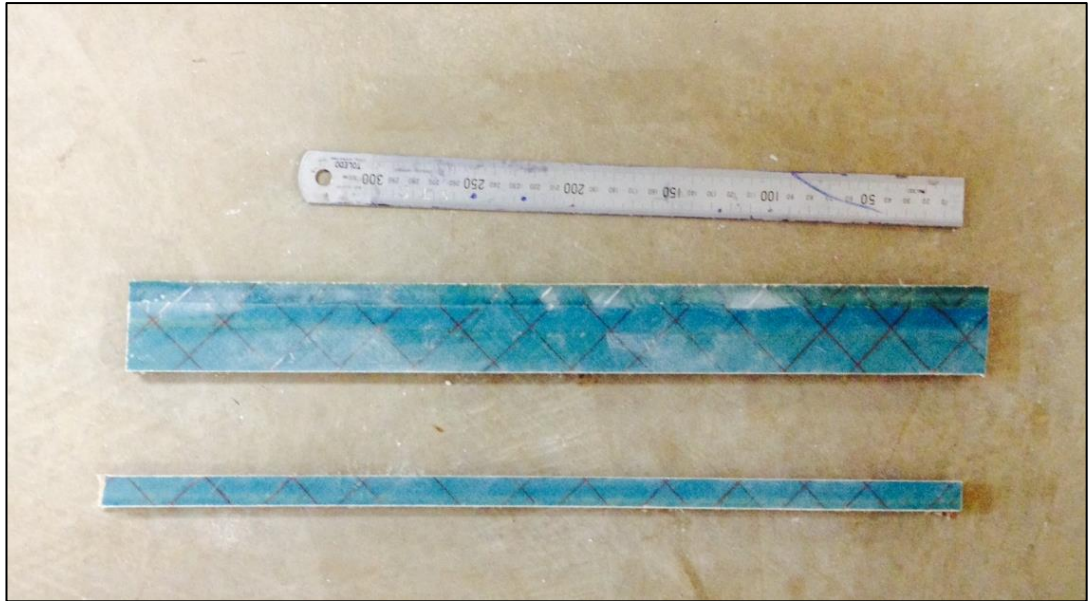


Figure 49. D-spar sample sections.

From the above sections the tensile and flexural testing coupons were manufactured in accordance with ISOs 14125, 527-1 and 527-4 as closely as possible.

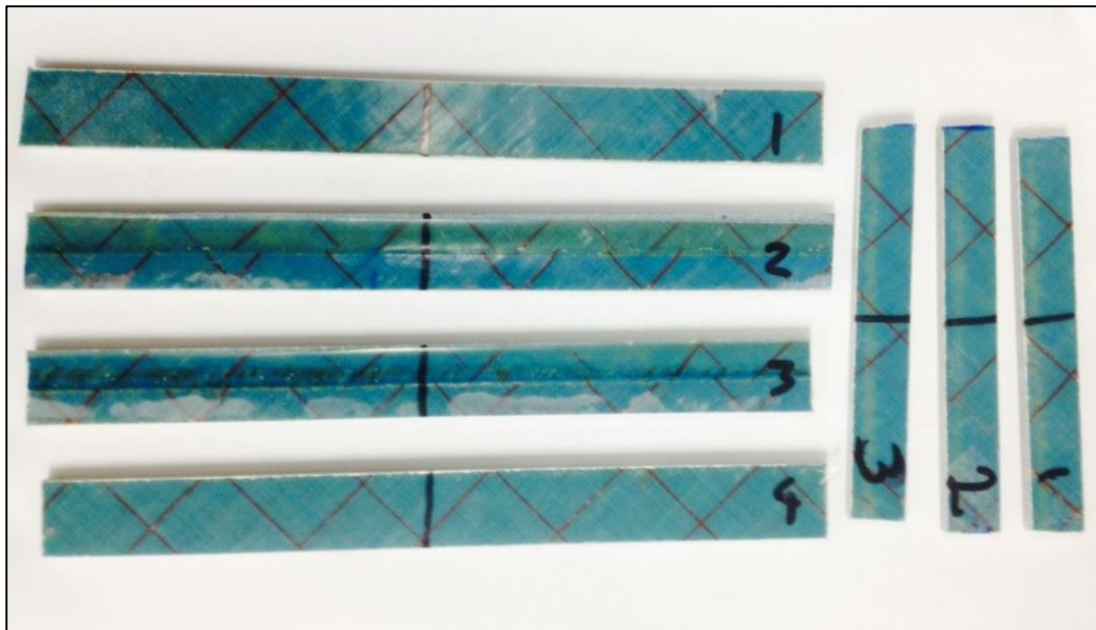


Figure 50. Final tensile (long) and flexural (short) testing coupons.

Calcination testing was conducted on both the D-spar and the skin with the skin samples pictured below.



Figure 51. Final skin calcination test samples.

Once the test coupons and samples were obtained final sizing and testing could commence.

9.3 FLEXURAL TESTING PROCEDURE AND RESULTS

Following is the procedure utilised for the flexural testing of the blade sub-components.

9.31 Determination of Flexural Properties

The manufacture and determination of the flexural properties of the spar and skin was conducted in accordance with ISO 14125, Fibre-reinforced plastic composites – Determination of flexural properties.

This standard and its methods are applicable to fibre-reinforced thermoplastic and thermosetting plastic composites from which the three point loading test method was adopted (referred to as Method A in the standard and subsequent extracts).

It was selected largely based on the availability of testing equipment at the USQ CEEFC and the requirement for a marginally smaller test sample size. A depiction of the three-point test loading, reference dimensions and arrangement is as follows:

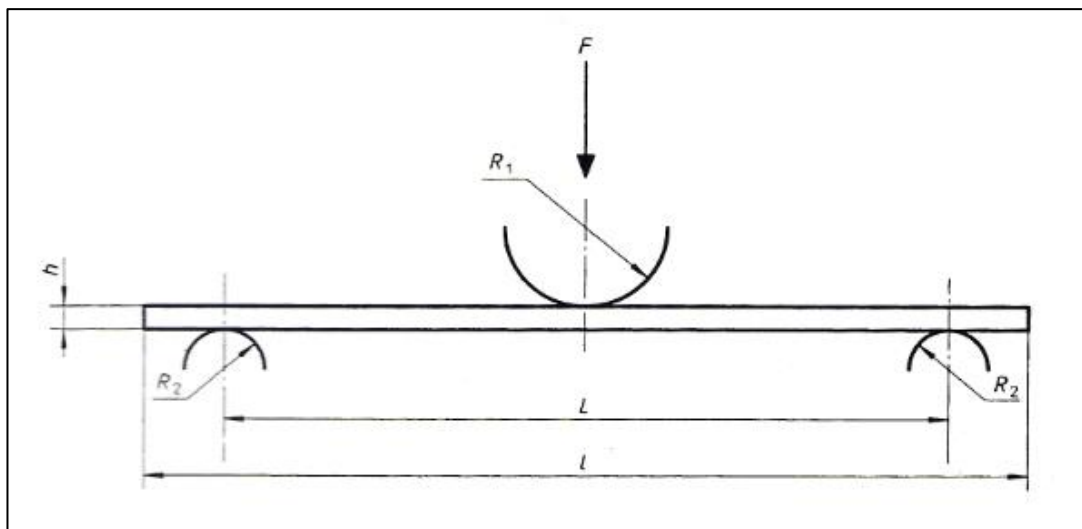


Figure 52. Three-point test diagram (Source: ISO 14125: 1998, p. 17).

9.32 Test Coupon Manufacture

The three samples used for flexural testing were machined to the ISO size from the blade spar section using a water lubricated, diamond blade table saw.

The samples were then sanded on the edges to reduce the effects of edged damage or the presence of surface discontinuities. Additionally, each sample was visually inspected (x10 magnification) for indications of damage such as delamination or cracking. One specimen was discarded as a result.

9.33 Determination of Specimen Material Class

In order to utilise ISO 14125, the material is required to be known. The rotor blade skin and spar are constructed of glass fibres; however, they are not solely transverse (90°) or unidirectional (0°) as such Material Class II was selected given the following ISO requirement: Class II Plastics reinforced with mats, continuous matting and fabrics, as well as mixed formats (ISO 14125: 1998, pp. 6).

9.34 Determination of Test Coupon Size

The following paragraphs detail the methodology used to determine the preferred sample sizes for both the D-spar and skin testing via material class II and the three-point testing method.

Table 9 presents the preferred values for flexural test specimen requirements (highlighted in red) with the test span (L) and specimen length (I) as a function of specimen thickness (h).

Table 9. Flexural test specimen requirements (Source: ISO 14125: 1998 pp.14).

Material class	Three-point		Four-point	
	L/h	l/h	L/h	l/h
I	16	20	16,5	20
II	16	20	16,5	20
III	20	30	22,5	30
IV	40	50	40,5	50

Table 10 details the thickness (h), calculation and results (mm) for the skin and D-spar test sample sizes as preferred by ISO 14125.

Table 10. Flexural test specimen length.

Dimension	Thickness (h)	Calculation	Result
Skin - Test Span (L)	1.0 mm	$L_{sk}/0.001 = 16$	16.0 mm
Skin -Test Sample Length (I)	1.0 mm	$I_{sk}/0.001 = 20$	20.0 mm
D-Spar - Test Span (L)	5.0 mm	$L_{sp}/0.005 = 16$	80 mm
D-Spar -Test Sample Length (I)	5.0 mm	$I_{sp}/0.005 = 20$	100 mm

Following Table 11 details the ISO 14125 preferred test sample width values (b) for Material Class II. The skin is indicated in red whilst the D-spar is in blue. The preferred width value for the skin and D-spar test sample was determined as 15 mm for both test specimens as detailed in the following table:

Table 11. Flexural test specimen width (Source: ISO 14125: 1998 pp.14).

Nominal thickness h	Width (b) Class I	Width (b) Classes II to IV
$1 < h \leq 3$	25	15
$3 < h \leq 5$	10	15
$5 < h \leq 10$	15	15
$10 < h \leq 20$	20	30
$20 < h \leq 35$	35	50
$35 < h \leq 50$	50	80

ISO 14125, Table 3 presents tolerances for the preferred test specimen dimensions and test span. For material class II in a three-point flexure test the preferred specimen dimensional tolerance (material class II) in millimetres are:

Table 12. Specimen dimensional tolerance (data extract from ISO 14125, Table 3, p. 6).

	Specimen Length (I)	Outer Span (L)	Width (b)	Thickness (h)
Tolerance	$\begin{matrix} -0 \\ +1.0 \end{matrix}$	± 1.0	± 0.5	± 0.2

The previous tables and calculations determined that the D-spar and skin final test sample preferred dimensions for a three-point flexural testing in accordance with ISO 14125 should be as follows:

Table 13. Final test sample preferred dimensions.

Sub-component	Length (I)	Width (b)	Thickness (h)
Skin	$20.0 \begin{matrix} -0 \\ +1.0 \end{matrix}$	15.0 ± 0.5	1.0 ± 0.2
D-spar	$100.0 \begin{matrix} -0 \\ +1.0 \end{matrix}$	15.0 ± 0.5	5.0 ± 0.2

The test coupons were prepared as closely as possible to these dimensions.

9.35 Flexural Testing Procedure

Flexural testing was conducted in accordance with ISO 14125 as closely as possible, with the exception of sample sizing and quantity.

As per ISO 14125, at least five test samples are required for a confidence interval probability of 95%. Due to the geometry of the rotor blade section and very limited availability of suitable cross-sectional material for testing, only three D-spar flexural test samples were able to be gained. The three flexural test coupons and the USQ CEEFC, MTS Alliance RT/10 testing machine use for the flexural testing are depicted in the following figure.

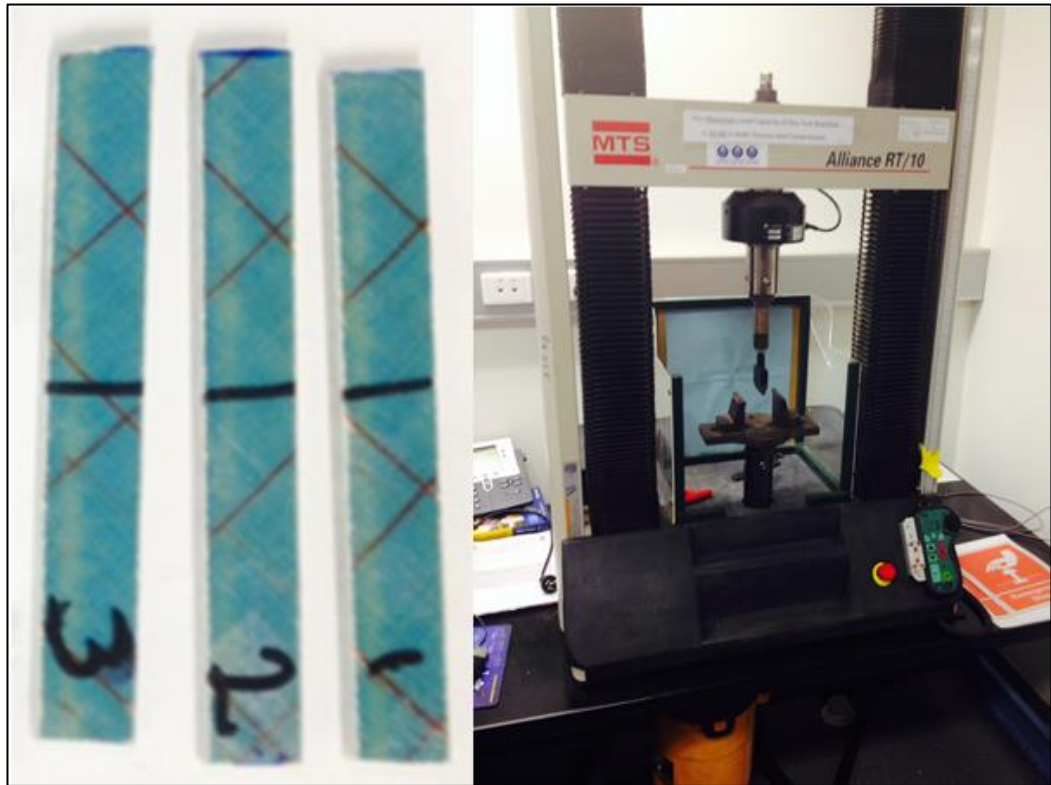


Figure 53. Flexural test coupons and testing machine.

A closer view of a flexural test conducted on a D-spar coupon is provided in the following figure.



Figure 54. Flexural test close up view.

9.36 Test Velocity

The following calculation as mandated by ISO 14125 was used to determine the appropriate load application speed for the three-point test:

$$V = \frac{\epsilon' L^2}{6h} \quad (9.1)$$

Where:

V = velocity of load application,

ϵ' = strain rate of 0.01 (1.0% per minute),

L = test span, and

H = thickness.

Therefore the required velocities are:

$$V_{\text{skin}} = \frac{0.01 \times 16^2}{6 \times 1} = 0.4267 \text{ mm/min}$$

$$V_{\text{spar}} = \frac{0.01 \times 80^2}{6 \times 5} = 2.1333 \text{ mm/min}$$

9.37 Loading Member and Support Dimensions

As per Fig. 52 the loading member and supports, R_1 and R_2 respectively, have been determined from ISO 14125 to be:

Table 14. Load and support member radius as derived from ISO 14125, Table 2 p. 5.

Dimension		Value
Skin	R_1	5.0 ± 0.2
	R_2 for $h < 3.0$ mm	2.0 ± 0.2
D-spar	R_1	5.0 ± 0.2
	R_2 for $h > 3.0$ mm	5.0 ± 0.2

9.38 Manual Calculation of Results

The following method of calculation was used to determine the flexural stress (σ_f) and the flexural modulus of elasticity (E_f) from the three-point flexure test, as taken from ISO 14125, p. 10. This process was only conducted on coupon 2 and was used as a broad verification of the computer generated results only.

Data such as deflection (mm) and load (N) was taken from the testing machine screen whilst the test was in progress.

Flexural Stress (σ_f). The flexural stress is given by the following equation:

$$\sigma_f = \frac{3 F L}{2 b h^2} \quad (9.2)$$

Where:

σ_f = flexural stress (MPa),

F = load (N),

L = test span (mm),

h = specimen thickness (mm), and

b = specimen width (mm).

Flexural Modulus (E_f). The flexural modulus is given by first calculating the mid-point deflections (s' & s'') of both the skin and spar test specimen using flexural strains (ε_f' and ε_f'') specified in ISO 14125:

$$E_f = 500 (\sigma_f'' - \sigma_f') \quad (9.3)$$

Where:

s' and s'' = mid-point deflections (mm):

$$s' = \frac{\varepsilon_f' L^2}{6 h} \quad (9.4)$$

$$s'' = \frac{\varepsilon_f'' L^2}{6 h} \quad (9.5)$$

From ISO 14125 the following is provided:

ε_f' = 0.0005 (flexural strain), and

ε_f'' = 0.0025 (flexural strain).

Yielding:

$$S_{\text{skin}}' = \frac{0.0005 \times 16^2}{6 \times 1} = 0.0213 \text{ mm}$$

$$S_{\text{skin}}'' = \frac{0.0025 \times 16^2}{6 \times 1} = 0.1067 \text{ mm}$$

$$S_{\text{spar}}' = \frac{0.0005 \times 80^2}{6 \times 5} = 0.1067 \text{ mm}$$

$$S_{\text{spar}}'' = \frac{0.0025 \times 80^2}{6 \times 5} = 0.5333 \text{ mm}$$

Where:

$$\sigma_f' = \text{is the stress measured at } s' \text{ (MPa),}$$

Yielding:

$$\sigma_f' = \frac{3 \times 19N \times 78}{2 \times 15 \times 5^2} = 5.928 \text{ MPa (0.100 mm deflection)}$$

Where:

$$\sigma_f'' = \text{is the stress measured at } s'' \text{ (MPa),}$$

Yielding:

$$\sigma_f'' = \frac{3 \times 100N \times 78}{2 \times 15 \times 5^2} = 31.2 \text{ MPa (0.500 mm deflection)}$$

The flexural modulus may then be calculated using:

$$E_f = 500 (\sigma_f'' - \sigma_f')$$

$$E_f = 500 (31.2 - 5.928)$$

Therefore the expected E_f for coupon 2 is:

$$E_f = 12636.0 \text{ MPa}$$

9.39 Flexural Test Results

The following computer generated data was obtained for the D-spar flexural testing using a three-point test. The results were verified by the manual check calculations above.

Table 15. Data obtained from the MTS Alliance RT/10 test machine.

Specimen #	Peak Flexural Stress (MPa)	Deflection at Peak (mm)	Peak Load (N)	Strain at Peak (%)	Flexural Modulus (MPa)
1	212.54	8.47	629	4.01	11787
2	211.82	7.51	583	3.45	12464
3	196.22	8.02	623	3.89	11730
Mean	206.86	8.00	612	3.79	11994
Std. Dev.	9.22	0.48	25	0.30	408

The following data was entered into the MTS Alliance RT/10 test machine data acquisition system. The thickness and width dimensions were actual measurements taken from the samples using Vernier callipers.

Table 16. Flexural testing manually entered data.

Specimen Number	Thickness 1 (mm)	Thickness 2 (mm)	Thickness 3 (mm)	Width 1 (mm)	Width 2 (mm)	Width 3 (mm)	Average Width (mm)	Average Thickness (mm)	Peak Load (N)
1	4.93	4.93	4.93	14.43	14.43	14.43	14.43	4.93	629
2	4.78	4.78	4.78	14.27	14.27	14.27	14.27	4.78	583
3	5.05	5.05	5.05	14.75	14.75	14.75	14.75	5.05	623
Mean	4.92	4.92	4.92	14.48	14.48	14.48	14.48	4.92	612
Std Dev	0.14	0.14	0.14	0.24	0.24	0.24	0.24	0.14	25

The following plot was generated by the flexural testing software and details the stress (MPa) vs strain (%) plot for the three individual D-spar test coupons.

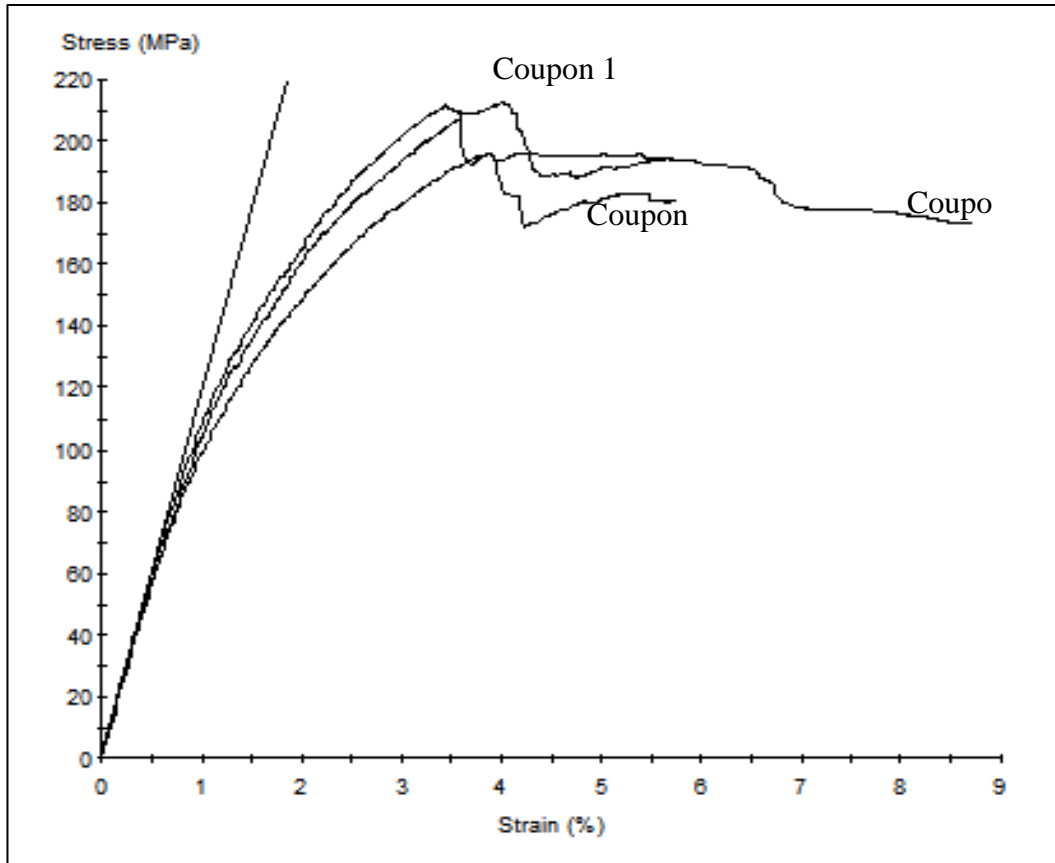


Figure 55. Flexural test stress vs strain plot.

9.39.1 Failure Modes

Following are typical failure modes for a three point loading test. Whilst not all inclusive it was reasonably expected that the final failure mode would be one of these, or a combination of modes.

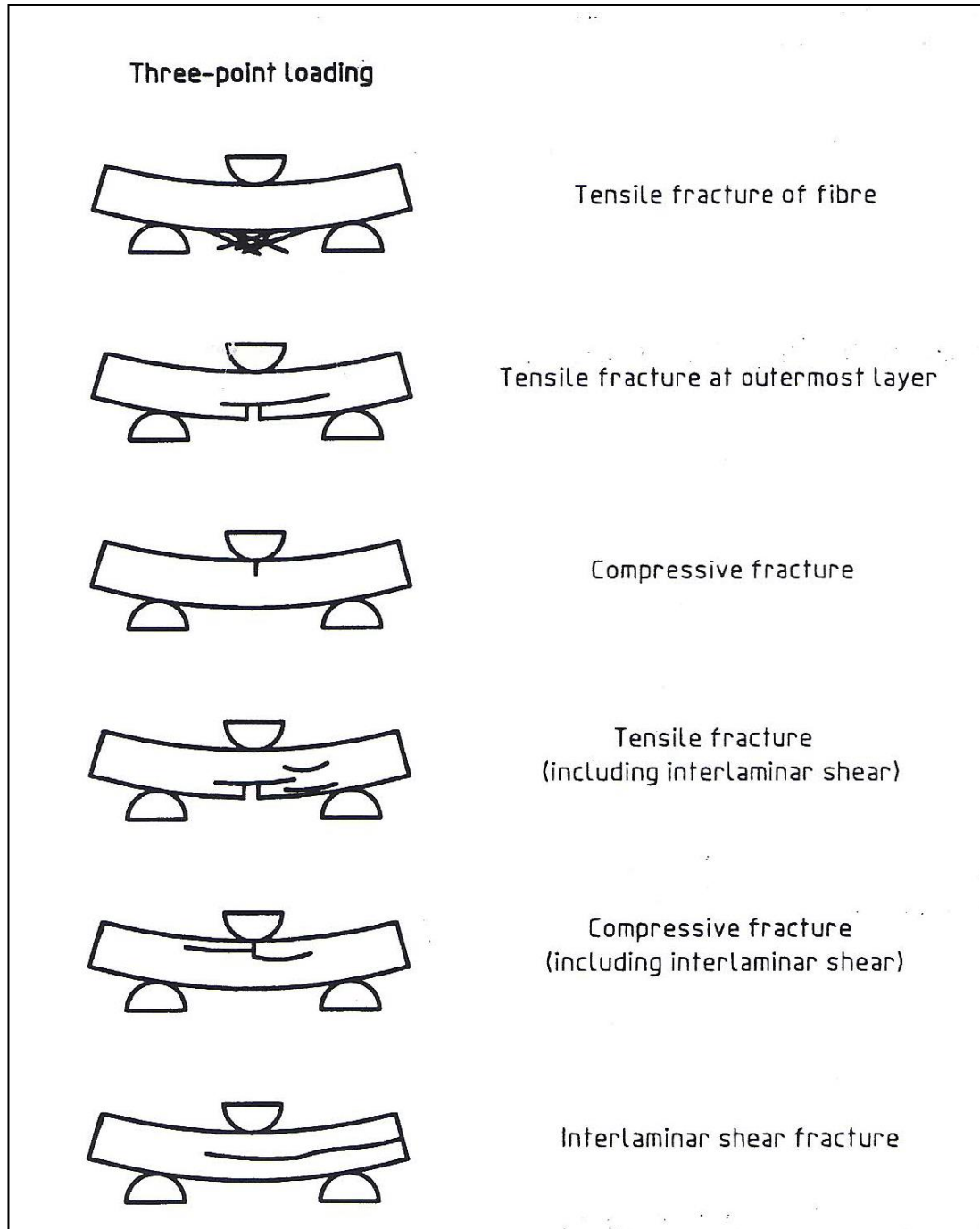


Figure 56. Three point bending test failure modes (Source: ISO 14125: 1998, pp 18).

The testing machine used was able to provide a report detailing the primary mode of failure for each coupon which is presented below in table format.

Table 17. Flexural test primary failure modes.

Specimen #	Failure Mode
1	Tensile Fracture at Outermost Layer
2	Tensile Fracture at Outermost Layer
3	Tensile Fracture at Outermost Layer

Whilst the test equipment recognised the failures as tensile fracture at the outermost layer, it can be seen in the following diagram of coupon 1, several modes of failure occurred. These include compressive fracture of the upper most surface, tensile fibre fracture and tensile fracture including interlaminar shear.

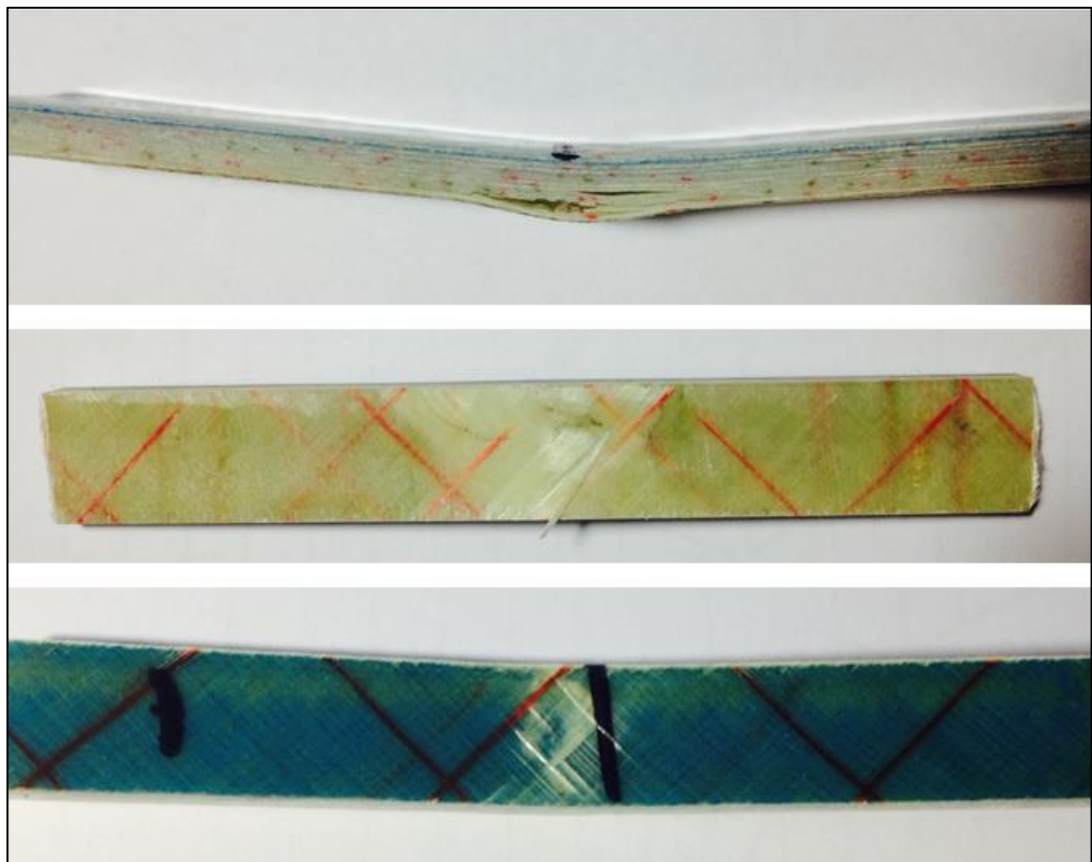


Figure 57. Flexural test coupon observed modes of failure.

The above flexural testing and resultant data was integral information utilised during the FEA modelling phase, in particular to that of the main structural component of the rotor blade, the D-spar.

Another primary property required for modelling is the D-spar's tensile strength.

9.4 TENSILE TESTING PROCEDURE AND RESULTS

Following is the procedure utilised for the tensile testing of the blade sub-components.

9.41 Determination of Tensile Properties

Determination of the tensile properties of the rotor blade spar and skin was conducted in accordance with ISO 527-1, Plastics – Determination of tensile properties - Part 1: General Principles and ISO 527-4, Plastics – Determination of tensile properties - Part 4: Test conditions for isotropic and orthotropic fibre-reinforced plastic composites.

In general, ISO 527-4 and its methods are applicable to fibre-reinforced thermosetting and thermoplastic composites incorporating non-unidirectional reinforcements and unidirectional reinforcements and multidirectional reinforced materials constructed from unidirectional layers. The reinforcement fibres covered include glass fibres, carbon fibres, aramid fibres and other similar fibres. Therefore, visual inspection both pre and post fibre-fraction testing determined these standards to be applicable and appropriate for the rotor blade spar and skin tensile testing.

9.42 Test Coupon Manufacture

The four samples used for tensile testing were machined to size from the blade D-spar section using a water lubricated, diamond blade table saw. The samples were then sanded on the edges to reduce the effects of edged damage or the presence of surface discontinuities. Additionally, each sample was visually inspected (x10 magnification) for indications of damage such as delamination or cracking. No samples were discarded.

9.43 Determination of Specimen Type

ISO 527-4 offers three types of specimen class being:

1. Type 1B, for fibre-reinforced thermoplastics; however, shall not be used for multidirectional, continuous-fibre-reinforced materials.
2. Type 2 (rectangular without end tabs), used for testing fibre-reinforced thermosets and thermoplastics with un-bonded end tabs.
3. Type 3 (rectangular with bonded end tabs), used for testing fibre-reinforced thermosets and thermoplastics if the testing as a Type 2 was unsatisfactory such as the specimen slips or breaks in the grips with un-bonded end tabs.

As a result of the three specimen testing options Type 2 was selected, with the intension to progress to Type 3 should the initial test fail.

9.44 Determination of Test Coupon Size

Following is the methodology used to determine the preferred sample sizes for both the D-spar and skin testing via test specimen Type 2.

ISO 527-4, p. 2 specifies the following in respect to sample sizes for tensile testing:

The preferred width of type 2 and type 3 specimens is 25 mm, but widths of 50 mm or greater may be used if the tensile strength is low due to the particular type of reinforcement used. The thickness of type 2 and type 3 specimens shall be between 2 mm and 10 mm.

Whilst every effort was made to adhere to the above requirements it was not possible to achieve a 25 mm width for the test samples without reducing the sample quantity to unacceptable levels. As a result a sample width of 20 mm was used. The following table was used to determine the remaining requirements such sample length and grip spacing. Centring holes were not utilised during this testing as alignment could be adequately achieved without them.

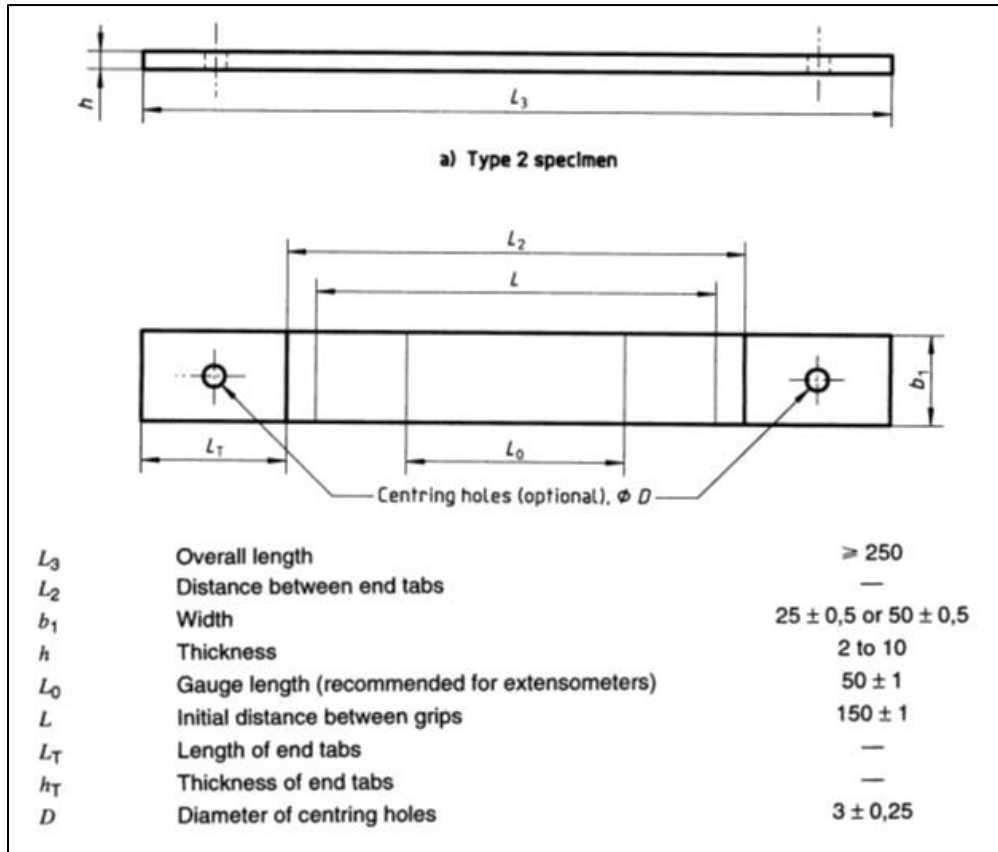


Figure 58. Summary of Type 2 tensile specimen dimensions (Source: ISO 527-4:1997, pp 4).

Table 18 details the final test sample dimensions following consideration given to the material constraints and testing equipment requirements, whilst remaining as closely as possible to the ISO specified dimensions.

Table 18. Tensile test specimen dimensions summary.

Dimension	ISO Required	Actual	Remarks
Width (mm)	25.0 ± 0.5	20.0 ± 0.5	Limited due sample material availability.
Thickness (mm)	2.0 – 10.0	5.0 (nominal)	OK
Length (mm)	>250.0	210.0	Limited due sample material availability.
Distance Between Grips (mm)	150.0 ± 0.25	125.0 ± 0.25	Adequate grip length & spacing for testing equipment used.

9.45 Tensile Testing Procedure

The tensile testing was conducted in accordance with ISO 527-1 and ISO 527-4 as closely as possible, with the exception of sample sizes and quantity.

ISO 527-1, requires at least five test samples for a confidence interval probability of 95%. Again due to the geometry of the rotor blade section and very limited availability of suitable cross-sectional material for testing, only four D-spar flexural test samples were able to be gained.

Tensile test samples 1-4 pre-trimming to final length with the surface ply fibre orientation clearly observable are presented in the following figure.

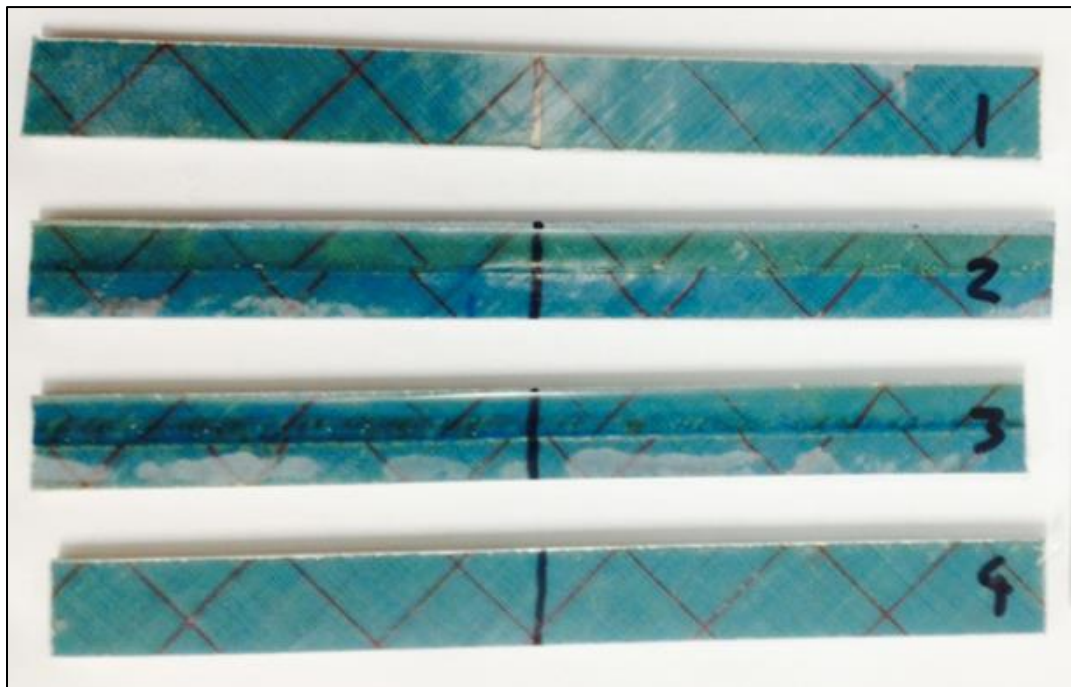


Figure 59. D-spar tensile test coupons.

The USQ CEEFC, MTS Insight tensile testing machine, which was used for the tensile testing, with a D-spar coupon installed is depicted in the Fig. 60.



Figure 60. MTS Insight tensile testing machine.

9.46 Test Velocity

ISO527-4 provides the following recommended test speeds for type 2 samples:

1. 5.0 mm/min for routine quality control, and
2. 2.0 mm/min for qualification tests.

Consultation with the CEEFC laboratory staff advised that a test load application speed of 2.0 mm/min was appropriate for this testing regime and the test equipment.

9.47 Grip Spacing

The previously determined grip spacing of 125.0 ± 0.25 mm was used for all four testing cycles.

9.48 Tensile Test Results

Fig. 61 is a screen capture of the computer calculated result data and a summary table for the four samples tensile tested:

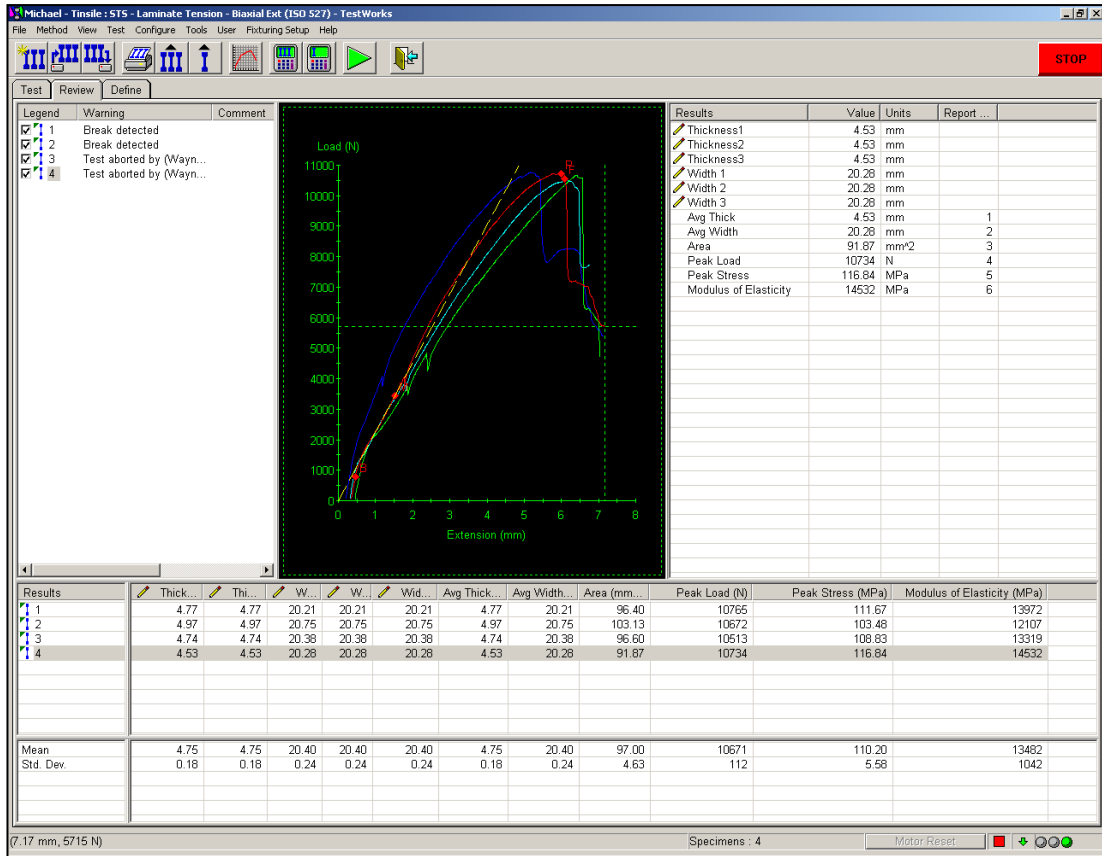


Figure 61. Tensile test computer screen shot plots and data.

The following results table details the determined modulus of elasticity for the material.

Table 19. Tensile test summary of results.

	Peak Load (N)	Peak Stress (MPa)	Modulus of Elasticity (MPa)
Mean	10671	110.20	13482
Std. Deviation	112	5.58	1042

9.49 Failure Modes

As can be observed in Fig. 62 the tensile specimens experienced transverse fibre stress and fracture, delamination and ply failure via fracture. It can also be observed that the surface transverse fibres are displaced and in some cases fractured where they are not constrained and supported by a subsequent ply.

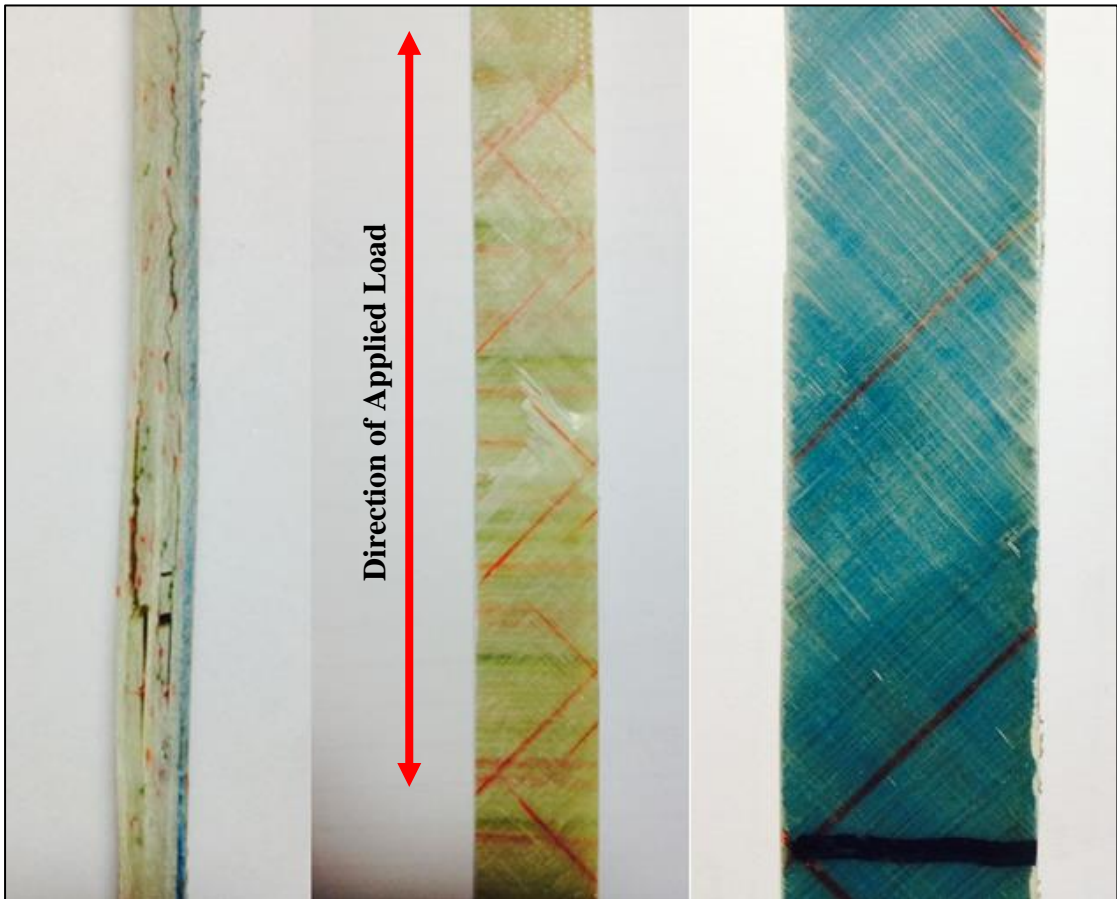


Figure 62. Failed tensile test sample.

9.5 FIBRE-FRACTION TESTING AND RESULTS

The following section describes the determination of fibre-fraction and fibre orientation for the rotor D-spar and skin.

9.51 Determination of Fibre-Fraction

The determination of the fibre-fraction properties of the spar and skin was conducted in accordance with ISO 1172, Textile-glass-reinforced plastics — Prepregs, moulding compounds and laminates — Determination of the textile-glass and mineral-filler content — Calcination methods.

This standard specifies calcination methods for the determination of the textile-glass content of reinforced plastics both when mineral fillers are present and when not. They are applicable for filled and unfilled textile-glass laminates made with thermosetting or thermoplastic resins.

ISO 1172 Method A: for the determination of the textile-glass content when no mineral fillers are present was used for this testing regime.

9.52 Calcination Sample Manufacture

In accordance with the ISO, the mass of each sample must be within 2 – 10 grams for laminates with a minimum of 2 test samples. The following figures depict the D-spar and skin test samples used, with the three D-spar samples and crucibles prior to calcination, and a sample placed within a crucible presented first.



Figure 63. D-spar calcination samples and crucibles.

The skin samples were approximately 25.0 mm x 25.0mm once removed from the rotor blade test sample. In the following figure the Nomex core is easily seen which was removed from the inner surface of the samples prior to calcination.

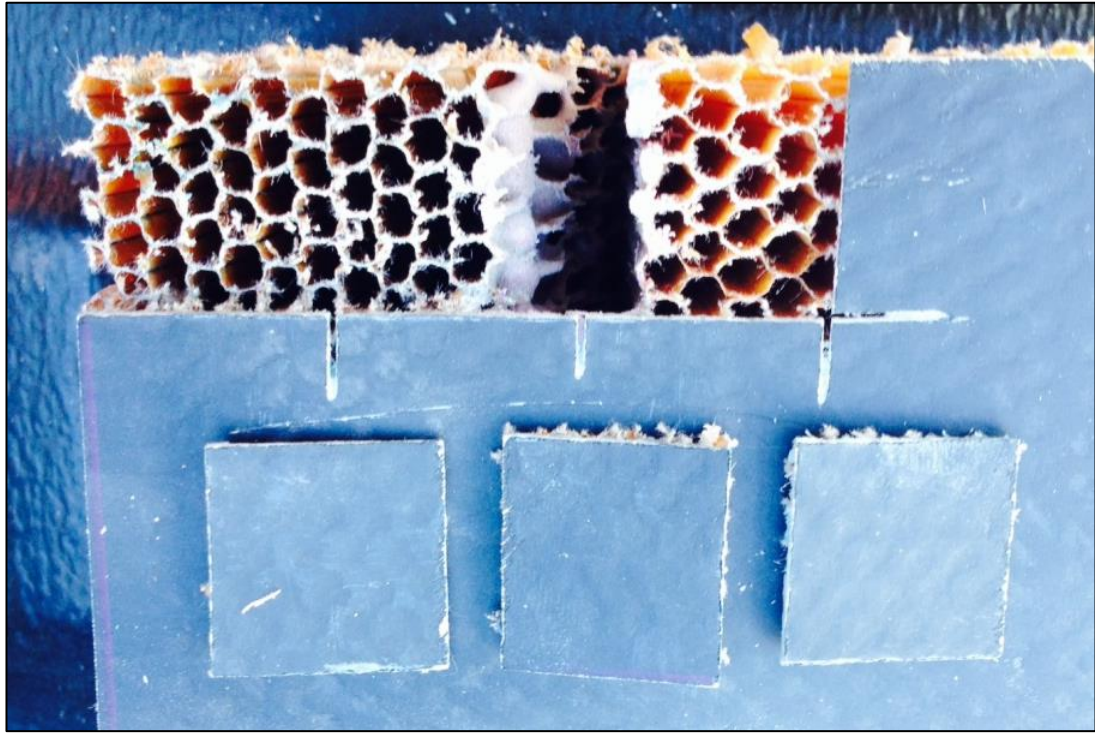


Figure 64. Calcination skin samples.

9.53 Calcination Testing Procedure

The calcination testing was conducted in accordance with ISO 1172.

ISO 1172 requires that at least two test samples be calcified. In contrast to previous tests, due to the relatively small size of the samples, three test samples for both the D-spar and skin were able to be manufactured and tested. The USQ CEEFC, calibrated electronic scales and temperature controlled furnace were used for the testing, and are depicted in the following figures.

As recommended by ISO 1177, 'For reinforced products with glass or filler which will not withstand this calcination temperature, a temperature between 500 °C and 600 °C may be used...'

As it was unclear what level of temperature could be withstood by the glass fibres a furnace temperature of $575^{\circ}\pm 25$ was determined as appropriate via consultation with the CEEFC laboratory staff.

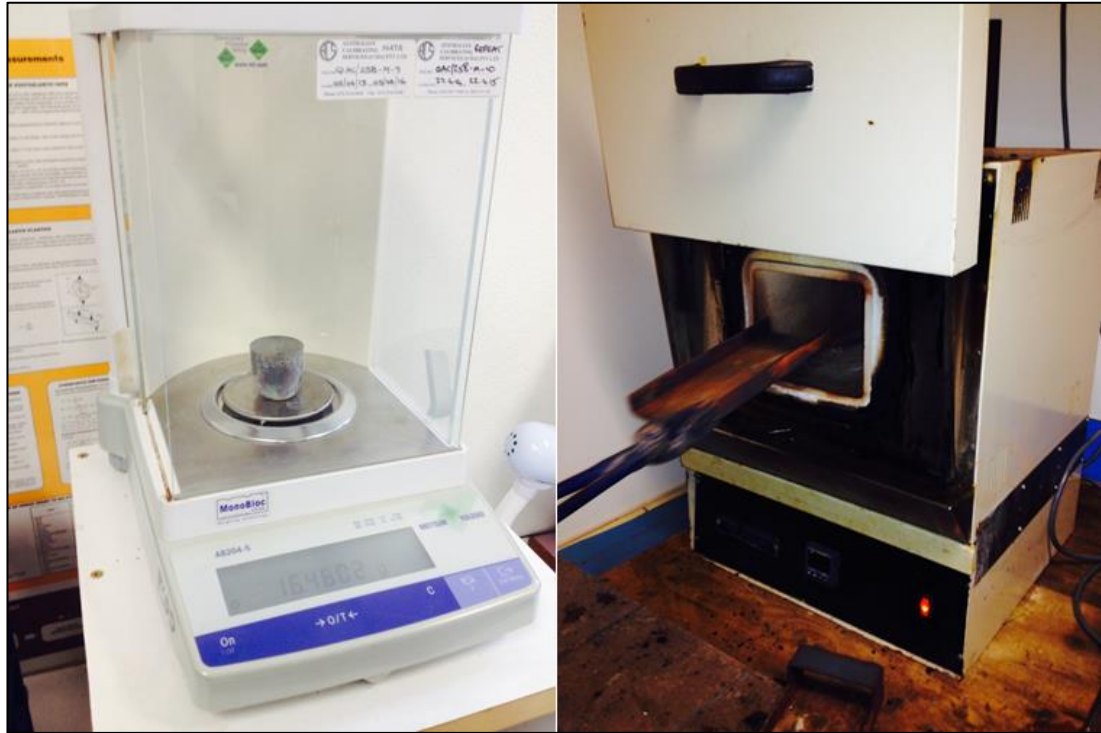


Figure 65. CEEFC electronic scale and temperature controlled furnace.

The following table contains the calcination test results and weight data taken from the glass content test form at Appendix E.

9.54 Results – Glass Content

The following table details the fibre-fraction or glass content of the samples tested.

Table 20. Glass content test results & data.

Crucible Number	Dry Crucible Mass (g)	Dry Specimen Mass (g)	Initial Dry Total Mass Crucible & Specimen (g)	Final Calcinated Total Mass Crucible & Specimen (g)	Glass Content (%)
7	16.094	3.572	19.666	18.684	72.51
8	16.509	3.828	20.337	19.305	73.04
9	16.461	3.454	19.915	18.972	72.70

9.55 Calculation of Glass Content

The following equation was used in the calculation of the final glass content in Table 20 above.

$$M_g = \frac{m_3 - m_1}{m_2 - m_1} \times 100 \quad (9.6)$$

Where:

m_1 = is the initial mass (g) of the crucible,

m_2 = is the initial mass (g) of the crucible plus dried specimen, and

m_3 = is the final mass (g) of the crucible plus residue after calcination.

Figures 66 and 67 depict the D-spar samples post calcination and the skin sample pre and post calcination. In order to determine the laminate lay-up sequence and plie orientation they were each carefully removed from the crucible after weighing for separation and visual examination.



Figure 66. Three D-spar samples post calcination.

The skin samples post calcination initially appeared to be a woven mat type. On closer inspection it was determined that the dimpled / woven appearance was a result of the underlying Nomex core.

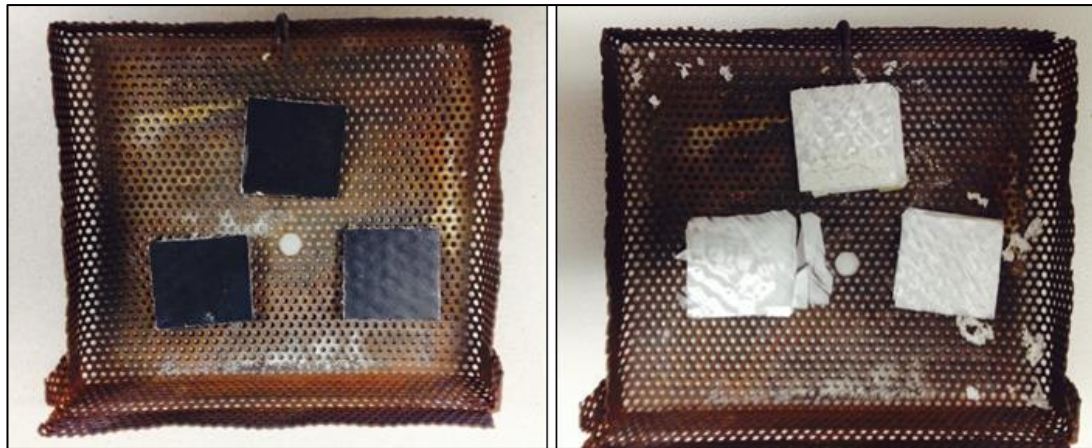


Figure 67. Skin samples pre and post calcination.

The D-spar samples, once removed from the crucible, were carefully separated into individual plies in order to determine the stacking sequence and orientation. Fig. 68 shows the D-spar plies post separation demonstrating the fragility of the plies and necessity for a methodical lay-out approach for inspection.



Figure 68. D-spar plies post separation demonstrating fragility.

Each sample was deconstructed with the plie orientation noted, as in the D-spar samples in Figures 69 and 70 below.

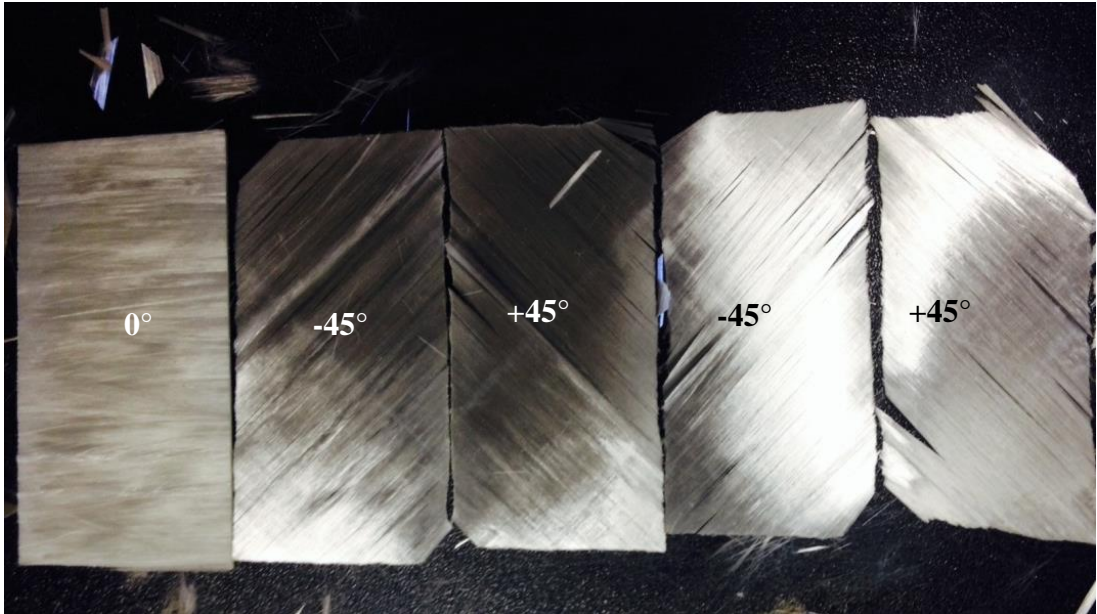


Figure 69. D-spar plie orientation magnified view.

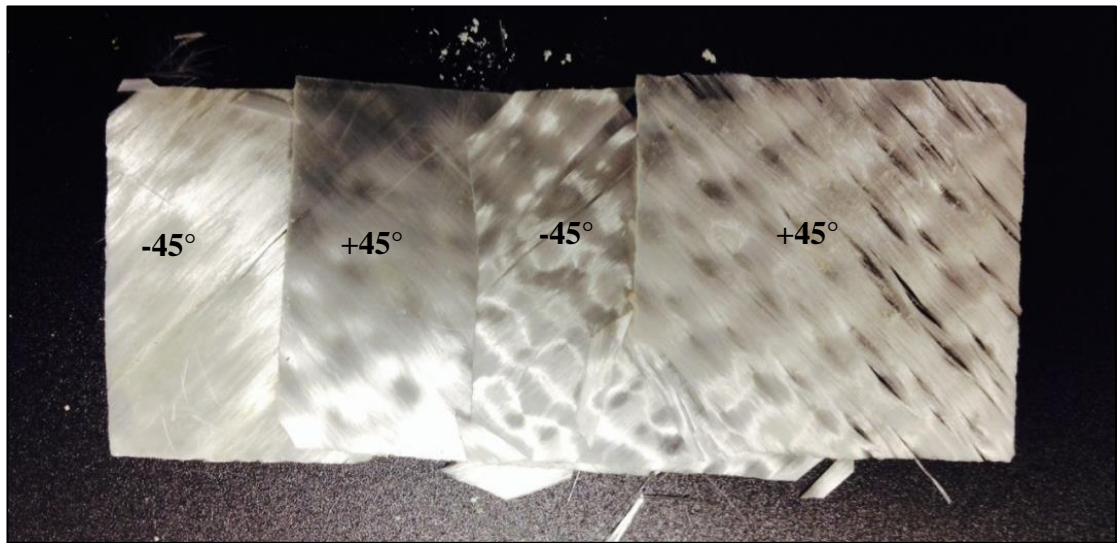


Figure 70. Skin sample with plies separated following calcination.

9.56 Results - Ply Stacking Sequence

The following table contains the consolidated results of the D-spar lay-up/orientation visual inspection. The difference between crucible 7 and 8 & 9 is due to the initial inspection of sample 7 not recognising the two, double 0° plie lay-ups, as they were in samples 8 and 9.

Table 21. D-spar plie orientation.

Crucible / Sample Number (Sample Nominal Mass: 3.62 grams)				Plie Position (Relative to Innermost Surface of the Spar)	
Plie #	Crucible 7	Crucible 8	Crucible 9		
1	+45°	+45°	+45°	Outer-most Plie	
2	-45°	-45°	-45°		
3	+45°	+45°	+45°		
4	-45°	-45°	-45°		
5	0°	0°	0°		
6	-45°	0°	0°		
7	+45°	-45°	-45°		
8	-45°	+45°	+45°		
9	+45°	-45°	-45°		
10	0°	+45°	+45°		
11	+45°	0°	0°		
12	-45°	0°	0°		
13	+45°	+45°	+45°		
14	-45°	-45°	-45°		
15	+45°	+45°	+45°		
16	-45°	-45°	-45°		
17	+45°	+45°	+45°		
18	-45°	-45°	-45°		
19	---	+45°	+45°		
20	---	-45°	-45°		Inner-most Plie
Remarks	Initial inspection did not identify the dual 0° plies in this sample. This was however identified in samples 8 & 9 and determined as correct.	Samples 8 & 9 are identical in the number of plies and orientation and are therefore considered as accurate for FEA Modelling purposed. Additionally, samples 8 & 9 are the same as sample 7 with the exception of the dual 0° plies.	Samples 8 & 9 are identical in the number of plies and orientation and are therefore considered as accurate for FEA Modelling purposed. Additionally, samples 8 & 9 are the same as sample 7 with the exception of the dual 0° plies.		

Table 22 contains the consolidated results of the skin lay-up/ orientation visual inspection.

Table 22. Skin laminate plie stacking sequence.

Skin Laminate Plie Stacking Sequence				
Plie #	Skin Sample 1	Skin Sample 2	Skin Sample 3	
1	-45°	-45°	-45°	Outer-most
2	+45°	+45°	+45°	
3	-45°	-45°	-45°	
4	+45°	+45°	+45°	Inner-most

The three testing methods mentioned within this chapter provided sufficient material property data for the remainder to be manually calculated, or inputted into Strand 7, for determination of other parameters that may be required for FEA modelling.

CHAPTER 10 - FEA MODELS

This chapter discusses the development and use of FEA models within this research.

10.1 General Overview

During the FEA process Microsoft Excel, MatLab, Strand 7 and Abaqus 6.12 software was used to varying degrees; however, Abaqus was the primary modelling software. It was utilised due to its advanced features and ability to model complex FRP arrangements. Several models were created to include the rotor blade sub-components, rotor blade assembly and a simplified flat plate simulation models.

Strand 7 was only used to assist in determining additional ply properties, whilst Abaqus was used for the simulations. Prior to model creation a verified coordinate set of the outer blade profile was required.

10.2 Rotor Profile Co-ordinates

To allow for the modelling, significant time was invested in accurately measuring and plotting the blade profile. Whilst a rough set of plotting coordinates was available, they proved inaccurate, necessitating the requirement for physical measurement and confirmation. To this end, Table 23 details the verified co-ordinates which were manually entered into Abaqus to create the rotor skin outer profile. Interpolation was utilised to create the profile from the points listed.

This profile was intern used as a reference datum from which the remaining sub-components models were created.

Table 23. Blade profile coordinates.

Rotor Surface Coordinates			
Upper Surface		Lower Surface	
X(mm)	Y(mm)	X(mm)	Y(mm)
815	4.075	0	0
782.4	4.075	4.075	-4.68625
762.025	5.053	8.15	-6.6015
741.65	8.5575	16.3	-8.8835
717.2	13.6105	24.45	-10.5135
688.675	19.1525	32.6	-11.7768
660.15	24.5315	40.75	-12.9178
627.55	30.481	48.9	-13.9365
594.95	36.4305	57.05	-14.7108
562.35	41.891	69.275	-16.1778
529.75	47.27	83.13	-17.4818
497.15	52.649	97.8	-18.6228
464.55	57.865	114.1	-19.6415
431.95	62.5105	130.4	-20.4565
399.35	66.504	146.7	-21.19
366.75	69.764	163	-21.679
334.15	72.2905	183.375	-22.2495
301.55	73.7575	207.825	-22.82
268.95	74.491	236.35	-23.2275
236.35	74.0835	268.95	-23.5535
207.825	72.698	301.55	-23.635
183.375	70.6605	334.15	-23.2275
163	68.297	366.75	-22.4125
146.7	65.852	399.35	-21.19
130.4	63.1625	431.95	-19.56
114.1	60.0655	464.55	-17.93
97.8	56.3165	497.15	-16.2185
83.13	52.5675	529.75	-14.5885
69.275	48.3295	562.35	-12.877
57.05	44.0915	594.95	-11.247
48.9	40.95375	627.55	-8.76125
40.75	37.53075	660.15	-6.88675
32.6	33.8225	688.675	-5.216
24.45	29.46225	717.2	-3.46375
16.3	24.287	741.65	-1.91525
8.15	17.767	762.025	-0.489
4.075	13.4475	782.4	0

The coordinate set was again checked for gross error by creating a simple plot in MS Excel. This initial plotting identified several discrepancies; in particular in the region of the rear tab and nose radius, however they were adequately rectified as presented below with the red cross (+) representing major data points.

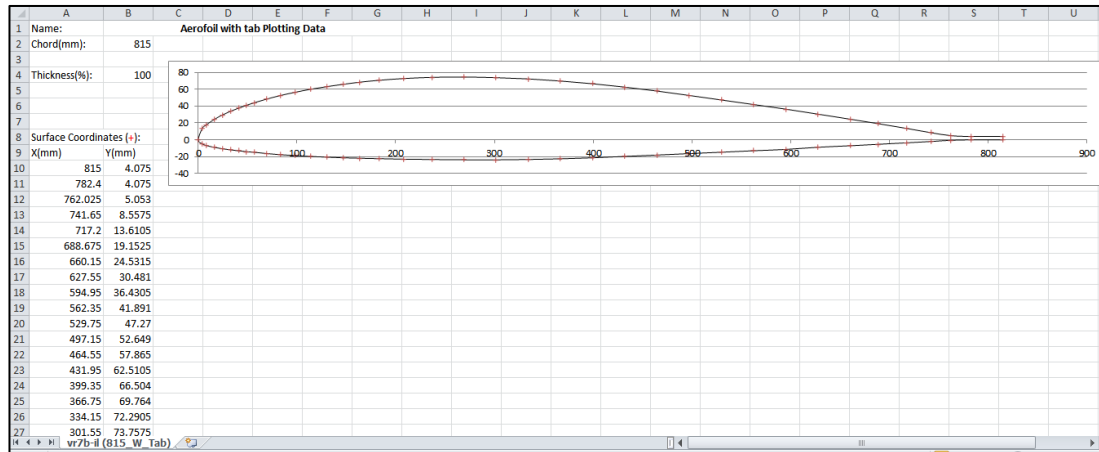


Figure 71. MS Excel data point confirmation plot.

Once the profile coordinate system was acceptable FEA modelling in Abaqus 6.12 commenced. A broad plan was created, as directed below, to allow subsequent creation of each part from the information provided by the previously modelled part.

10.3 Sub-component Modelling

The rotor modelling was broken down into the four parts, which when combined formed the rotor system assembly model. The logic applied to the modelling task is presented in the following diagram.

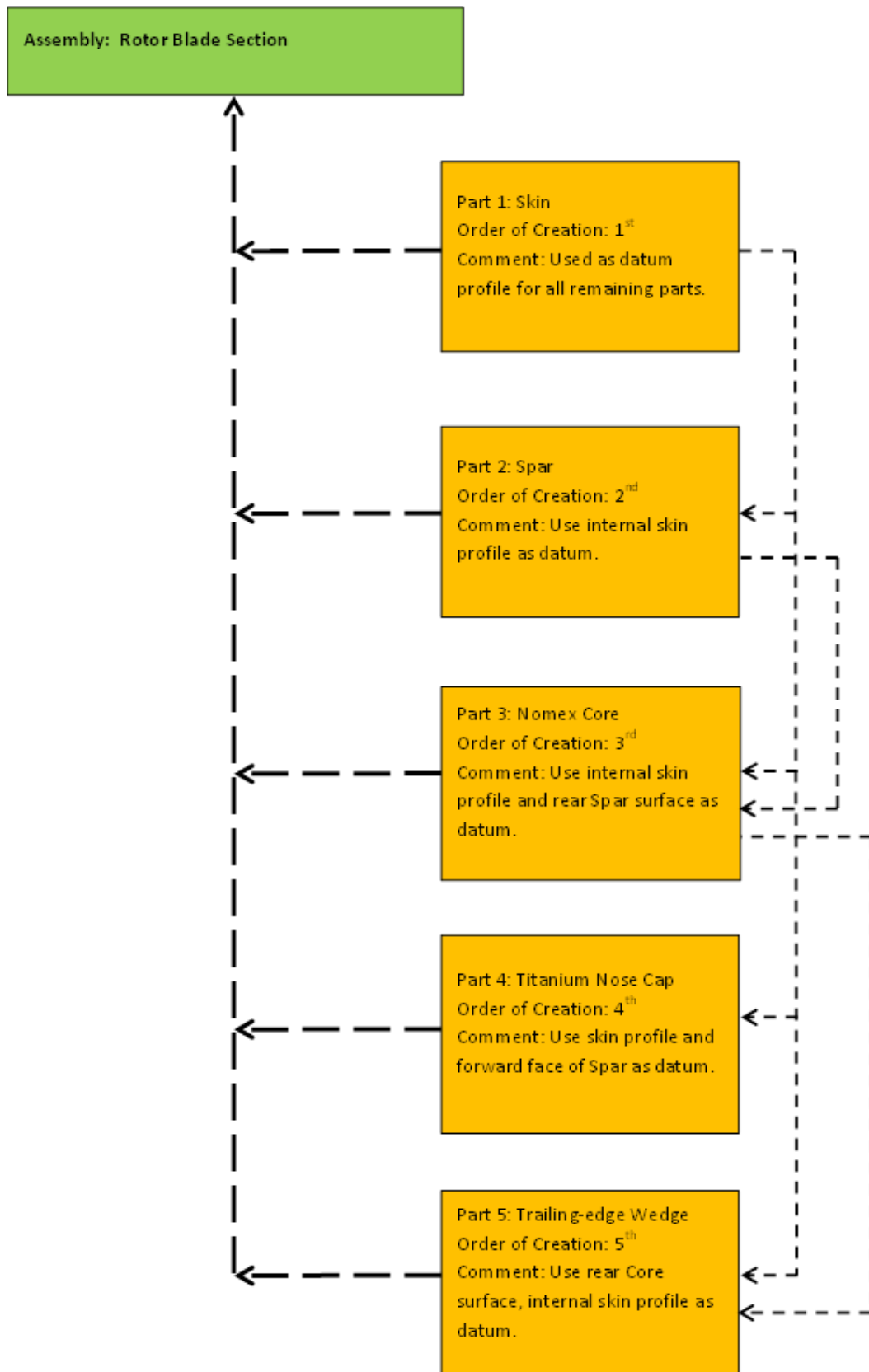


Figure 72. Graphical layout of FEA part creation order.

The process of creating the model in Abaqus was significantly underestimated, both in terms of time but also complexity.

This resultant loss of time and lack of in-depth usage knowledge impacted on the author's ability to produce optimal models; however, an acceptable level of modelling was achieved to verify some physical testing results.

10.4 Rotor Skin

The initial part created was the rotor skin which was subsequently utilised to create the remaining parts for the assembly. Of note is that the dark longitudinal lines in the following figures do not represent sudden changes in geometry; they are 'save points' created during the use of the Abaqus 6.12 spline interpolation function between each coordinate.

The following four figures are Abaqus 6.12 screen captures of the rotor sub-components, presented in order of creation along with each component's initial element mesh.

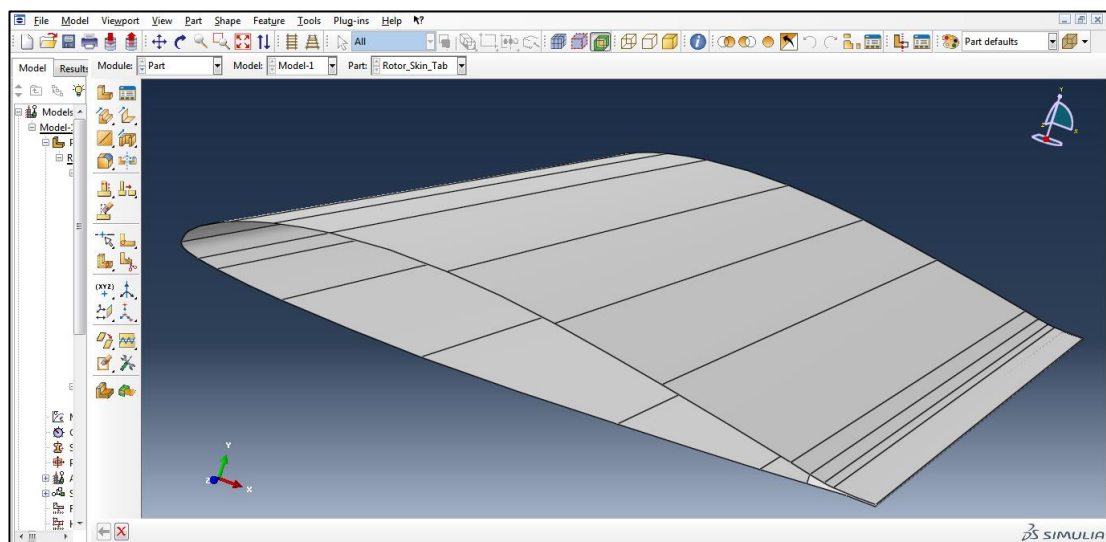


Figure 73. FEA skin model and datum.

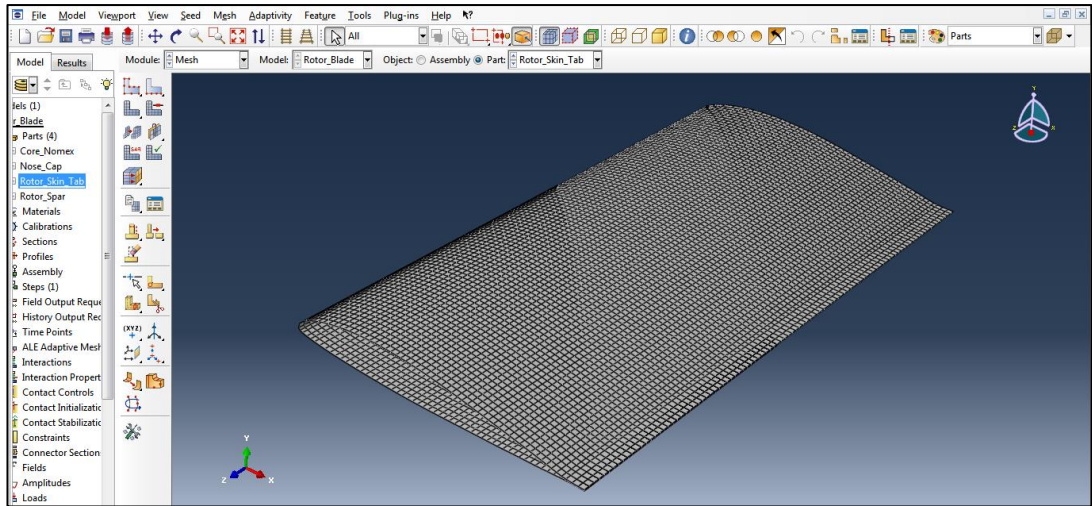


Figure 74. FEA Skin model mesh grid with 11500 elements.

10.5 Rotor D-spar

The D-spar, as with the testing, was the most critical component given its role in the structure. Therefore particular attention was given to the accuracy of the profile established in Abaqus.

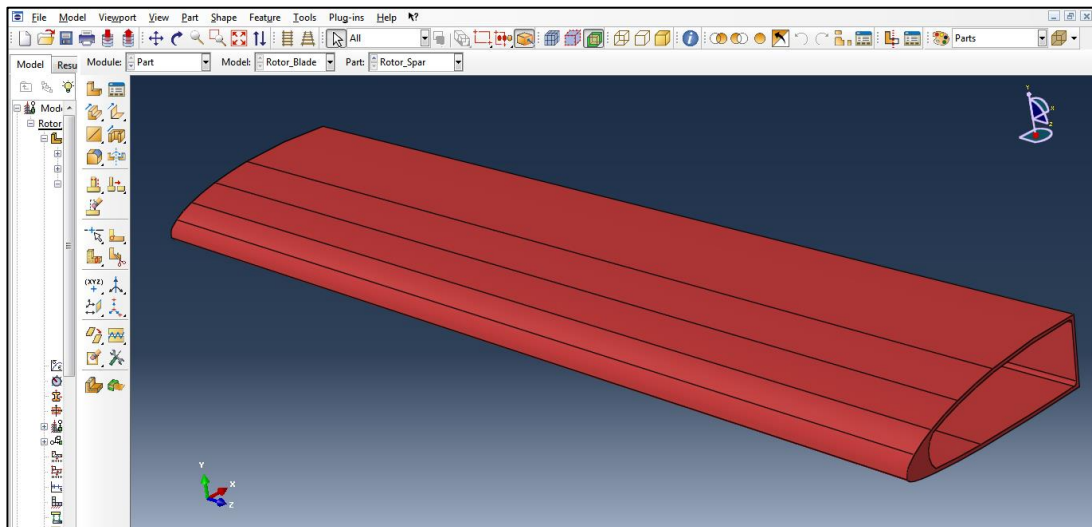


Figure 75. FEA rotor spar model.

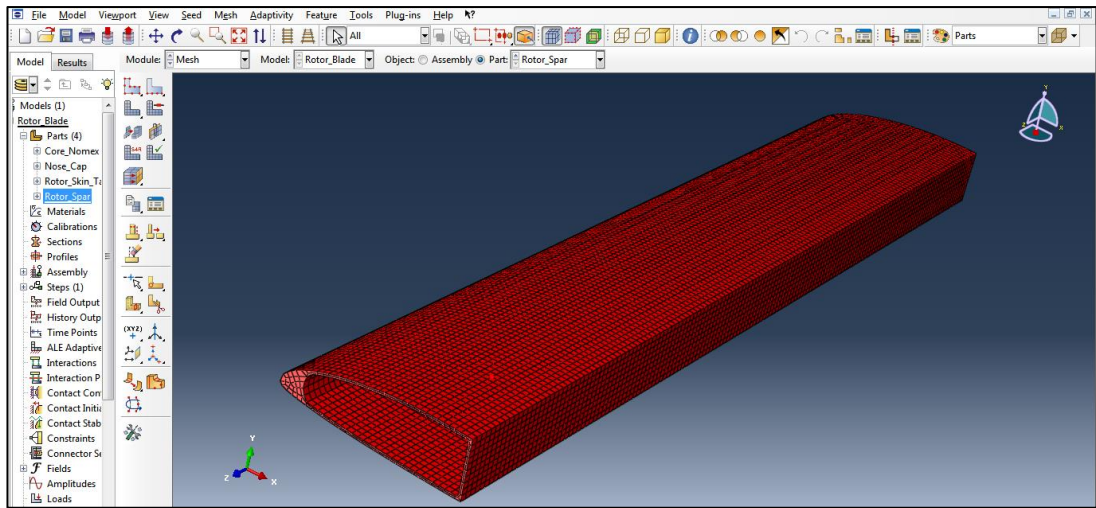


Figure 76. FEA D-spar model mesh grid of 23550 elements.

10.6 Erosion Cap

The titanium nose / erosion cap was modelled with relative ease given the profile is the same as the outer skin although problems were experienced during the model assembly.

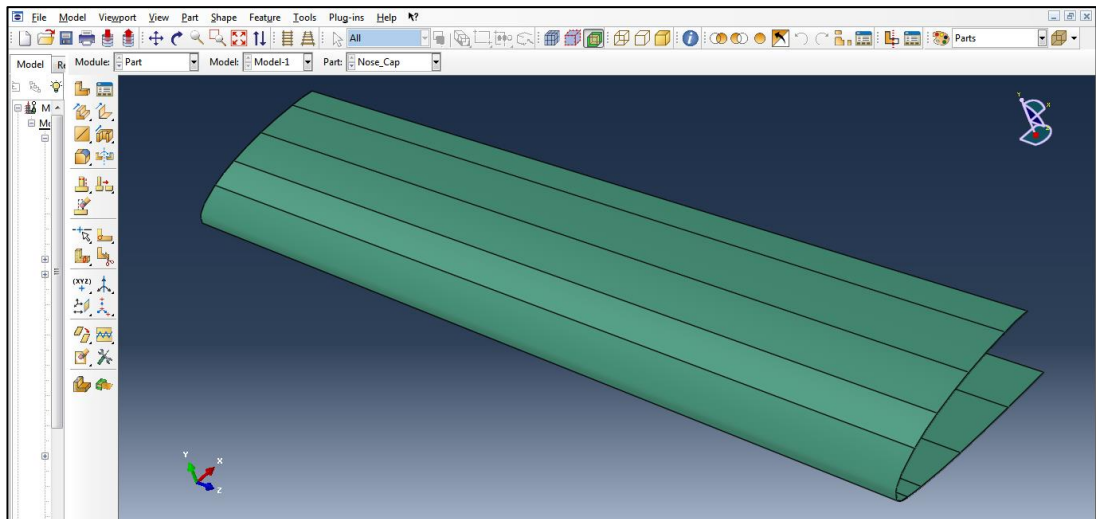


Figure 77. FEA titanium erosion nose cap.

A larger initial mesh size was applied to the nose cap as no sensors were applied to it during testing.

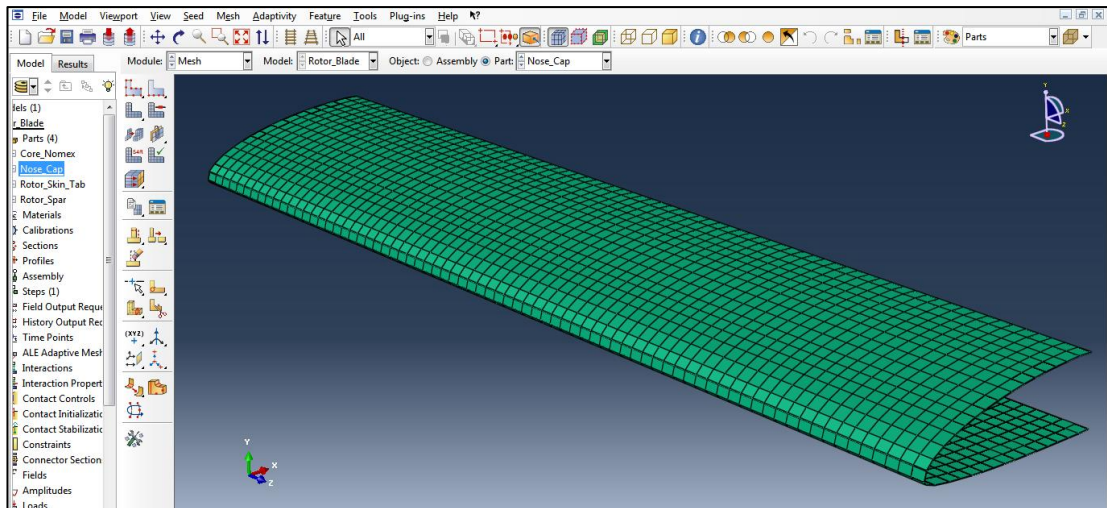


Figure 78. FEA titanium erosion nose cap mesh grid of 2400 elements.

10.7 Honeycomb Core

The Nomex honeycomb core was modelled as an isotropic material due to the lack of physical property data available in the public domain and the inability to determine the type of Nomex used. It was noted that the material has far greater compressive and tensile strength in the direction of the core perforations as opposed to transverse to them. As such a 50% reduction factor was assumed as adequate and applied.

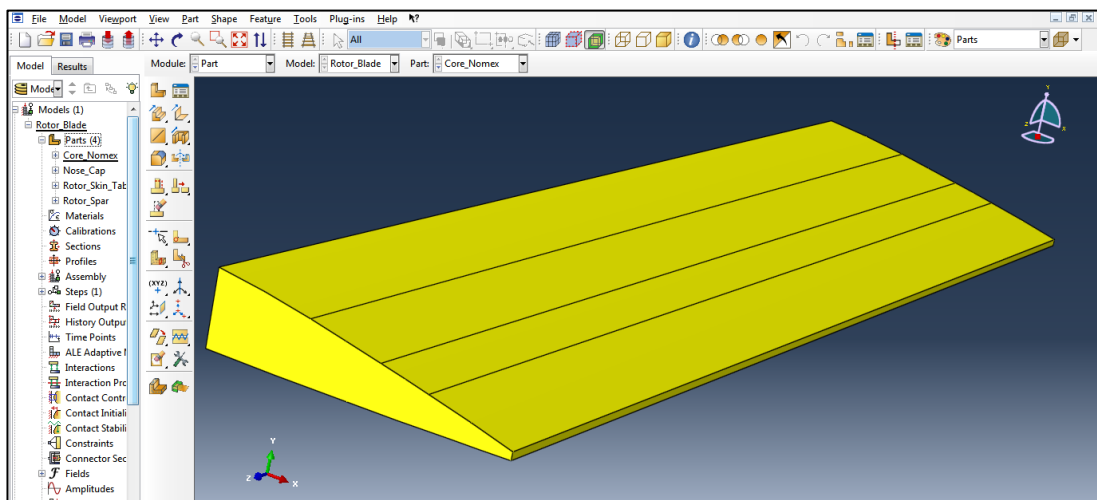


Figure 79. FEA Nomex honeycomb core model.

Again, a larger mesh was applied to this sub-component based largely on its role within the structure which largely to resist compressive forces on the outer skin to which it is attached. Again no sensors are directly attached to this sub-component.

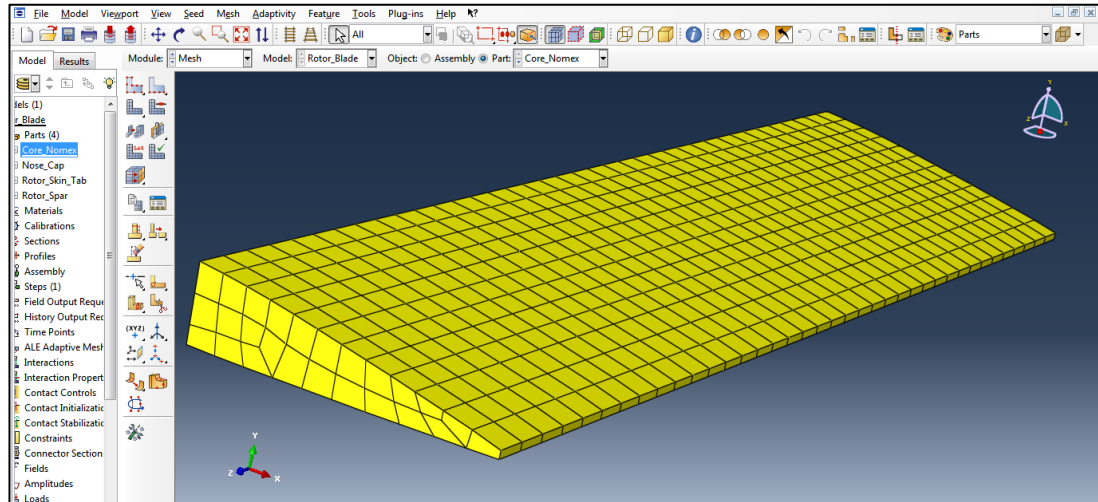


Figure 80. FEA Nomex core section initial mesh grid of 950 elements.

10.8 Meshed FEA Rotor Assembly

The following Abaqus screen captures depict the meshed model as a completed assembly. The process of assembly presented several challenges and limitations, in particular adequate sub-component surface to surface interaction and constraints was difficult to achieve and proved restrictive later when nodal strains measurements were required.

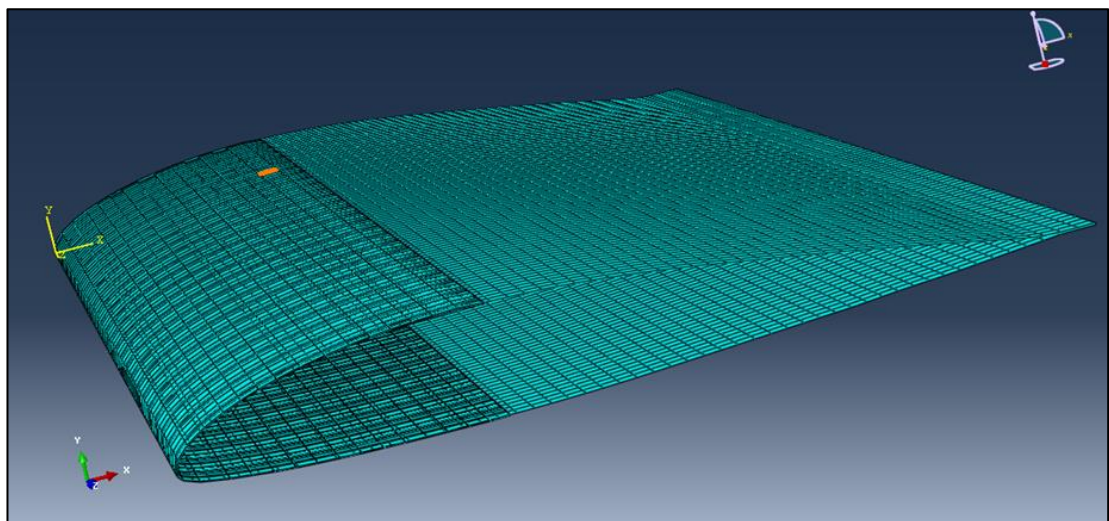


Figure 81. FEA model of skin and erosion cap meshed assembly.

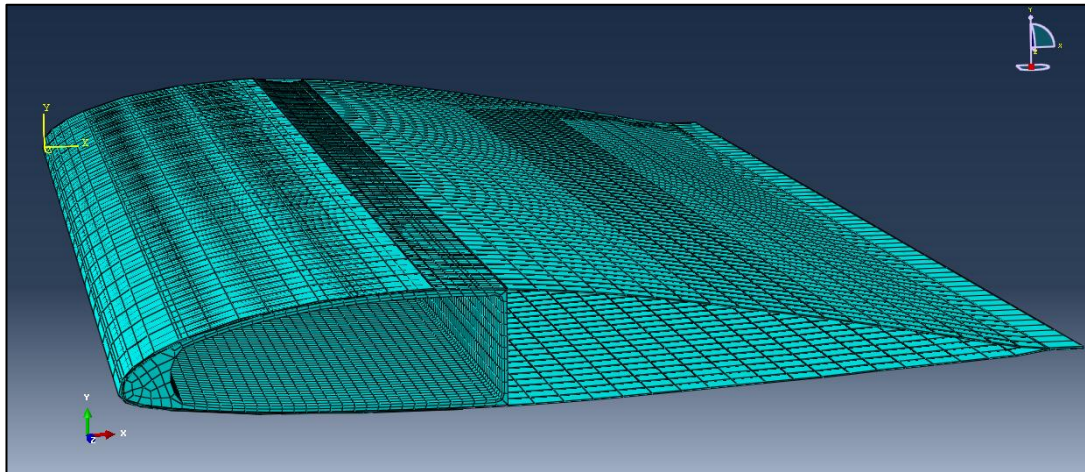


Figure 82. FEA model of D-spar, skin and erosion cap meshed assembly.

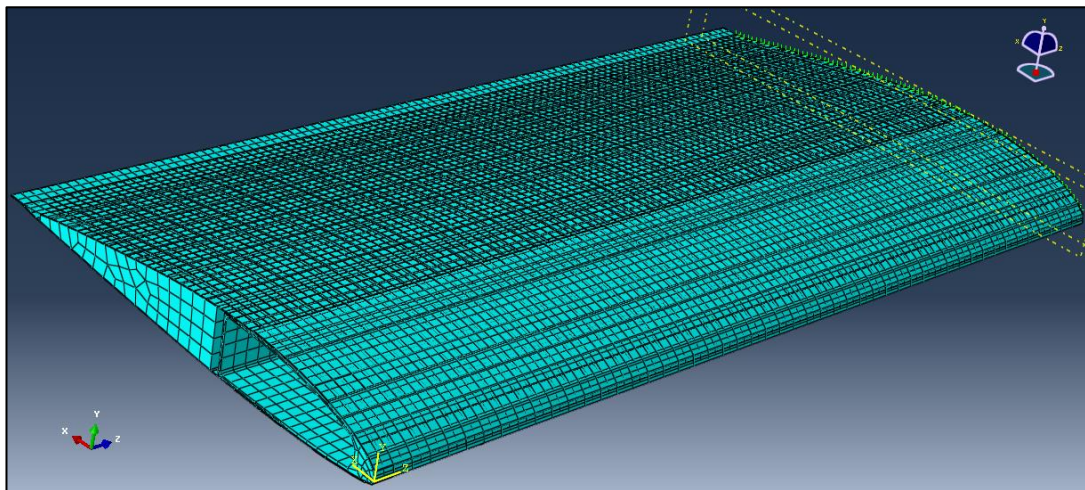


Figure 83. FEA model of D-spar, skin, erosion cap and core, meshed final assembly.

10.9 Strand 7

In addition to the modelling conducted in Abaqus, Strand 7 was utilised to determine the laminate properties for the blade sub-components. Strand 7 was used due to its relatively simple operation and comprehensive graphical representation at the laminate level.

This additional modelling served a twofold purpose; firstly it further confirmed the validity of the physical flexural and tensile testing previously carried out and secondly it determined additional required laminate properties to be inputted into the Abaqus model. These properties include:

1. E_{xy} , Elastic Modulus applicable to subscripted plane indicating transverse or longitudinal direction,
2. G_{xy} , Shear Modulus in the applicable subscripted axes, and
3. ν_{xy} . Major (xy) or minor (yx) Poisson's ratio.

The following screen captures provide the ply properties used in order to determine the laminate properties. E-glass data has been adopted and applied as a unidirectional weave as presented below.

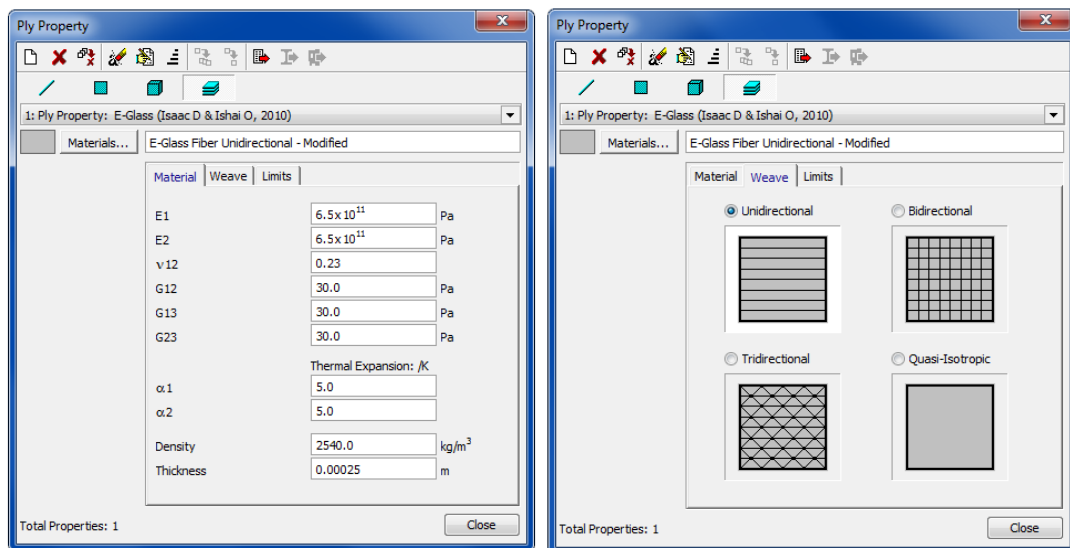


Figure 84. Ply properties entered into Strand 7.

Once the ply properties were established, the laminate stacking sequence as determined during the calcination testing was entered into Strand 7 for both the D-spar and skin. From this the E , G and ν was able to be determined as presented in the following Strand 7 screen captures. In addition, these figures clearly present the stacking sequence for the skin and D-spar which accurately reflects, and confirmed the physical sequence.

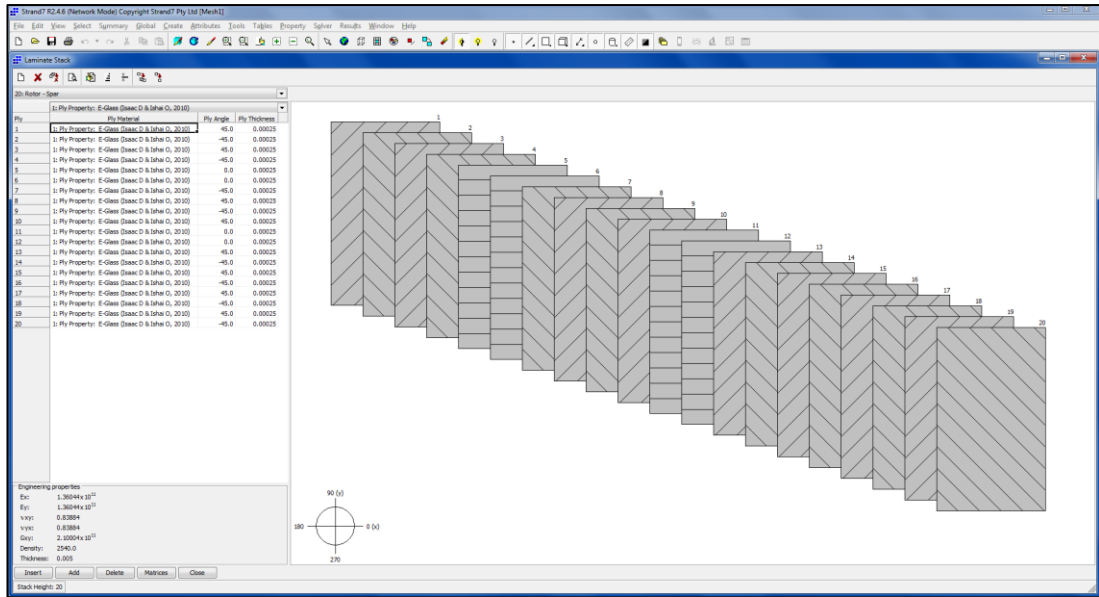


Figure 85. Strand 7 D-spar laminate model detailing the results for E , ν and G .

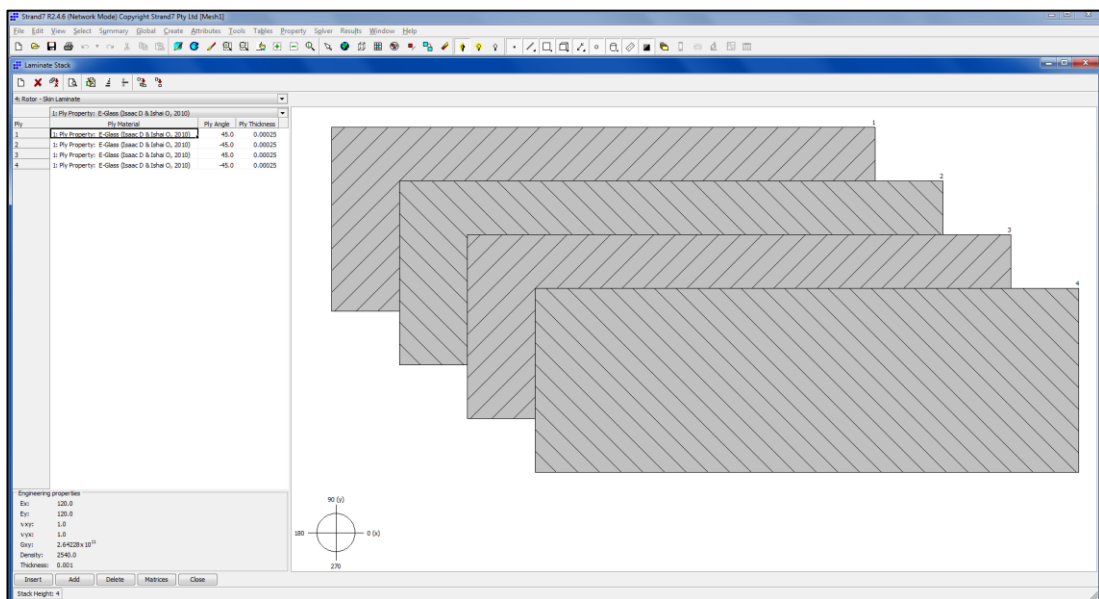


Figure 86. Strand 7 skin laminate model detailing the results for E , ν and G .

The following table summarises the sub-component laminate properties as determined with Strand 7. Of note, the elastic modulus using both Strand 7 and physical testing are a very close match, providing a high level of confidence for the remaining Strand 7 determined parameters.

Table 24. Summary of Strand 7 calculated results and actual tested modulus.

	E_x (Pa) Test Result	E_x (Pa)	E_y (Pa)	ν_{xy}	ν_{yx}	G_{xy} (Pa)	Thickness (m)
D-spar	1.38×10^{11}	1.36×10^{11}	1.36×10^{11}	0.839	0.839	2.11×10^{11}	0.005
Skin		120	120	1.0	1.0	2.64×10^{11}	0.001

10.10 Abaqus Ply Stack Plot

Once the physical property data was collected and verified it was then entered into Abaqus and applied to the respective model sub-components. An example of the Abaqus generated Ply Stack Plot showing the stacking sequence, fibre orientation, material and thickness for the D-spar follows. This process was also applied to the skin.

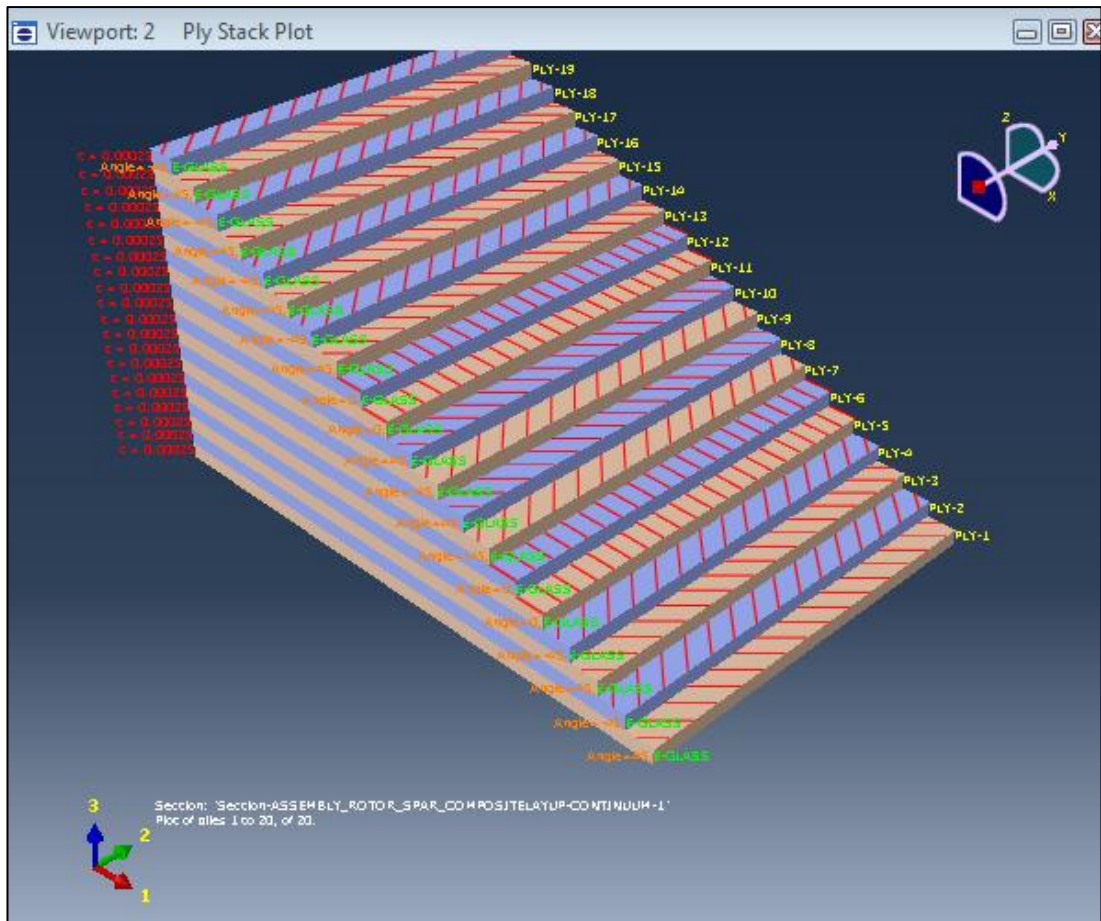


Figure 87. Abaqus D-spar plie stack plot.

The development of the FEA model was completed in parallel to the development and application of the FBG sensor system.

CHAPTER 11 FBG SENSOR SYSTEM

This chapter discusses the development, structure and use of the FBG strain data collection system.

11.1 General Overview

The FBG sensor system was used to measure the micro strain on the internal, upper surface of the rotor D-spar. This is the opposite surface to the initial, partial simulated damage.

The FBG system consisted of a lap-top computer containing Micron Optics – ENLIGHT software, a Micron Optics sm125, four channel optical sensing interrogator and a 5.0 mm FBG sensor.

The utilised FBG specification and tested data is as follows:

Table 25. FBG specification data.

Technica SA – Fibre Bragg Grating (S/N 101121106075)		
Nomenclature	Tolerance	As Tested
Centre Wavelength (CW)	1550 ± 0.3 nm	1549.99 nm
Length	5.0 mm	5.0 mm
FWHM Bandwidth (BW)	< 0.5 nm	0.34 nm
Reflectivity	> 50%	54.501%
Fibre Type	SMF-28C	SMF-28C
Connector	FC / APC	FC / APC

A diagrammatical summary of the FBG system is presented below with red arrows representing information flow via fibre-optics and the blue arrow representing information follow via a standard electrical patch lead. This system is discussed in greater depth in later paragraphs.



Figure 88. Overview of major FBG system components.

11.2 FBG / Optic Fibre Connection Process

The connection of FBG sensors to optical fibre, whilst relatively simple, was rehearsed in anticipation of potential failure or accidental breakage. Additionally the same technique could be applied should the requirement arise for an extended optical fibre length. The following process was utilised to splice the FBG to an optical fibre:

1. **Cutting to length:** As part of the initial process a section of optical fibre is required to be trimmed to length. Once the length is determined the fibre can easily be ‘kinked’ and broken in the desired location by gently pulling the fibre taut.
2. **Stripping of outer cladding layer:** Once the desired length is obtained the end of the fibre to be spliced with the FBG is stripped of the lower refractive index cladding. This is achieved by using fibre optic stripping pliers with the correct diameter stripping recess relative to the fibre diameter.



Figure 89. Typical optic fibre strippers.

- Squaring of optical fibre ends:** Once the cladding is stripped squaring on the optic-fibre and FBG ends to be spliced is required. This is achieved by aligning the fibre within a high precision fibre cleaver, as depicted below. Internal magnetic clamps locate and hold the fibre whilst a weighted blade mechanism cleaves the fibre in a single pass producing a square end to the fibres axis. Square ends are required on the both the FBG and fibre for accurate splicing.



Figure 90. The Vitel high precision fibre cleaver.

4. **Fusion splicing of FBG to optical fibre:** Splicing is achieved with the use of a direct core monitoring machine which creates a single fibre which may contain one or more FBGs. The actual splicing is a three phase process plus final test, once the squared fibre and FBG ends cleaned and positioned within the splicer. The fibres are restrained and located by a magnetic clamping arrangement. Once positioned, and the relevant information for the operation and fibre type are entered the machine begins the splice. This is an automated four stage process as follows:

a. **Alignment:** Small precision motors within the splicer make minute adjustments to the fibres' position until they are aligned accurately enough to provide a seamless and attenuation-free join as possible. During alignment it is possible to view the magnified fibre alignment via the machine display. As a function of this process the machine performs a self-test for alignment accuracy. Should this test fail an error message will be presented. Re-seating of the fibres within the splicer is usually all that is required to rectify this problem; however, it may require re-seating several times of both fibres. Alternatively, a fibre end may be an excessive distance from the fusion zone and the machine may not have adequate travel to compensate. Again, repositioning of the fibre is required so that the ends are located within the allocated zone.

b. **Impurity Burn-Off:** Micro-impurities such as dust or cladding debris can significantly degrade a splice's ability to transmit optical signals. Even though the fibres are cleaned prior the splicer incorporates an extra cleaning step prior to fusing, where it generates an arc between the fibre ends, to burn off any remaining contaminants or moisture.

- c. **Fusion:** Once the fibres are correctly positioned and any contaminants burned off the fibre ends are fused together to form a permanent splice. The splicer emits a larger spark that melts the optical fibre end faces without causing the fibres' cladding and molten glass core to run together. The molten fibre ends are then joined creating the final fibre splice.

- d. **Test:** A self-test of the resultant splice is conducted by the machine to estimate the refractive losses across the splice. Most fibre fusion splices typically display an acceptable optical loss of < 0.1 dB.



Figure 91. The Vitel v. 2000 s175 fusion splicing machine.

On several occasions whilst attempting to splice fibres errors occurred. These were largely due to contamination within the splicing process which required additional hand cleaning, and misalignment of the fibres within the fusion splicer. The misalignment was usually the result of the fibre fractionally moving during the clamping process and was easily rectified with adjustment. In all cases an adequate splice was achieved which passed the machine self-test.

11.3 FBG Position

The FBG system, whilst only consisting of one FBG, was the key system for this project as it was itself being assessed for performance within this application.

Importantly, the FBG was located in a critical high strain area, on an internal surface of the D-spar. The FBG was within close proximity to two electrical strain gages for comparison purposes. Primarily the #1 strain gauge location was used for this purpose. The location of the FBG was determined initially by the FEA model; however, this location had to be revised due to internal D-spar access difficulties.

The finalised internal FBG position within the D-spar was as follows.

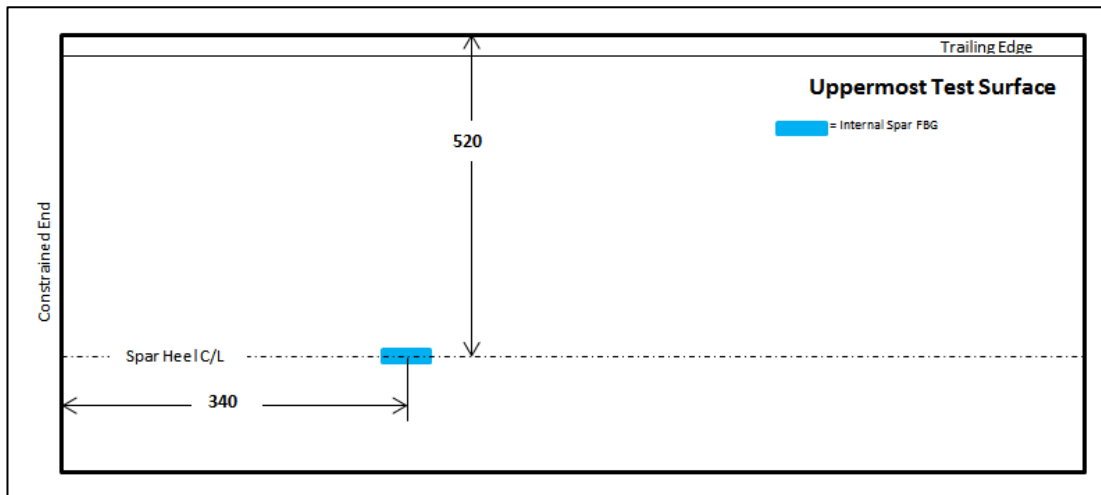


Figure 92. Internal to D-spar FBG location (mm)

Whilst all internal strain gages were very difficult to accurately position, the FBG was particularly difficult. This was due to several factors which included:

1. The difficult to access position (internal D-spar area) resulted in a very confined workspace with limited light,
2. The high accuracy of alignment with respect to the blade lengthwise axis was required to ensure accuracy in subsequent results,

3. The delicate nature of FBG sensors and the fibre-optical cable they are attached to required very careful manual handling,
4. The requirement for the creation of innovative application method and tools to ensure accuracy of position and adequacy of FBG bonding to the surface, and
5. The use of rapidly curing Cyanoacrylate adhesive to secure the FBG in location resulted in little scope for error.

Figure 93 details the FBG location and demonstrates the application issues described above.

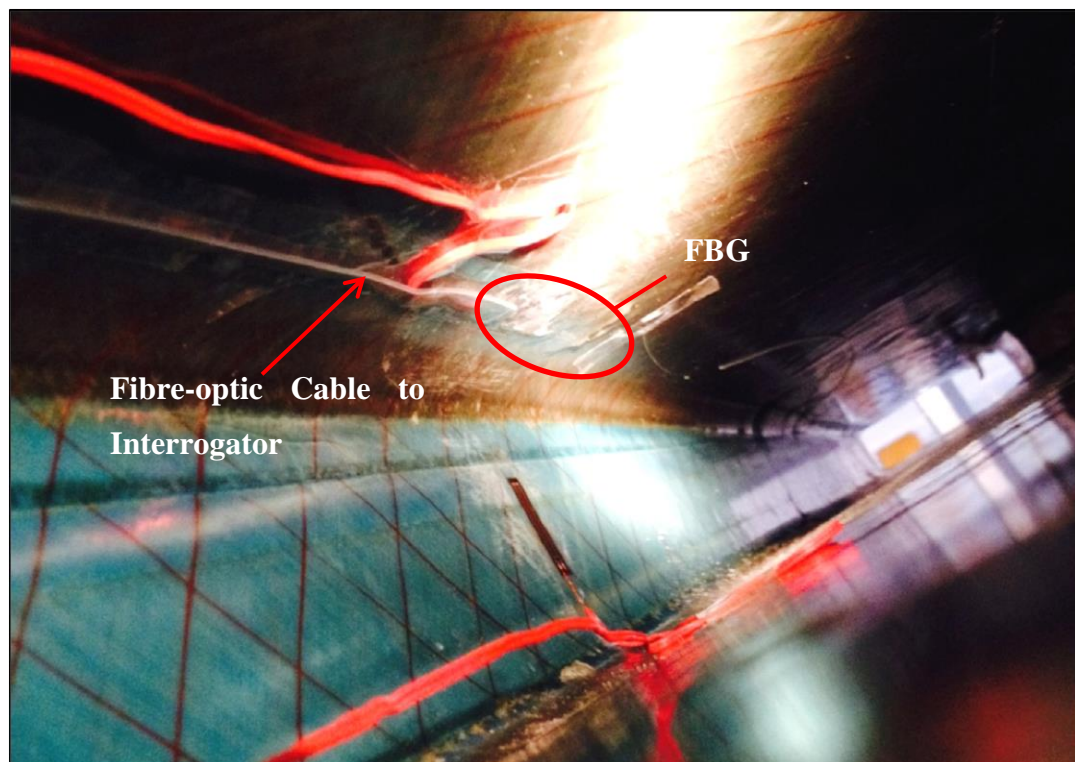


Figure 93. Location of the FBG sensor.

11.4 FBG System Operation

System operation occurs as light is passed into the fibre-optic cable from the interrogator which is reflected back from the FBG. The reflected peak is altered pending a tensile or compressive force being experienced. The reflected light travels back to the interrogator's photo detectors and is compared to the wavelength referenced data so that the instrument can determine the position of the centre wavelength of the subject FBG.

Wavelength information is then converted to engineering units such as Pico-meters (pm) of wavelength shift. This can then be equated to micro-strain data for that sensor. A photo of the Micron Optics sm125 four channel optical sensing interrogator used during the testing detailing the FBG input, PC output and fibre-optic cable follows.

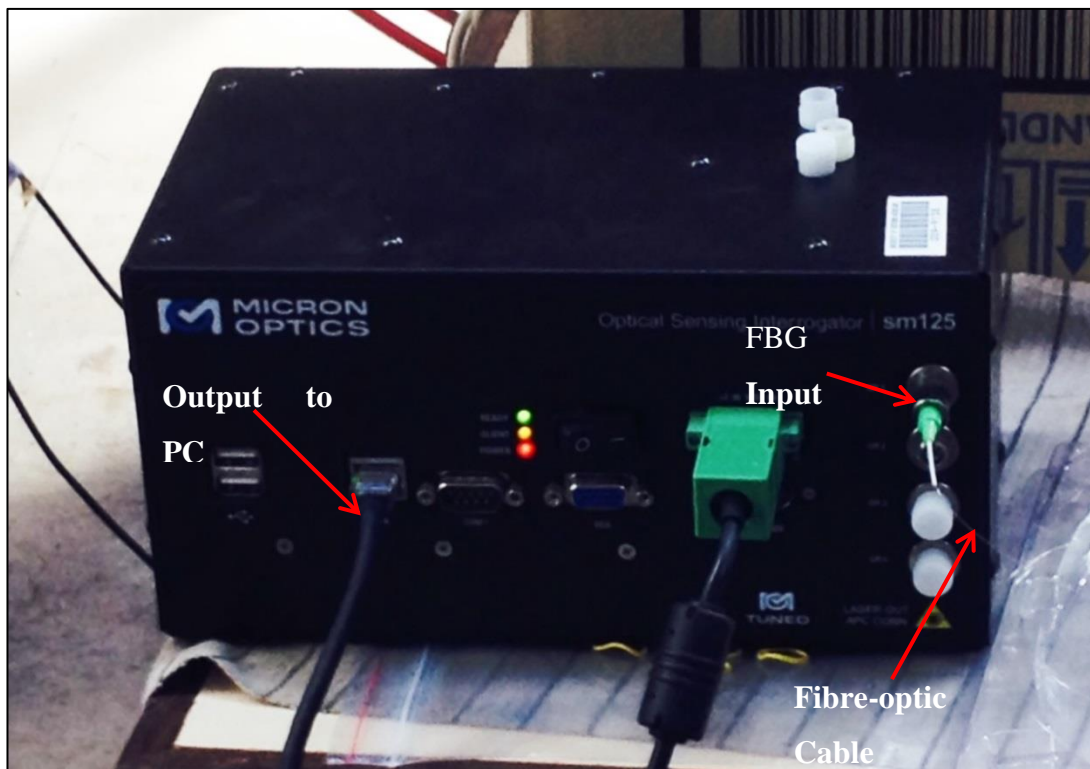


Figure 94. Micron Optics sm125 four channel optical sensing interrogator.

The primary role of the FBG software is to convert the collected optical data parameters from the FBG into useable engineering units and a 'real time' graphical display. The output screen displays both power (dBm) and wavelength (nm) in this graphical form for easier interpretation. Of particular interest is the centre wavelength shift, either to the left or right as load is applied. This peak shift represents increasing strain in either compression (left shift) or tension (right shift). Nil movement is representative of no change in strain levels with an applied load.

Figure 95 is a screen capture during actual testing depicting the movement of the peak value from the 1550.0 nm reference to the right indication a tensile strain condition.

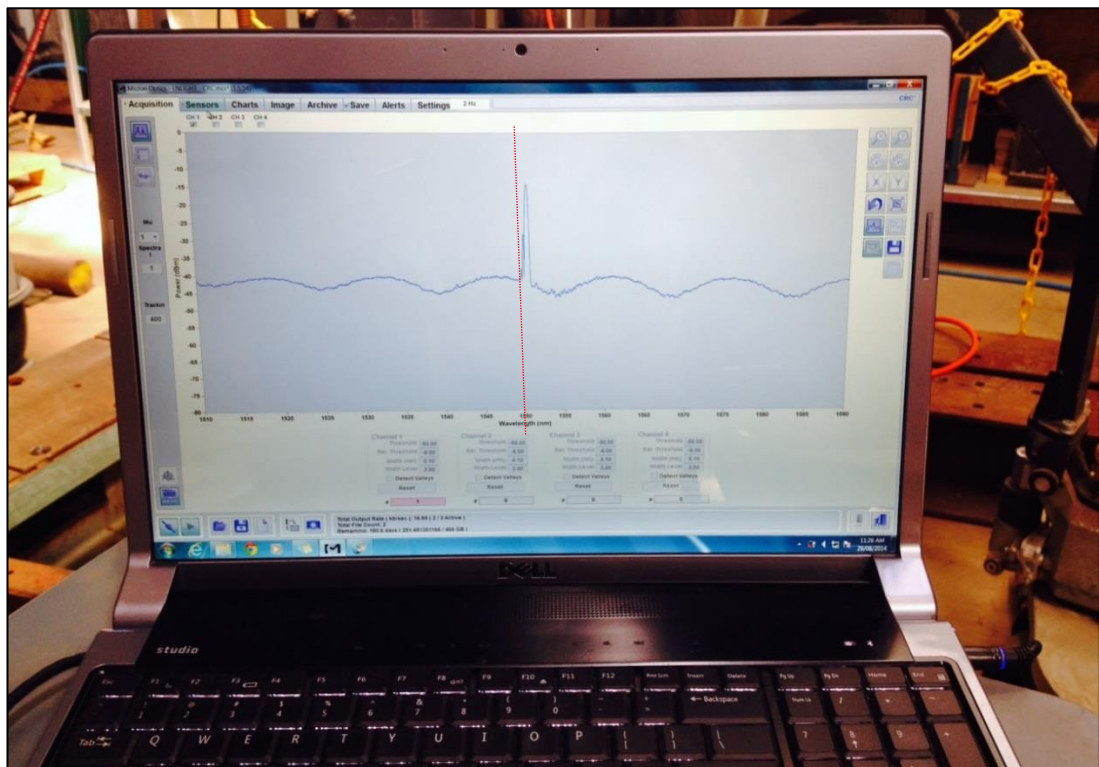


Figure 95. Micron Optics, Enlight software was used for the FBG analysis.

11.5 FBG Confirmation Testing

Confirmation testing of the FBG system was required to validate the operation of both the FBG and the connecting fibre-optic cable and extension cable. This was a simple process of connecting the system and passing light from the interrogator to the FBG. The returned signal from the FBG could then be analysed and represented on the PC. This process initially identified that the FBG was not returning a signal. This was of significant concern as the probable cause for a 'no return signal' is a damaged FBG or fibre-optic cable. Given the high level of care taken to both position and restrain the FBG and fibre a process of elimination was followed to confirm that it was the FBG at fault.

This process revealed that the intermediate extension fibre-optic cable to be at fault and not the fragile FBG or fibre. As a result the intermediate extension cable was discarded and the FBG connected directly to the optical sensing interrogator. Subsequent self-testing indicated a fully functioning system with correct, unloaded, spectral return signals. Testing was now able to be performed both with and on the FBG system.

Results obtained from the FBG system are discussed in detail within Chapter 15 - Results.

CHAPTER 12 - ELECTRICAL STRAIN GAUGE SENSOR SYSTEM

This chapter discusses the development, structure and use of the electrical strain data collection system.

12.1 General Overview

Due to the high relative cost of FBG sensors, electronic strain gauges were used in the majority of locations. Nine, 20.0 mm Kyowa strain gauges were positioned on the blade surface at varying locations primarily along the axis of the blade.

Two gauges were placed internal to the spar section on both the upper surface and on the rear vertical wall. Additionally, two gauges were positioned axial and oblique to the blade axis in the near vicinity of damage which occurred to the blade test section whilst in storage (cause unknown), prior to testing.

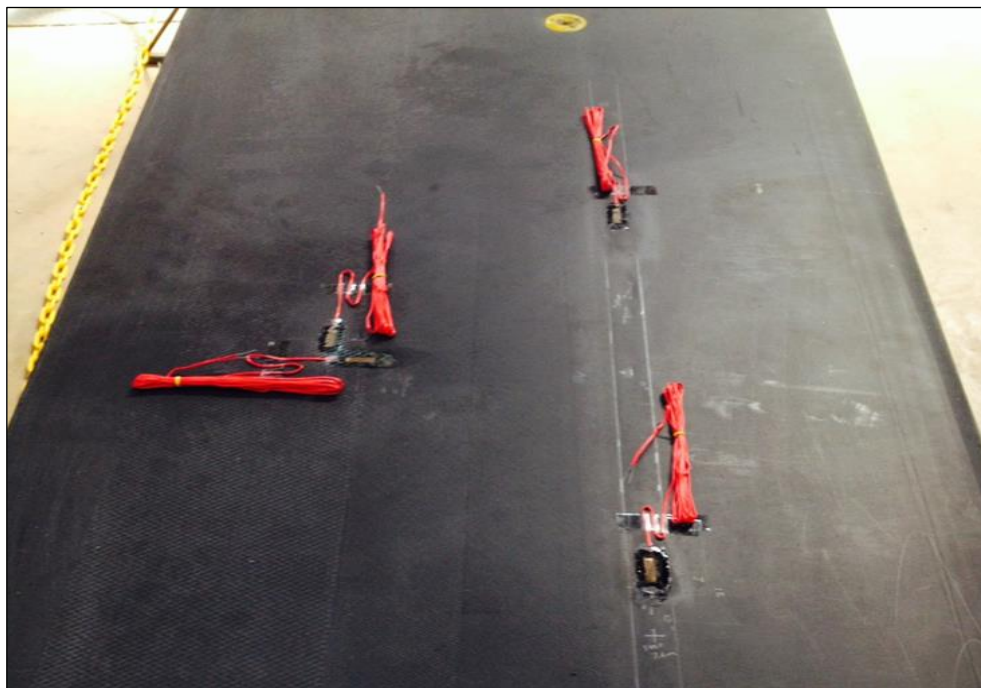


Figure 96. Upper surface strain gauges.

The strain gauge system consisted of nine strain gauges, nine connector ends, a data acquisition system and a PC displaying the StrainSmart Online Display strain software.

The strain gauges were a 20.0 mm foil type gage as pictured below.

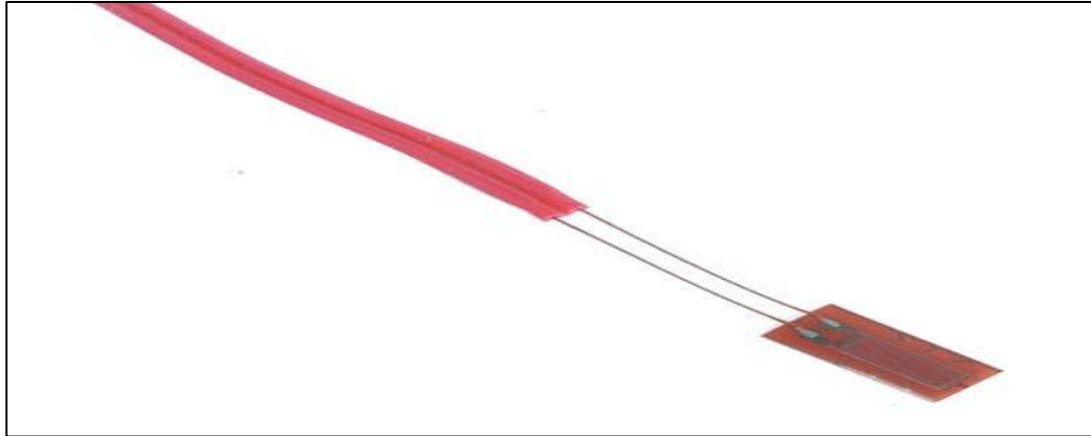


Figure 97. Typical pre-wired foil type strain gauge.

The strain gauges used were all from the same manufacturer and batch providing uniformity. All gauges had the following manufacturer specifications:

Table 26. Strain gauge data.

Kyowa Strain Gauge - Japan	
Gage Factor	2.05 ±1.0%
Gage Length	20.0 mm
Gage Resistance	120.4 ± 0.4Ω
Thermal Expansion	11.7 PPM/°C
Temperature Coefficient Gage Factor	+0.008 %/°C

12.2 Strain Gauge Electrical Attachment

Whilst the strain gauges had 1.5 m of attachment wiring they did not have any form of electrical connector with which to interface with the data acquisition system (StrainSmart System 5000). As a result nine, 9 pin PC connection sockets were required to be modified and joined to the strain gauge wires so they could be used.

This was achieved in the following manner:

1. Each connection had two bridge wires soldered in place, and
2. Each connection had two connecting wires soldered in place.

The following diagram depicts the modification of the nine pin plugs to allow strain gauge use.

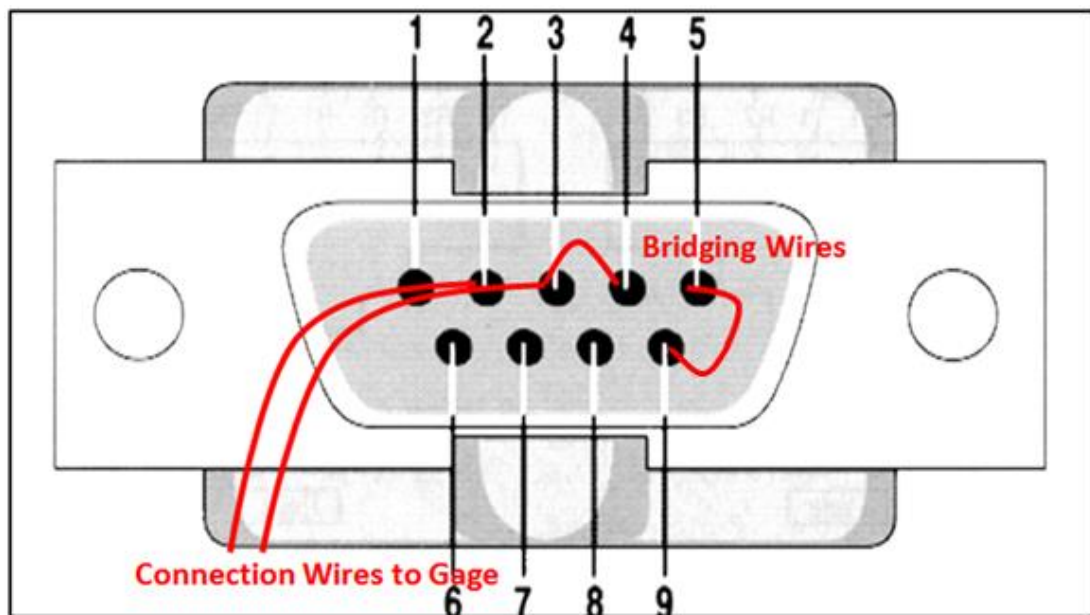


Figure 98. Nine pin plug modification.

The above modification, along with wire stripping and end tinning was completed using a soldering iron and improvised clamping arrangement as pictured below.

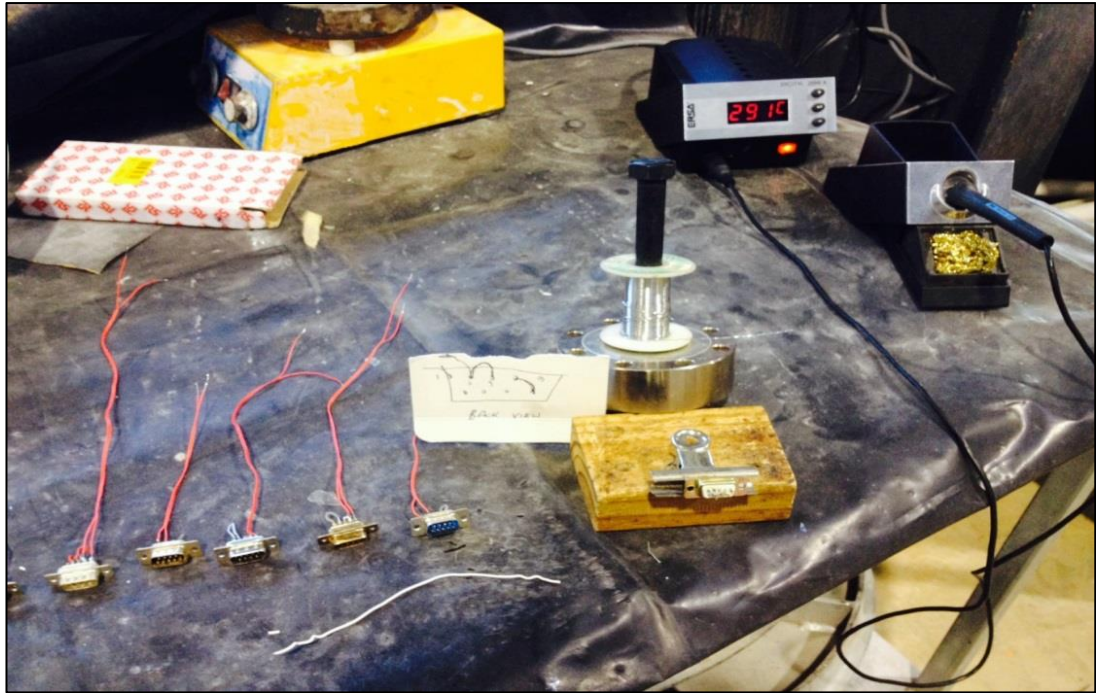


Figure 99. Modification of the 9 pin connector plugs.

12.3 Strain System Components

Once the bridged connectors had been completed they were each soldered to a strain gauge ready for use with the data acquisition system; the StrainSmart 5100B. This unit is able to accept 20 channels of inputs. Acceptable unit inputs relevant to this testing include strain gauges, strain gauge based transducers (load cells) and linear variable differential transformers (LVDT).

The load cell, LVDT and nine strain gauges were each assigned a channel within the software and provided a data input port into the data acquisition system pictured below.



Figure 100. StrainSmart System 5000 (5100B) data acquisition system.

The load cell provided load information in Newtons and allowed for accurate load application via a manually operated hydraulic pump. The LVDT provided displacement information to the data acquisition system in millimetres. Both parameters and the strain readings from all strain gauges were recorded for each test performed. This information allowed for comparative analysis as described in the following chapters.

The load cell, LVDT and 200 kN hydraulic cylinder are depicted below (without the blade test section installed).

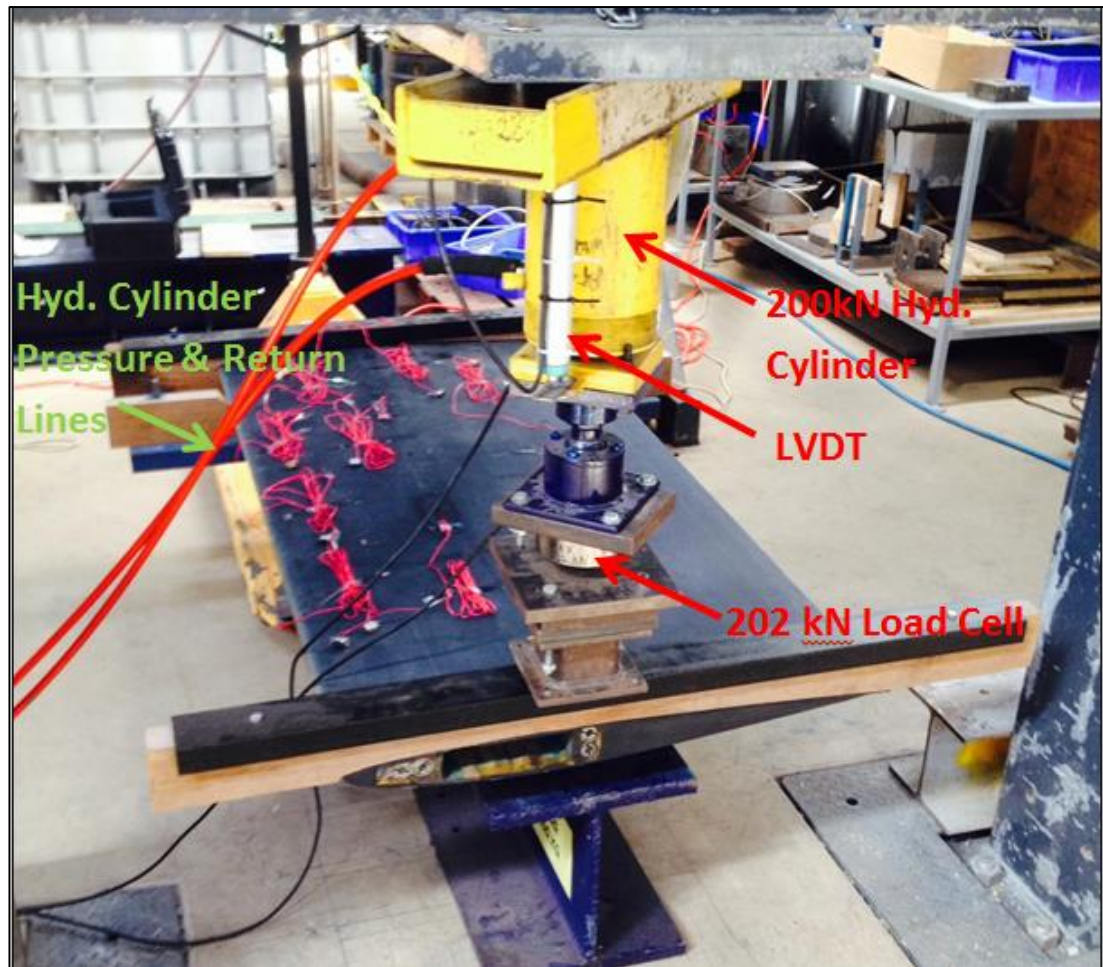


Figure 101. Hydraulic cylinder, lines, LVDT and load cell with FBG and strain gauge connectors present.

The strain gauge position was largely determined by the FEA model; however, intuition, accessibility of highly stressed areas and the event of un-planned damage was also a consideration.

12.4 Strain Gauge Location

As a result a map of the strain gauge location, and a position number which was correlated to a channel within the analysis software, was created and is presented below. The map was required to ensure accurate positioning could be recalled for subsequent testing and for FEA model comparison / modification if required.

The upper test surface depicted below is the lower blade (flight surface) surface. This orientation was used to allow for the load to be applied to the lower flight surface to better replicate the blade deflection experienced in flight.

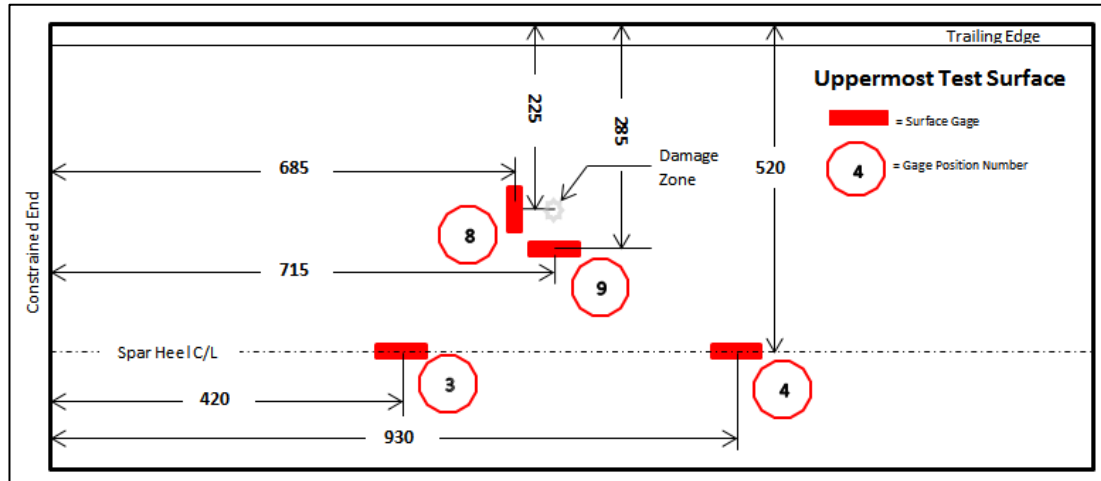


Figure 102. Upper test surface strain gauge positions (mm).

The lower test surface depicted below is the upper flight surface. This diagram also details the position of the internal D-spar strain gauges.

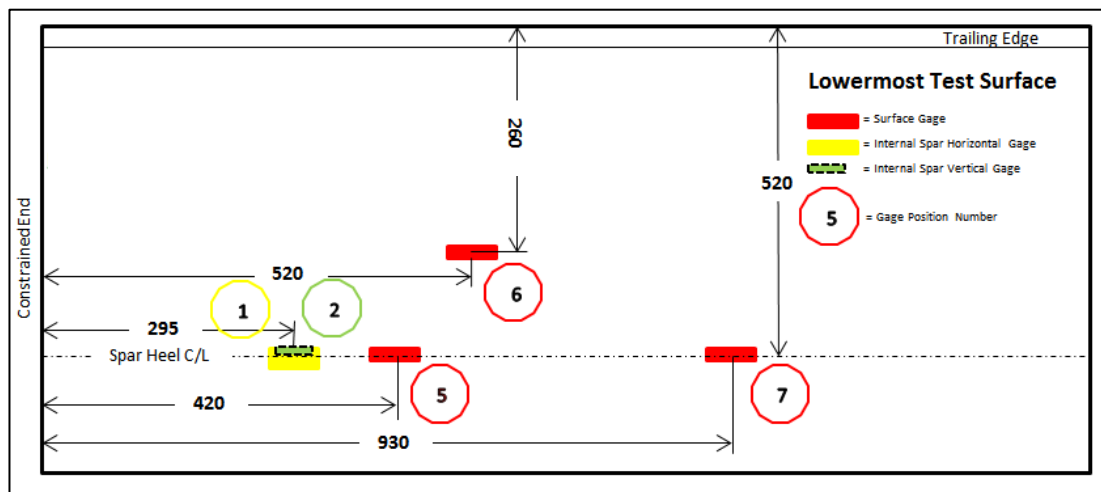


Figure 103. Lower test surface strain gauge positions (mm).

12.5 Strain Gauge Channel & Position Number

Table 27 details the input channel number and corresponding gauge position number later used for results data analysis.

Table 27. Data acquisition input channel and position number.

Data Acquisition System - Channel Number	Blade Test Section – Gauge Position Number
2	LVDT
9	1
8	Load Cell
7	2
10	3
11	4
12	5
13	6
14	7
15	8
16	9

Once the strain gauge location had been determined, the gauges were attached to the blade test section.

12.6 Strain Gauge Attachment

Strain gauges were attached in the following manner to ensure reliable strain readings from the system.

Each gauge location was lightly sanded with fine emery paper to provide a good key and was thoroughly cleaned with acetone. As with the FBG, the strain gauges were adhered with rapidly curing Cyanoacrylate adhesive. Again there was little scope for error in positioning; however, unlike the FBG all gauge locations, with the exception of the internal locations, were very easily accessible.

The two internal locations were positioned using a rudimentary method of attaching the gauge to a steel ruler with adhesive tape, applying the Cyanoacrylate adhesive evenly to the gauge surface and waiting until the glue semi-cured. The ruler was then used to measure the distance from the datum edge and provided a parallel edge from which to measure the distance from the D-spar internal heel surface.

Once positioned, moderate hand pressure was applied for several minutes to provide an adequate bond.

The following figure details the internal D-spar strain gauge positions prior the FBG being installed.

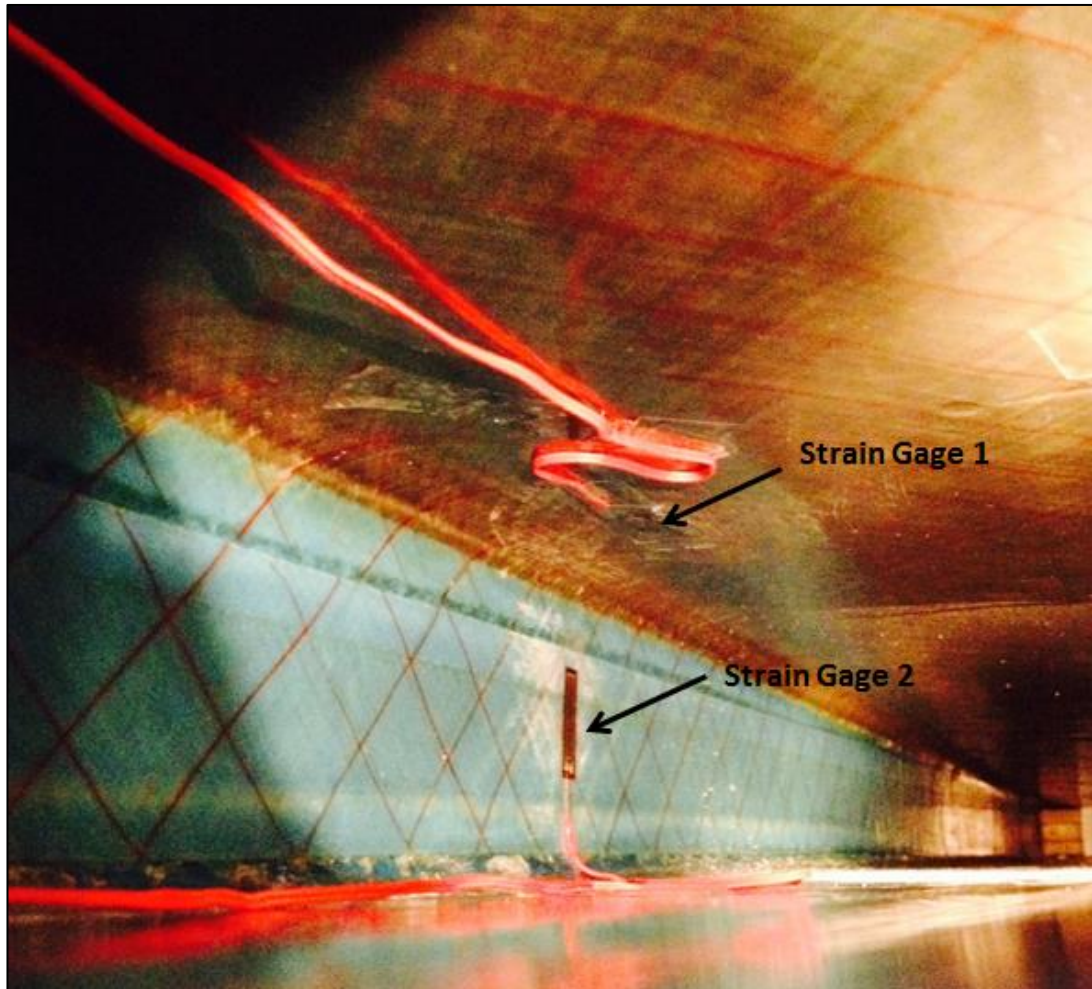


Figure 104. Internal D-spar strain gauges.

Once the strain gauges were attached to the blade surfaces they were connected to the data acquisition system at the respective channel location and a system self-check performed. The initial test failed at one channel; however, replacing the failing channel connector plug resulted in all strain gauges passing the subsequent self-check.

12.7 Unplanned Damage Area Strain Gages

Whilst in storage at the CEEFC (prior to testing) the blade test section was damaged. It is not known how the damage occurred; however, it was decided to use the damage as part of the testing regime.

On close inspection it was determined to be impact damage resulting in radial crack propagation. This compressive damage had ruptured the full thickness of the skin with cracking radiating outward in three places (7.5 mm maximum length) as pictured below.

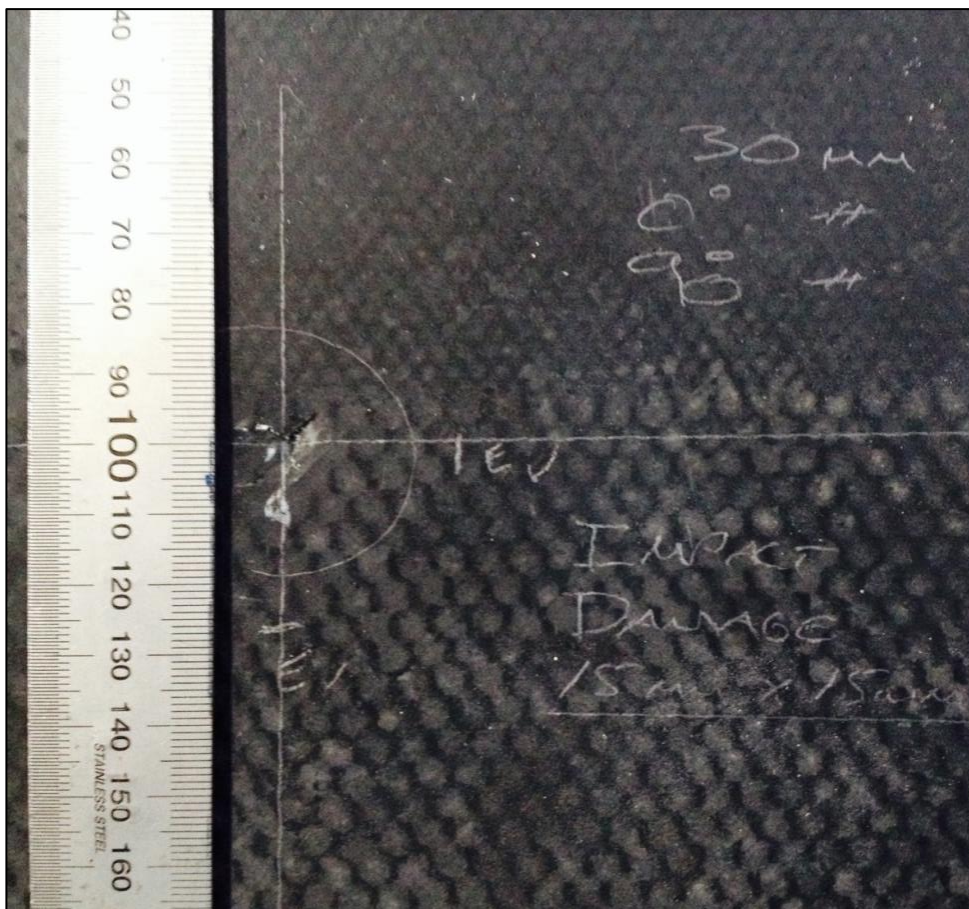


Figure 105. Blade test section 'accidental' damage.

The general form of this damage is similar to that experienced by rotor blades in service. In particular, on military helicopters which are required to operate in areas other than hard-stand and are subjected to small stone or gravelly operating environments.

This debris, during take-off or final approach may be lifted by the rotor system downwash and recirculated through the rotors possibly impacting on the blade surface causing low level, compressive surface damage.

Typically this type of damage occurs on the lower blade surface and is more frequently occurring in the 'softer' trailing edge region. Coincidentally, the storage damage occurred in the same region.



Figure 106. Impact damage location with strain gauges.

As a result of this damage a longitudinal and transverse strain gauge was placed in close proximity to the damage in order to obtain strain readings for later comparison with the FEA model. These two gauges are at positions eight and nine respectively and are approximately 30.0 mm from the centre of the damage site as pictured below.

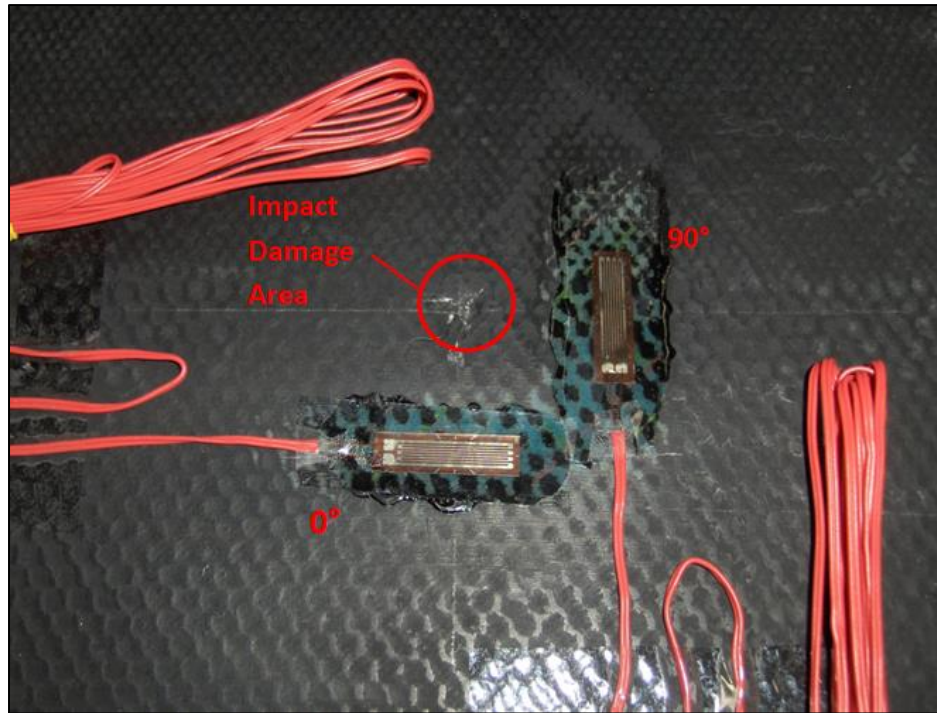


Figure 107. Accidental damage strain gauge orientation.

Whilst this damage was not intended, nor its actual cause known, it did present an opportunity to conduct additional testing; the results of the testing are discussed in later chapters.

CHAPTER 13 - BALLISTIC TESTING TRIALS

This chapter discusses the ballistic testing method and resultant conclusions.

13.1 General Overview

Due to the blade test section being the only available test piece, caution had to be applied both when designing the tests and when pre-empting results and possible excessive damage to both the blade test section and the sensor systems.

As a result, a representative test sample of the rotor D-spar section was used to determine if the blade test section and sensor systems could sustain physical ballistic damage or if it should be simulated in a more controllable manner, such as a mechanical material removal method.

13.2 Ballistic Test Sample

This ballistic impact test was design to replicate the probable damage that would occur to the blade D-spar when impacted by a high velocity small calibre projectile.

A locally sourced pultruded FRP, E-glass RHS was selected due to the physical similarities to the rotor blade D-spar construction on which many of the sensors were attached and damage was to be applied during blade testing. The FRP, RHS utilised has the following tabulated data:

Table 28. Ballistic test sample specifications.

RHS E-Glass Test Sample	
Parameter	Dimensions (mm)
Material	E-Glass / Epoxy (combinations of 0°, -45°, +45° fibre orientations)
Length	≈175.0
Width	100.0
Thickness	75.0
Wall Thickness	5.0

The test sample was then subjected to small arms ballistic damage.

13.3 Test Conditions.

NOTE: This test was conducted whilst adhering to strict safety requirements and supervision at an authorised weapons firing range.

Table 29 details the test conditions during which the un-restrained test sample was fired at, and impacted twice.

Table 29. Ballistic test data.

7.62 x 51 mm NATO	
Calibre	7.62 mm (≈.308 in)
Projectile Construction	Copper Jacket, Lead Core
Projectile Mass	147-grain (9.5 g)
Range	≈100.0 m
Velocity	≈ 839 m/s

13.4 Test Results

The results of the test are depicted below and demonstrate the significant, traumatic damage to the FRP section. It can be seen that both shots 1 and 2 impacted adjacent to the corner of the RHS approximately 125.0 mm from the bottom. Whilst the impact / entry point of the projectile is relatively neat the subsequent damage as the projectile passed through each exit and entry phase significantly worsens.

This is a result of the projectile design and the deformation it undergoes as it strikes a surface. The following figures and table detail this progression of damage from initial entry to final exit which exhibits the most significant damage.

The following table is a summary of the damage as determined by unaided visual inspection:

Table 30. Ballistic test damage data.

	Shot 1 – Damage Area	Shot 2 – Damage Area
1st Surface Entry	50.0 x 10.0 = 500 mm² (0.0005m ²)	50.0 x 12.0 = 600 mm² (0.0006m ²)
1st Surface Exit	95.0 x 12.0 = 1140 mm² (0.00114m ²)	91.0 x 13.0 = 1183 mm² (0.00118m ²)
2nd Surface Entry	61.0 x 26.0 = 1586 mm² (0.001586m ²)	52.0 x 24.0 = 1248 mm² (0.00125m ²)
2nd Surface Exit	101.0 x 33.0 = 3333 mm² (0.00333m ²)	105.0 x 26.0 = 2730 mm² (0.00273m ²)

It can be seen from Table 30 that the damage area increases as the projectile passes through the full thickness of the section. This is expected due to projectile tumbling and the deformation following initial impact. As can be seen in the following figures the damage also increases in its severity with respect to compressive fracture of the impact surfaces and tensile fracture of the outer-most exit surface layers.

There is also evidence of significant inter-laminar shear fracture which can also be seen in the following figures.

Whilst not clearly observable, the hole diameter from initial entry to exit increases from ≈ 7.0 mm to ≈ 21.0 mm which represents a 200% increase in marital completely displaced from the structure.

The following picture details the resultant ballistic damage (external) of the entry and exit and direction of shots one and two.



Figure 108. Resultant ballistic damage (external).

The following top, internal view of the sample demonstrates the increase in damage levels as the projectile passed through and exited each surface.

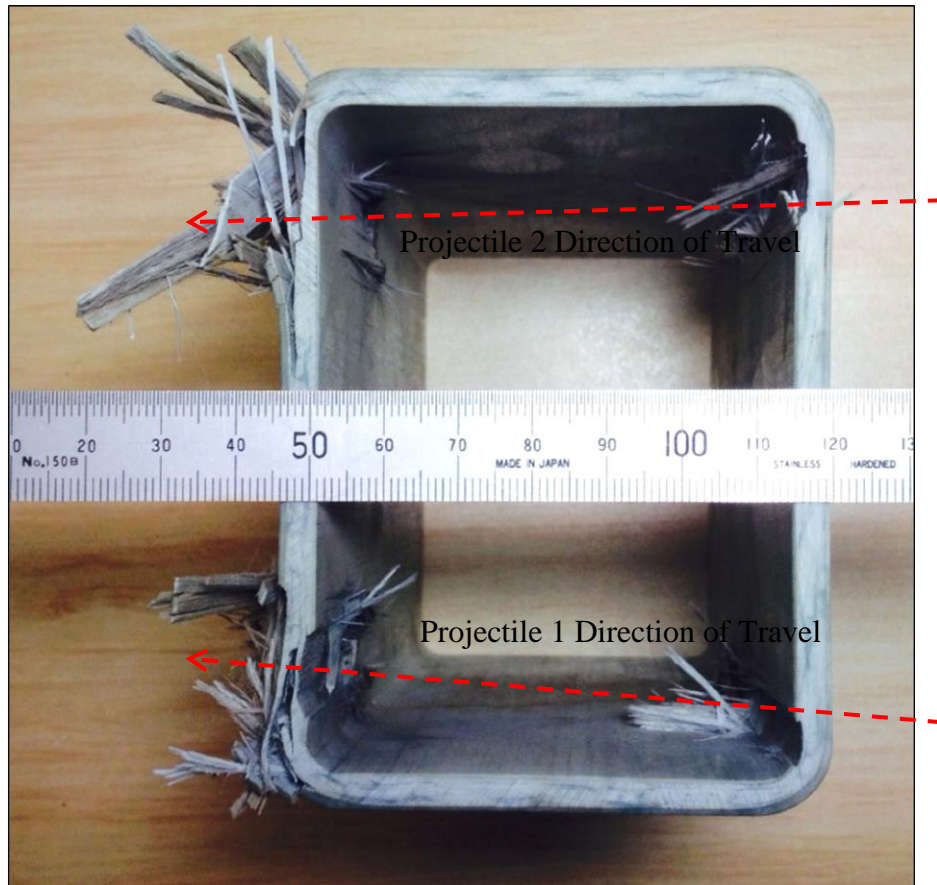


Figure 109. Top view of internal ballistic damage.

The results of this test, whilst indicative only, demonstrated that if actual ballistic damage was applied to the blade test section it could reasonably be expected to be severe in nature and extremely difficult to model using FEA software.

As a result it was decided that given the limited resources such as testing equipment availability, FBG sensors and available rotor blade sections actual ballistic damage would not be applied to the blade test section and that an alternative, controlled method would be used to damage the D-spar section.

The method chosen was to drill an 8.0 mm hole at varying depth intervals followed by a full-thickness hole through the upper surface only of the D-spar. Two additional through holes were also drilled as part of the testing regime.

CHAPTER 14 - BLADE SECTION TESTING

This chapter discusses the testing and resultant conclusions from the blade section physical testing regime.

14.1 General Overview

The following chapter discusses the physical blade testing phase. As a result of the indicative ballistic trials it was determined that to impart actual ballistic projectile damage could adversely affect the ability to perform subsequent testing. This was enlarged due to the significant damage area and the inability to predict damage orientation and size with respect to the sole FBG location. This could in turn damage the FBG to a point that it became inoperable. It was for these reasons that simulated battlefield damage was applied as it could be controlled with minimal risk to the FBG and electrical sensor systems.

The testing regime consisted of nine tests; Two quality tests (tests 1-2), one confirmation test (test 3) and six primary data tests (tests 4-9).

14.2 Maximal Load

As mentioned in paragraph 2.14, the approximate maximum DL may be calculated, which in turn can be mathematically reduced for the area of the blade test section as follows.

$$DL = \frac{\text{Rotor Thrust}}{\text{Disk Area}} \quad (14.1)$$

Assuming:

$$\text{Rotor Thrust} = \text{Aircraft Gross Weight}$$

Yields:

$$DL = \frac{22700\text{kg}}{526\text{m}^2}$$

$$DL = 43.156 \text{ kg/m}^2$$

With the disk loading established a ratio reduction may be applied in order to determine the blade test loading (BTL).

Determining the blade surface area yields:

$$0.81 \text{ m} \times 8.0 \text{ m} = 6.48 \text{ m}^2$$

Once the area of the blade is established the load may be calculated:

$$BTL = \text{Area} \times DL \tag{14.2}$$

Giving:

$$6.48 \text{ m}^2 \times 43.156 \frac{\text{kg}}{\text{m}^2} = 279.651 \text{ kg}$$

Or:

$$279.651 \text{ kg} \times 9.81 = 2743.38 \text{ N}$$

Where:

$$g = 9.81 \text{ m/s}^2$$

As a result, the maximum load of 2743.38 N was determined for the tests.

Additional research of other rotor blade testing, such as that conducted by Pawar and Ganguli (2006) determined the maximum change in vertical blade root forces to be about 2500 N for the blade tested. As a result the maximum load applied to this test regime was limited to 2500 N until the final test when a 3000 N load would be considered.

14.3 Quality Assurance Tests

Tests 1 & 2 are not represented in this report in detail as they were quality checks only and resulted in mainly unusable data files.

These tests were used to determine correct testing fixture operation, sensor system operation (FBG and strain gauge) and the load application recording system (hydraulic press, LVDT and load cell) operation.

Tests 1 and 2 revealed several issues with their respective corrective action detailed in the following table:

Table 31. Identified testing faults and corrective action.

Serial	System	Fault Description	Corrective Action
1	Test Fixture	Excessive Test Fixture Flexure at the Root-End Clamp allowing blade tip displacement to exceed the 80.0 mm calculated limit.	The Lower Adjustable Support position was revised from 100.0 mm to 185.0 mm. This allowed for all testing at the 2500N maximum load to be conducted without blade tip contact.
2	FBG System	No FBG signal.	Fault finding via a process of component elimination was conducted ultimately identifying the optical fibre extension lead as being unserviceable. It was removed and the FBG signal was restored.
3	FBG System	FBG data collection soft-ware returning incomplete and incorrect data.	The FBG soft-ware required a self-test and calibration to the FBG in use following which correct data was obtained.
4	Strain Gauge System	Strain Gauge #2 not sending data signal.	Fault finding via a process of component elimination was conducted ultimately identifying the modified connector plug as being unserviceable. It was removed and replaced restoring the strain gauge signal.

14.4 Testing Conditions

Table 32 details each set of test conditions employed for test three through nine.

Table 32. Test Conditions.

Test #	Lower Adjustable Support Position (mm)	Upper Load Plate Position (mm)	Load (N)	Comments	
	All positions relative to Root-End Clamp along the Main Support.			All forces applied to upper test surface.	
3	1500.0	750.0	1000	Single load	No Damage
4	185.0	1500.0	500 – 2500	Load applied in 500 N increments	No Damage
5	185.0	1500.0	500 – 2500		Spar - 3.0 mm depth, 8.0 mm dia. hole.
6	185.0	1500.0	500 – 2500		Spar - 6.0 mm depth, 8.0 mm dia. hole.
7	185.0	1500.0	500 – 2500		Spar - 1 x 8.0 mm dia. through hole
8	185.0	1500.0	500 – 2500		Spar - 2 x 8.0 mm dia. through hole.
9	185.0	1500.0	500 – 2500		Spar - 2 x 8.0 mm dia. through hole and 1 x 8.0 mm dia. transverse through hole.

The testing was conducted with the coordinated ‘start’ of both the FGB and strain gauge systems. Once started, the load was applied via the manual operated hydraulic pump. In general 500 N load increments were applied and were monitored by the strain gauge system software, via the load cell. The load cell output, in newtons, was clearly observable on the strain gauge system computer screen.

Once each load interval (500 N) was reached a delay of approximately 60 seconds was enforced to allow the blade structure to stabilise and sensors to return stabilised strain data. This process was repeated at all five load levels from 0 to 2500 N.

Additionally, deflection of the blade tip (or blade mid-point in the case of Test 3) was recorded by the LVDT and again displayed by the strain gauge system software.

The mid-span load testing (Test 3) is pictured below as a guide to the test set-up.



Figure 110. Mid-span load testing (Test 3).

At no time during any testing did the blade contact the test fixture main support compromising results. Under maximal load (2500N) the blade tip came to within 10.0 mm of the test fixture as presented below.

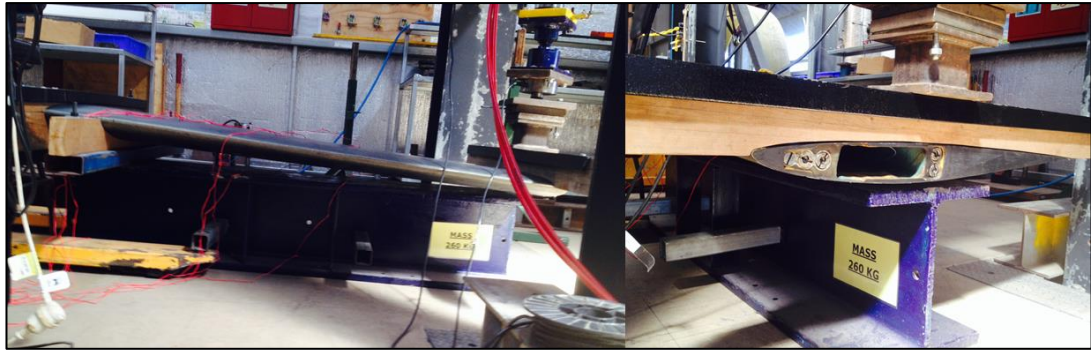


Figure 111. Blade deflection at the maximal 2500N cantilever load.

14.5 Incremental Damage Application

Following the completion of Test 3 and 4, incremental damage was applied to the blade section. It was applied at the D-spar upper, rear most area adjacent to the upper surface and vertical surface junction. The general location and orientation of the three damage holes is presented on the Abaqus D-spar FEA model below.

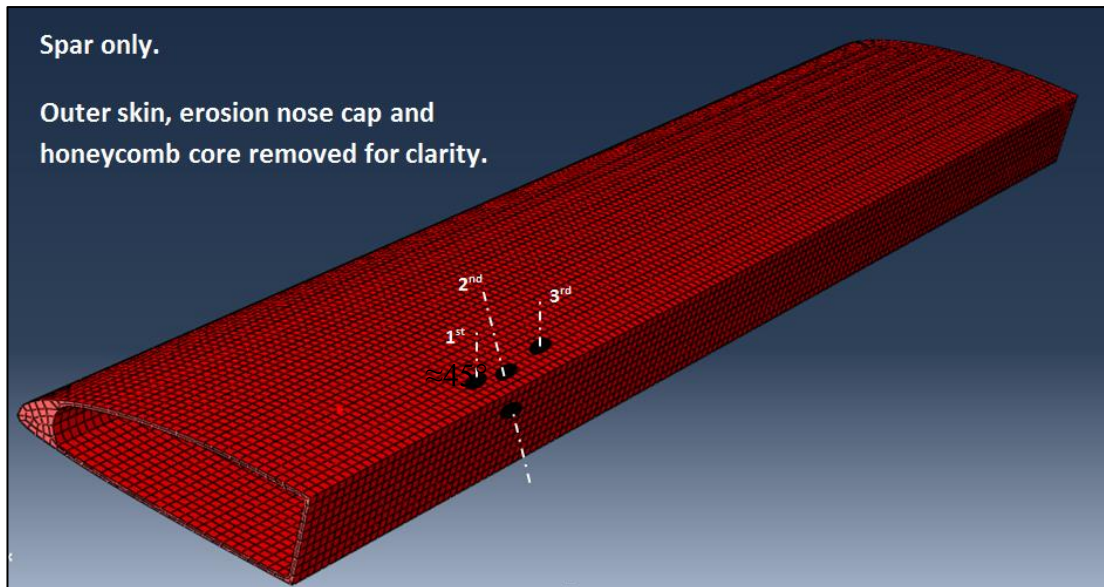


Figure 112. Location, axis and order of damage holes relative to the D-spar.

Hole one was used in the partial depth tests (Tests 5 & 6) in two increments from 3.0 mm and 6.0mm and was subsequently used as the initial, single full thickness hole in Test 7, which is depicted below.



Figure 113. Hole 1 at 3.0 mm depth and full thickness.

The second damage hole was the transverse ‘corner’ hole which passed completely through the D-spar section at two places. With the exception of the initial hole, no attempt was made to create a ‘clean’ hole. The drill bit was rapidly and forcefully fed through the section in an attempt to partially rupture through the inner spar surface as opposed to cutting through with even material removal. This was intended to replicate ballistic damage as closely as possible within the methods at hand whilst not damaging the nearby sensor systems.

The ruptured fibres of the inner D-spar surface can be seen in the following diagram for holes two and three. This was only partially achieved for hole one given the incremental nature of the test at this point.

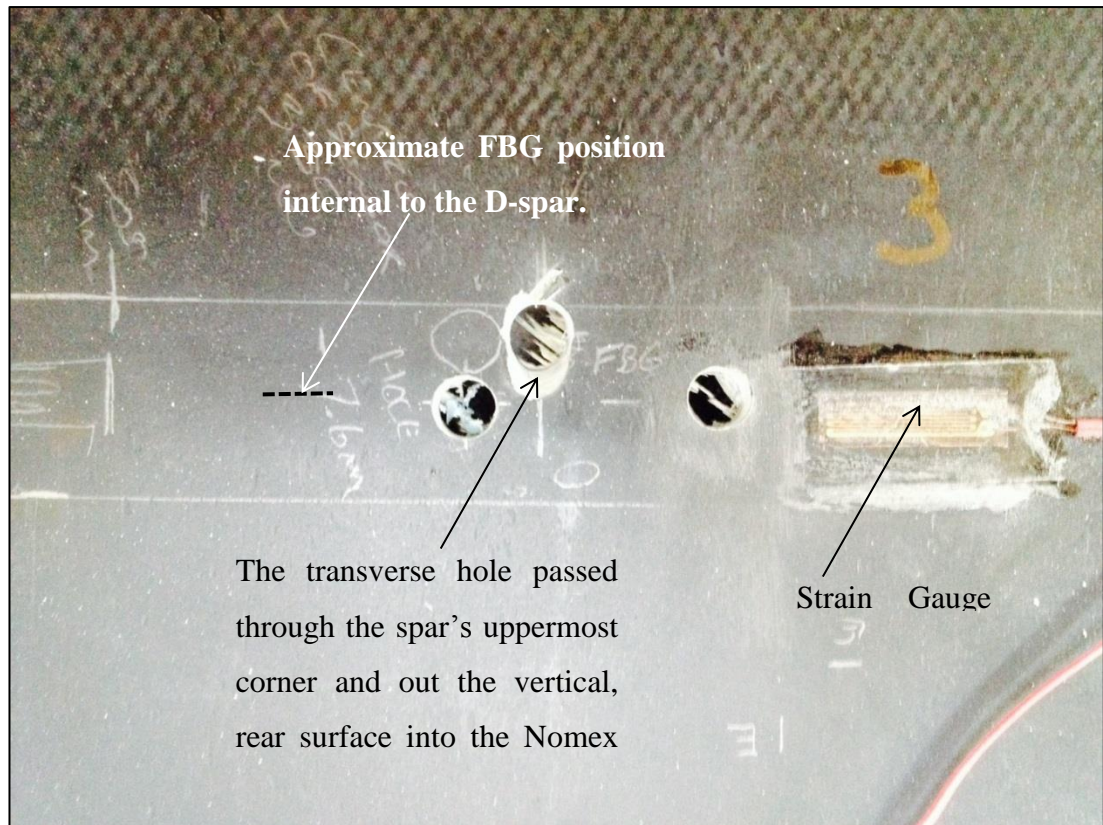


Figure 114. Blade surface with three completed damage holes post testing.

14.6 Testing Cessation

At higher load levels, fibre fracture and structural failure was audibly observable.

This became more pronounced during each subsequent test as increasing levels of mechanical damage were inflicted on the D-spar section. The pronounced audible nature of the failure was a contributing factor in the decision not to progress the load to 3000 N during the final Test 9 cycle as planned. Cessation at 2500 N during Test 9 was enlarge to protect the integrity of the blade test section for subsequent testing if required in addition to the scope of this research.

Whilst the testing methodology was modified as a result of the ballistic damage trial results, it was still a success providing sound data and results from which to draw conclusions.

CHAPTER 15 - RESULTS

This chapter discusses the results and conclusions drawn from the testing and FEA model comparison.

15.1 General Overview

The following chapter details the results obtained from the blade testing phase. This includes the data collected for both the FBG and the strain gauge systems, which are compared in order to draw conclusions and comparisons. Additionally, the FEA results are presented in support of these results.

15.2 FBG System Results

The results obtained from the FBG system were enlarge as expected with micro-strain readings correlating with those obtained from the number 1 position strain gauge, being the closest gauge to the FBG with the same orientation.

During testing, real time results were obtained from the Micron Optics – ENLIGHT software which demonstrated a shift in the central wavelength response from the left to the right as the load was increased. Following is a screen shot of the test data screen taken during Test 7 at 2500N load indicating the peak shift to the right indicating a tensile strain condition.

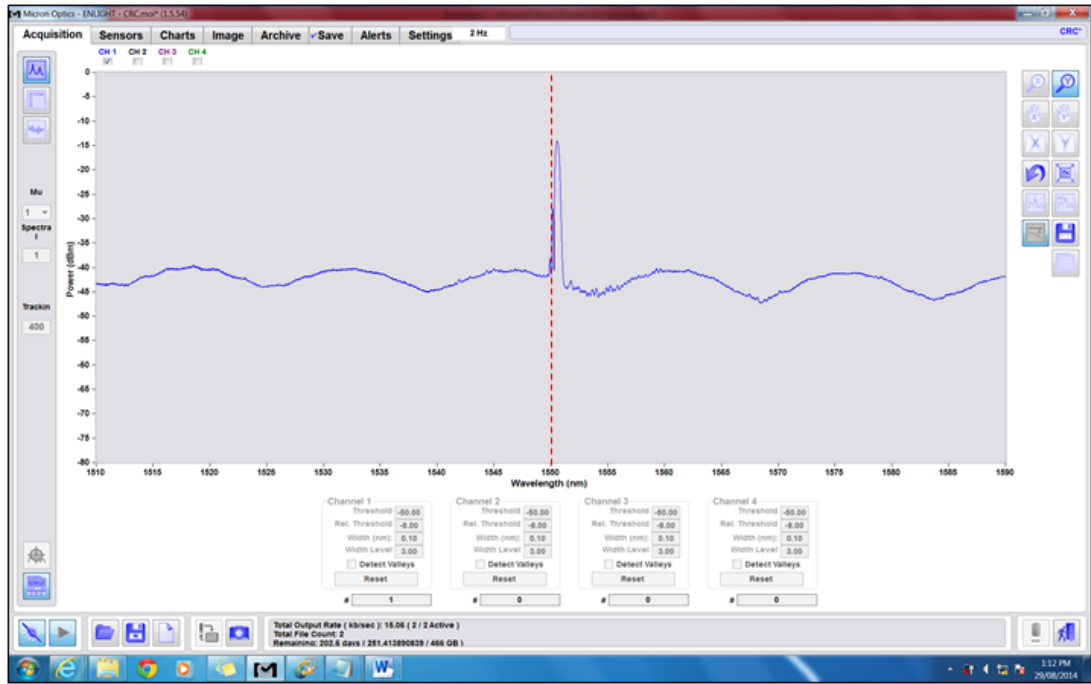


Figure 115. Micron Optics – ENLIGHT software screen shot.

The following plots depict a shift in the FBG central wavelength peak from left to right. This shift indicates that the FBG was experiencing a tensile force as expected, which was later verified by both the FEA model and the nearest #1 strain gauge.

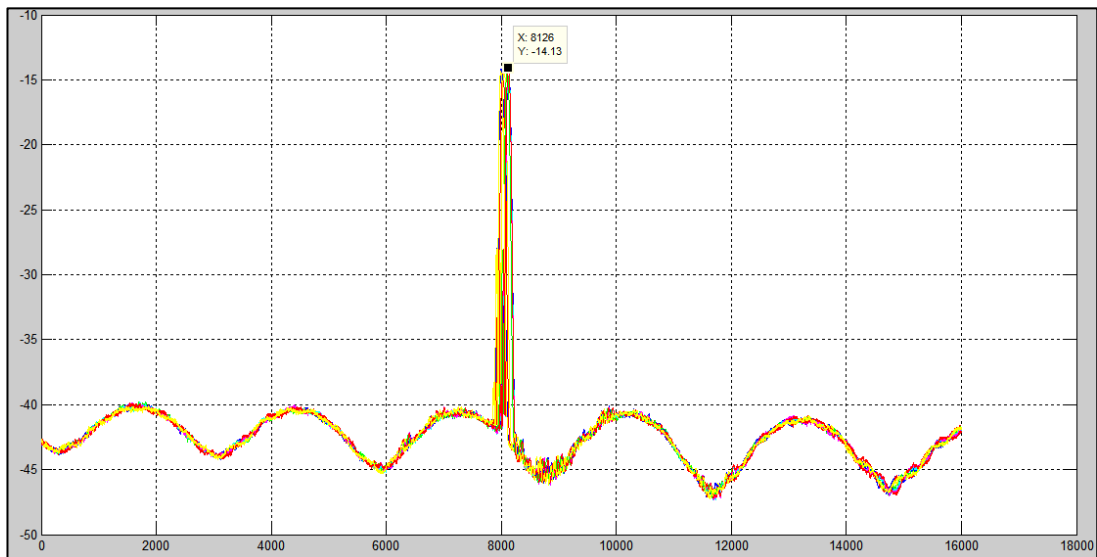


Figure 116. MatLab plot of FBG Test 9 results.

As can be seen in Fig. 116, the deviation along the X axis is not pronounced and only equates to several hundred increments out of approximately 16000 data point increments taken by the software during each test. Changing the scale of the plot provides more clarity with each peak representing a change in micro-strain as the 500N load increments were applied. It also details a peak shift from the right to the left as the load was removed at completion of the testing cycle. These ‘reverse peaks’ are easily identifiable within tests’ response .TXT data file; however have been left in following plots as repeated colours.

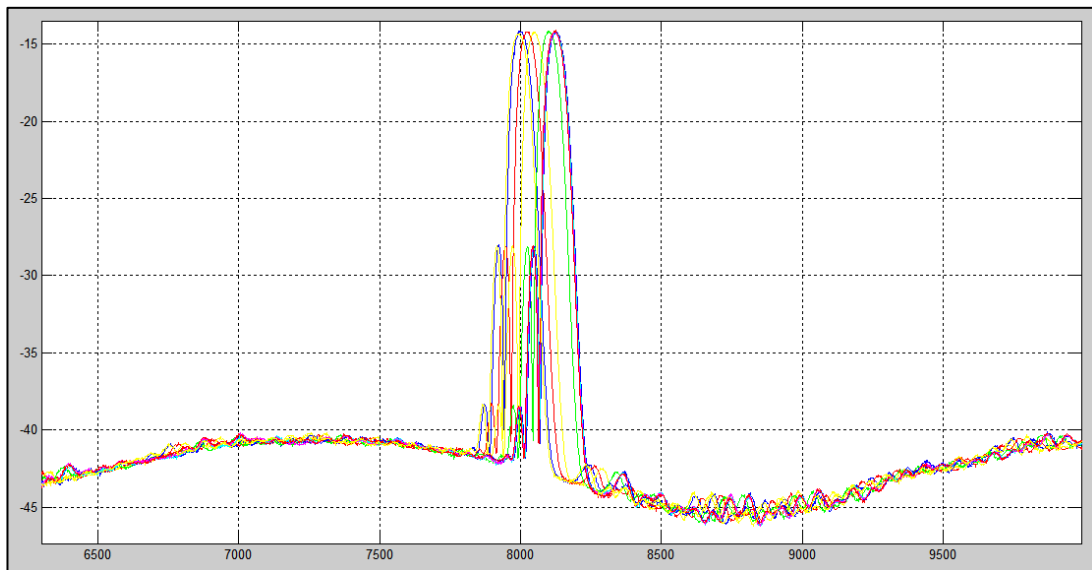


Figure 117. MatLab plot of Test 9 FBG peak shift to the right indicating tensile strain.

The Y axis in the above plot represents the intensity in dBm which is a negative value whilst the X axis is the unit wavelength response (nm) test increment. This increment maybe used to calculate the micro-strain experienced at any given point via the following equations:

$$RCWL = \text{Test Increment} \times (\Delta W - WS) \quad (15.1)$$

Where:

Test Increment = Taken from FBG plot x-axis (Range = 0 <16001)

ΔW = Wavelength Delta (nm),

WS = Wavelength Start (nm), and

RCWL = Response Centre Wavelength

The above required information was taken from the each test response data file (extract below) and may be used to determine the RCWL at any given point.

```
CH 4 Configuration:
  Distance Compensation Enabled: False
  Spectral Average Count: 1
  Threshold: -50.00 dB
  Rel. Thresh.: -8.00 dB
  Width Level: 3.00 dB
  Width: 0.10 nm
  Detect Valley: False

Wavelength start (nm): 1510.00000
Wavelength Delta (nm): 0.0050
Number of Points: 16001
```

Figure 118. Micro Optics ENLIGHT response data file extract.

Alternatively, if only the maximum RCWL is required it may be taken directly from the Micro Optics – ENLIGHT peaks data file. This was achieved by sorting the data in MS Excel and applying the above equation.

Once the RCWL has been determined the micro-strain value at a given point may be calculated using the following equation:

$$\text{Micro-Strain } (\mu\epsilon) = \frac{\text{RCWL} - \text{Original FBG WL}}{0.793 * 10^6} \quad (15.2)$$

Where:

Original FBG WL = 1549.99 nm from manufacturer's documentation.

The above calculation was applied as a confirmatory check against the results returned by the FBG and strain gauge systems.

Fig. 119 following is a view of the previous FBG plot clearly showing the peak shift from 0.00 $\mu\epsilon$ to a maximal value of 515.55 $\mu\epsilon$. Again, this value was calculated manually and compared to that returned by the FBG system.

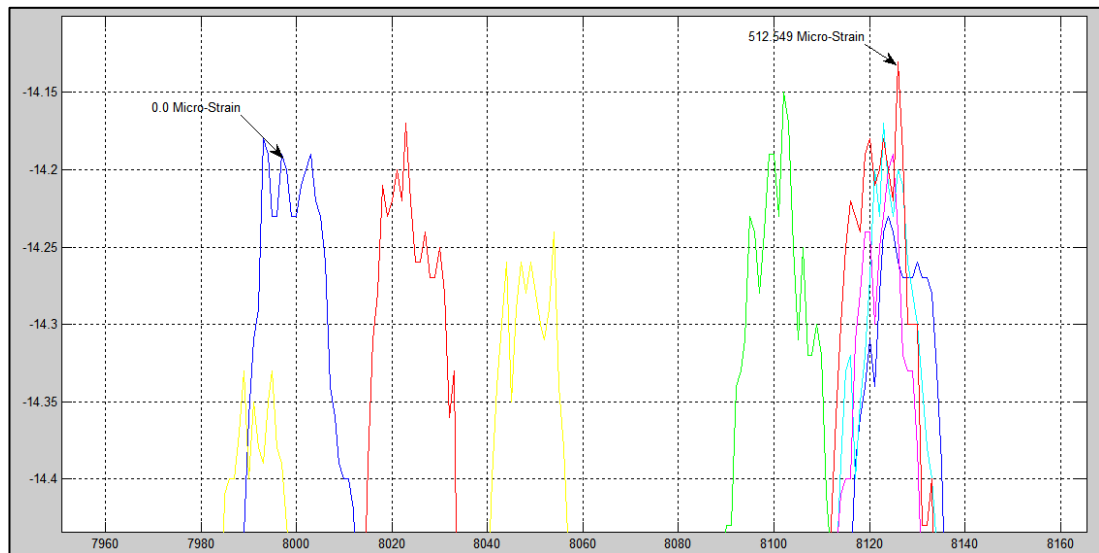


Figure 119. MatLab plot of FBG peaks (zoom view).

15.3 FBG & Strain Gauge Results Comparison

Following is a summary of maximal results and the difference between the FBG micro-strain response and the #1 strain gauge micro-strain response for all tests. It should be noted that the FBG and the strain gauges are both averaging devices and that the FBG was 5.0 mm in length and the strain gauges 20.0 mm in length.

This difference in length may result in response deviations if located on areas experiencing a significant strain gradient change within the region covered, in particular the strain gauges due to their larger comparative length.

Additionally, the FBG and strain gauge #1 were separated by approximately 45.0 mm, centre to centre. It was therefore reasonable to expect that these factors will cause a deviation between the two results; however, it was expected that this deviation would remain relatively constant although increasing with additional load.

Following, Table 33 is an overview of the FBG and #1 position strain gauge results for all nine tests. The results were calculated via software and randomly, manually cross checked for data verification.

Table 33. FBG & Strain Gauge (# 1) Results Comparison.

FBG & Strain Gauge (# 1) Results Comparison						
Test	Load (N)	Displacement (mm)	FBG ($\epsilon\mu$)	Strain Gage #1 ($\epsilon\mu$)	Delta ($\epsilon\mu$)	Test Conditions
1	1507.6 1 (Max)	60.82	284.75	311.39	26.64	Lower Support – 0.0 mm from clamp.
2	2033.0 (Max)	17.25	-51.16	-39.08	12.08	Central Load (750.0mm). Resulted in compressive strain.
3	1051.1 8 (Max)	34.54	176.56	211.63	35.07	Lower Support – 185.0 mm
4	2517.3	63.9	436.57	519.24	82.67	No Hole. Lower Support – 185.0 mm
5	2517.3	59.47	450.41	509.97	59.56	Hole 3.0 mm depth. Lower Support – 185.0 mm
6	2517.2 9	65.4	463.49	509.94	46.45	Hole 6.0 mm depth. Lower Support – 185.0 mm
7	2531.4 5	61.23	469.95	513.86	43.91	Hole Full Thickness. Lower Support – 185.0 mm
8	2517.2	63.7	534.96	508.48	26.48	2 Holes Full Thickness. Lower Support – 185.0 mm
9	2518.0	68.8	516.92	504.07	12.85	3 Holes – 2 Full Thickness, 1 Transverse in Spar upper rear corner. Lower Support – 185.0 mm

For comparison purposes the resultant data plots from tests 4 and 9 are presented below. The intermediate tests of 5-8 are not presented here as the results from tests 4 to 9 represent the upper and lower extremes in micro-strain results.

The results for all tests are located at Appendices G through O should further review be required.

15.4 Test 4 vs FBG Results

The following plot of Test 4 details the FBG vs strain gauge position #1 trend line. It details an increase in the strain detected by both systems as the load is increased. It can be seen that the trends of each system have resulted in a close correlation of micro-strain sensed. The maximal strain for the FBG was $\approx 436.5\mu\epsilon$ whilst the #1 strain gauge recorded $\approx 518.75\mu\epsilon$ as can be seen below.

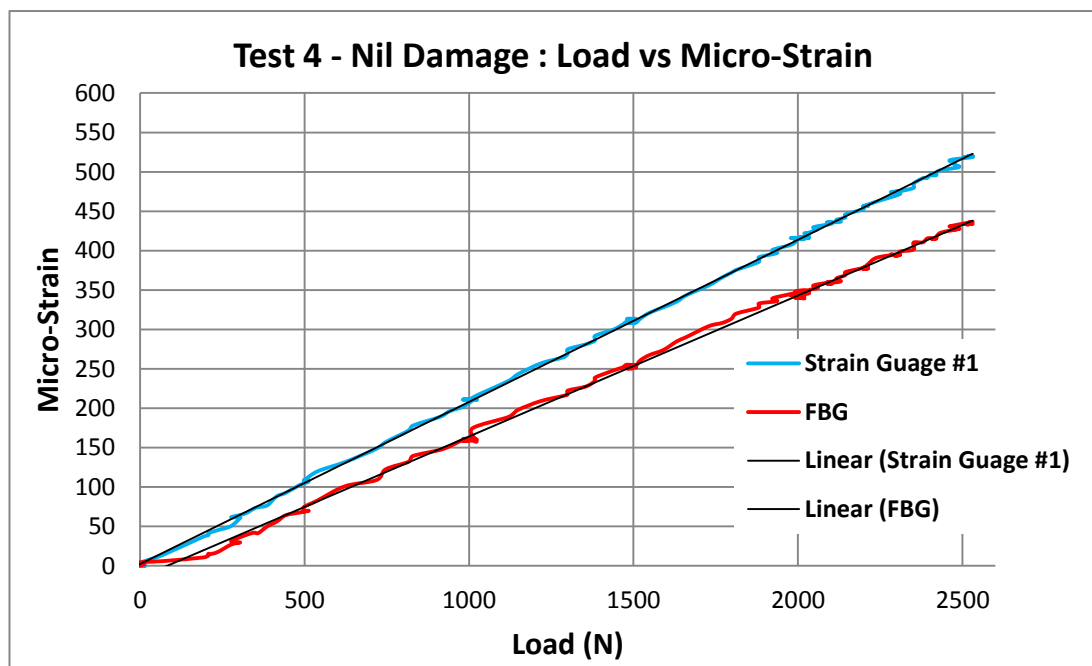


Figure 120. Test 4 load vs Micro-strain plot.

The difference in strain above and in subsequent plots is a result of the differing location of each sensor as they were separated by ≈ 45.0 mm.

Following, Fig. 121 presents all Test 4 strain gauge response as load (N) vs micro-strain ($\mu\epsilon$) along with the FBG result. As can be seen the gauges located on the lower test surface are experiencing a compressive strain.

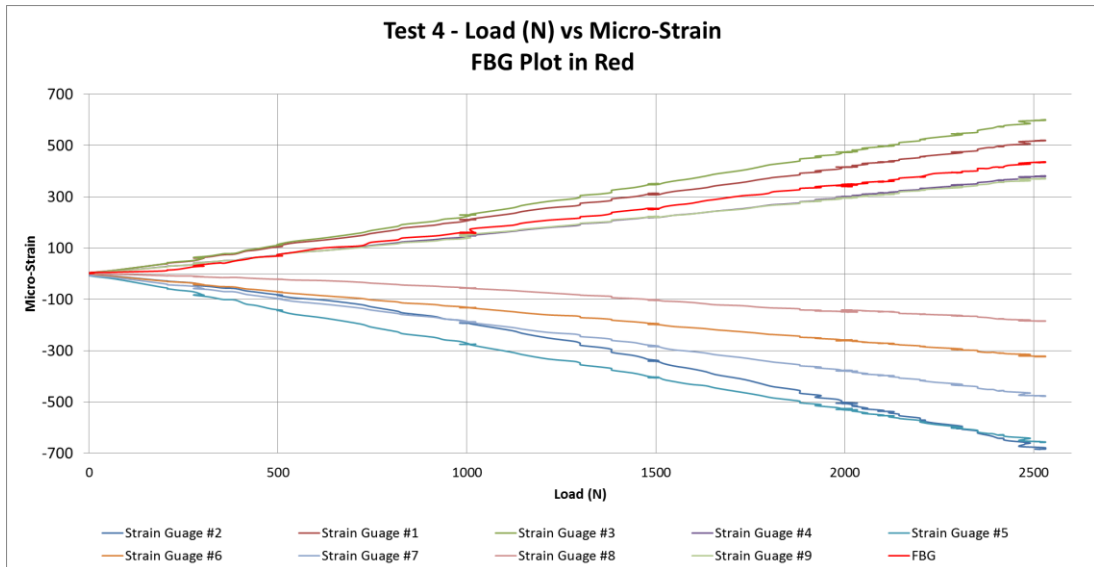


Figure 121. Test 4 – Load & strain gauge / FBG comparison plot.

The upper surface being in tension and the lower in compression was reflected for all tests with the exception of the mid-span load test (Test 3) in which the sense of strain was largely reversed. Fig. 122 is a plot of the Test 3 results.

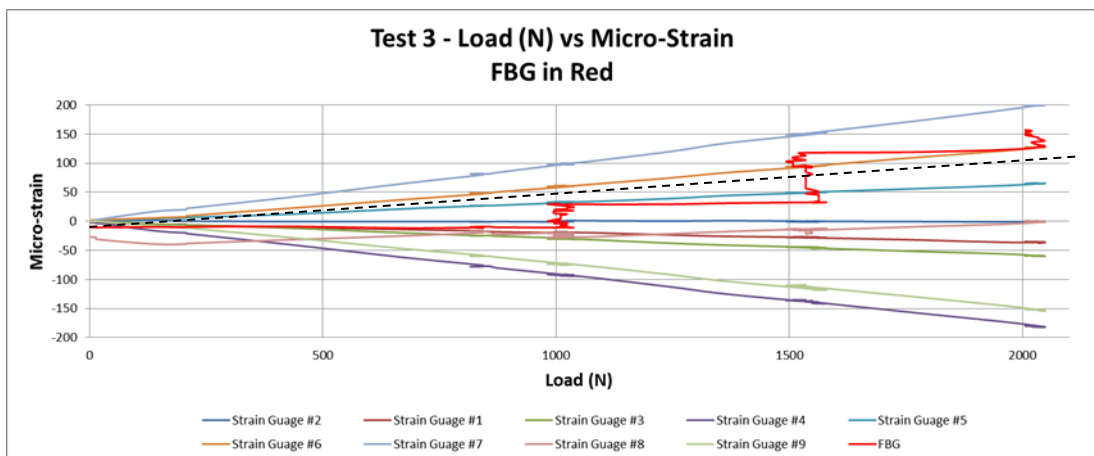


Figure 122. Test 3 – Load & strain gauge plot (1000N) FBG comparison.

It is unclear why the FBG data line in the FBG / strain gauge comparison above is stepped in nature. It is believed this is a result of the FBG data points having to be reduced by 60% in order to allow plotting with the strain gauge data. However, the mean line (---) once again indicates a correlation between the FBG and strain gauge #1 located in the number one position.

15.5 Test 9 vs FBG Results

The following plot of Test 9 details the FBG vs strain gauge position #1 trend line. It shows an increase in the strain detected by both systems as the load is increased. As can be seen the trends of each system have resulted in a close correlation of micro-strain sensed. The maximal strain for the FBG was $\approx 516.92 \mu\epsilon$ whilst the #1 strain gauge recorded $\approx 504.07 \mu\epsilon$ as can be seen below.

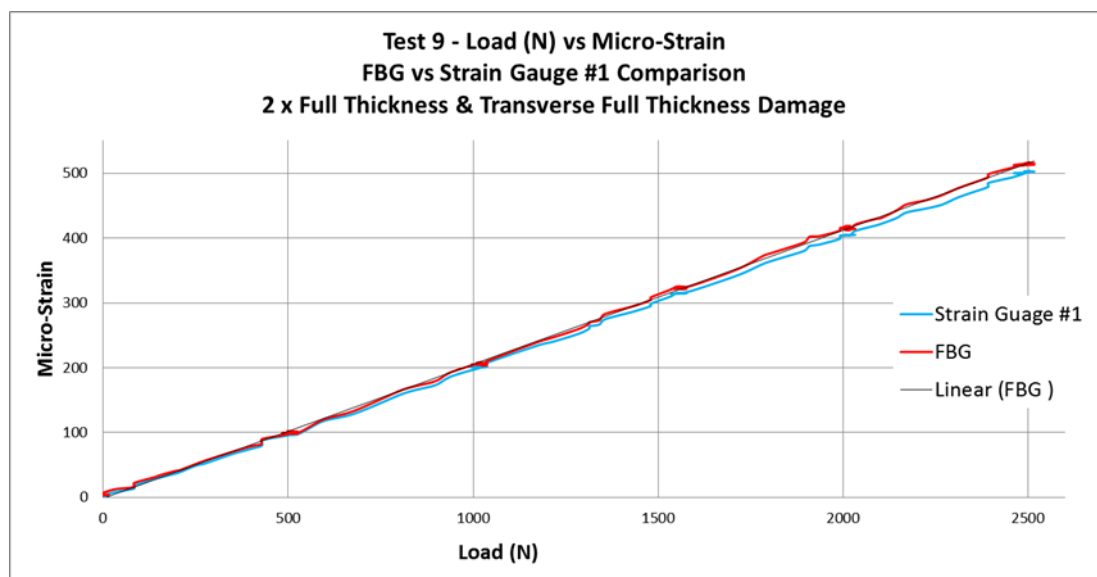


Figure 123. Test 9 – Load & strain gauge / FBG comparison plot.

The following plot presents all Test 9 strain gauge and the FBG response as load (N) vs micro-strain ($\mu\epsilon$). As can be seen the gauges located on the lower test surface are again experiencing a compressive strain.

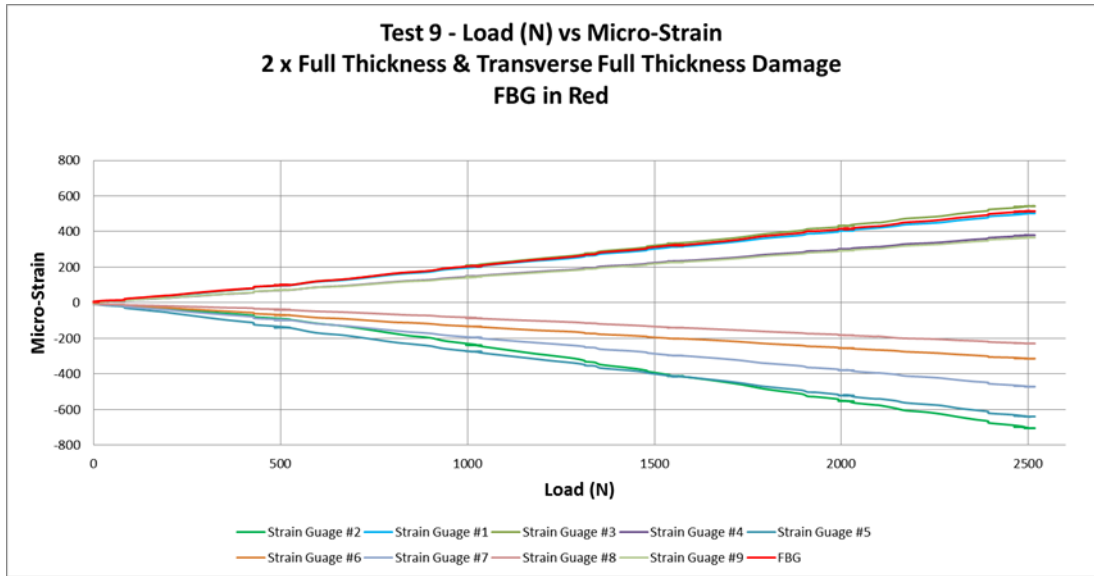


Figure 124. Test 9 – Load & strain gauge / FBG comparison plot.

15.6 Test 4-9 and FBG Results

A table of comparison for Test 4 and Test 9 FBG and strain gauge position #1 results is presented below. It can be seen that there is a significant increase in the FBG micro-strain as the damage level was increased on the blade. However the strain gauge reading had little change. It is believed that this is a result of the strain gauge being located farther away from the damage site by approximately 65.0 mm. This was later confirmed by the simplified FEA model detailing very localised stress concentrations in the vicinity of the FBG and damage.

Table 34. Table of comparison for Tests 4 and 9.

	Test 4		Test 9	
	µε	Delta (µε)	µε	Delta (µε)
FBG	436.57	82.67	516.92	12.85
Strain Gauge #1	519.24		504.07	

15.7 Tests 1 – 9 Correlations

Fig. 125 is a comparison of the Tests 1 through 9 maximum micro-strain. It can be seen that there is a general correlation from tests 1 to 3. There is then a convergence of sensed strain by the two systems.

This convergence commenced at Test 5, with the initial application of damage of 3.0mm depth. As the damage level was increased through the subsequent tests this trend continues.

It is believed that this change is a result of both the distance separating the two sensors and the damage acting as a stress raiser. This stress raiser action is detected by the FBG from initiation at Test 5; however, the additional stress is significantly dispersed throughout the structure prior to being detected by the position #1 strain gauge which is located further away. This theory was supported by subsequent flat plate FEA modelling to be discussed in subsequent paragraphs.

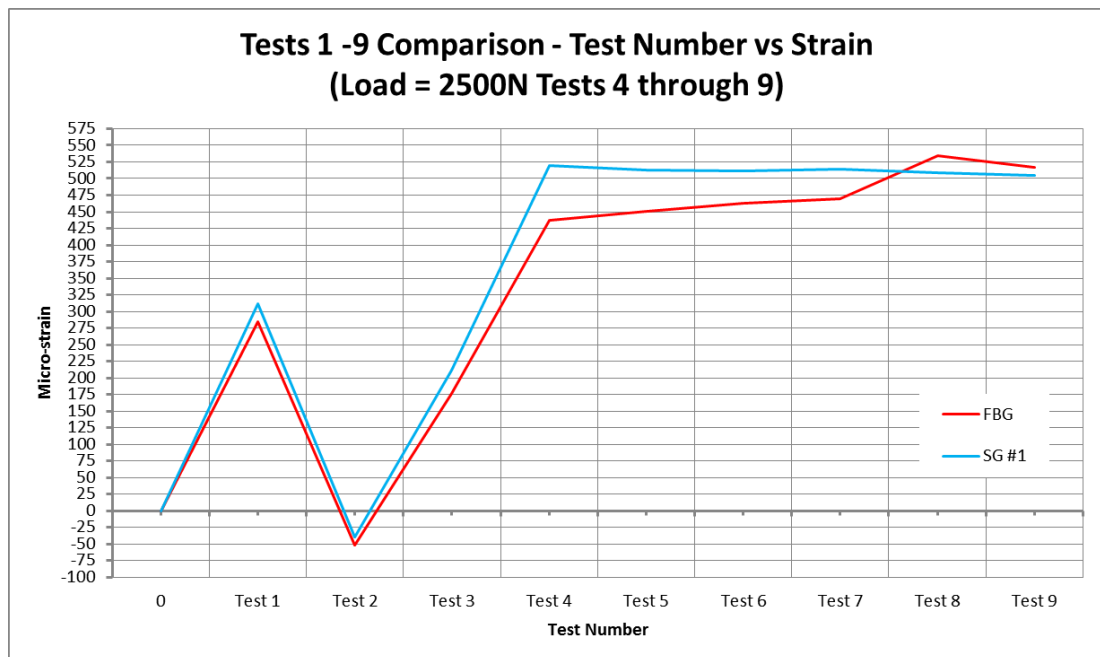


Figure 125. Test 1 – 9 Comparison plot of FBG & strain gauge #1.

The general trend of both the FBG and strain gauge #1 for Tests 4 through 9 can be seen in the following simplified bar chart.

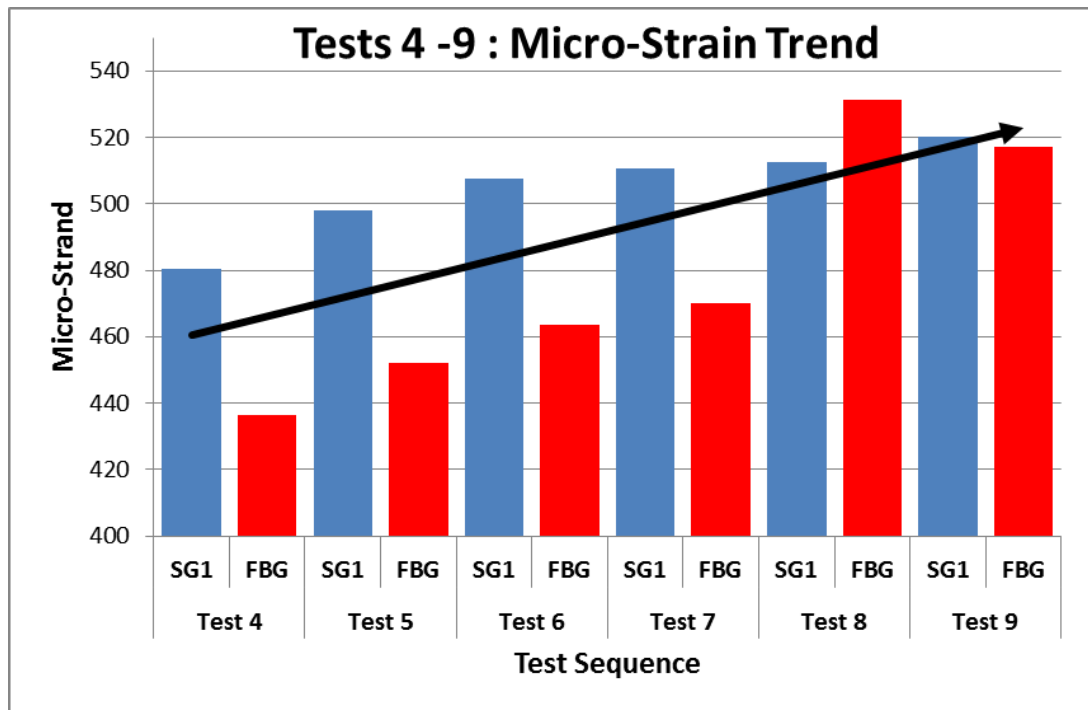


Figure 126. FBG and strain gauge trend.

As evidenced in Fig. 127 below, the change in response to the application of incremental damage is limited for the two strain gauges located at positions #1 and #3; however, the FBG is sensing a greater rate of strain increase due to its proximity and localised stress concentrations. The drop in FBG detected strain during Test 9 with respect to Test 8 is believed to be a result of localised yielding due to increased level of damage having a greater effect. This reduction was later confirmed as accurate in the flat plate FEA modelling.

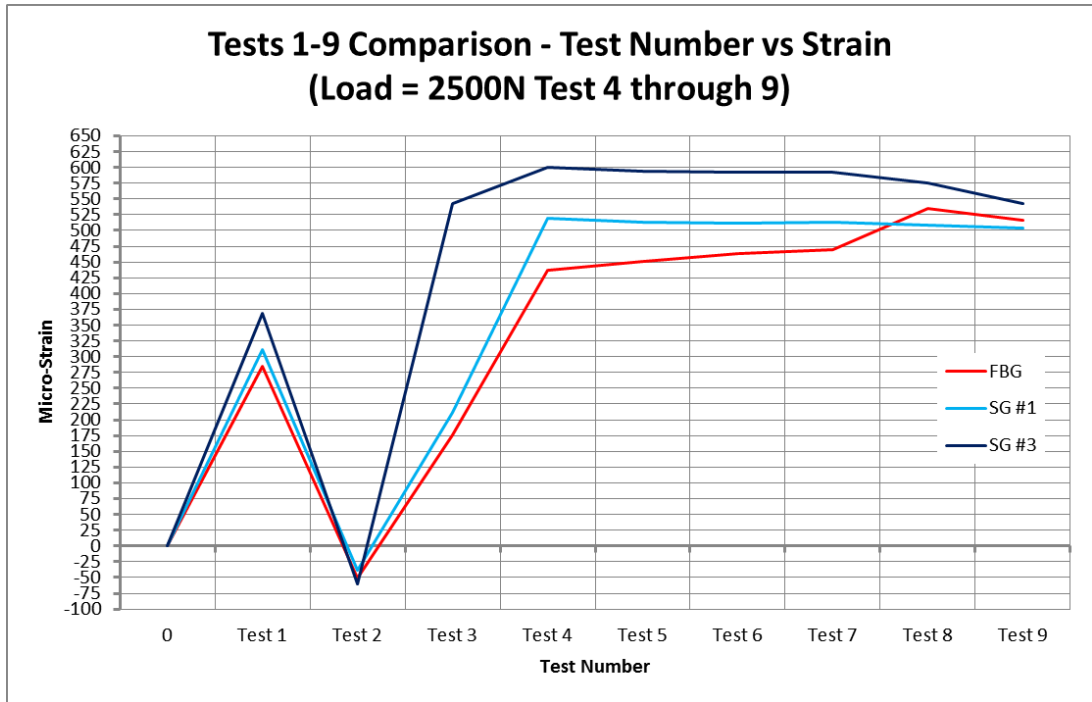


Figure 127. Test 1 – 9 Comparison plot of FBG & strain gauges #1 & #3.

Test results for the remaining strain gauges, to include the lower test surface and the un-planned damage site remained largely unchanged as a result of incremental application of damage. The average delta between the remaining strain gauges between Tests 1 and 9 averaged less than ten micro-strains, which is detailed in Table 35.

Table 35. Lower surface strain comparison ($\mu\epsilon$).

	Test 4	Test 7	Test 9
Strain Gauge #5	-655.12	-648.23	-638.40
Strain Gauge #6	-322.45	-312.90	-313.43
Strain Gauge #7	-475.19	-469.90	-471.00

The results for the un-planned damage showed little change in the strain reading for the strain gauge located at position #9 which was axially orientated; however, the corresponding transverse strain gauge located at position #8 recorded an increase in strain levels. These results are presented in Table 36 for Tests 4 and 9 only, being the extreme results ranging from no incremental damage to the maximal damage of three through holes. The intermediate tests have been omitted for clarity.

Table 36. Un-planned damage area surface strain comparison ($\mu\epsilon$).

	Test 4	Test 9
Strain Gauge #8	-184.29	-228.29
Strain Gauge #9	370.12	366.62

An increase of approximately 44.0 micro-strain was recorded at position #8 across Tests 4 to 9, whilst position #9 remained unchanged.

15.8 Blade Assembly FEA Results

The FEA blade assembly model was found to have some correlation between the D-spar and that of the sensor systems. However, significant discrepancies occurred on the skin and areas of the D-spar in relation to the FEA results when compared to the sensor system. This was for both the upper and lower test surface strain gauge locations.

It is believed this is a result of the FEA assembly process in which the interactions and constraints established between the sub-component surfaces required for assembly have deficiencies. Unfortunately, the creation of the FEA model consumed a far greater amount of time than anticipated, due enlarge to a lack of advanced working knowledge of the Abaqus software and the software complexity.

Whilst the bulk of the modelling was completed, in order to finalise the remaining outstanding project tasks, refinement of the blade assembly FEA model was not able to be achieved. This resulted in a model which was moderately accurate in areas; however, was not representative in others.

Should time have been permitting the following tasks would have been conducted in order to refine the model:

1. Revise and confirm the composite plie orientation for the skin and D-spar,
2. Revise and correct inter-component relationships,
3. Refine the mesh grid in local areas of interest, and
4. Confirm all data co-ordinate dimensions.

Figure 128 following demonstrated reasonable correlations with the sensor systems for the internal D-spar surface and strain gauge position #1. However, outside of these areas the model elemental strain readings were erratic and often in a reversed sense rendering the data unreliable. The following Abaqus screen captures display the Probe Values windows. These windows detail the micro-strain at each selected mesh element, which is both listed on the model as a data tab, and as a list point in the window itself. The Probe Values window is again utilised in subsequently presented Abaqus plots.

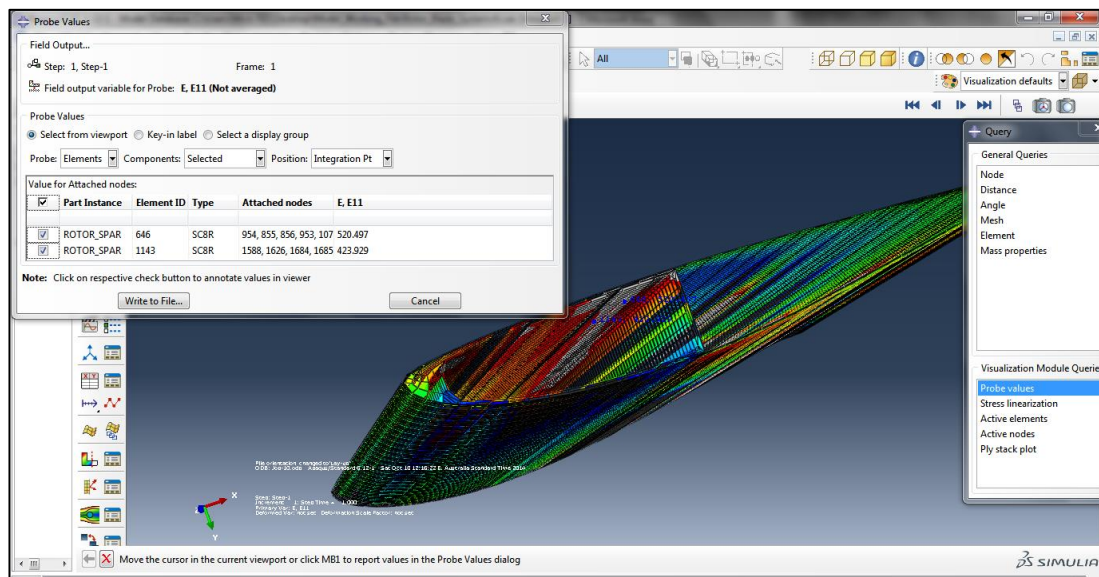


Figure 128. Abaqus D-spar FBG and Strain gauge #1 micro-strain.

As with Fig. 128, the figure below demonstrated reasonable correlations with the sensor systems for the position number three strain gauge, located on the upper test surface. However, outboard of this area the model element strain readings again became erratic.

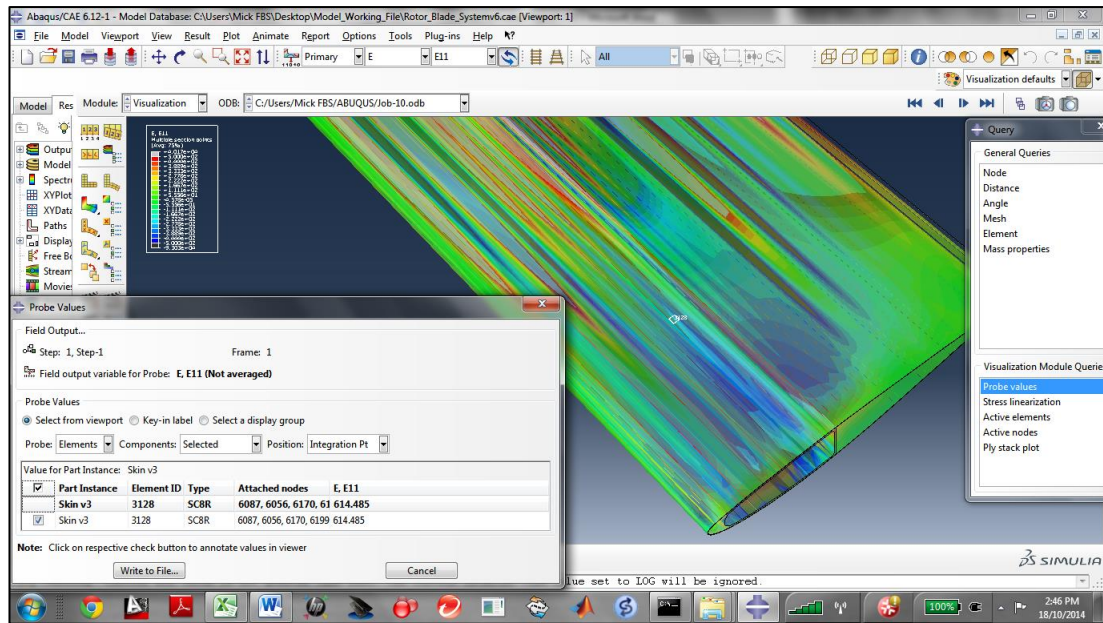


Figure 129. Abaqus Skin FEA strain gauge position #3 micro-strain (semi-translucent plot).

The following table is a comparison between the FBG, strain gauges #1 and #3 and the FEA determined strain at each approximate location. Position #3 is an axial orientated gauge which is located ≈ 430.0 mm from the root end clamp, or out board of the damaged area.

Table 37. Test 4 FEA / testing results comparison.

FEA and FBG / Strain Gauge Position #1 and #3 Test 4 Comparison						
Location	FEA Probe: Skin #3	Strain Gauge #3	FEA Probe: Position #1	Strain Gauge #1	FEA Probe: FBG	FBG
Micro-Strain ($\mu\epsilon$)	614.49	597.76	520.49	519.24	423.93	436.57

Whilst Table 37 shows a good correlation between the FEA model, the FBG sensor and the strain gauges at position #1 and #3 it must be noted that these results only apply to Test 4, being a nil damage test.

All attempts at the application of damage within the model failed during analysis or created significant errors. Additionally, FEA strain values for the remaining strain gauge locations varied significantly with respect to the tested values.

As a result of the limited success and ability to apply the incremental damage within the model it was decided that a simplified FEA model was required for validation purposes. As a result, a flat plate simulation was modelled in an attempt to again draw correlations in data.

15.9 Flat Plate FEA Results

The following flat plate FEA simulations are of the D-spar and skin combination which support the Tests 7 through 9 results relevant to strain increase and decrease trends.

The laminate layup utilised is the same as that for the previous rotor assembly FEA model; however, the skin and D-spar laminates have been combined to form a single, 24 ply laminate structure. This composite lay-up and orientation is detailed as follows in Fig. 130.

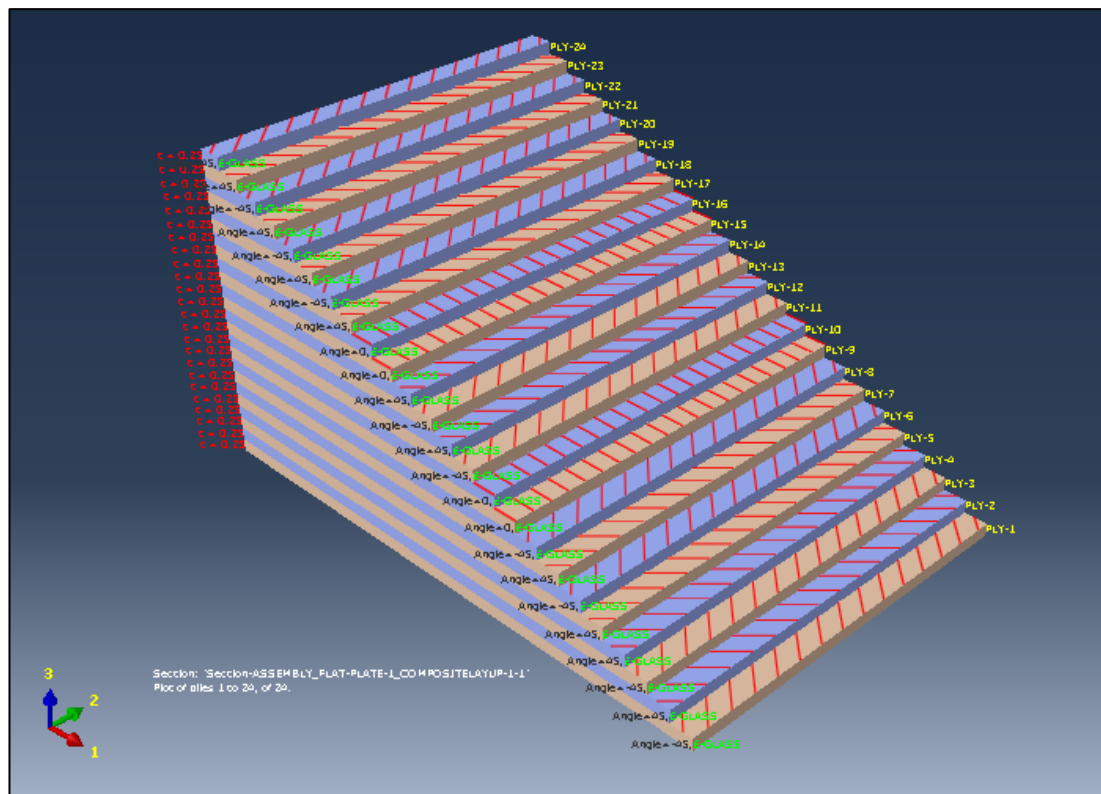


Figure 130. Flat plate simulation composite layup.

The load applied to the model remained as a segregated UDL across the tip at the maximum of 2400N. The model was fully constrained at the opposing end.

As detailed below, a relatively fine mesh was utilised to enable close examination of the strain levels adjacent to the damage site whilst minimising computational time.

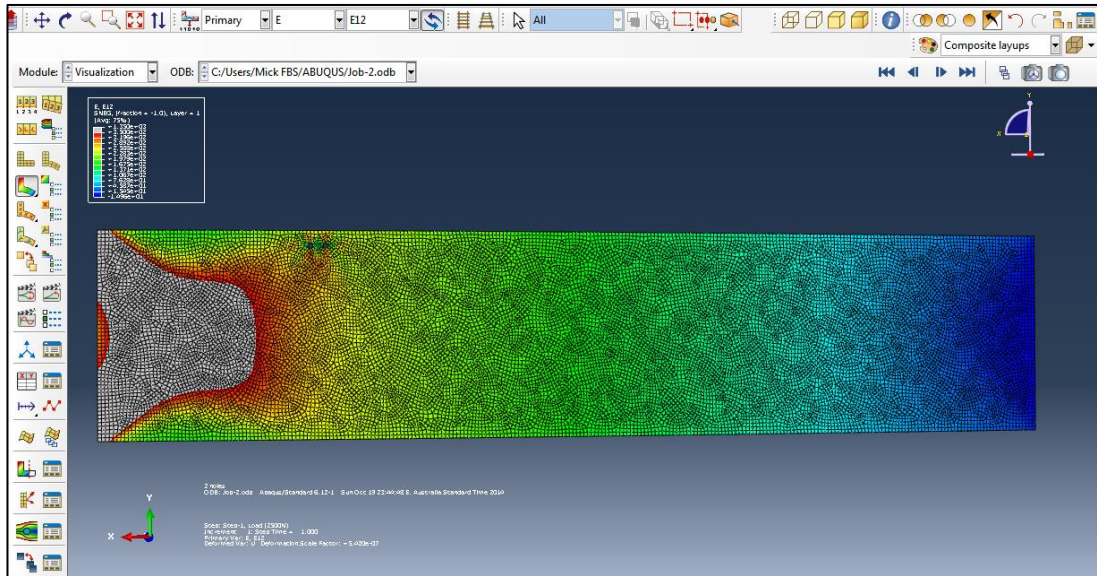


Figure 131. Flat plate verification fine model mesh (two through holes).

The simulation of Test 7, comprising of one complete 8.0 mm through hole yielded the following results as detailed within the Probe Value window.

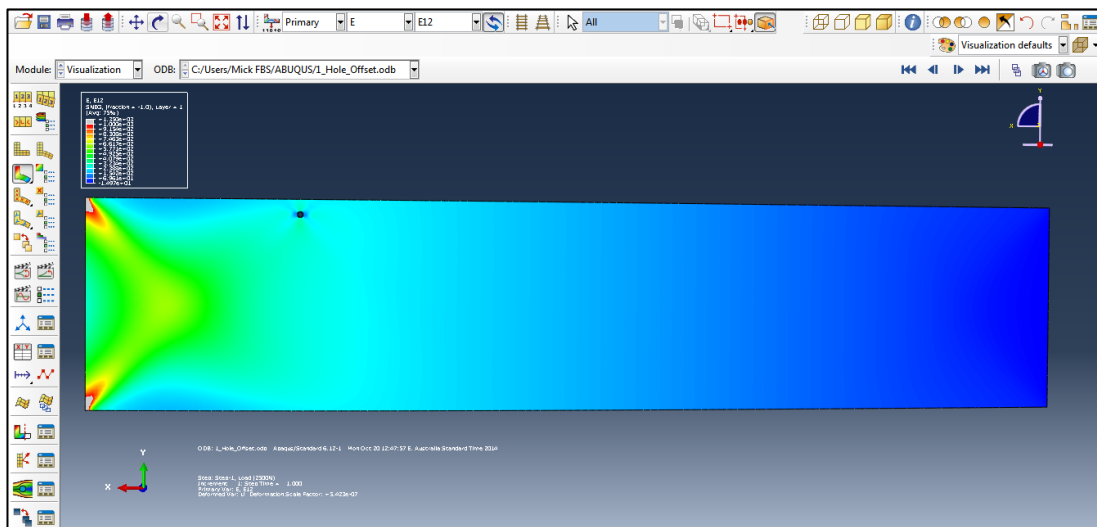


Figure 132. Test 7 FEA simulation results overview.

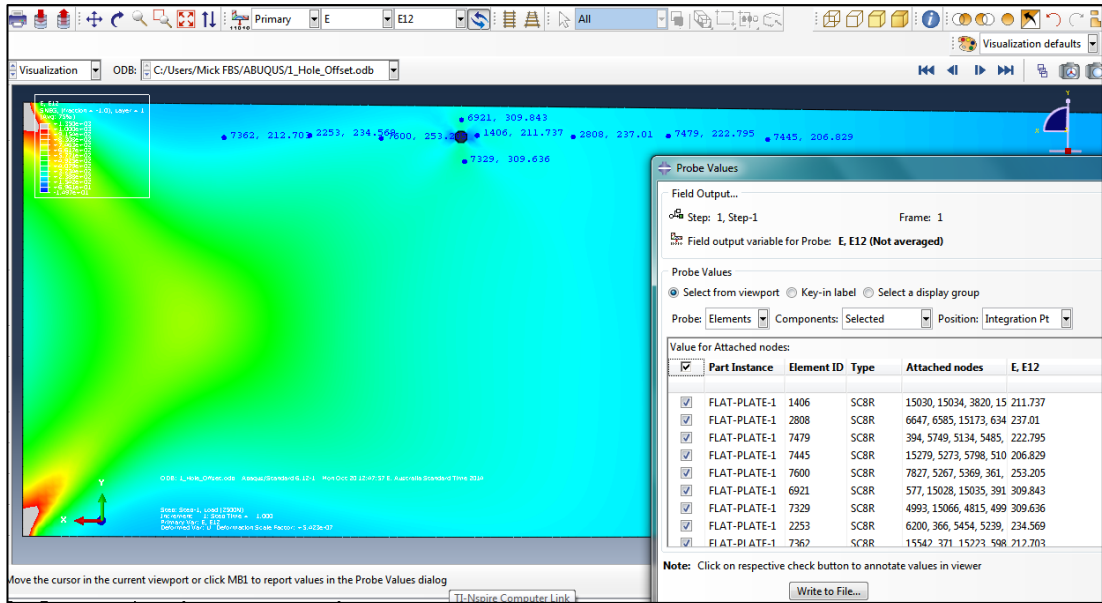


Figure 133. Test 7 FEA simulation micro-strain values.

Simulation of Test 8 comprising of two complete 8.0 mm through holes (one offset by 8.0mm) yielded the following results as detailed within the Probe Value window.

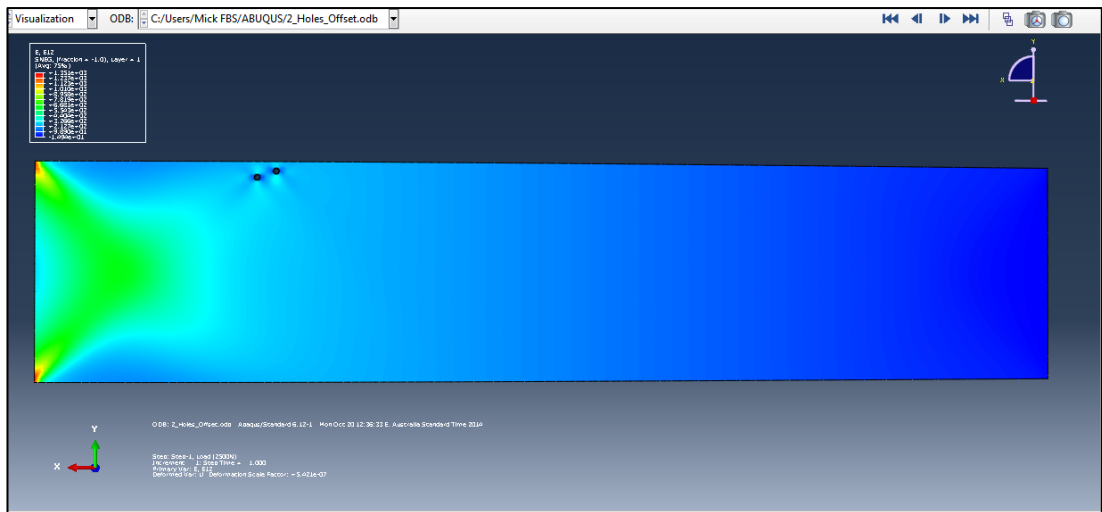


Figure 134. Test 8 FEA simulation results overview.

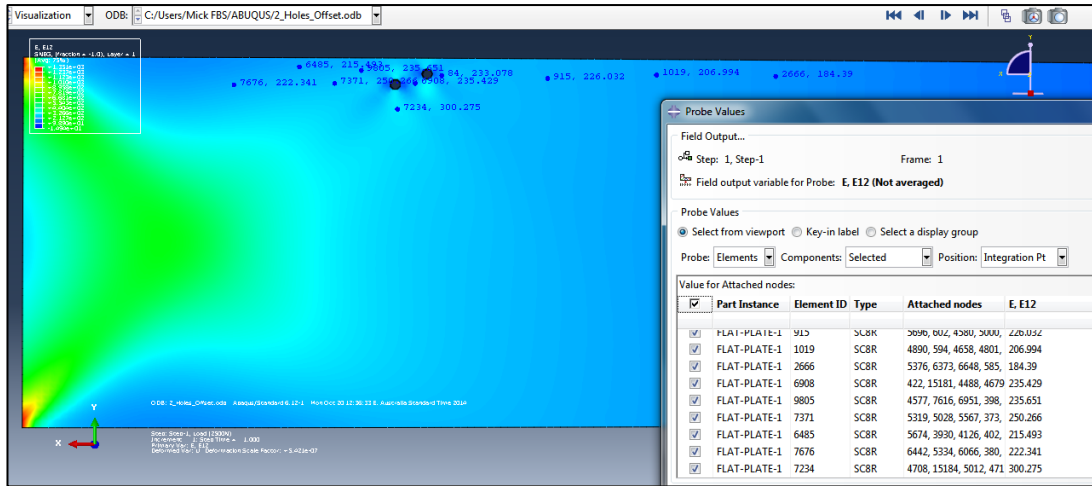


Figure 135. Test 8 FEA simulation micro-strain values.

Simulation of Test 9, comprising of three complete 8.0 mm through holes (one offset) yielded the following results as detailed within the Probe Value window.

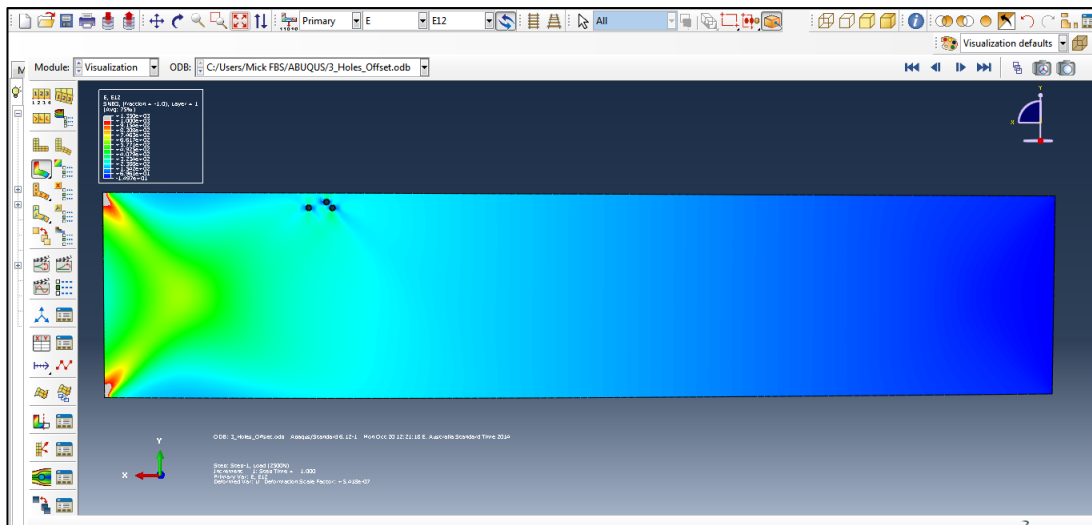


Figure 136. Test 9 FEA simulation results overview.

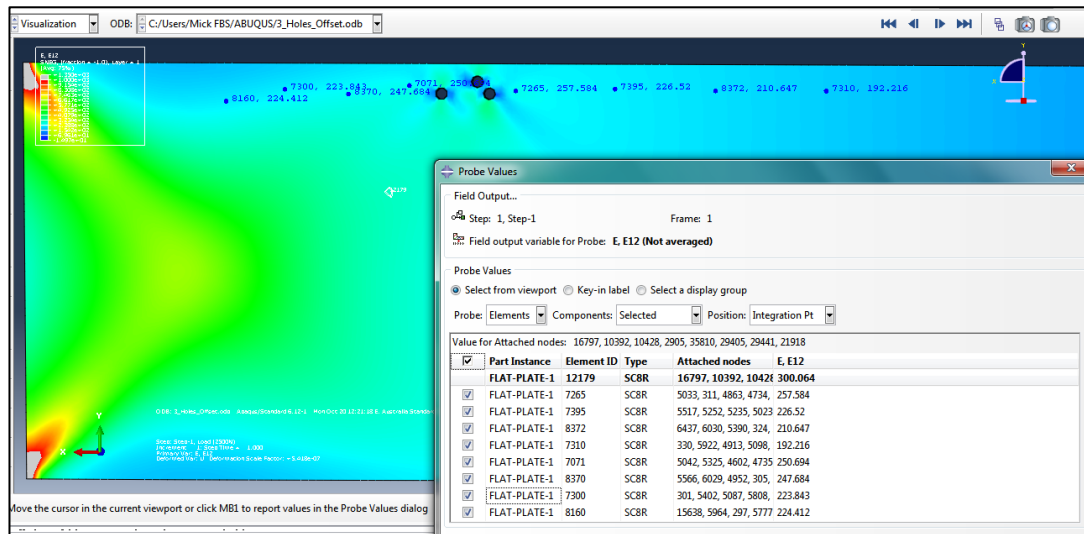


Figure 137. Test 9 FEA simulation micro-strain values.

Moving from left to right on the above plots the intensity of the strain increases as the distance approaching the damage decreases. Within very close proximity to the damage site, the strain level again decreases prior to increasing as the distance once again increases whilst moving away from the damage, before once again decreasing and stabilising over the remaining length of the model.

This again explains and confirms the greater strain experienced by the FBG when compared to that of the strain gauge position #1 due to the FBG being physically located closer to the damage site.

This was consistent for all flat plate FEA simulations, and largely validates both the FBG and strain gauge reading trends as correct. Table 38 is a comparison of micro-strain results for the FBG and flat plate FEA for Tests 4 - 7.

Table 38. FBG and flat plate FEA results comparison.

	FBG Results ($\mu\epsilon$)	Flat Plate Approximated Results ($\mu\epsilon$)
Test 4	436.57	247.86
Test 5	469.95	254.86
Test 6	534.96	271.87
Test 7	516.92	268.79

The general trend for the flat plate FEA simulation is an increase in strain levels within the approximate area of the FBG as damage levels are increased. Whilst the micro-strain values are significantly reduced, these results again correlate trend-wise with those obtained via the physical testing.

CHAPTER 16 - DISCUSSION

This chapter discusses the results of the project, interprets and explains these results in detail, and compares the results to the aim of the project. Limitations and improvements to the project are also discussed.

16.1 Interpretation of Results

Detailed results of the project research are contained within Chapter 15 – Results, and Appendices G through O; however, considering the scope of the research project, comparison of the FBG micro-strain data results to that of the number one strain gauge data results and their analysis is of primary significance.

The outcomes used the results of the physical testing and FEA for comparison of the obtained data. The following determinations were concluded:

1. The physical testing determined that strain was experienced at all sensor locations on the blade test section in the correct sense and magnitude, which was confirmed by FEA methods (to a limited extent at some locations).
2. The FBG system was able to detect small, incremental damage level increases on an opposing surface within a complex composite structure, indicating its suitability for such SHM applications.
3. The FBG system was able to detect large, incremental damage level increases in a complex composite structure, indicating its suitability for such SHM applications.
4. The FBG system response was able to be validated by the strain gauge system and FEA methods.

5. FEA is not a suitable method for the modelling of small arms ballistic damage in complex composite structures. This is due to the random and complex nature of the damage being difficult to accurately model. As such FEA is not an appropriate method from which ‘quick-time’ airworthiness or structural integrity decisions should be made, in particular in a field environment.
6. FEA is not an appropriate method for the in-service SHM of composite rotor blades due to the random and complex nature of small arms ballistic damage being difficult to accurately model. This in turn produces un-reliable modelling results of damage propagation.
7. FBG sensor systems may be an appropriate method for real-time, in-service SHM of complex composite structures with further research. However, they may be best suited to in-service lifing reductions when components such as rotor blades are utilised outside of their design usage spectrum for extended periods, such as during high tempo military operations.

16.2 Comparison with the Project Aim

The projects aim as detailed in the specification was to, ‘*...investigate the use of fibre-optic (FBG) sensors in the structural health monitoring of a fully fibre-composite constructed, battlefield helicopter rotor blade (CH47 Chinook) via the use of FEA modelling, vibration and fatigue testing for both pre and post simulated battlefield damage*’.

This was to be achieved via the following programme:

1. Research helicopter rotor blade construction, maintenance, dynamic loading, fatigue, stresses and strains.
2. In particular, research CH47 Chinook (medium lift) battlefield helicopter mission profiles and loads, construction, typical battlefield damage and published OEM damage criteria.

3. Create an appropriate FEA model using CREO 2.0 and/ or Abaqus software via physical measurement and profiling of the rotor blade.
4. Manufacture appropriate rotor blade testing clamp and jig.
5. Conduct structural testing to validate FEA model using FBG sensors via the use of dynamic analysis in parallel with static testing.
6. Inflict appropriate simulated battlefield damage on rotor blade (physical) and modify FEA model to reflect this damage.
7. Re-conduct structural testing to validate FEA model using FBG sensors via the use of dynamic analysis in parallel with static testing.

As time permits:

1. Conduct testing of distributed and point loading and vibration assessments of undamaged rotor blade.
2. Conduct testing of distributed and point loading and vibration assessments of damaged rotor blade.
3. Investigate to use of the FEA model for use by military engineers in the application of rapid damage assessment in a combat environment for 'emergency' flight approval.

This was an ambitious research project in terms of scope, but also in terms of technical application and resource requirements and management.

It is acknowledged that some of the specification requirements may not be fully met, and that the overall intent of the research may have been achieved in a differing manner to that initially envisaged. This was particularly the case for the physical testing for which the required resources were a critical and limiting factor.

Whilst the dynamic testing was unable to be achieved due to time constraints for usage of the CEEFC equipment, all static testing was successfully conducted in parallel to the FEA modelling for pre and post simulated battlefield damage.

This revised testing and modelling methodology proved adequate, yielding significant useable data and results from which direct correlations were able to be drawn as presented in previous chapters and the attached annexes.

16.3 Limitations and Improvements

A significant limitation to this research was its inherent complexity and scope.

The volume of tasks to be completed often conflicted with one another resulting in time management overlaps and additional resource coordination and management complexity. This was enlarged due to the lack of publically available material data and information, necessitating the requirement for unplanned tensile, flexural and calcination testing. Time management was also compounded by an unexpected delay in Abaqus FEA software access.

This research project was also restricted by the complexity of the rotor blade construction and the sophistication of the FEA required to model it. The developed FEA model was not able to accurately replicate the sensor system strain readings in all locations, and was only partially adequate as a verification method for these locations as a result. This included the ‘un-planned’ damage area. Whilst this was a limiting factor for this research, a significantly more accurate FEA model of the rotor blade would have been achieved with additional time allocation and research into the advanced use of the Abaqus software. This may be achieved for any future research.

Attempts at FEA modelling the random and severe ballistic damage as determined in ballistic testing was not achievable. Whilst it is possible to adequately model projectile impact on composite structures (Simula 2007), modelling of the resultant damage is very difficult. The very nature of the damage and applying it within a model is beyond the ability of FEA methods. This necessitates that damage be overly simplified within the model which in turn leads to inaccurate results.

The use of both FBG and strain gauge systems led to additional work both in the testing set-up phases and actual test conduct which significantly increased the data analysis complexity. Additionally, it added to the resource requirements and coordination of the research.

This research was limited to one FBG sensor located on the surface of the composite rotor blade, along the 00 axis. Further research is required to extend the methodology to multiple FBG systems on complex composite structures with a view towards imbedding these systems within the structure at manufacture.

16.4 Recommendations

The following recommendations are made as a result of this research:

1. Any future work in this area should begin with a comprehensive FEA model of the structure on which the FBG sensor system is to be assessed.
2. A solely fibre-optic FBG sensor system should be used as opposed to a dual FBG / strain gauge data collection methodology.
3. Additional FBG multiplexed systems should be applied to the structures surface.

This research has demonstrated that the use of fibre-optic FBG systems as a SHM tool within a complex damage and composite environment is a valid area for continued research. As a result it is the recommendation of this project that this research be continued into the future.

CHAPTER 17 – CONCLUSION & RECOMMENDATIONS FOR FUTURE RESEARCH

This chapter presents the conclusion and suggested areas of possible future research. These are based on the evaluation and key findings of the project, and where used to form the recommendations for future research which may be undertaken to build upon the findings of this research project.

17.1 Conclusion

A fibre-optical FBG system was applied to an internal surface of a fully composite constructed helicopter rotor blade test section for the purposes of evaluating the FBG as a SHM technique in such applications.

The FBG system was monitored, and validated by both an electrical strain gauge system and FEA methods.

The FBG and strain gauge locations were initially determined by identifying stress concentrations via FEA methods which were later modified by engineering judgment, physical access, application techniques and testing requirements.

The rotor blade test section was exposed to nine tests comprising of both cantilever and mid-point load applications. This application consisted of varying loads up to a maximum of 2500N at 500N intervals. In addition, varying degrees of incremental damage was applied at each test. Within this testing regime, data systems and test fixture quality checks were performed.

FEA models and methods were utilised to establish both a rotor blade test section assembly model and a D-spar surface ‘flat plate’ simulation as a verification tool for the physical testing. In order to establish the FEA models, blade geometric profiling along with physical tensile, flexural and calcination testing was conducted.

The resultant FBG and strain gauge systems test data was analysed and compared with that determined via FEA methods which found correlations across all three systems and methods.

Additionally, engineering intuition supported the majority of findings.

It was concluded that the research had revealed that fibre-optic FBG systems used in a complex damage and composite structure environment are a valid method for SHM and warrants additional future research.

17.2 Further Work

The following is recommended as possible future work:

1. Investigation of the use of multiple and multiplexed fibre-optic FBG sensor system on complex composite structure surfaces for strain sensing SHM applications.
2. Investigate the use of multiple and multiplexed fibre-optic FBG sensors for use as ‘live data acquisition’ for real-time SHM, both on and within complex composite structures.
3. Investigate the imbedding at component level manufacture of single, multiple and multiplexed fibre-optic FBG sensor systems within complex composite structures for strain sensing applications of SHM.

Additionally, the development of both ‘real-time’ SHM techniques and ‘at manufacture’ fibre-optic FBG system integration will be of interest to all composite fibre component manufacturers whom have an interest in the performance, lifing, safety and SHM of their product. This is particularly true for the civil and military aviation sectors.

LIST OF REFERENCES

- Aerospace metals, *Nickel Alloy*, viewed 20 May 2014, <http://www.aerospacemetals.com/nickel_alloy.html>.
- Airfoil Tools, 2014, *Boeing-Vertol VR-7 Airfoil with tab (vr7b-il)*, viewed 16 March 2014, <<http://airfoiltools.com/airfoil/details?airfoil=vr7b-il>>.
- Ashby, M 2007, *Materials : engineering, science, processing and design*, Elsevier Butterworth-Heinemann, Oxford.
- Askeland, D & Phule, P 2006, *The Science & engineering of materials*, 5th edn, CD-ROM, Nelson Cengage Learning.
- Askeland, D & Phule, P 2008, *The science and engineering of materials*, 5th edn, Cengage Learning, Stamford USA.
- ASM, *Failure Analysis Centre*, viewed 03 April 2014, <<http://products.asminternational.org.ezproxy.usq.edu.au/fahb/index.jsp>>.
- ASM Handbooks Online*, viewed 01 March - 12 April 14, <<http://products.asminternational.org.ezproxy.usq.edu.au/hbk/index.jsp>>.
- Augusta-Westland 2011, *Composite helicopter structures*, viewed 10 March 2014, <<http://www.ncn-uk.co.uk/uploads/Michael%20Overd.pdf>>.
- Boeing 2014, *CH-47D/F Chinook technical specifications*, viewed 20 February 2014, <<http://www.boeing.com/boeing/rotorcraft/military/ch47d/ch47dspec.page>>.
- Chandra, R, Chopra, I 1992, 'Structural response of composite beams and blades with elastic couplings' *Composite Engineering*, vol. 5, pp. 347-374.
- Charles, J & Crane, F 1989, *Selection and use of engineering materials*, 2nd edn, Butterworth & Co., Great Brittan.
- Cline, C et al 2011, 'Battle damage assessment method for composite rotor blades', *Proceedings of the 67th American Helicopter Society International Annual Forum 2011*, American Helicopter Society, Virginia Beach, USA.
- Chow-Shing, Shin et al, 2014, 'Post-impact fatigue damage monitoring using fiber bragg grating sensors', *Sensors*, vol. 14, no. 3, pp. 4144-4153, viewed 02 June 2014 <<http://www.mdpi.com/1424-8220/14/3/4144/htm>>.
- Daniel, I & Ishai, O 2006, *Engineering mechanics of composite materials*, 2nd edn, Oxford University Press, USA.

Doyle, C 2003, *Fibre Bragg Grating Sensors- An Introduction to Bragg Gratings and Interrogation Techniques*, Smart Fibres Ltd., viewed 20 March 2014, <<http://www.smartfibres.com/Attachments/Smart%20Fibres%20Technology%20Introduction.pdf>>.

Dragan, K, Polish Air Force Institute of Technology/Poland 2011, '*Structural health monitoring and damage detection of the helicopter main rotor blades with the structure integrated sensors*', paper presented to 7th DSTO International Conference on Health & Usage Monitoring, Australia, viewed 01 April 2014, <http://www.dsto.defence.gov.au/attachments/Dragan_K_Structural_Health_Monitoring_and.pdf>.

Erdogan, T 1997, Fiber Grating Spectra, *Journal of Lightwave Technology*, vol. 15, no. 8, pp 1277–1294 August.

Ertas, A & Jones, J 1996, *The engineering design process*, 2nd edn, John Wiley & Sons, USA.

Farrar, C & Worden, K 2006, *An introduction to structural health monitoring*, viewed 12 April 2014, <<http://rsta.royalsocietypublishing.org/content/365/1851/303.full.pdf>>.

Gordon Leishman, J & Johnson, B 2007, *Engineering Analysis of the 1907 Cornu Helicopter*, Department of Aerospace Engineering, University of Maryland, USA.

Groover, M 2007, *Fundamentals of modern manufacturing*, John Wiley & Sons, USA.

Hodgkinson, J 2000, *Mechanical testing of advanced fibre composites*, Woodhead Publishing Limited, Cambridge England.

Honeywell Aerospace 2005, *T55 turbo-shaft engine*, viewed 20 February 2014, <http://aerospace.honeywell.com/~media/UWSAero/common/documents/myaeroacecatalog-documents/Helicopters-documents/T55-L-714A__CH47_Engine_.pdf>.

International Organisation for Standardisation 1996, ISO 1172, *Textile-glass-reinforced plastics—Prepregs, moulding compounds and laminates — Determination of the textile-glass and mineral-filler content — Calcination methods*, ISO, Genève, Switzerland.

International Organisation for Standardisation 1998, ISO 14125, *Fibre-reinforced plastic composites – determination of flexural properties*, ISO, Genève, Switzerland.

International Organisation for Standardisation 1994, ISO 527-1, *Plastics — Determination of tensile properties — Part 1: General principles— Part 5*, ISO, Genève, Switzerland.

International Organisation for Standardisation 1997, ISO 527-4, *Plastics — Determination of tensile properties — Part 4: Test conditions for isotropic and orthotropic fibre-reinforced plastic composites— Part 4*, ISO, Genève, Switzerland.

International Organisation for Standardisation 1997, ISO 527-5, *Plastics – determination of tensile properties – Part 5*, ISO, Genève, Switzerland.

Kahandawa, G, Epaarachchi, J, Wang, H & Lau, K 2012, 'Use of FBG sensors for SHM in aerospace structures', *Photonic Sensors*, vol. 2, no. 3, pp. 203-214.

Karbhari, VM, Steenkamer, DA & Wilkins, DJ 1997, 'Application of Composite Materials to the Renewal of Twenty-First Century Infrastructure', 11th International Conference on Composite Materials , Australian Composite Structures Society, Gold Coast, Queensland, Australia.

Khalid, K et al 2012, Simulation and analysis of Gaussian apodized fibre Bragg grating strain sensor, University of Engineering & Technology - Taxila, Pakistan, viewed 12 May 2014, < <http://opticjourn.ifmo.ru/file/article/8229.pdf>>.

Kim, K 2004, *Analytical Calculation of Helicopter Main Rotor Blade Flight Loads in Hover and Forward Flight*, Army Research Laboratory, Aberdeen Proving Ground, USA.

Logan D 2012, *A first course in the finite element method*, 5th edn, Cengage Learning, USA.

Mandell et al 2003, Prediction of delamination in wind turbine blade structures, Montana State University, USA, viewed 27 May 2014, < http://www.coe.montana.edu/composites/documents/AIAA_2003_0697.pdf>.

Marks' 2008, *Standard handbook for mechanical engineers*, 11th edn, McGraw-Hill, USA.

Mathew, F et al 2000, Finite element modelling of composite materials and structures, Woodhead Publishing Ltd, Cambridge, England.

Office of regulatory services ACT, 2014, *Worksafe ATC*, viewed 20 May 2014, <<http://www.worksafe.act.gov.au/page/view/1432>>.

Paschotta, R 2013, *Fiber Bragg Gratings*, RP Photonics, viewed 23 April 2014, <http://www.rp-photonics.com/fiber_bragg_gratings.html>.

Pawar, P & Ganguli, R 2006, 'On the effect of progressive damage on composite helicopter rotor system behaviour', *Journal of Composite Structures*, vol. 78, January, pp. 410-423.

Simula 2007, *Projectile Impact on a Carbon Fiber Reinforced Plate*, viewed 23 August 2014, <<http://www.3ds.com/fileadmin/PRODUCTS/SIMULIA/PDF/tech-briefs/Aero-Projectile-Impact-on-a-Carbon-Fiber-Reinforced-06.pdf>>.

Smart fibres 2014, *Technology - fibre bragg grating*, viewed 17 April 2014, <<http://www.smartfibres.com/fibre-bragg-grating>>.

Smithsonian National Air and Space Museum 2014, *Inventing a flying machine*, viewed 12 April 2014 <<https://airandspace.si.edu/exhibitions/wright-brothers/online/fly/1903/>>.

Technica SA 2014, *Fiber Technology Sense the World*, viewed 15 August 2014 <http://www.technicasa.com/www/index.php/En/product_details/tid/119>.

U.S. Army 2002, *CH-47 Helicopter repairer supervisor*, Student Hand-Out, U.S. ARMY Aviation Logistics School, Virginia, USA.

University of Southern Queensland 2012, *MEC3203 Materials Technology Resource Book*, University of Southern Queensland, Toowoomba, Australia.

Wagners 2014, *Products & technical documents*, viewed 01 March 2014, <<http://www.wagnerscft.com.au/technical/>>.

Wood Solutions 2014, *Properties- White Cypress & Spotted Gum*, viewed 13 March 2014, <<http://www.woodsolutions.com.au/Wood-Species/white-cypress>>.

APPENDICES

Appendix A: Project Specification

ENG4111 / 4112 Research Project 2014 Project Specification

For: Mr Chris Snook

Topic: **USE OF FIBRE-OPTIC (FBG) SENSORS IN THE STRUCTURAL HEALTH MONITORING OF A BATTLEFIELD HELICOPTER ROTOR BLADE**

Supervisors: Dr Jayantha Epaarachchi

Enrolment: ENG 4111 Semester 1 2014
ENG4112 Semester 2 2014

Project Aim: This project seeks to investigate the use of fibre-optic (FBG) sensors in the structural health monitoring of a fully fibre-composite constructed, battlefield helicopter rotor blade (CH47 Chinook) via the use of FEA modelling, vibration and fatigue testing for both pre and post simulated battlefield damage.

Programme (v1.1 – 18 March 14):

1. Research helicopter rotor blade construction, maintenance, dynamic loading, fatigue, stresses and strains.
2. In particular, research CH47 Chinook (medium lift) battlefield helicopter mission profiles and loads, construction, typical battlefield damage and published OEM damage criteria.
3. Create an appropriate FEA model using CREO 2.0 and/ or Abaqus software via physical measurement and profiling of the rotor blade.
4. Manufacture appropriate rotor blade testing clamp and jig.
5. Conduct structural testing to validate FEA model using FBG sensors via the use of dynamic analysis in parallel with static testing.
6. Inflict appropriate simulated battlefield damage on rotor blade (physical) and modify FEA model to reflect this damage.
7. Re-conduct structural testing to validate FEA model using FBG sensors via the use of dynamic analysis in parallel with static testing.

As time permits:

1. Conduct testing of distributed and point loading and vibration assessments of undamaged rotor blade.
2. Conduct testing of distributed and point loading and vibration assessments of damaged rotor blade.
3. Investigate to use of the FEA model for use by military engineers in the application of rapid damage assessment in a combat environment for 'emergency' flight approval.

AGREED:

Student.

Date.

Supervisor.

Date.

Appendix B: Risk Management and Hazard Reduction

Division: University of Southern Queensland		Section/Unit: School of Mechanical & Electrical Engineers		
Document number 1	Initial Issue date 01 June 2014	Current version V1.0	Current Version Issue date 01 June 2014	Next review date N/A

For additional information refer to the publication *6 Steps to Risk Management* or the ACT OHS Commissioner's website - www.worksafety.act.gov.au .

Risk Assessment title:
ENG4111 - Final Year Project Risk Assessment - Manufacture and Testing Phases

Step 1: Identify the activity

Describe the activity:

- 1) Cutting of GFRP helicopter rotor blade.
- 2) Manufacture of hardwood timber blade test fixture.
- 3) Rotor blade sample tab preparation.
- 4) Tab flexural and tension testing.
- 5) Surface preparation of rotor blade for bonding of strain sensors.
- 6) Use of hydraulic test equipment - press.
- 7) Use of electrical data collection equipment.
- 8) Working in a workshop environment.

Describe the location where the activity occurs:

- 1) Army Aviation Center, Oakey, QLD
- 2) Own Home - garage, Toowoomba QLD
- 3) Own Home - garage, Toowoomba QLD
- 4) USQ Z9 laboratory, Toowoomba QLD
- 5) CEEFC Building P9, Toowoomba QLD
- 6) CEEFC Building P9, Toowoomba QLD
- 7) CEEFC Building P9, Toowoomba QLD
- 8) CEEFC Building P9, Toowoomba QLD

Step 2: Identify who may be at risk by the activity

- 1) One person may be at risk - self.
- 2) One person may be at risk - self.
- 3) One person may be at risk - self.
- 4) One or more may be at risk - primarily self, possible assistant or observers.
- 5) One or more may be at risk - primarily self, possible assistant or observers.
- 6) One or more may be at risk - primarily self, possible assistant or observers.
- 7) One or more may be at risk - primarily self, possible assistant or observers.
- 8) One or more may be at risk - primarily self, possible assistant.

Steps 3 to 7: Identify the hazards, risks, and rate the risks

1. An activity may be divided into tasks. For each task identify the hazards and associated risks.
2. List existing risk controls and determine a risk rating using the Risk Rating Table on page 4.
3. Additional risk controls may be required to achieve an acceptable level of risk. Re-rate the risk if additional risk controls used.

Tasks	Hazards (Step 3)	Associated risks (Step 4)	Existing risk controls	Risk rating with existing controls * (Step 5)			Additional risk controls required (Step 6) (Apply the hierarchy of risk controls)	Risk Rating with additional controls * (Step 7)		
				I	L	R		I	L	R
1) Cutting of GFRP helicopter rotor blade.	Cuts, abrasions from power tools. Eye damage from foreign objects. Inhalation of GFRP fibers and / or dust from cutting operation.	Tripping hazard. Crush hazards to feet from falling items.	Power tool guards in place. Safety glasses. General purpose filtration mask. Safety boots. Clean work area free of tripping hazards.	A	2	M	Perform in well-ventilated area.	A	2	M

<p>2) Manufacture of hardwood timber blade test fixture.</p>	<p>Cuts, abrasions from power tools.</p> <p>Eye damage from foreign objects.</p> <p>Inhalation of wood fibers and / or dust from cutting operation.</p> <p>Lifting of heavy objects (timber).</p>	<p>Tripping hazard.</p> <p>Crush hazards to feet from falling items.</p>	<p>Power tool guards in place.</p> <p>Safety glasses.</p> <p>General purpose filtration mask.</p> <p>Safety boots.</p> <p>Clean work area free of tripping hazards.</p> <p>Use appropriate lifting technique (ie bend at knees and hip, not back) and seek assistance as required.</p>	<p>A</p>	<p>2</p>	<p>M</p>	<p>Perform in well-ventilated area.</p>	<p>A</p>	<p>2</p>	<p>M</p>
<p>3) Rotor blade sample tab preparation.</p>	<p>Cuts, abrasions from power tools.</p> <p>Eye damage from foreign objects.</p> <p>Inhalation of GFRP fibers and / or dust from cutting operation.</p>	<p>Tripping hazard.</p>	<p>Power tool guards in place.</p> <p>Safety glasses.</p> <p>General purpose filtration mask.</p> <p>Safety boots.</p> <p>Clean work area free of tripping hazards.</p>	<p>A</p>	<p>2</p>	<p>M</p>	<p>Perform in well-ventilated area.</p>	<p>A</p>	<p>2</p>	<p>M</p>
<p>4) Tab flexural and tension testing.</p>	<p>Eye damage from foreign objects.</p>	<p>Tripping hazard.</p>	<p>Safety glasses.</p> <p>Clean work area free of tripping hazards.</p> <p>Follow established USQ workshop safety rules.</p>	<p>B</p>	<p>1</p>	<p>L</p>	<p>-N/A-</p>	<p>--</p>	<p>--</p>	<p>--</p>

<p>5) Surface preparation of rotor blade for bonding of strain sensors.</p>	<p>Eye damage from foreign objects.</p> <p>Inhalation of GFRP fibers and / or dust from cutting operation.</p> <p>Use of cyanoacrylate adhesives resulting in skin contact.</p>	<p>Tripping hazard.</p>	<p>Safety glasses.</p> <p>General purpose filtration mask.</p> <p>Safety boots.</p> <p>Use of protective gloves and PPE.</p> <p>Clean work area free of tripping hazards.</p> <p>Follow established USQ workshop safety rules.</p>	<p>B</p>	<p>1</p>	<p>L</p>	<p>Perform in well-ventilated area.</p>	<p>B</p>	<p>1</p>	<p>L</p>
<p>6) Use of hydraulic test equipment - press.</p>	<p>Eye or body injury from pressurized fluid.</p> <p>Crush injury from equipment movement.</p>	<p>Tripping Hazard.</p>	<p>Safety glasses and PPE.</p> <p>Safety boots.</p> <p>Employ safety distance and guards when equipment is in use.</p> <p>Clean work area free of tripping hazards.</p> <p>Follow established USQ workshop safety rules.</p>	<p>A</p>	<p>1</p>	<p>M</p>	<p>-N/A-</p>	<p>--</p>	<p>--</p>	<p>--</p>
<p>7) Use of electrical data collection equipment.</p>	<p>Electrical Shock.</p>	<p>Tripping Hazard.</p>	<p>Ensure equipment safety tag is present.</p> <p>Do not operate if in doubt.</p> <p>Clean work area free of tripping hazards.</p> <p>Follow established USQ workshop safety rules.</p>	<p>A</p>	<p>1</p>	<p>M</p>	<p>-N/A-</p>	<p>--</p>	<p>--</p>	<p>--</p>

8) Working in a workshop environment.	Tripping, crushing, cuts and abrasion, electrical shock and eye damage.		Wear appropriate PPE. Only use equipment for which training has been provided. Clean work area free of tripping hazards. Follow established USQ workshop safety rules.	A	2	M	-N/A-	--	--	--
Intentionally Left Blank										

* I = impact or consequence L = likelihood R = risk rating from the Risk Rating Table (page 4)

Step 8 Documentation and supervisor approval

Completed by: (name)	(signature)	Authorised by: (name)	(signature)	Date:
----------------------	-------------	-----------------------	-------------	-------

Step 9: Implement the additional risk controls identified

Indicate briefly what additional risk controls from Step 6 above were implemented, when and by whom.		
Risk control: Be conversant with all relevant USQ facility safety requirements.	Date: 01 June 2014	Implemented by: M. Fairbanks-Smith

Step 10: Monitor and review the risk controls

It is important to monitor risk controls and review risk assessments regularly. Review is required when there is a change in the process, relevant legal changes, and where a cause for concern has arisen. Reviews could be scheduled on an annual basis. If the risk assessment has substantially changed a new risk assessment is warranted.		
Review date: 01 June 2014	Reviewed by: M. Fairbanks-Smith	Authorised by:
Review date:	Reviewed by:	Authorised by:

ACT OHS Commissioner OHS Risk Rating Table

IMPACT: Catastrophic Major Moderate Minor Insignificant	<i>How severely could someone be hurt</i> death or permanent disability to one or more persons hospital admission required medical treatment required first aid required injuries not requiring first aid
LIKELIHOOD: Almost certain Likely Possible Unlikely Rare	<i>How likely are those consequences?</i> expected to occur in most circumstances will probably occur in most circumstances could occur at some time is not likely to occur in normal circumstances may occur only in exceptional circumstances

IMPACT	LIKELIHOOD				
	Rare 1	Unlikely 2	Possible 3	Likely 4	Almost Certain 5
Catastrophic A	M	M	H	C	C
Major B	L	M	M	H	C
Moderate C	L	M	M	M	H
Minor D	L	L	M	M	M
Insignificant E	VL	VL	L	L	M

Risk level	Required action
Critical	<u>Act immediately:</u> The proposed task or process activity must not proceed. Steps must be taken to lower the risk level to as low as reasonably practicable using the hierarchy of risk controls.
High	<u>Act today:</u> The proposed activity can only proceed, provided that: <ul style="list-style-type: none"> (i) the risk level has been reduced to as low as reasonably practicable using the hierarchy of risk controls; (ii) the risk controls must include those identified in legislation, Standards, Codes of Practice etc. (iii) the risk assessment has been reviewed and approved by the Supervisor and (iv) The supervisor must review and document the effectiveness of the implemented risk controls.
Medium	<u>Act this week:</u> The proposed task or process can proceed, provided that: <ul style="list-style-type: none"> (i) the risk level has been reduced to as low as reasonably practicable using the hierarchy of risk controls; (ii) the risk assessment has been reviewed and approved by the Supervisor.
Low	<u>Act this month:</u> Managed by local documented routine procedures which must include application of the hierarchy of controls.
Very Low	<u>Keep a watching brief:</u> Although the risk level is low the situation should be monitored periodically to determine if the situation changes.

Hierarchy of controls

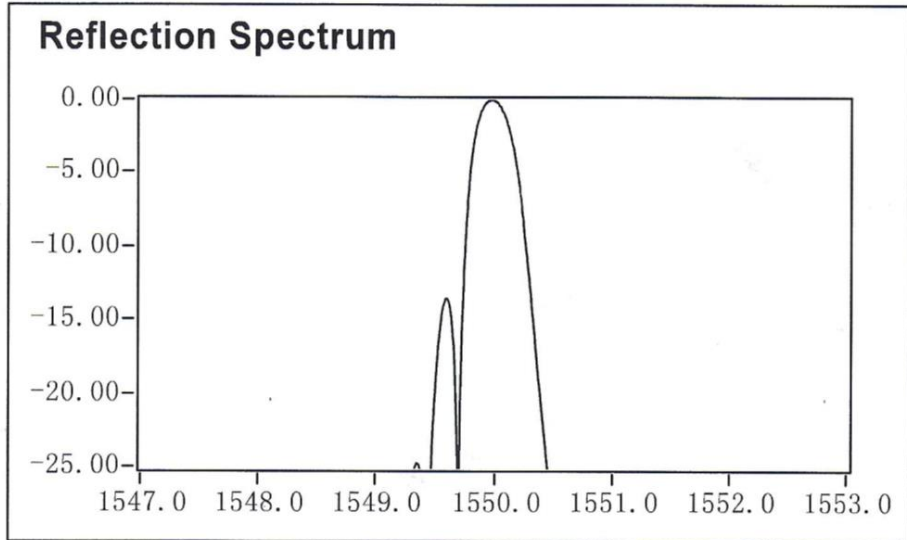
1	Eliminate the hazard — remove it completely from your workplace.	<i>If this isn't practical, then...</i>
2	Substitute the hazard — with a safer alternative.	<i>If this isn't practical, then...</i>
3	Isolate the hazard — as much as possible away from workers.	<i>If this isn't practical, then...</i>
4	Use engineering controls — adapt tools or equipment to reduce the risk.	<i>If this isn't practical, then...</i>
5	Use administrative controls — change work practices and organisation.	<i>If this isn't practical, then...</i>
6	Use personal protective equipment (PPE) — this should be the last option after you have considered all the other options for your workplace.	

Appendix C: Fibre Bragg Grating Data Sheet

Technica SA

S/N: *101121106075*

Test Type: FIN



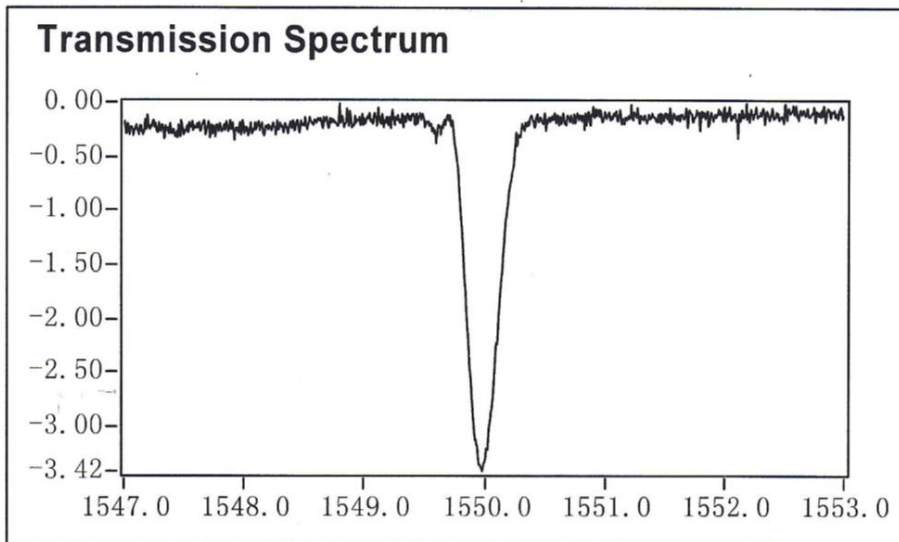
RCWL@-3dB: 1549.99 nm

TCWL@-3dB: 1549.99 nm

RBW@-3dB: 0.33 nm

FWHM: 0.34 nm

Reflectivity: 54.501 %



Appendix D: Strain Gauge Data Sheet

KYOWA		MADE IN JAPAN	
TYPE	KFG-20-120-C1-11L3M2R		
GAGE FACTOR (24°C,50%RH)	2.05 ± 1.0%	LOT No. Y4191S	BATCH 089A N09
GAGE LENGTH	20 mm	TEMPERATURE COEFFICIENT OF GAGE FACTOR	+0.008 %/°C
GAGE RESISTANCE(24°C,50%RH)	120.4 ± 0.4 Ω	APPLICABLE GAGE CEMENT	CC-33A, EP-34B
ADOPTABLE THERMAL EXPANSION	11.7 PPM/°C	QUANTITY	10

KYOWA STRAIN GAGES

共和ひずみゲージのお取扱いは裏面をご覧ください。
See the back of package for installation of Kyowa strain gages.



KYOWA

STRAIN

GAGES

株式会社 共和電業

〒182-8520 東京都調布市調布ヶ丘3-5-1
TEL : 042-488-1111(大代) FAX : 042-481-3258
URL : <http://www.kyowa-ei.co.jp>

KYOWA

KYOWA ELECTRONIC INSTRUMENTS CO., LTD.
3-5-1, Chofugaoka, Chofu, Tokyo, 182-8520, Japan
Phone : +81-42-488-1111 Fax : +81-42-481-3258
URL : <http://www.kyowa-ei.com>



表紙, 台紙



外袋 : PP
ゲージ保護シート : PET
接着用フィルム : PE

Appendix E: USQ Glass Content Performa

Glass Content Test

ISO Standard - 1172 Determination of Glass Content



Client Sample ID:		ROTOR BLADE SPAR SECTION		
Client:		M. FAIRBANKS-SMITH		
Test Date:		22-07-2014		
Crucible No	Dry Crucible Mass (g)	Initial Dry Total Mass Crucible & Specimen (g)	Final Calcinated Total Mass Crucible & Specimen (g)	Glass Content (%)
7	16.094	19.666	18.684	72.51
8	16.509	20.337	19.305	73.04
9	16.461	19.915	18.972	72.70
			AVG.	72.75
			S.D.	0.27

Calcination Temperature 575 °C ± 20°C

Sample Mass nominally 7grams

Lay-up Details Supplied: NO

Comments: (layup) LAYUP DETERMINED VIA VISUAL INSPECTION POST CALCINATION.

Signed: M. FAIRBANKS-SMITH
STUDENT



Appendix F: Flexural / Tensile Test Performa

Measure Sheet * SPAR SECTION ONLY						
CH-47 ROTOR BLADE TEST SHEET						
Test Standard:		ISO 14125:1998 & ISO 527				
Client Sample ID:						
Client:		M. FAIRBANKS - SMITH				
Test Date:		22 JUL 2014				
Specimen Orientation:		0° (TENSILE)		Cut Size:		
Specimen No	FLEXURAL, ISO 14125:1998 (mm)			TENSILE, ISO 527 (mm)		
	WIDTH	THICK.	SPAN	WIDTH	THICK.	LENGTH.
1	14.43	4.93	79.0	20.21	4.77	210
2	14.27	4.78	76.5	20.75	4.97	210
3	14.75	5.05	80.8	20.38	4.74	210
4				20.28	4.53	210
5						
6	SPAN = 79 (16 x 4.7)					
7	2 mm/min.					
8						
9						
10						
11						
12						

Temperature: 23 °C Humidity: 46 % R.H.

Notes: UNABLE TO SUPPLY 5x TEST SPECIMENS DUE TO MATERIAL QTY LIMITATIONS.

SPAN AVERAGE $\frac{(79.0 + 76.5 + 80.8)}{3} = 78.77 \approx 79.0 \text{ mm}$

Signed: [Signature]
Testing Officer
M. FAIRBANKS - SMITH

Appendix G: Test One Discussion

Test 1: Conditions, Data and Result Plots

The following information is applicable to the testing regime applied during Test 1 only.

This was largely a quality assurance (QA), confirmation test to ensure the both the FBG and strain gauge data collection system's integrity and operational ability.

Test Conditions

A physical test was conducted on the blade test section with the following conditions:

Table 39. Test 1 - General Conditions

	Details	Remarks
Load Range (N)	0 - 1500	Test not completed due FBG return signal not being present.
Max. Load (N)	1507.62	
Load Increment (N)	≈500	
Load Position (mm)	1500.0	
Adjustable Lower Support Position (mm)	100.0	
Max. Deflection	60.82	

No adjustable lower support extension was used for this test as it was positioned at the 100 mm minimum; however, it was noted that some deflection was occurring at the blade root clamp. This deflection was determined to be unacceptable from the clearance perspective with concerns that the blade tip may contact the fixture support beam.

Whilst this deflection was rectifiable with additional work to the test fixture, due to time constraints and equipment availability, the decision was made to relocate the adjustable lower support to 185.0 mm outboard from the root end clamp. This was applied to all subsequent testing regimes with the exception of Test 2 (mid-span load).

Following is an extract of data for the FBG peak and response signal. This data is for general background purposes only and is not provided in subsequent test annexes. The reason for this is the amount of data collect is significant and would total many pages.

As can be seen by the following FBG peak data, channel 4 (FBG channel) is displaying zeros. This was the initial indicator that a system fault was present:

Test Data (extract & not complete) – FBG Peak

Culture: en-AU
Date: 29/08/2014 11:23:05.38410
ENLIGHT Version: 1.5.54

Data Save Interval: 1
Timestamp Format: Full

Name:
Description:
Module Type: SM125
Mux Level: No Switch
HW Acquisition Rate: 2 Hz
Wavelength Tracking: 400 pm / acquisition
Normalized: True

IP Address: 10.0.0.122
Port: 50000

IDN: : sm125 v2, Rev 2.109, Date Created: Mon Nov 14 15:26:50 EST 2011
Image ID: 2.109
S/N: SIA9KC

CH 4 Configuration:
Distance Compensation Enabled: False
Spectral Average Count: 1
Threshold: -50.00 dB
Rel. Thresh.: -8.00 dB
Width Level: 3.00 dB
Width: 0.10 nm
Detect Valley: False

Timestamp	# CH 1	# CH 2	# CH 3	# CH 4
29/08/2014 11:23:06.49410	0	0	0	0
29/08/2014 11:23:06.99410	0	0	0	0
29/08/2014 11:23:07.49410	0	0	0	0
29/08/2014 11:23:07.99410	0	0	0	0
29/08/2014 11:23:08.49410	0	0	0	0
29/08/2014 11:23:08.99410	0	0	0	0
29/08/2014 11:23:09.49410	0	0	0	0
29/08/2014 11:23:09.99410	0	0	0	0
29/08/2014 11:23:10.49410	0	0	0	0
29/08/2014 11:23:10.99410	0	0	0	0...

The following FBG response data totalled some 16000 wavelength check point and often resulted in a matrix exceeding [16000 x 40]. Again for this reason only and indicative extract has been provided as follows:

Test Data (extract not complete) – FBG Response

Culture: en-AU
Date: 29/08/2014 11:23:07.22410

ENLIGHT Version: 1.5.54

Data Save Interval: 60
Timestamp Format: Full

Name:
Description:
Module Type: SM125
Mux Level: No Switch
HW Acquisition Rate: 2 Hz
Wavelength Tracking: 400 pm / acquisition
Normalized: True

IP Address: 10.0.0.122
Port: 50000

IDN: : sm125 v2, Rev 2.109, Date Created: Mon Nov 14 15:26:50 EST 2011
Image ID: 2.109
S/N: SIA9KC

CH 4 Configuration:
Distance Compensation Enabled: False
Spectral Average Count: 1
Threshold: -50.00 dB
Rel. Thresh.: -8.00 dB
Width Level: 3.00 dB
Width: 0.10 nm
Detect Valley: False

Wavelength Start (nm): 1510.00000
Wavelength Delta (nm): 0.0050
Number of Points: 16001

29/08/2014 11:23:08.48410

-42.23	-42.20	-42.26	-42.31	-42.36	-42.34	-42.25	-42.25	-42.34	-42.29	-42.37
-42.33	-42.22	-42.30	-42.30	-42.26	-42.26	-42.25	-42.23	-42.31	-42.29	-42.20
-42.26	-42.25	-42.22	-42.22	-42.25	-42.25	-42.16	-42.19	-42.21	-42.26	-42.25
-42.24	-42.24	-42.23	-42.17	-42.12	-42.22	-42.24	-42.21	-42.17	-42.19	-42.20
-42.25	-42.27	-42.24	-42.21...							

Result Plots

The following FBG plot does not detail a response shift due to initial system faults; however, the response data was collected as system verification. This is depicted below and does not demonstrate a peak shift due to the absence of a change in load magnitude at the time.

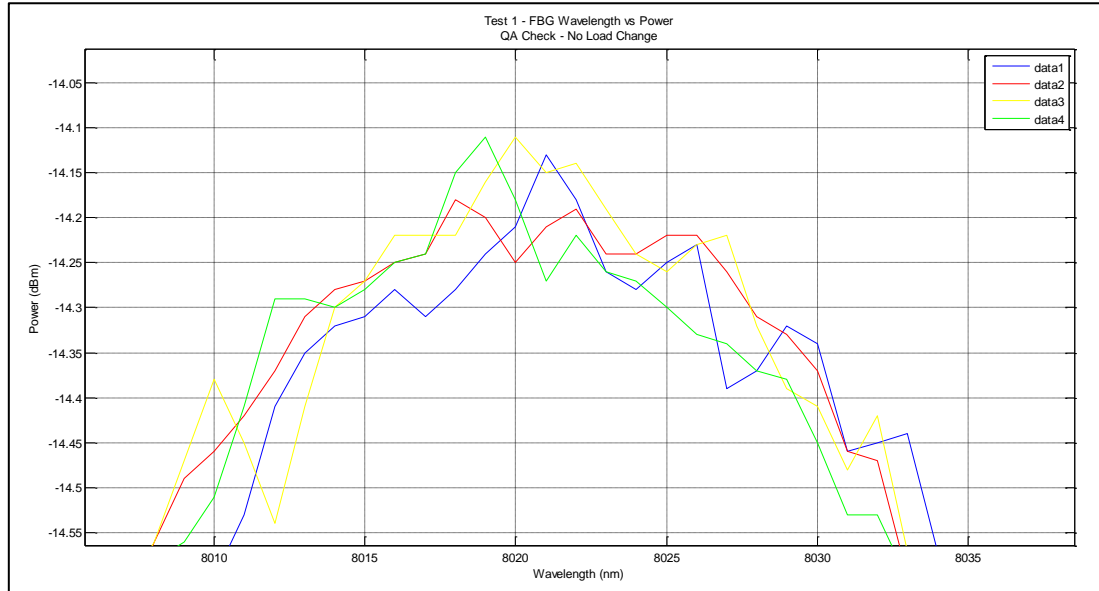


Figure 138. Test 1 plot of wavelength vs power.

Once all faults had been rectified the following plot at Fig. 139 was achieved which demonstrates a peak response shift from the left to the right, as to be expected in a tensile application.

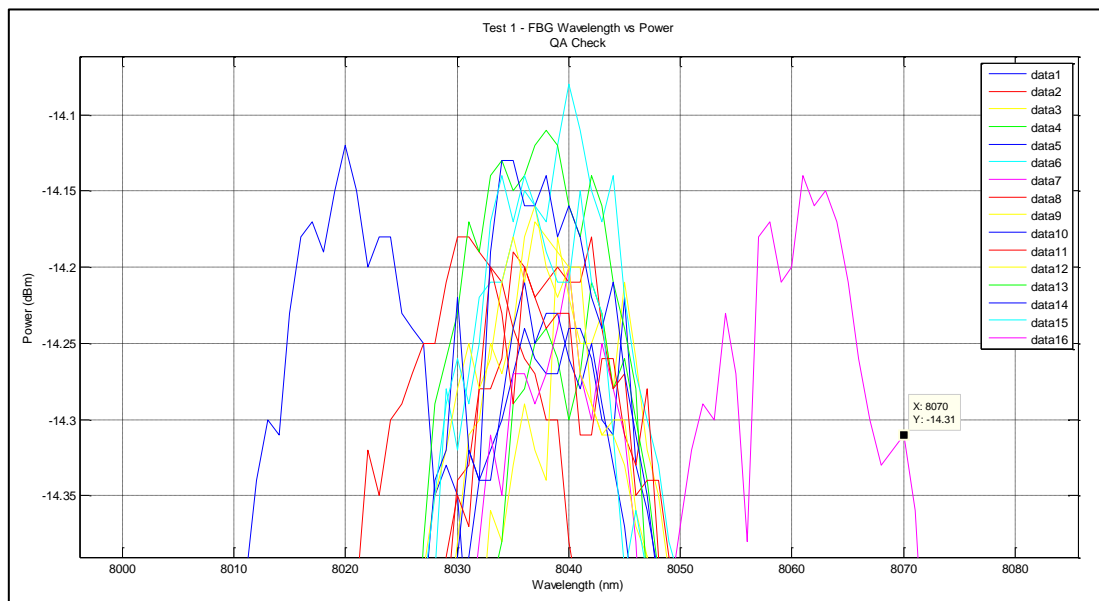


Figure 139. Test 1 plot of peak wavelength vs power.

This also confirmed the correct operation of the data acquisition system and display as seen in Fig. 140 below.

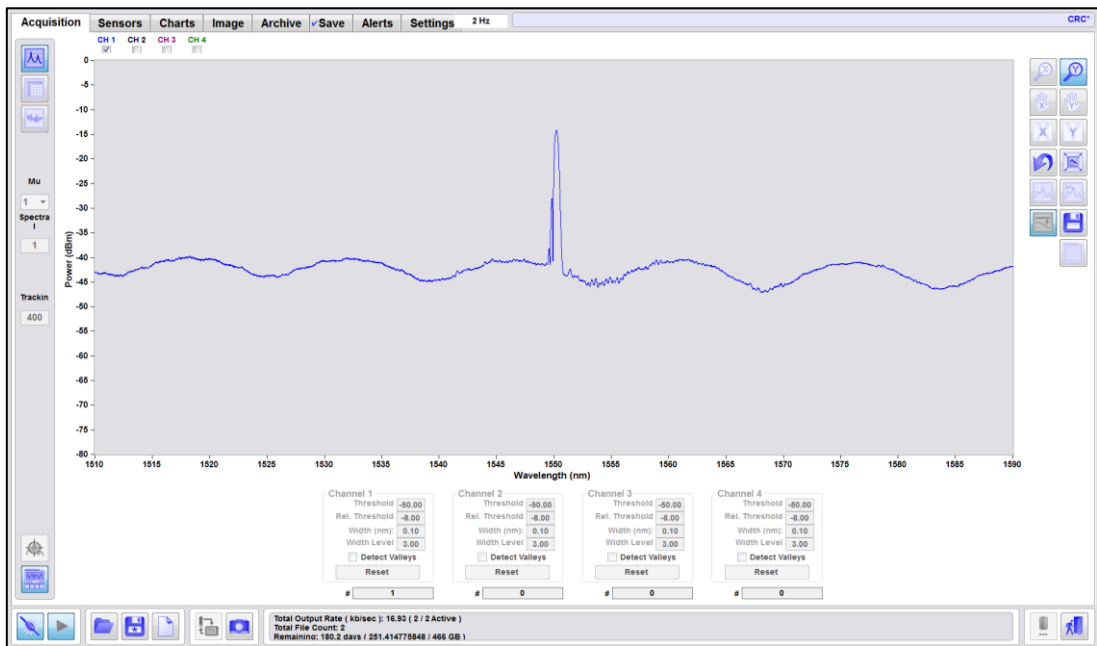


Figure 140. FBG data acquisition system display.

The following diagram is a screen capture of the strain gauge (SmartStrain) data acquisition system which was also verified as serviceable during the quality checks.

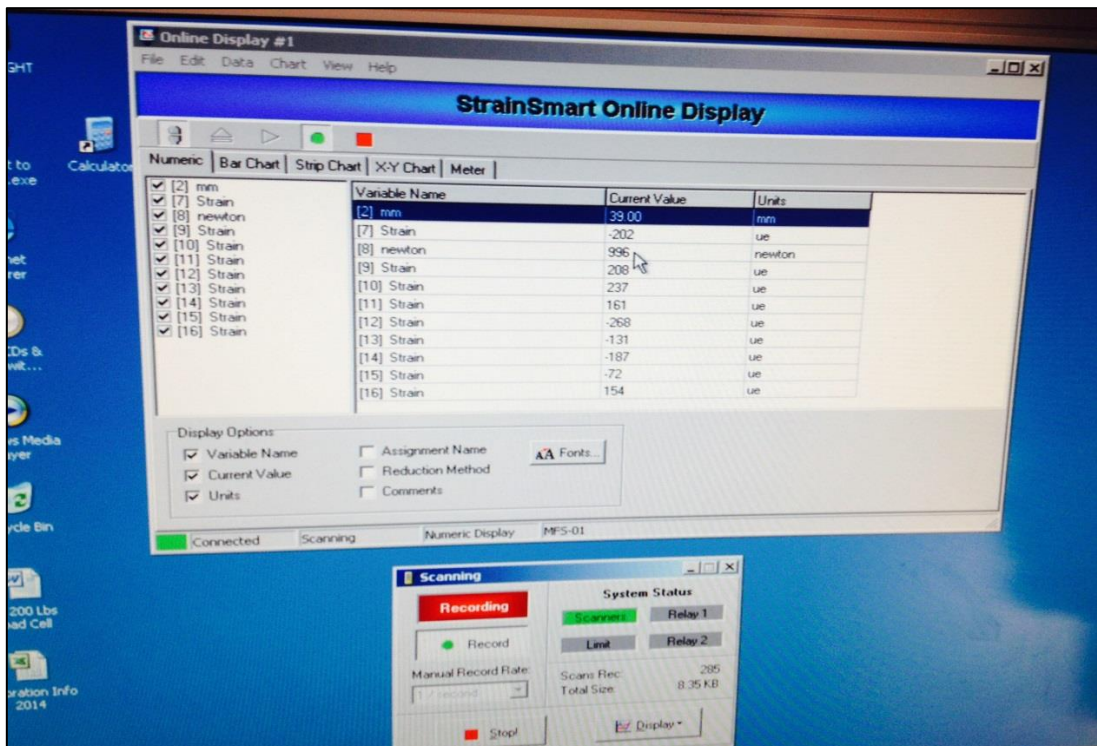


Figure 141. Strain gauge (SmartStrain) data acquisition system screen.

The following strain gauge plot indicates each relative gauge location and local strain ($\mu\epsilon$) at a given load and time. The red line indicates the load (N).

Figure 142 was created in MS Excel using the data collected via the SmartStrain software package, once imported and converted from a .TXT format.

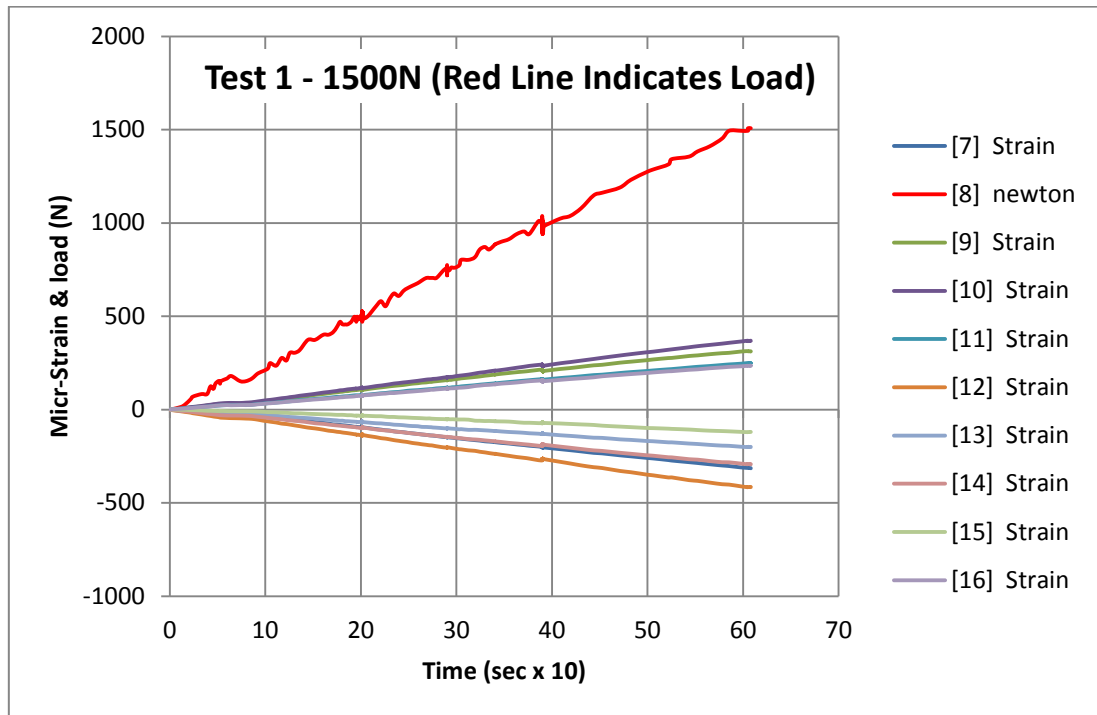


Figure 142. Test 1 – Load & strain gauge micro-strain ($\mu\epsilon$) plot.

The data collected post maximal deflection and load is omitted from the above style of plot (to include all subsequent test annex plots) as it is indicative only of a rapid decline in both strain and deflection as the load is removed and needlessly complicates the information. This is demonstrated in the following figure (which may or may not be included in subsequent test annexes).

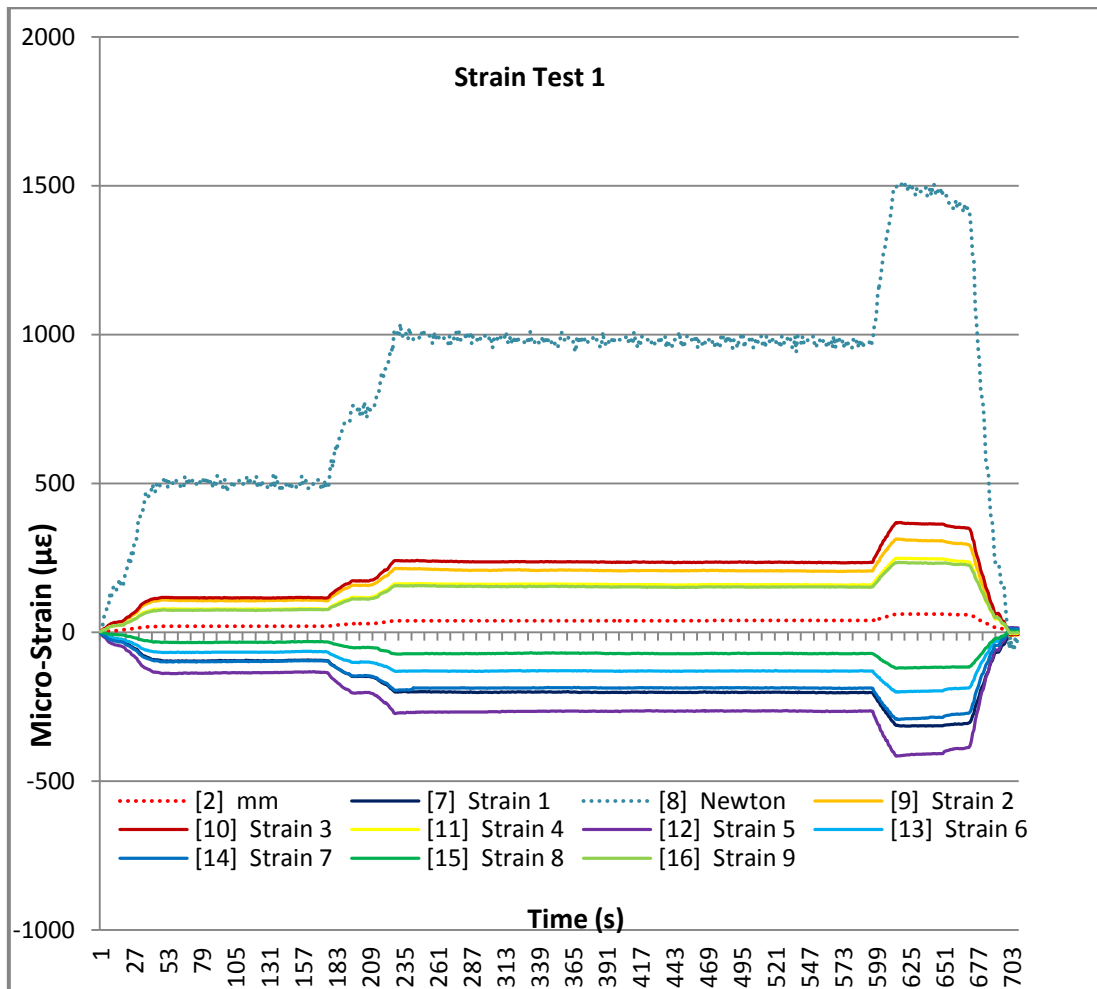


Figure 143. Test 1 – Load & strain gauge plot including load removal.

Test 1 Summary Table

The following table is a summary of the data collected during Test 1. Of particular interest is the comparison between the FBG and strain gauge at position #1 (SG #1); however, it must be remembered that they are located approximately 40.0mm apart in an axial orientation.

Table 40. Test 1 - data summary table.

Sensor Type / Location	Max. Load (N)	Max. Deflection (mm)	Max. Micro-Strain ($\mu\epsilon$)
FBG	1507.62	60.82	284.75 (Manually calculated from Fig. 2 data point)
SG #1			311.39
SG #2			-314.77
SG #3			368.06
SG #4			248.12
SG #5			-414.25
SG #6			-199.61
SG #7			-292.01
SG #8			-119.56
SG #9			234.58

Table 40 details several micro-strains readings as a negative value which is indicative of a compressive strain, whilst a positive return is a tensile strain.

Conclusions

It is clear from the FBG Peak data at channel four (CH 4) that no return signal was being received from the FBG. This was the result of defective fibre-optical extensions and initial data acquisition software set-up. These issues were rectified and the correction validated prior to subsequent testing regimes.

The strain gauge system functioned as expected with micro-strain sense being correct with respect to compression and tensile strains. These figures approximate the strains determined via FEA methods.

Appendix H: Test Two Discussion

Test 2: Conditions, Data and Result Plots

The following information is applicable to the testing regime applied during Test 2 only.

This was a mid-span applied load test. This test was used as both confirmation test and data collection test. It was anticipated that this test, having the load applied at the mid-point of the blade test section, would result in the strain gauges and FBG experiencing the strain in the opposite sense (ie. tension as opposed to compression).

In addition this test was used to confirm the FBG/ strain gauge and data collection system operation.

Test Conditions

A physical test was conducted on the blade test section with the following conditions:

Table 41. Test 2 - General Conditions

	Details	Remarks
Load Range (N)	0 - 2000	Test completed without fault. Data acquisition soft-ware adjustments from Test 1 verified.
Max. Load (N)	2033	
Load Increment (N)	500	
Load Position (mm)	750.0 (mid-span)	
Adjustable Lower Support Position (mm)	0.00	
Max. Deflection (mm)	17.25	

Result Plots

The following plots were prepared from the collected data, some of which may also be presented within the report main body.

Fig. 1 & 2 present the strain gauge data plots for all strain gauges with the micro-strain and load presented on the y axis.

The sense of most strain gauges changed from a tensile strain to a compressive strain reading and vice versa. This was expected, and verified against other test data, and is presented in the following figures.

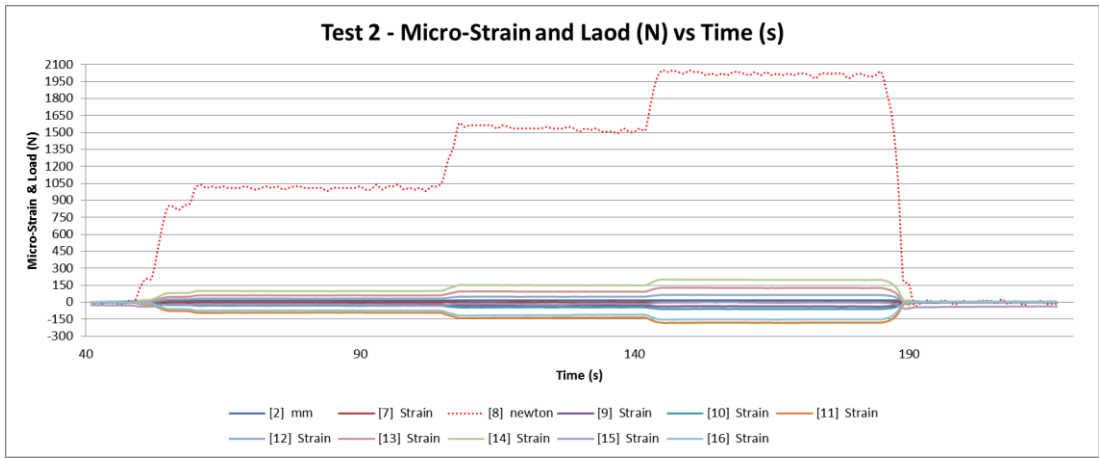


Figure 144. Test 2 – Load & strain gauge plot including load removal.

In particular channel seven [7] (strain gauge #1) in both Fig. 144 and 145 is reading a small compressive strain.

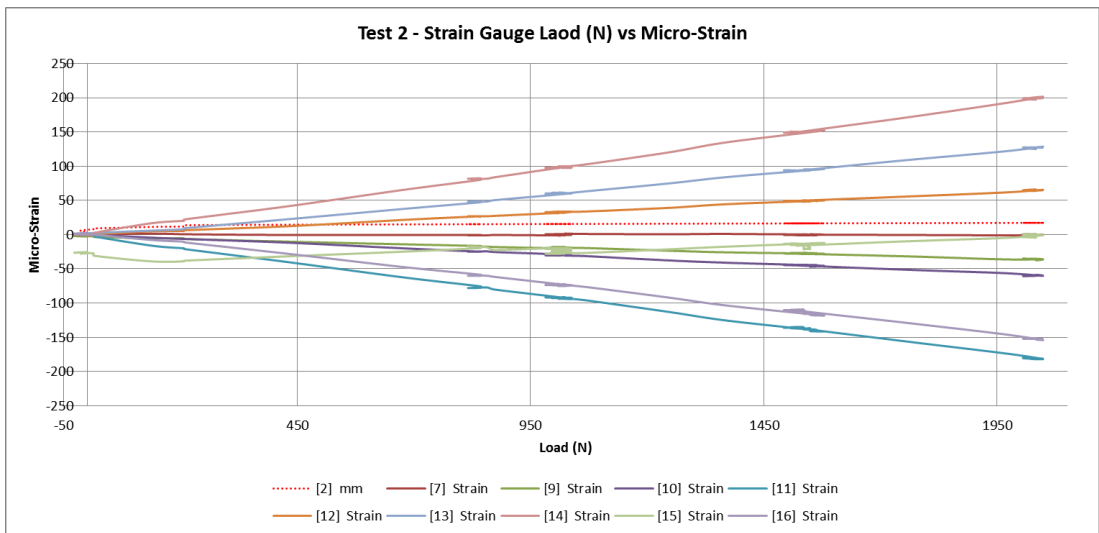


Figure 145. Test 2 – Load & strain gauge micro-strain ($\mu\epsilon$) plot.

Chanel [7] is the strain gauge located at position #1 and is use as the primary comparison strain gauge for the FBG results. This is due to its close proximity and the same axial orientation.

A comparison between channel [7] on the above plots and the following FBG data plots indicates a correlation of compressive strain for both systems.

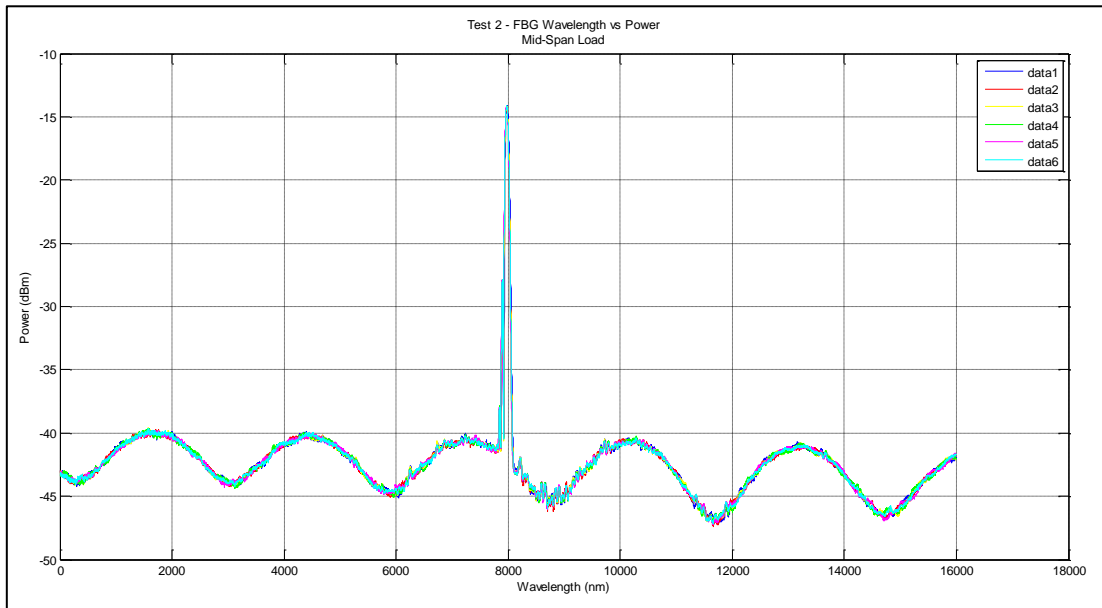


Figure 146. Test 2 - FBG wavelength vs power complete plot.

The following plot details the peak shift from right to left indicating a compressive strain being sensed by the FBG.

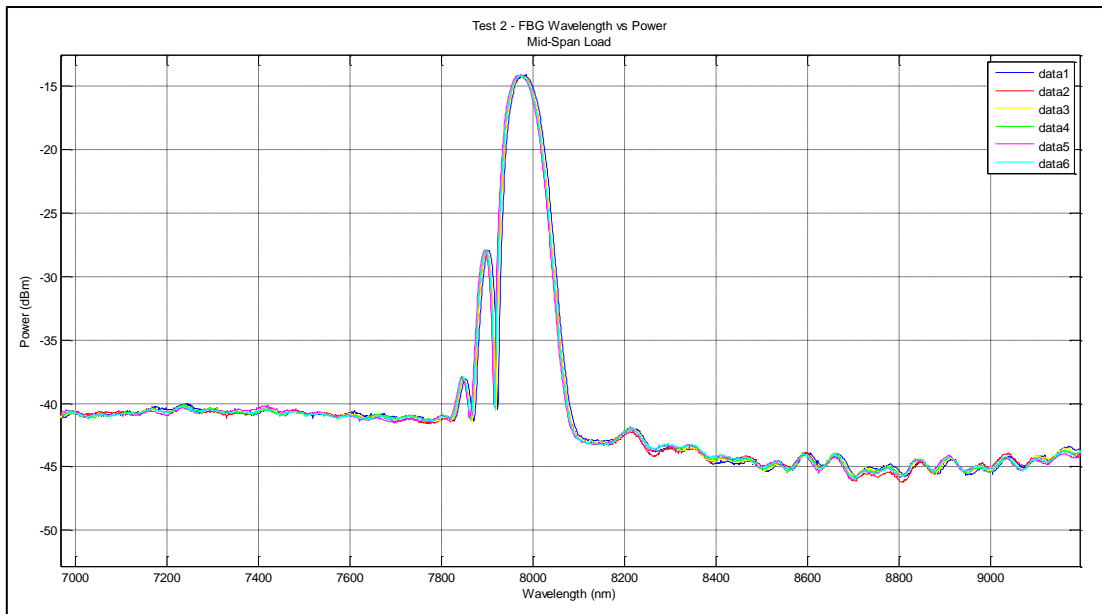


Figure 147. Test 2 - FBG wavelength vs power reduced scale plot.

The peak shift from right to left can clearly be seen in the following plot. In addition, chirping can be seen as indicated by the individual minor-peaks within this 'zoomed' plot.

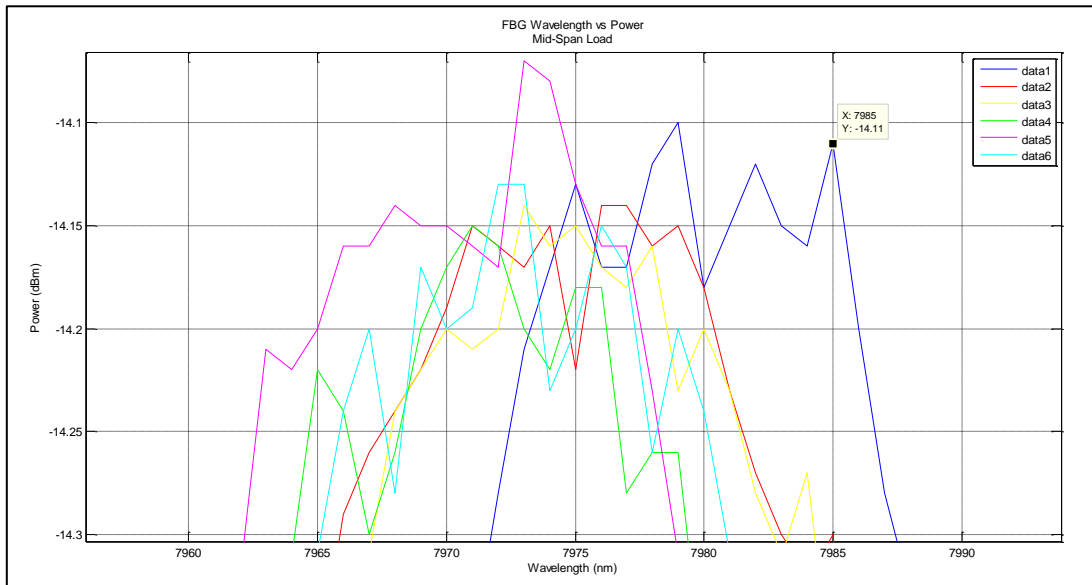


Figure 148. Test 2 - FBG wavelength vs power peak plot with chirping.

Test 2 Summary Table

The following table is a summary of the data collected during Test 2. Of particular interest is the comparison between the FBG and strain gauge at position #1 (SG #1); however, it must be remembered that they are located approximately 40.0mm apart in an axial orientation.

Table 42. Test 2 - data summary table.

Sensor Type / Location	Max. Load (N)	Max. Deflection (mm)	Max. Micro-Strain ($\mu\epsilon$)
FBG	2033.1	17.25	-51.16 (Manually calculated from Fig. 5 data point)
SG #1			-39.08
SG #2			-36.15
SG #3			-60.15
SG #4			-180.12
SG #5			64.48
SG #6			125.03
SG #7			197.33
SG #8			-4.39
SG #9			-151.8737

Table 42 details several micro-strains readings as a negative value which is indicative of a compressive strain, whilst a positive return is a tensile strain.

Conclusions

When compared with previous and subsequent data it is confirmed that the strain sense is opposite confirming correct operation of the strain gauge and FBG sensing systems.

Appendix I: Test Three Discussion

Test 3: Conditions, Data and Result Plots

The following information is applicable to the testing regime applied during Test 3 only.

This was the initial cantilevered applied load test. This test was used as both confirmation test and data collection test. Being the initial cantilevered test a lower load was applied in order to assess the testing fixture performance and deflection.

Test Conditions

A physical test was conducted on the blade test section with the following conditions:

Table 43. Test 3 - General Conditions

	Details	Remarks
Load Range (N)	0 - 1000	Test completed without fault.
Max. Load (N)	1051.18	
Load Increment (N)	1000	
Load Position (mm)	1500 (tip load)	
Adjustable Lower Support Position (mm)	185.0	
Max. Deflection (mm)	34.54	

This was the initial test with the adjustable lower support in the 185.0 mm position; as such as reduced load was applied (1000 N) as a precautionary intermediate step. As this load was achieved without issue it was determined that subsequent test loads will be incrementally increased to the pre-determined 2500 (N).

Result Plots

The following plots were prepared from the collected data, some of which may be presented within the report main body.

As mentioned this was the initial test with the revised adjustable lower support position, as such it was anticipated that the strain levels would begin to increase in all positions given the closer proximity around which a moment was created.

This proved to be the case, and all subsequent testing was performed with the adjustable lower support in the 185.00 mm position for uniformity.

The following plots are representative of a relatively slow load application and holding at a constant load for approximately 15 minutes whilst physical checks were again conducted on the test fixture.

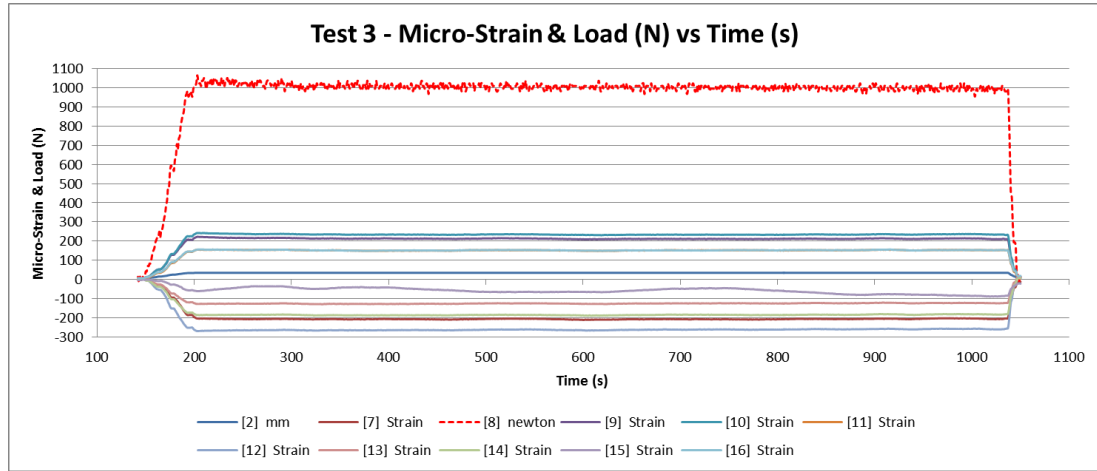


Figure 149. Test 3 – Load & strain gauge plot (1000N) including load removal.

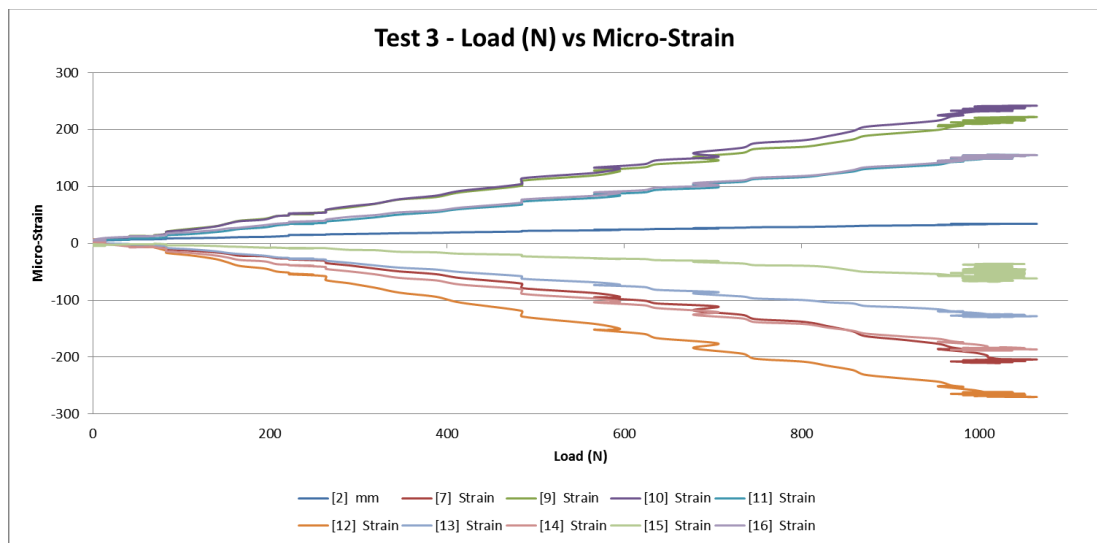


Figure 150. Test 3 – Load & strain gauge plot held at 1000N.

The above strain gauge plot has distinct repeating signals around the 1000N load mark. This is due to that load being held for a prolonged period.

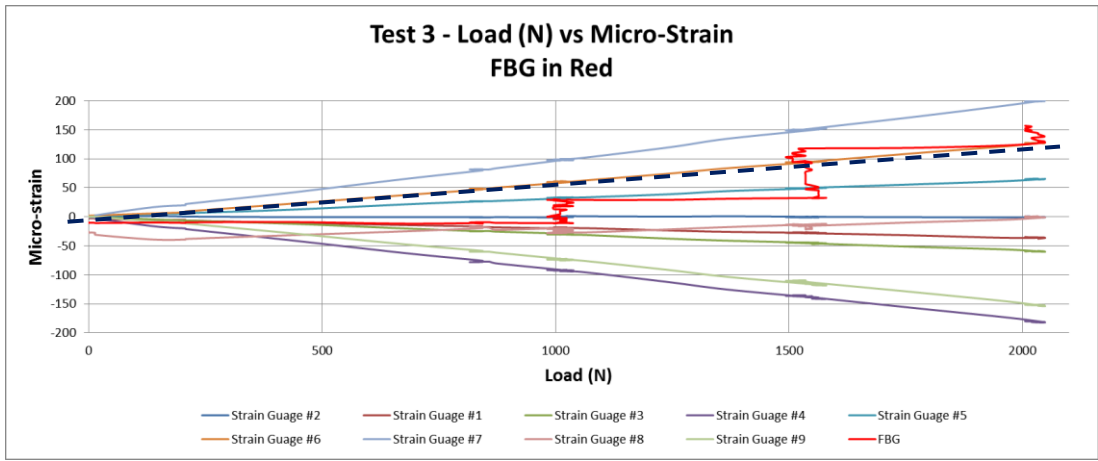


Figure 151. Test 3 – Load & strain gauge plot (1000N) FBG comparison.

It is unclear why the FBG data line in the FBG / strain gauge comparison above is stepped in nature. It is believed this is a result of the FBG data points having to be reduced by 60% in order to allow plotting with the strain gauge data. However, the mean line (---) presented once again indicates a correlation between the FBG and strain gauge #7 located in the number one position.

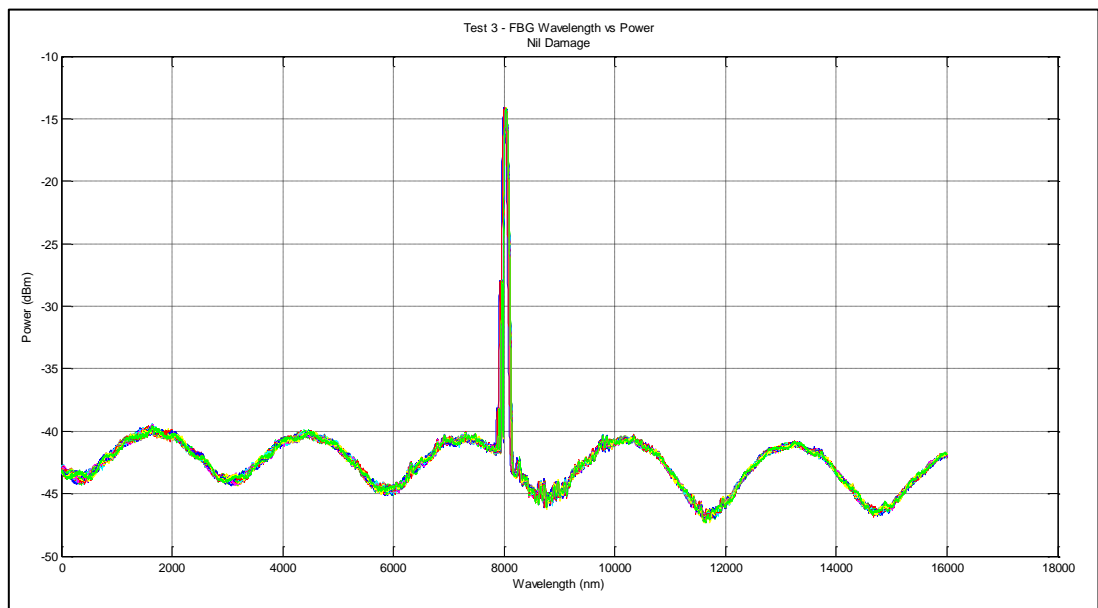


Figure 152. Test 3 - FBG wavelength vs power complete plot.

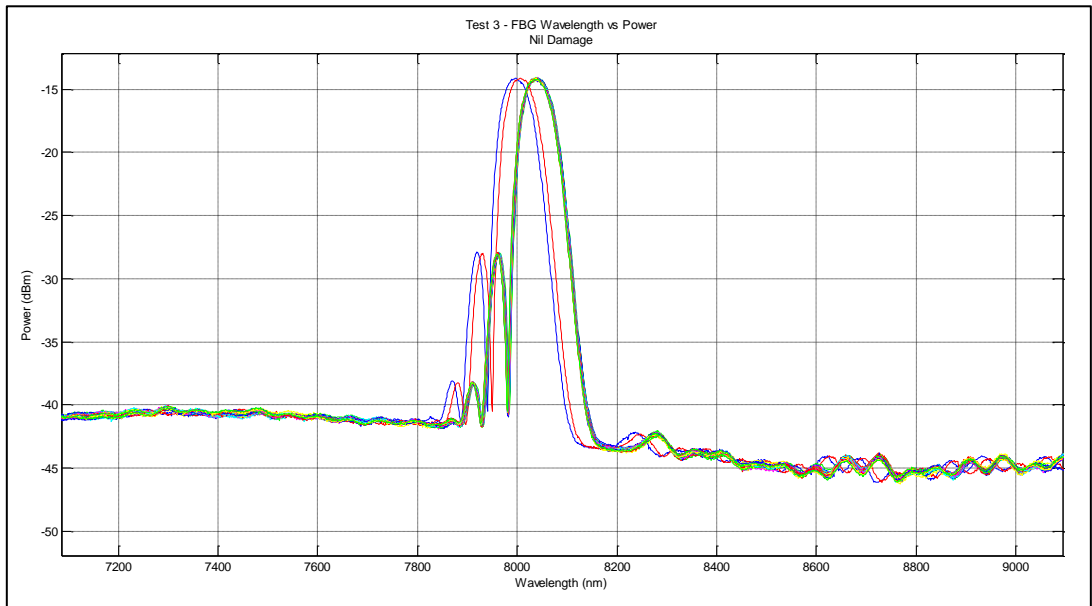


Figure 153. Test 3 - FBG wavelength vs power reduced scale plot.

The following figure details a peak shift from the left to the right again indicating a tensile strain being sensed by the FBG. The massing of peaks between the 8030 to 8050 wavelength range is a result of the load being held at 1000N over an extended period. Chirping is again evident.

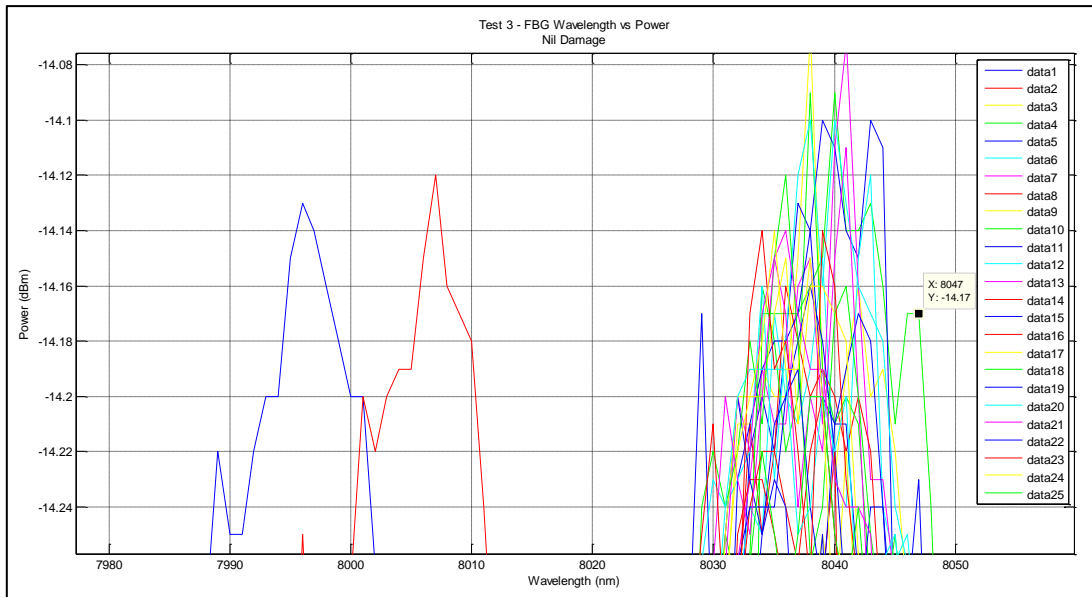


Figure 154. Test 3 - FBG wavelength vs power peak plot with massed response.

Test 3 Summary Table

The following table is a summary of the data collected during Test 3. Of particular interest is the comparison between the FBG and strain gauge at position #1 (SG #1); however, it must be remembered that they are located approximately 40.0mm apart in an axial orientation.

Table 44. Test 3 - data summary table.

Sensor Type /Location	Max. Load (N)	Max. Deflection (mm)	Max. Micro-Strain ($\mu\epsilon$)
FBG	1051.18	34.54	176.56
SG #1			211.63
SG #2			-208.90
SG #3			232.45
SG #4			150.42
SG #5			-265.04
SG #6			-126.91
SG #7			-187.85
SG #8			-65.03
SG #9			151.48

Table 44 details several micro-strains readings as a negative value which is indicative of a compressive strain, whilst a positive return is a tensile strain.

Conclusions

It was determined that the revised adjustable support location was appropriate for further testing and that the relocation had adequately resolved the flexure within the test fixture whilst maintaining adequate blade to main support clearance.

The data obtained from the test again confirmed that the FBG sensed strain was in close correlation to the strain gauge located in the number #1 position using the mean line.

Additionally, the results of this test confirmed that subsequent testing could be performed with a detailed focus on data collection with confidence in both the test fixture and data collection systems performance.

Appendix J: Test Four Discussion

Test 4: Conditions, Data and Result Plots

The following information is applicable to the testing regime applied during Test 4 only.

This was the second cantilevered applied load test and represented commencement of actual data collection. This test was used as a data collection test.

Test Conditions

A physical test was conducted on the blade test section with the following conditions:

Table 45. Test 4 - General Conditions

	Details	Remarks
Load Range (N)	0 - 2500	Initial data acquisition test. No simulated damage applied. Test completed without fault.
Max. Load (N)	2517.3	
Load Increment (N)	500	
Load Position (mm)	1500 (tip load)	
Adjustable Lower Support Position (mm)	185.0	
Max. Deflection (mm)	63.9	
Damage Depth (mm)	Nil	

Result Plots

The following plots were prepared from the collected data, some of which may be presented within the report main body.

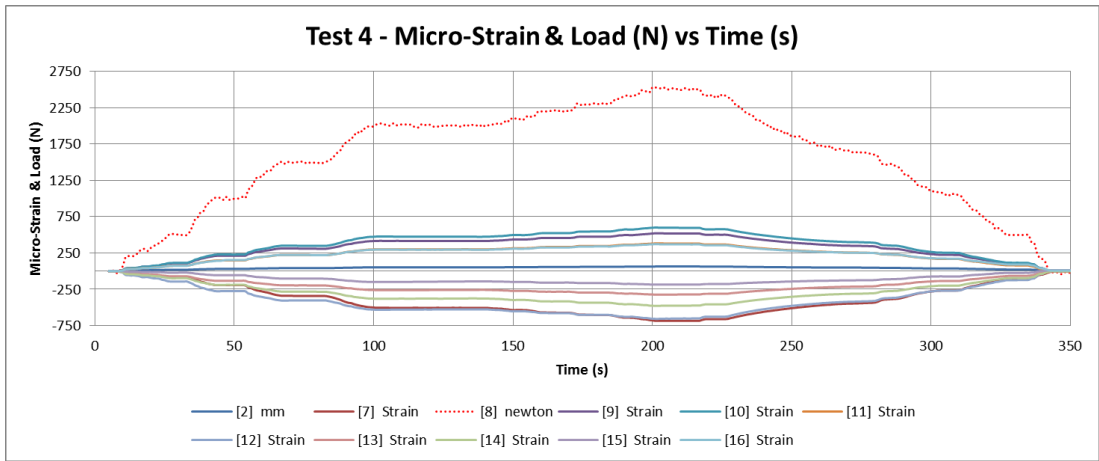


Figure 155. Test 4 – Load & strain gauge plot including load removal.

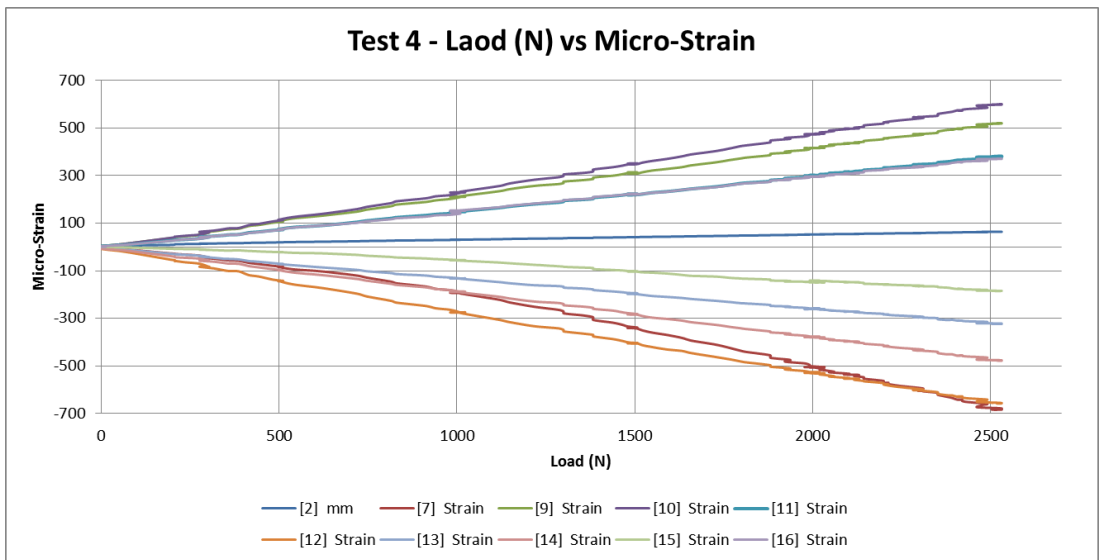


Figure 156. Test 4 – Load & strain gauge plot.

The following plot depicts the close correlation between the FBG and strain gauges in tension.

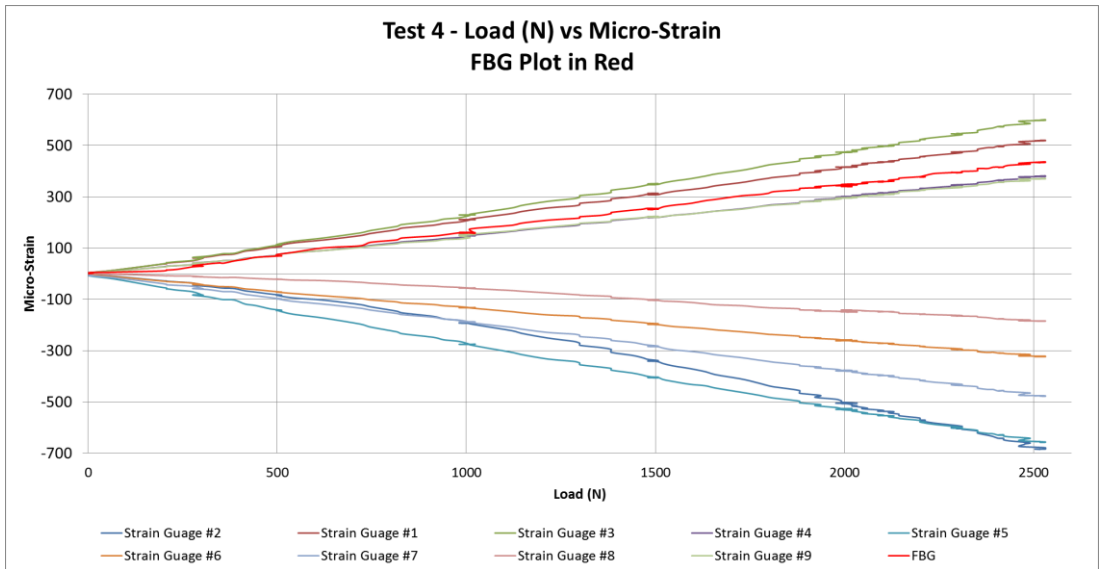


Figure 157. Test 4 – Load & strain gauge / FBG comparison plot.

The linear FBG line in the following plot again indicates a close correlation between the FBG and strain gauge #7, located in the number one position and being the closest FBG replicating strain gauge.

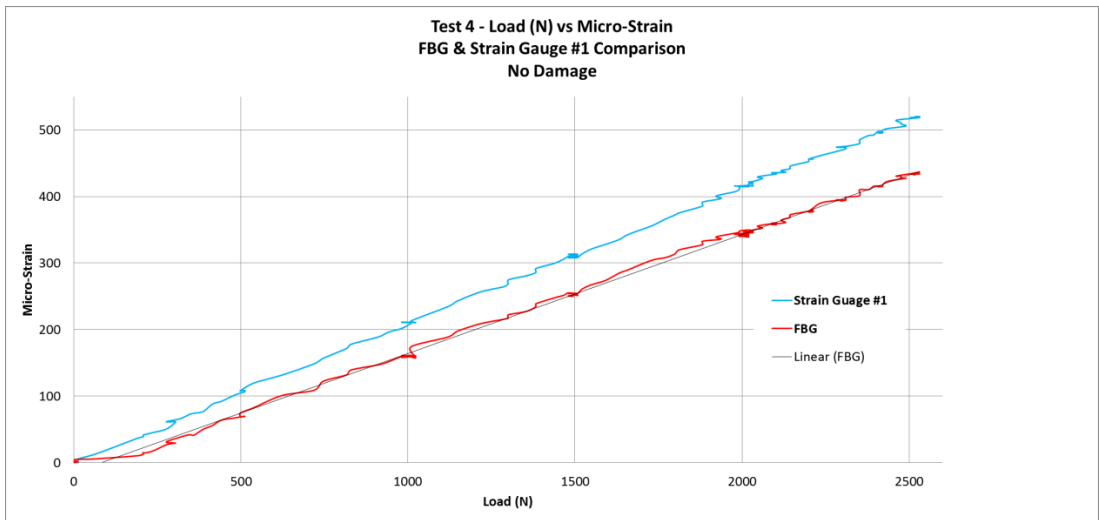


Figure 158. Test 4 - FBG and strain gauge #1 comparison.

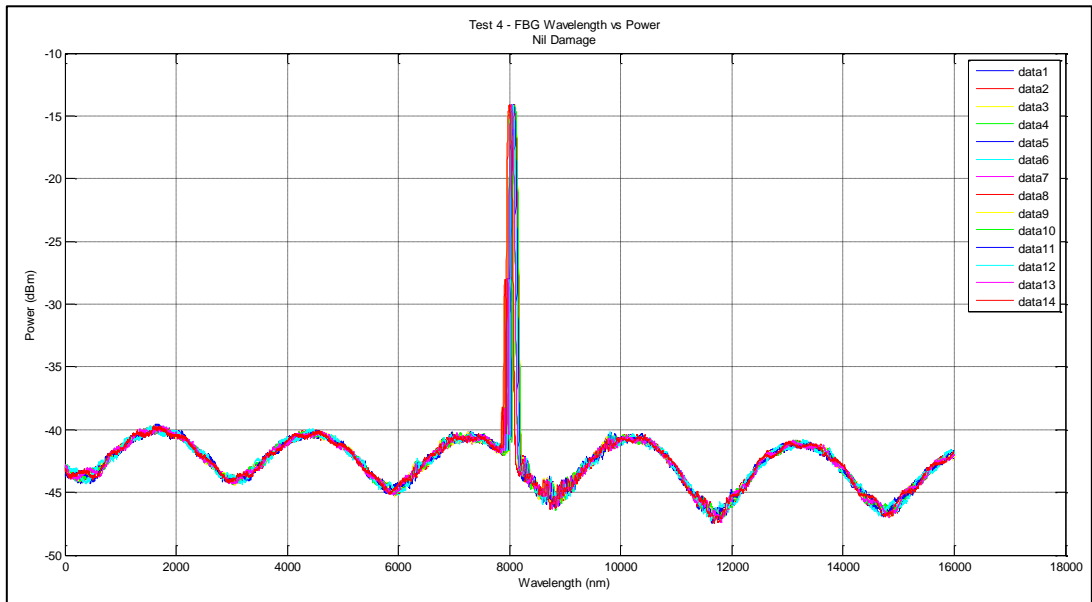


Figure 159. Test 4 - FBG wavelength vs power complete plot.

The following FBG plot depicts a peak shift from left to right indicating a tensile strain.

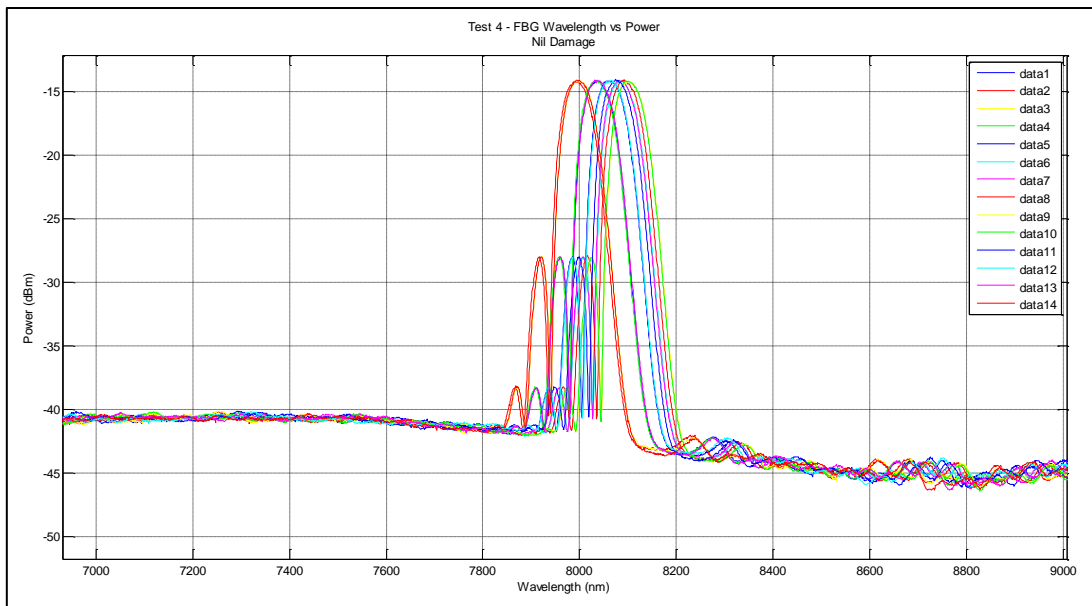


Figure 160. Test 4 - FBG wavelength vs power reduced scale plot.

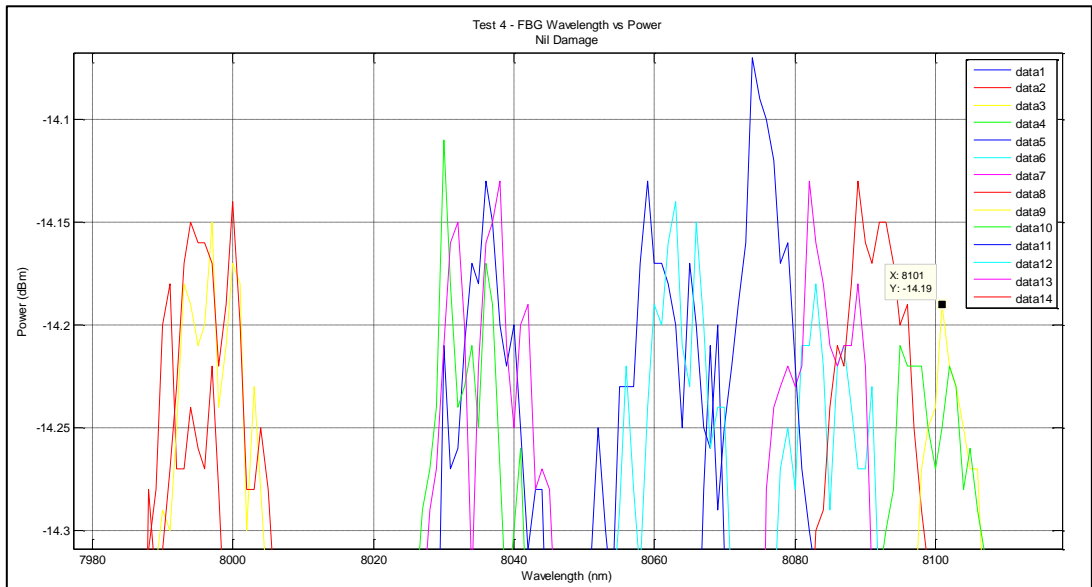


Figure 161. Test 4 - FBG wavelength vs power peak plot with massed response.

Test 4 Summary Table

The following table is a summary of the data collected during Test 4. Of particular interest is the comparison between the FBG and strain gauge at position #1 (SG #1); however, it must be remembered that they are located approximately 40.0mm apart in an axial orientation.

Table 46. Test 4 - data summary table.

Sensor Type / Location	Max. Load (N)	Max. Deflection (mm)	Max. Micro-Strain ($\mu\epsilon$)
FBG	2517.31	63.9	436.57
SG #1			519.24
SG #2			-684.71
SG #3			597.76
SG #4			379.08
SG #5			-653.83
SG #6			-323.09
SG #7			-475.40
SG #8			-185.28
SG #9			369.04

Table 46 details several micro-strains readings as a negative value which is indicative of a compressive strain, whilst a positive return is a tensile strain.

Conclusions

The initial data acquisition test detailed a close comparison between the FBG and strain gauge #1 with both being sensing tensile strain. This indicates that it is reasonable to expect that an FBG applied in each of the strain gauge locations would perform and return commensurate data as that provided by the strain gauge system when no simulated damage was in-place.

Appendix K: Test Five Discussion

Test 5: Conditions, Data and Result Plots

The following information is applicable to the testing regime applied during Test 5 only.

This was the initial cantilevered applied load test with simulated damage. This test was used as a data collection test only.

Test Conditions

A physical test was conducted on the blade test section with the following conditions:

Table 47. Test 5 - General conditions with damage.

	Details	Remarks
Load Range (N)	0 - 2500	Test completed without fault. Partial damage applied in position one to a depth of 3.0 mm. Forceful feed rate used.
Load Increment (N)	500	
Max. Load (N)	2517.3	
Load Position (mm)	1500 (tip load)	
Adjustable Lower Support Position (mm)	185.0	
Max. Deflection (mm)	59.47	
Damage Type	Partial Hole Position 1	
Damage Depth (mm)	3.0	
Damage Diameter	≈8.0	

Result Plots

The following plots were prepared from the collected data, some of which may be presented within the report main body.

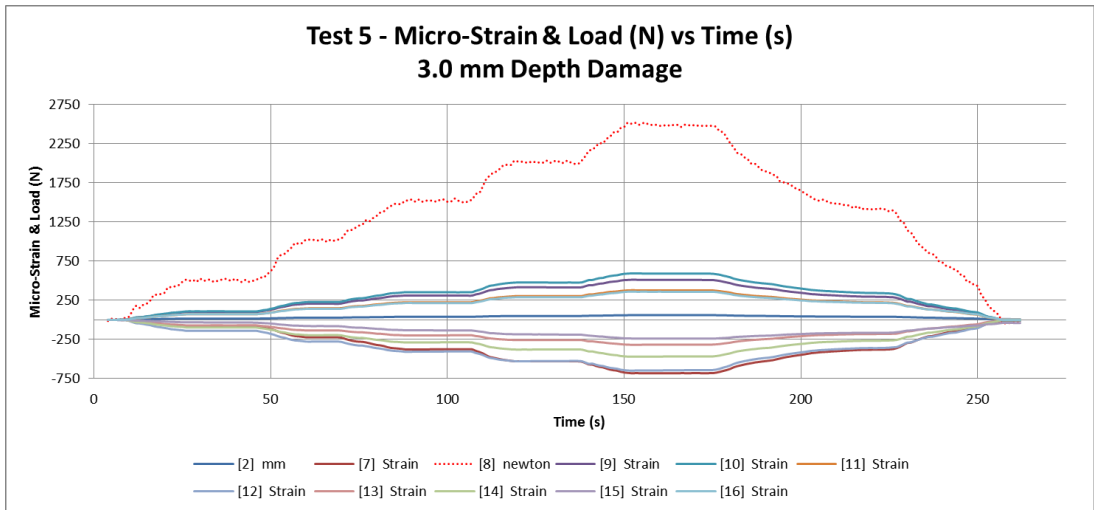


Figure 162. Test 5 – Load & strain gauge plot including load removal.

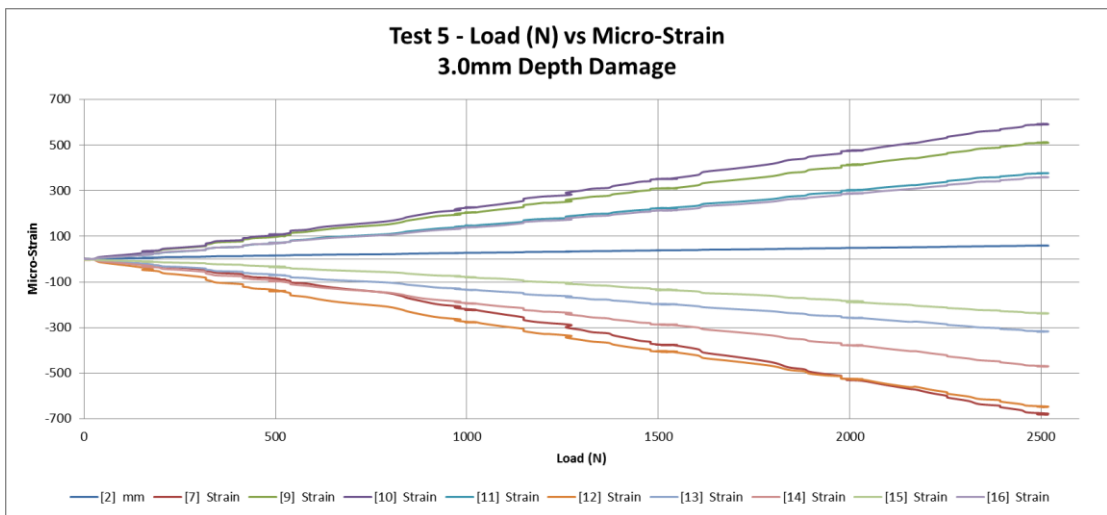


Figure 163. Test 5 – Load & strain gauge plot.

The following plot depicts the close correlation between the FBG and strain gauges in tension.

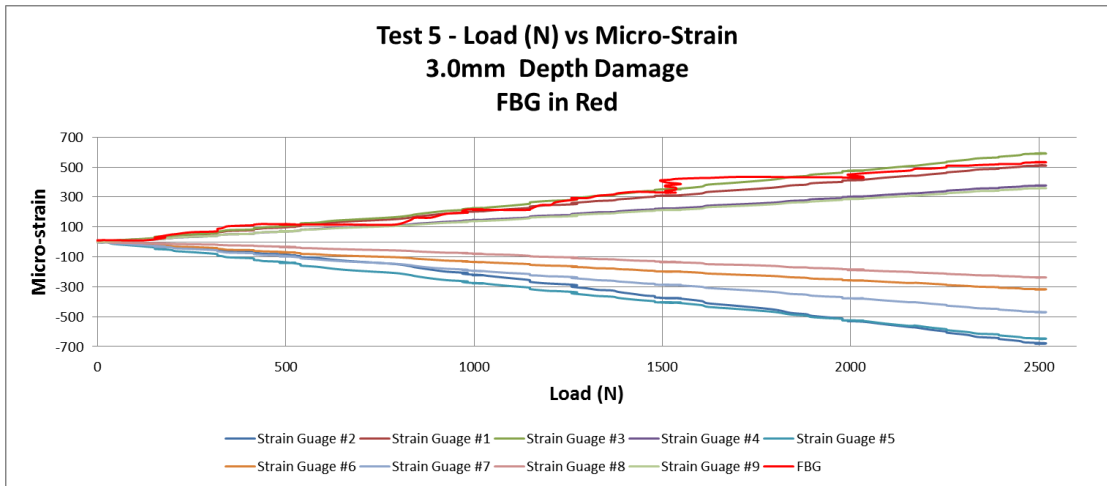


Figure 164. Test 5 – Load & strain gauge / FBG comparison plot.

The linear FBG line in the following plot again indicates a close correlation between the FBG and strain gauge #7, located in the number one position and being the closest FBG replicating strain gauge. As in Test 4 this correlation has continued with the application of simulated battlefield damage.

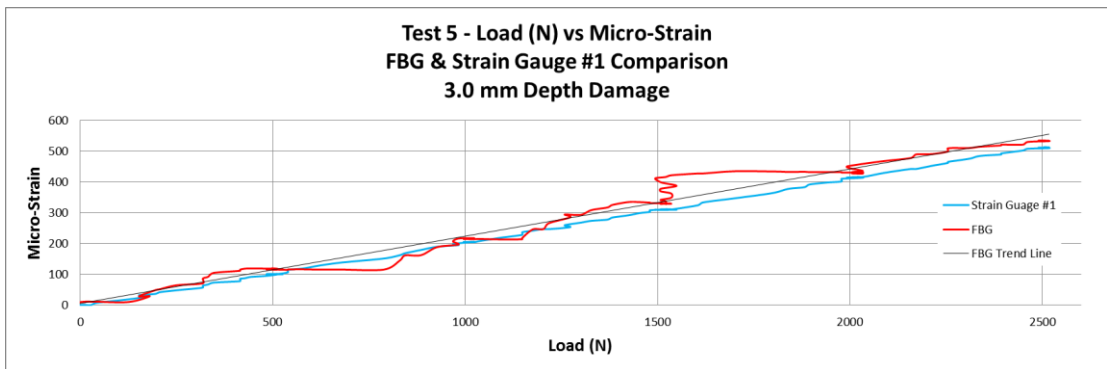


Figure 165. Test 5 - FBG and strain gauge #1 comparison.

The following FBG plots present a tensile sensing condition.

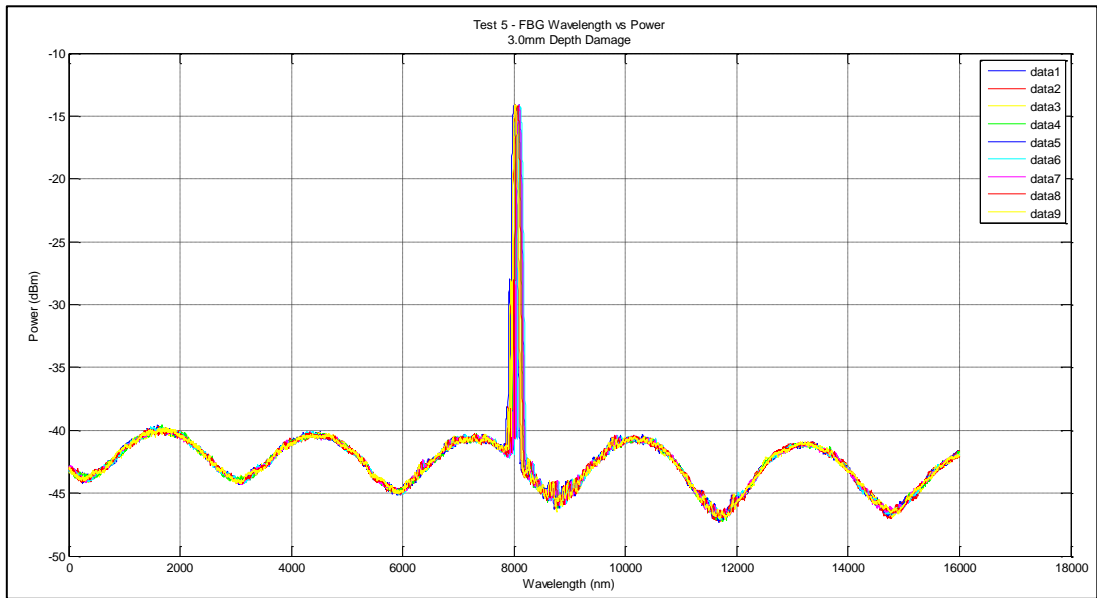


Figure 166. Test 5 - FBG wavelength vs power complete plot.

The following FBG plot clearly depicts a peak shift from left to right indicating a tensile strain sensed by the FBG.

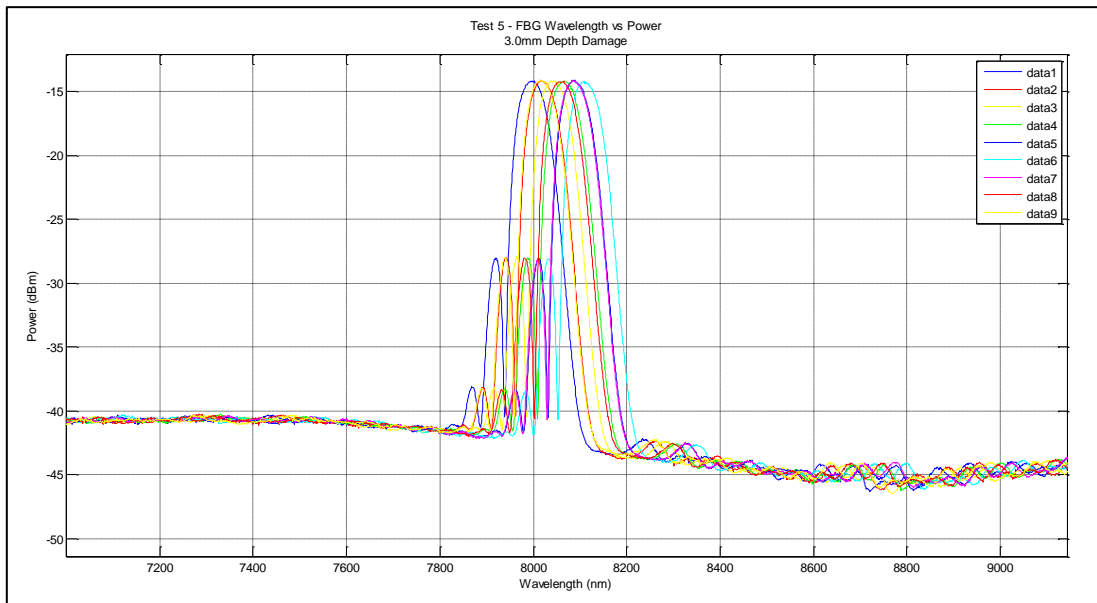


Figure 167. Test 5 - FBG wavelength vs power reduced scale plot.

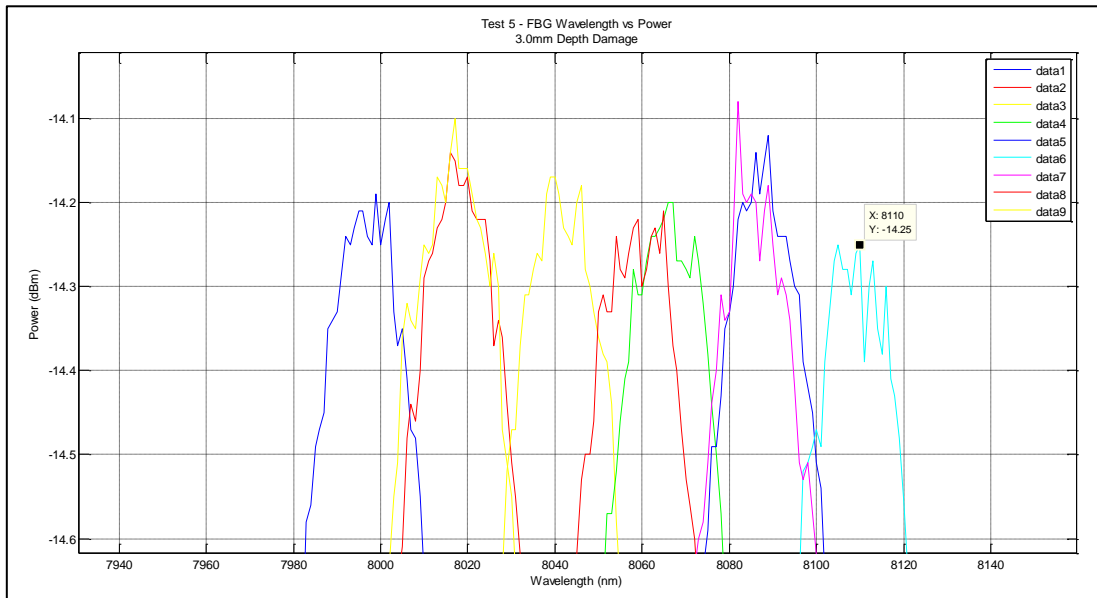


Figure 168. Test 5 - FBG wavelength vs power peak plot with chirping depicted.

Test 5 Summary Table

The following table is a summary of the data collected during Test 5. Of particular interest is the comparison between the FBG and strain gauge at position #1 (SG #1); however, it must be remembered that they are located approximately 40.0mm apart in an axial orientation.

Table 48. Test 5 - data summary table.

Sensor Type/ Location	Max. Load (N)	Max. Deflection (mm)	Max. Micro-Strain ($\mu\epsilon$)
FBG	2517.3	59.47	450.41
SG #1			509.97
SG #2			-681.76
SG #3			591.41
SG #4			376.65
SG #5			-646.52
SG #6			-317.72
SG #7			-469.99
SG #8			-239.02
SG #9			358.79

Table 48 details several micro-strains readings as a negative value which is indicative of a compressive strain, whilst a positive return is a tensile strain.

Conclusions

The second dedicated data acquisition test detailed a close comparison between the FBG and strain gauges, in particular, strain gauge #1 with both being sensing tensile strain. This indicates that it is reasonable to expect that an FBG applied in each of the strain gauge locations would perform and return commensurate data as that provided by the strain gauge system when limited simulated battlefield damage of 3.0 mm depth is in-place.

Appendix L: Test Six Discussion

Test 6: Conditions, Data and Result Plots

The following information is applicable to the testing regime applied during Test 6 only.

This was the second cantilevered applied load test with simulated damage. This test was used as a data collection test only.

Test Conditions

A physical test was conducted on the blade test section with the following conditions:

Table 49. Test 6 - General conditions with damage.

	Details	Remarks
Load Range (N)	0 - 2500	Test completed without fault. Partial damage applied in position one to a depth of 6.0 mm. Forceful feed rate used.
Load Increment (N)	500	
Load Position (mm)	1500 (tip load)	
Max. Load (N)	2517.29	
Adjustable Lower Support Position (mm)	185.0	
Max. Deflection (mm)	65.4	
Damage Type	Partial Hole Position 1	
Damage Depth (mm)	6.0	
Damage Diameter	8.0	

Result Plots

The following plots were prepared from the collected data, some of which may be presented within the report main body.

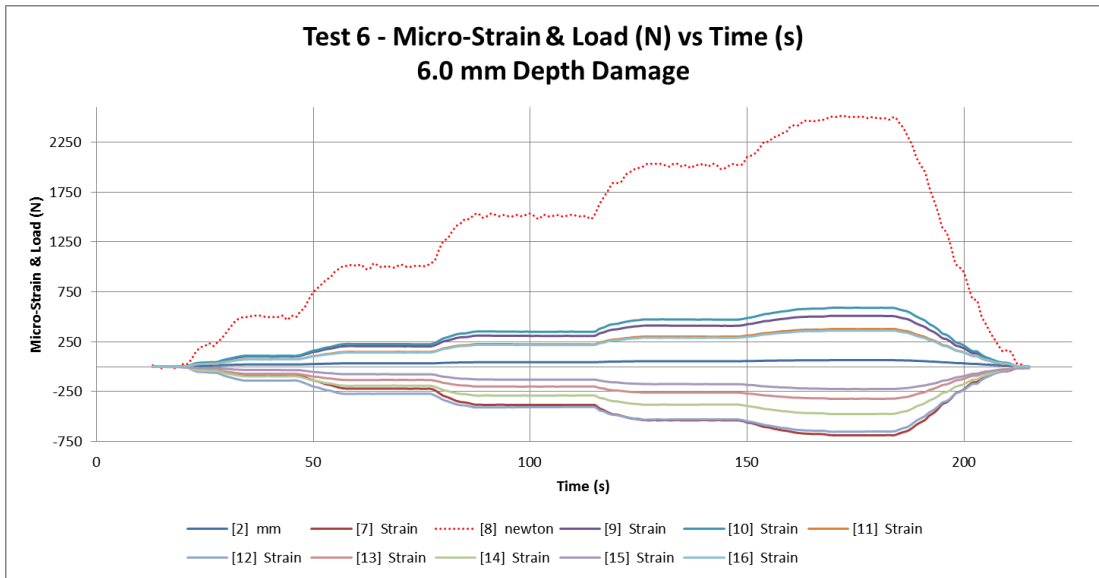


Figure 169. Test 6 – Load & strain gauge plot including load removal.

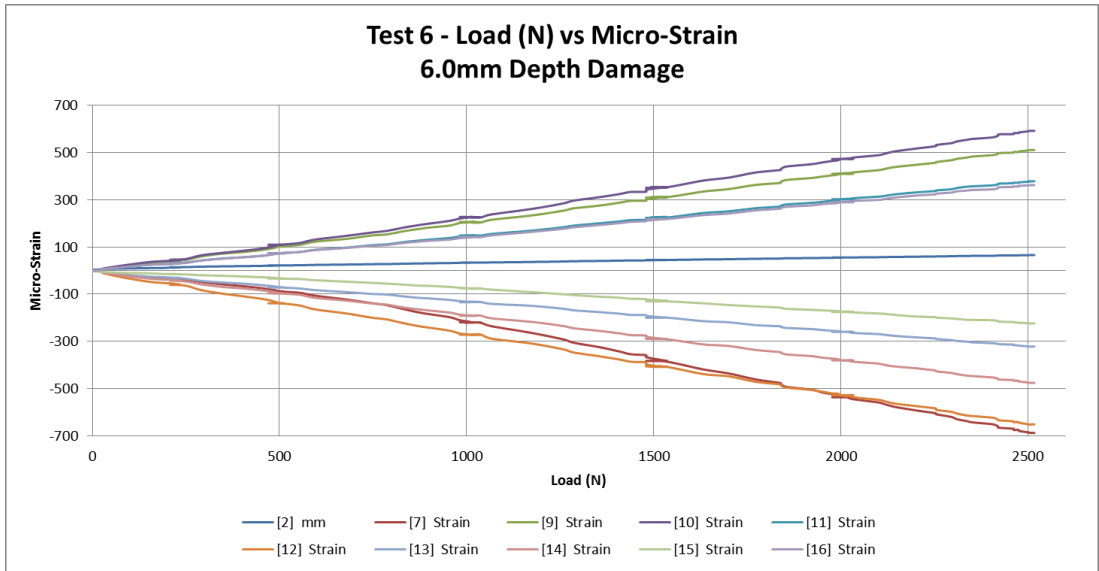


Figure 170. Test 6 – Load & strain gauge plot.

The following plot depicts the close correlation between the FBG and strain gauges in tension.

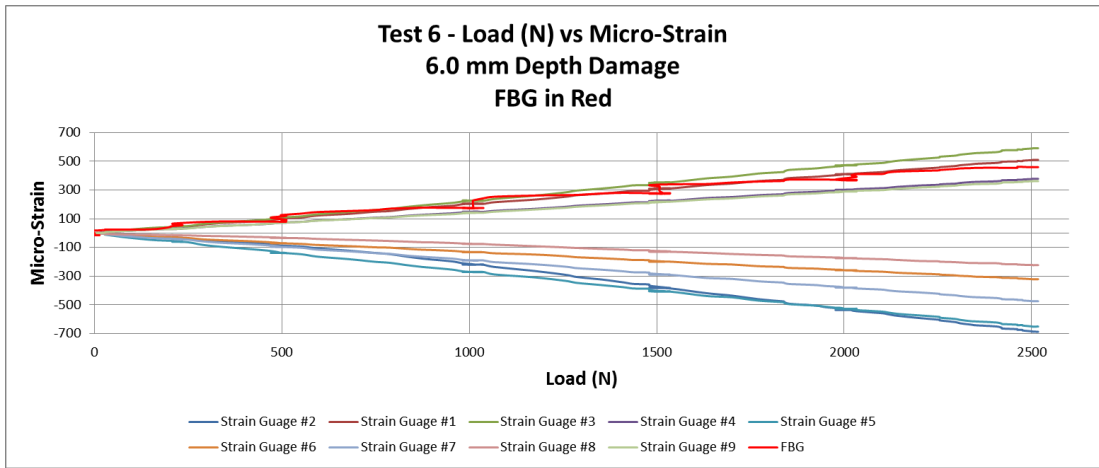


Figure 171. Test 6 – Load & strain gauge / FBG comparison plot.

The linear FBG line in the following plot again indicates a close correlation between the FBG and strain gauge #7, located in the number one position and being the closest FBG replicating strain gauge. As in Test 4 and 5 this correlation has continued with the application of increased simulated battlefield damage.

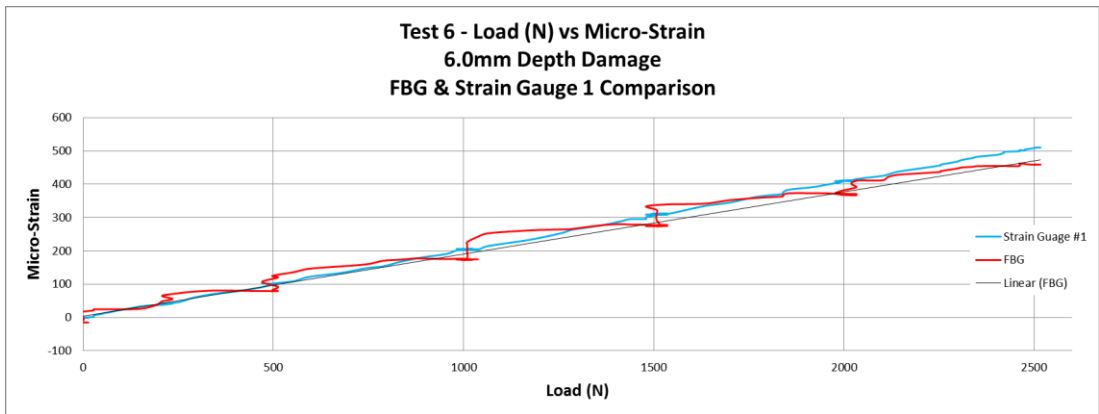


Figure 172. Test 6 - FBG and strain gauge #1 comparison.

The following FBG plots present a tensile sensing condition.

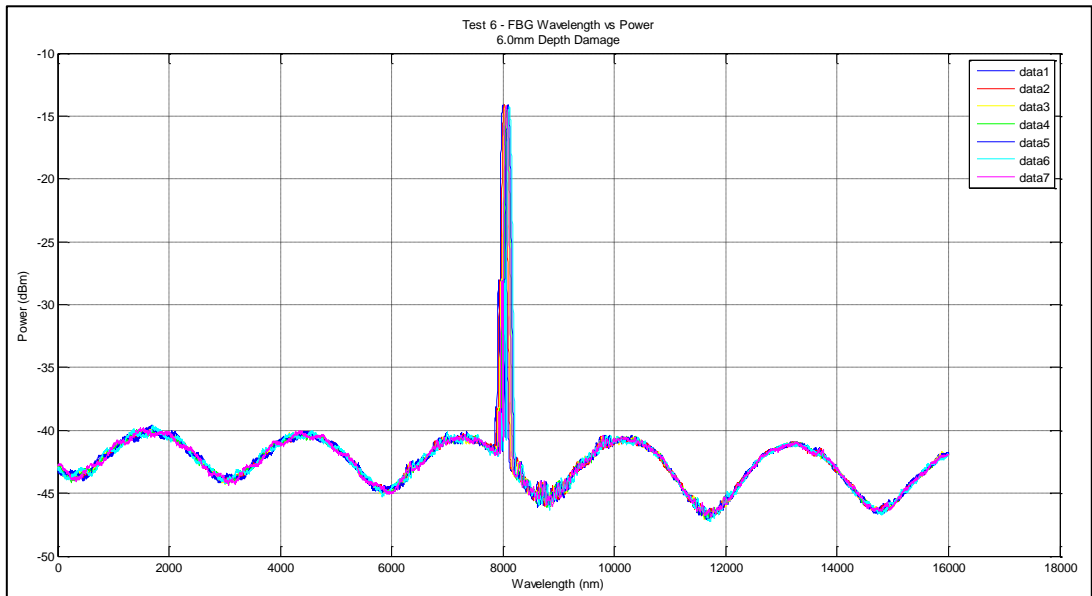


Figure 173. Test 6 - FBG wavelength vs power complete plot.

The following FBG plot clearly depicts a peak shift from left to right indicating a tensile strain sensed by the FBG.

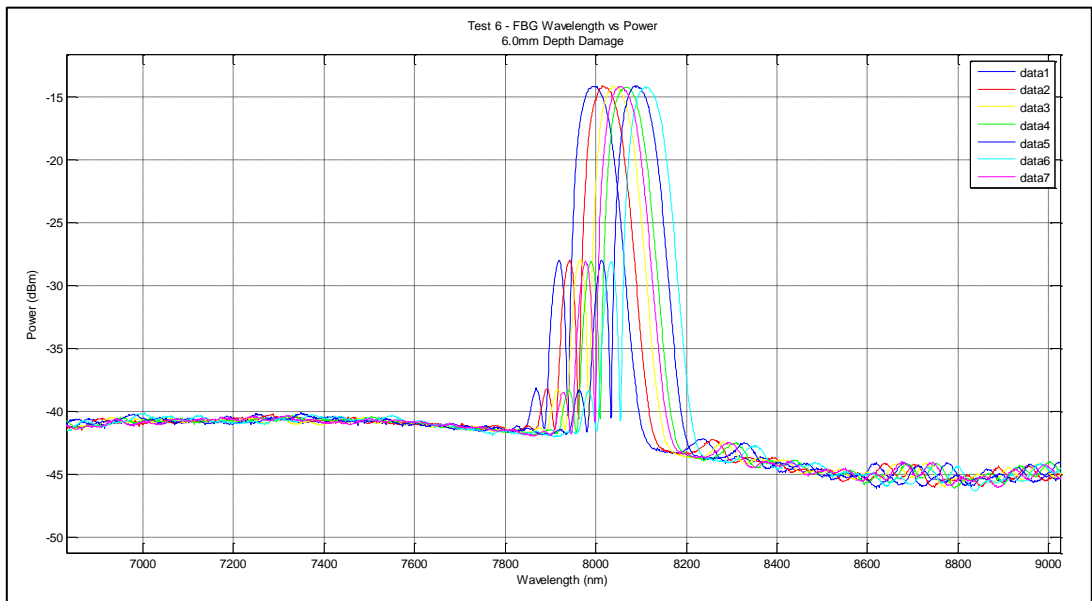


Figure 174. Test 6 - FBG wavelength vs power reduced scale plot.

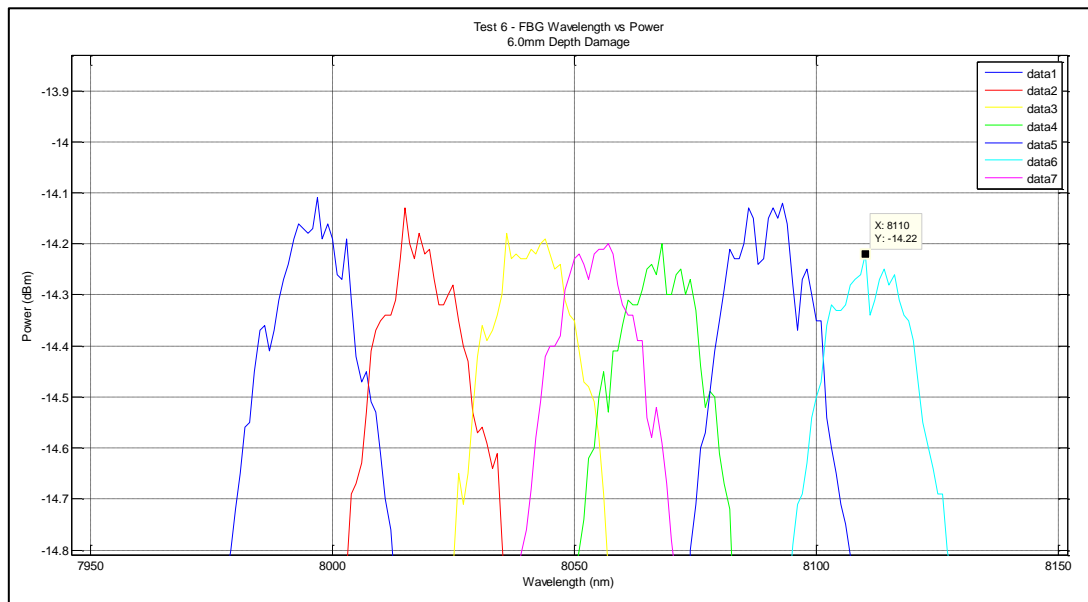


Figure 175. Test 6 - FBG wavelength vs power peak plot with chirping depicted.

Test 6 Summary Table

The following table is a summary of the data collected during Test 6. Of particular interest is the comparison between the FBG and strain gauge at position #1 (SG #1); however, it must be remembered that they are located approximately 40.0mm apart in an axial orientation.

Table 50. Test 6 - data summary table.

Sensor Type / Location	Max. Load (N)	Max. Deflection (mm)	Max. Micro-Strain ($\mu\epsilon$)
FBG	2571.29	65.4	463.49
SG #1			509.94
SG #2			-687.16
SG #3			590.90
SG #4			378.12
SG #5			-650.93
SG #6			-321.15
SG #7			-474.91
SG #8			-223.36
SG #9			361.2255

Table 50 details several micro-strains readings as a negative value which is indicative of a compressive strain, whilst a positive return is a tensile strain.

Conclusions

The second dedicated damage data acquisition test detailed a close comparison between the FBG and strain gauges, in particular, strain gauge #1 with both being sensing tensile strain. This indicates that it is reasonable to expect that an FBG applied in each of the strain gauge locations would perform and return commensurate data as that provided by the strain gauge system when limited simulated battlefield damage of 6.0 mm depth is in-place.

Appendix M: Test Seven Discussion

Test 7: Conditions, Data and Result Plots

The following information is applicable to the testing regime applied during Test 7 only.

This was the third cantilevered applied load test with simulated damage. This test was used as a data collection test only.

Test Conditions

A physical test was conducted on the blade test section with the following conditions:

Table 51. Test 7 - General conditions with damage.

	Details	Remarks
Load Range (N)	0 - 2500	Test completed without fault. Damage applied in position one passing through the full structure thickness. Forceful feed rate used.
Load Increment (N)	500	
Max. Load (N)	2531.45	
Load Position (mm)	1500 (tip load)	
Adjustable Lower Support Position (mm)	185.0	
Max. Deflection (mm)	61.23	
Damage Type	Through Hole Position 1	
Damage Depth (mm)	Full Thickness	
Damage Diameter	8.0	

Result Plots

The following plots were prepared from the collected data, some of which may be presented within the report main body.

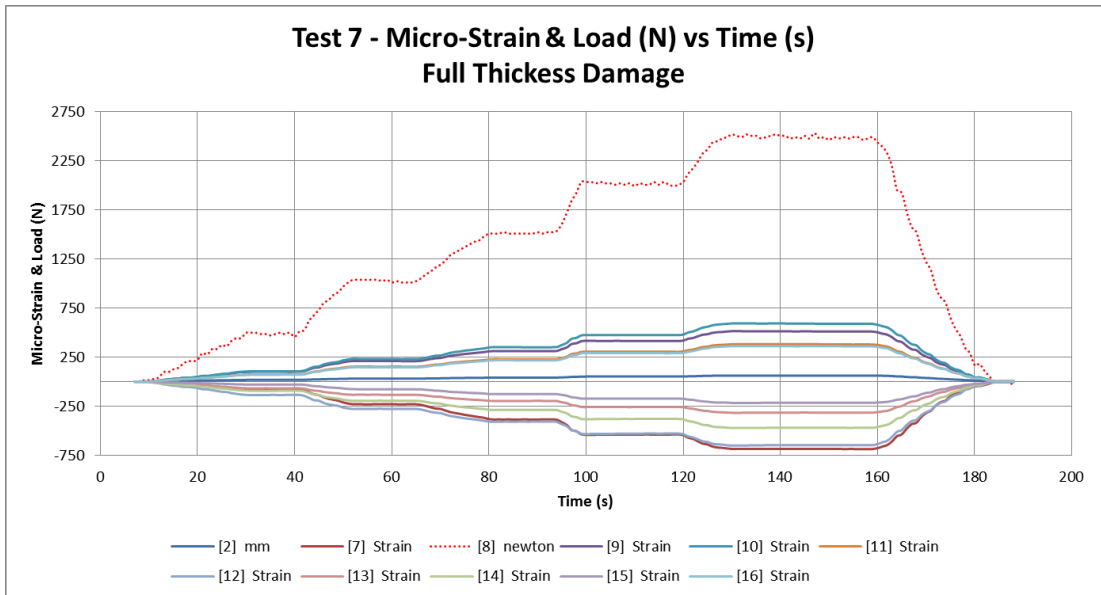


Figure 176. Test 7 – Load & strain gauge plot including load removal.

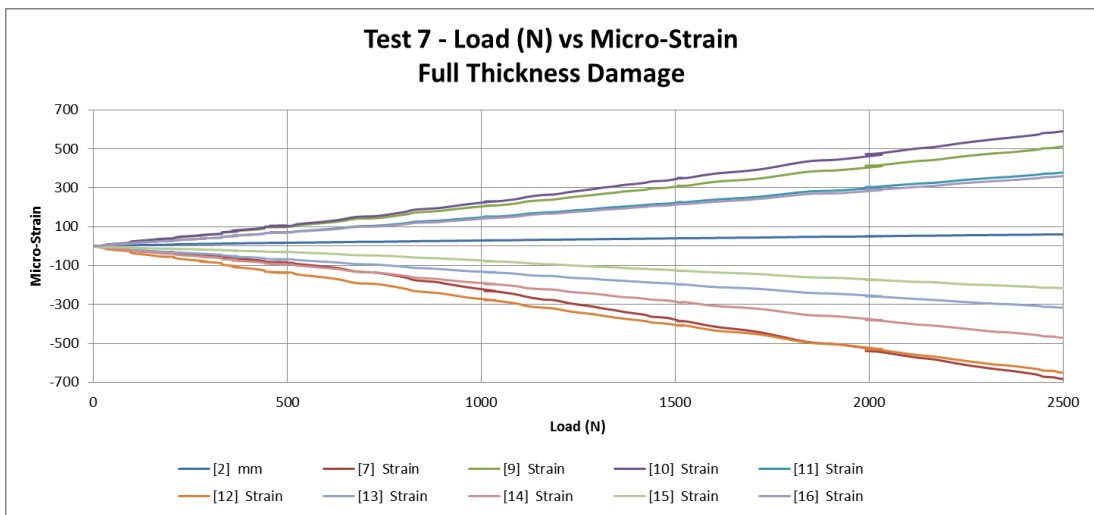


Figure 177. Test 7 – Load & strain gauge plot.

The following plot depicts the close correlation between the FBG and strain gauges in tension.

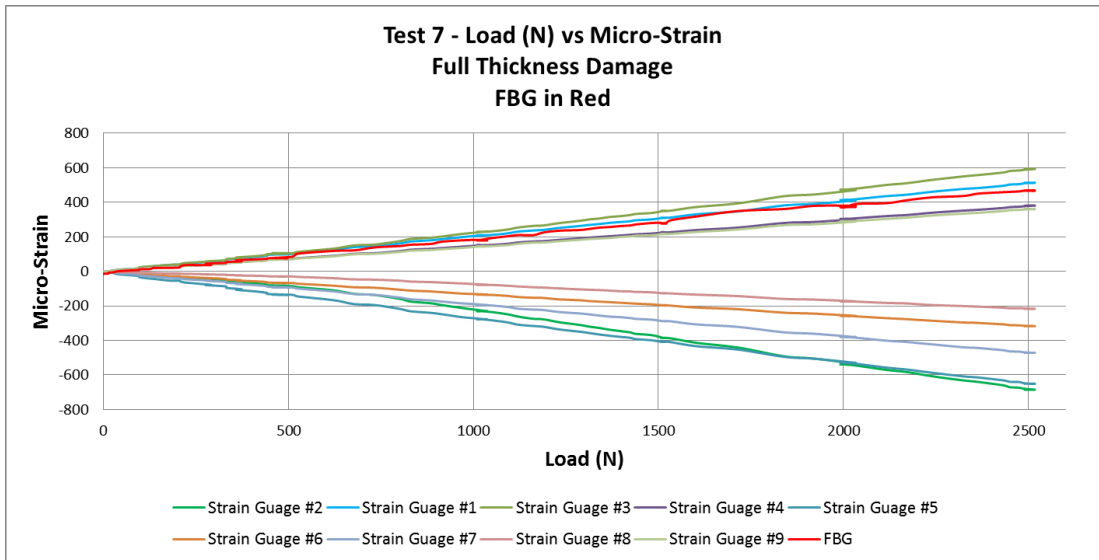


Figure 178. Test 7 – Load & strain gauge / FBG comparison plot.

The linear FBG line in the following plot indicates a close correlation between the FBG and strain gauge #7, located in the number one position and being the closest FBG replicating strain gauge. As in Test 4 thru 6 this correlation has continued with the application of increased simulated battlefield damage to a full thickness level.

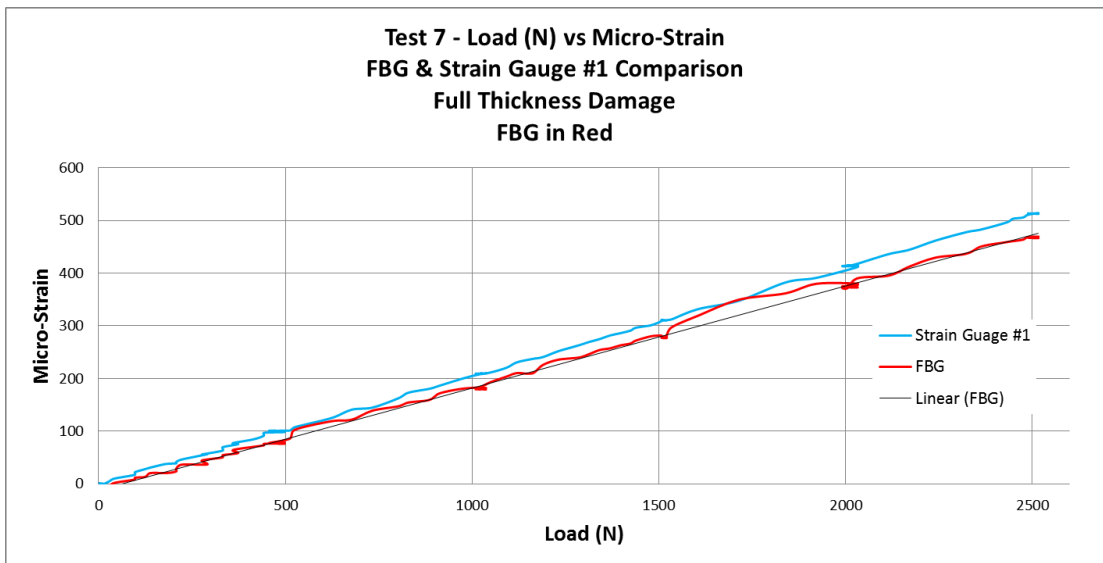


Figure 179. Test 7 - FBG and strain gauge #1 comparison.

The following FBG plots present a tensile sensing condition.

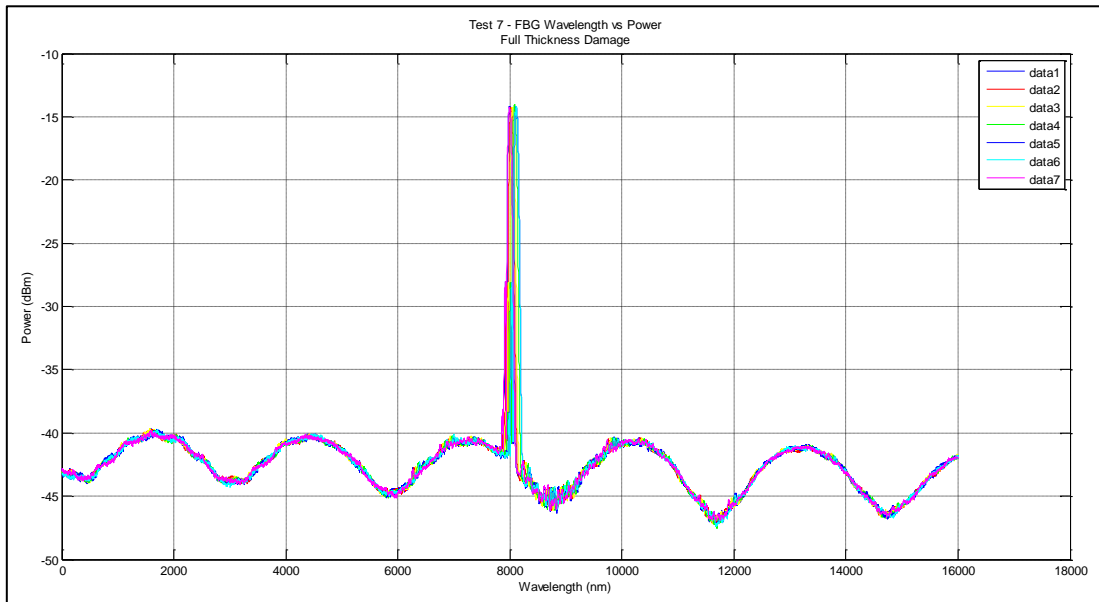


Figure 180. Test 7 - FBG wavelength vs power complete plot.

The following FBG plot clearly depicts a peak shift from left to right indicating a tensile strain sensed by the FBG.

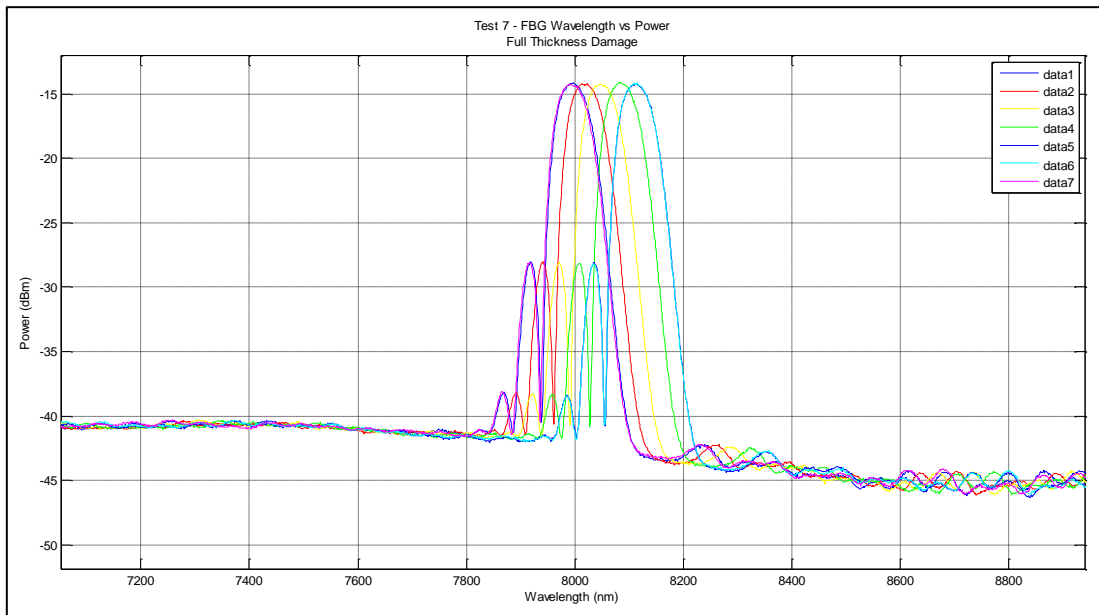


Figure 181. Test 7 - FBG wavelength vs power reduced scale plot.

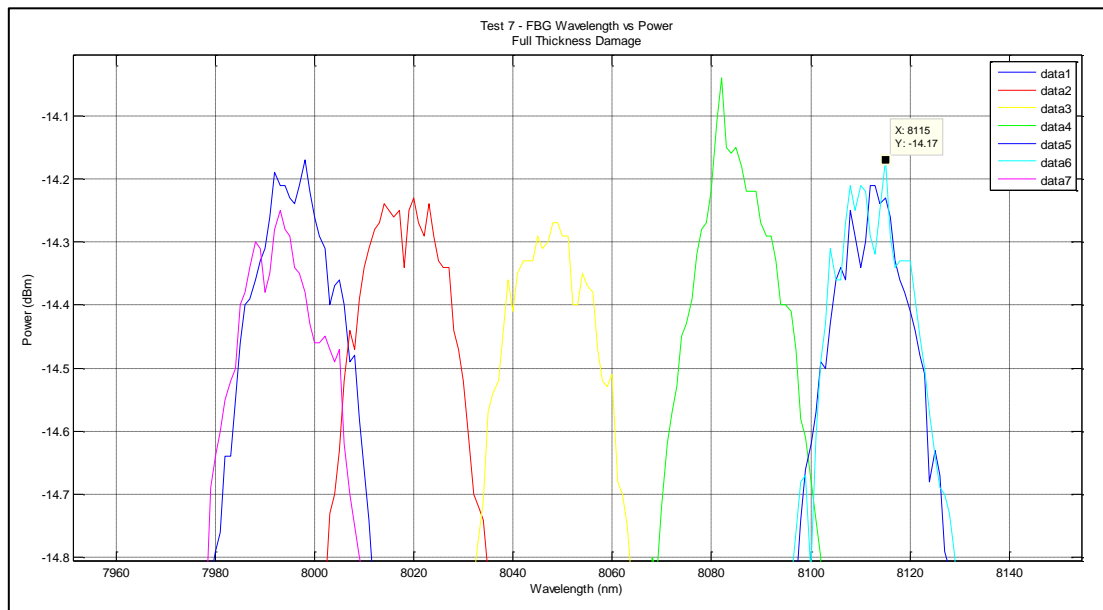


Figure 182. Test 7 - FBG wavelength vs power peak plot with chirping depicted.

Test 7 Summary Table

The following table is a summary of the data collected during Test 7. Of particular interest is the comparison between the FBG and strain gauge at position #1 (SG #1); however, it must be remembered that they are located approximately 40.0mm apart in an axial orientation.

Table 52. Test 7 - data summary table.

Sensor Type / Location	Max. Load (N)	Max. Deflection (mm)	Max. Micro-Strain ($\mu\epsilon$)
FBG	2531.45	61.23	469.95
SG #1			513.86
SG #2			-685.20
SG #3			592.85
SG #4			381.05
SG #5			-651.90
SG #6			-317.24
SG #7			-471.95
SG #8			-217.00
SG #9			361.23

Table 52 details several micro-strains readings as a negative value which is indicative of a compressive strain, whilst a positive return is a tensile strain.

Conclusions

The third dedicated damage data acquisition test detailed a close comparison between the FBG and strain gauges, in particular, strain gauge #1 with both sensing tensile strain. This indicates that it is reasonable to expect that an FBG applied in each of the strain gauge locations would perform and return commensurate data as that provided by the strain gauge system when simulated battlefield damage of a full thickness penetration depth hole is in-place.

Appendix N: Test Eight Discussion

Test 8: Conditions, Data and Result Plots

The following information is applicable to the testing regime applied during Test 8 only.

This was the fourth cantilevered applied load test with simulated damage. This test was used as a data collection test only.

Test Conditions

A physical test was conducted on the blade test section with the following conditions:

Table 53. Test 8 - General conditions with damage.

	Details	Remarks
Load Range (N)	0 - 2500	Test completed without fault. Damage applied in position one passing through the full structure thickness. In addition a transverse through hole was positioned in the upper rear corner of the rotor spar. Forceful feed rate used.
Load Increment (N)	500	
Max. Load (N)	2517.2	
Load Position (mm)	1500 (tip load)	
Adjustable Lower Support Position (mm)	185.0	
Max. Deflection (mm)	63.7	
Damage Type	Through Hole Position 1 Through Hole Position 2 - Transverse 45° Through Hole	
Damage Depth (mm)	Full Thickness	
Damage Diameter	8.0	

Result Plots

The following plots were prepared from the collected data, some of which may be presented within the report main body.

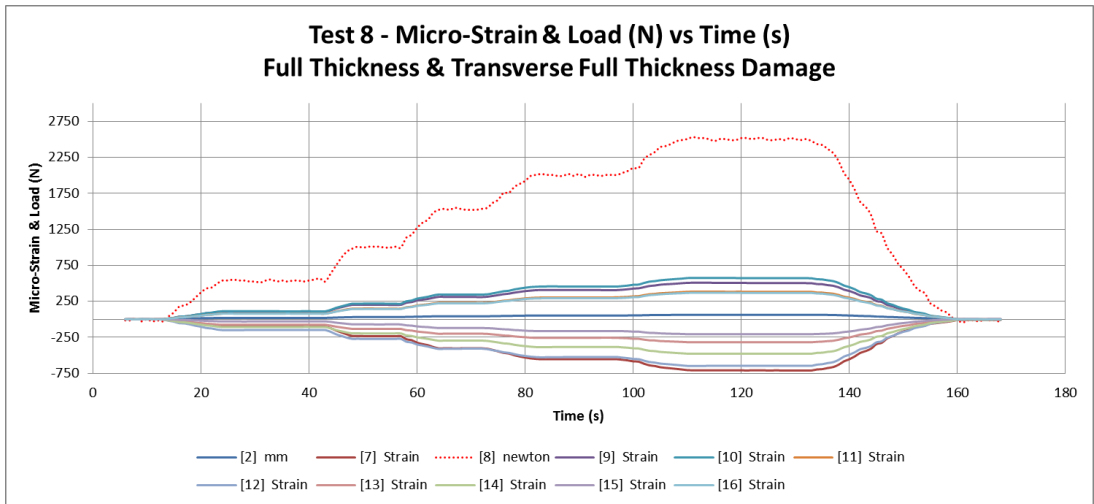


Figure 183. Test 8 – Load & strain gauge plot including load removal.

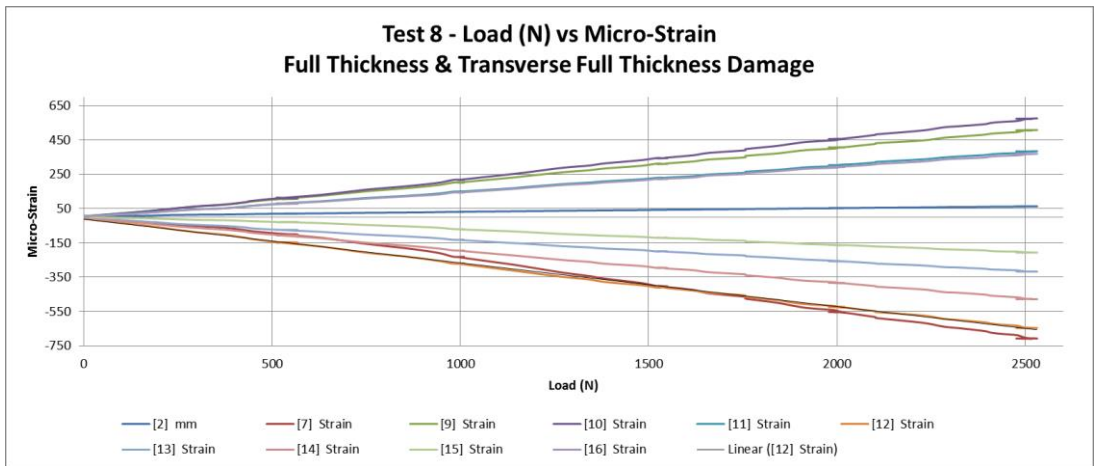


Figure 184. Test 8 – Load & strain gauge plot.

The following plot depicts the close correlation between the FBG and strain gauges in tension.

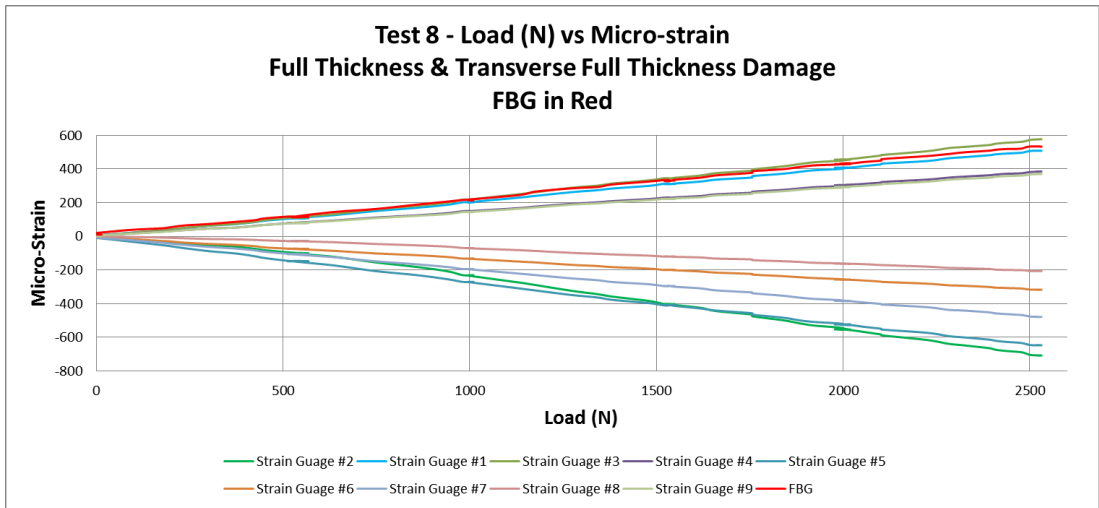


Figure 185. Test 8 – Load & strain gauge / FBG comparison plot.

The linear FBG line in the following plot indicates a close correlation between the FBG and strain gauge #7, located in the number one position and being the closest FBG replicating strain gauge. As in Test 4 thru 7 this correlation has continued with the application of increased simulated battlefield damage to a 2 x full thickness hole level of damage.

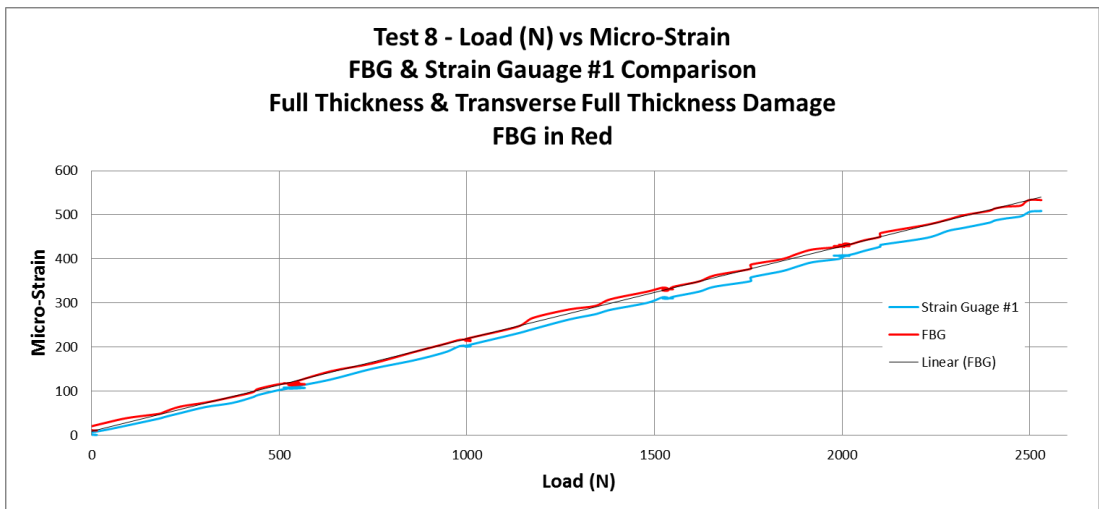


Figure 186. Test 8 - FBG and strain gauge #1 comparison.

The following FBG plots present a tensile sensing condition.

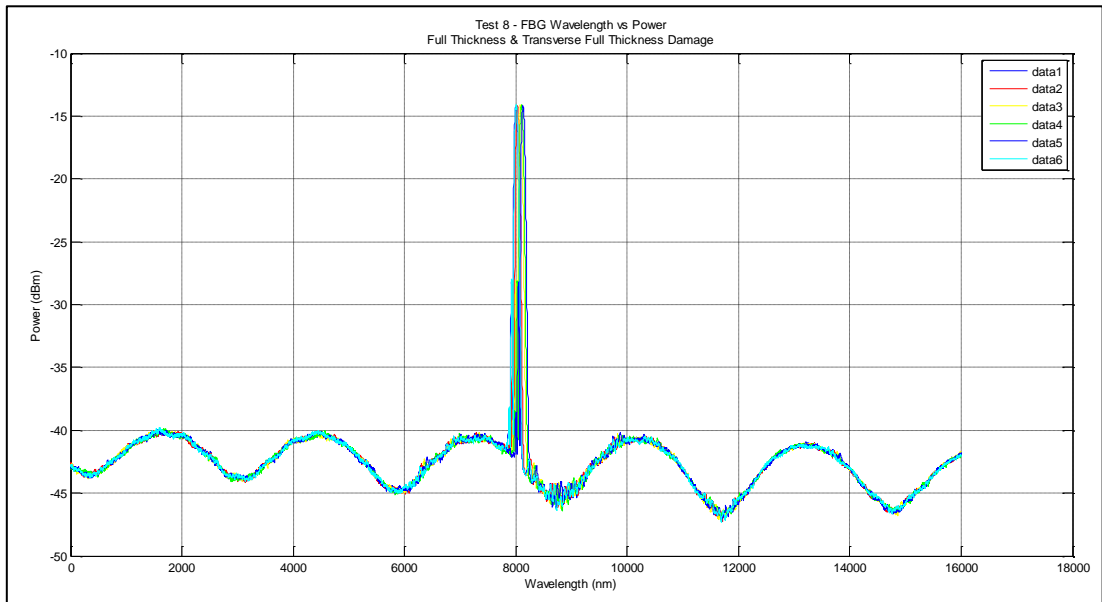


Figure 187. Test 8 - FBG wavelength vs power complete plot.

The following FBG plot depicts a peak shift from left to right indicating a tensile strain sensed by the FBG.

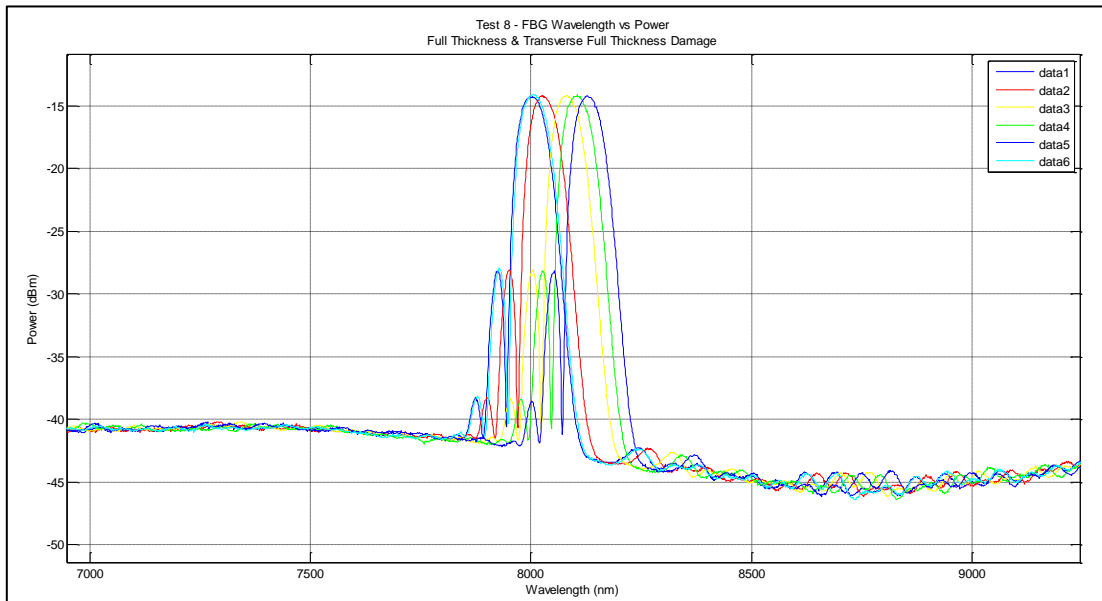


Figure 188. Test 8 - FBG wavelength vs power reduced scale plot.

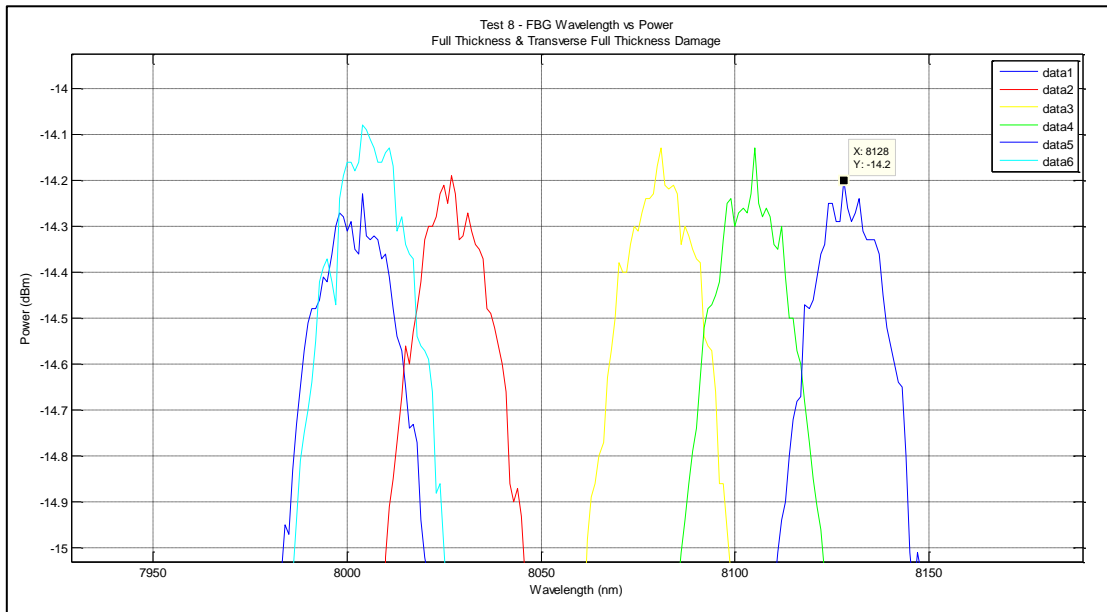


Figure 189. Test 8 - FBG wavelength vs power peak plot with chirping depicted.

Test 8 Summary Table

The following table is a summary of the data collected during Test 8. Of particular interest is the comparison between the FBG and strain gauge at position #1 (SG #1); however, it must be remembered that they are located approximately 40.0mm apart in an axial orientation.

Table 54. Test 8 - data summary table.

Sensor Type / Location	Max. Load (N)	Max. Deflection (mm)	Max. Micro-Strain ($\mu\epsilon$)
FBG	2517.2	63.7	534.96
SG #1			508.48
SG #2			-708.23
SG #3			573.24
SG #4			383.01
SG #5			-644.59
SG #6			-316.76
SG #7			-475.89
SG #8			-205.78
SG #9			368.08

Table 54 details several micro-strains readings as a negative value which is indicative of a compressive strain, whilst a positive return is a tensile strain.

Conclusions

The fourth dedicated damage data acquisition test detailed a close comparison between the FBG and strain gauges, in particular, strain gauge #1 with both sensing tensile strain. This indicates that it is reasonable to expect that an FBG applied in each of the strain gauge locations would perform and return commensurate data as that provided by the strain gauge system when simulated battlefield damage of 2 x full thickness penetration depth holes are in-place.

Appendix O: Test Nine Discussion

Test 9: Conditions, Data and Result Plots

The following information is applicable to the testing regime applied during Test 9 only.

This was the fifth cantilevered applied load test with simulated damage. This test was used as a data collection test only.

Test Conditions

A physical test was conducted on the blade test section with the following conditions:

Table 55. Test 9 - General conditions with damage.

	Details	Remarks
Load Range (N)	0 - 2500	Test completed without fault. Damage applied in position one passing through the full structure thickness. A second, transverse through hole was positioned in the upper rear corner of the rotor spar. In addition a third hole passing through the full structure thickness was located at position three. Forceful feed rate used.
Load Increment (N)	500	
Max. Load (N)	2518.0	
Load Position (mm)	1500 (tip load)	
Adjustable Lower Support Position (mm)	185.0	
Max. Deflection (mm)	68.8	
Damage Type	Through Hole Position 1 Through Hole Position 2 - Transverse 45° Through Hole Through Hole Position 3	
Damage Depth (mm)	Full Thickness	
Damage Diameter	8.0	

Result Plots

The following plots were prepared from the collected data, some of which may be presented within the report main body.

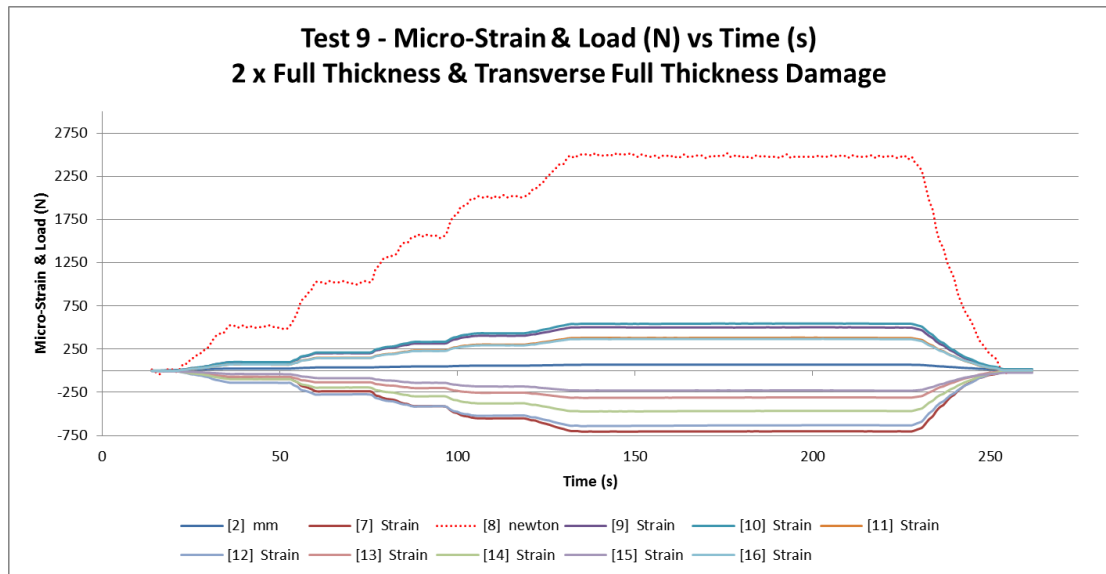


Figure 190. Test 9 – Load & strain gauge plot including load removal.

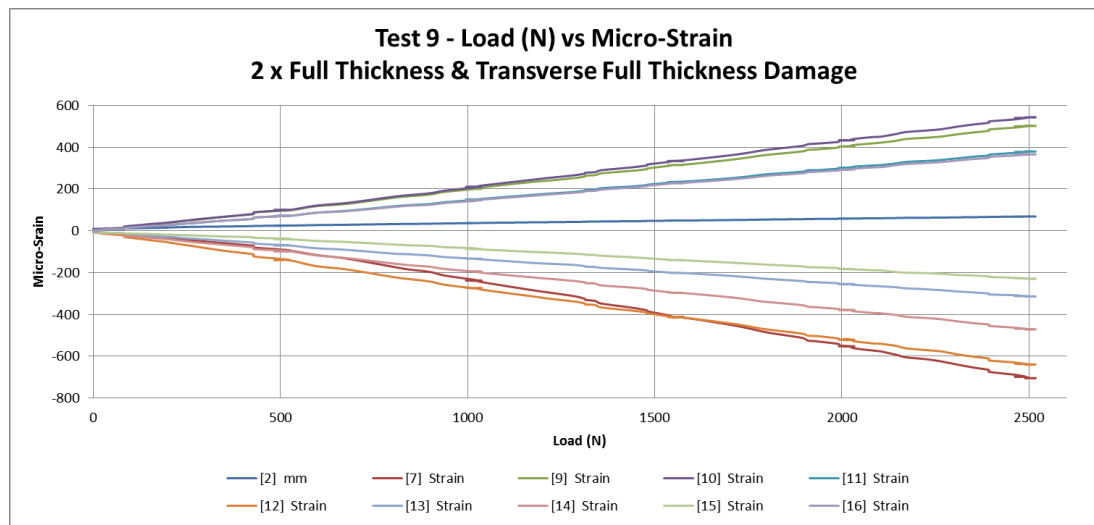


Figure 191. Test 9 – Load & strain gauge plot.

The following plot depicts the close correlation between the FBG and strain gauges in tension.

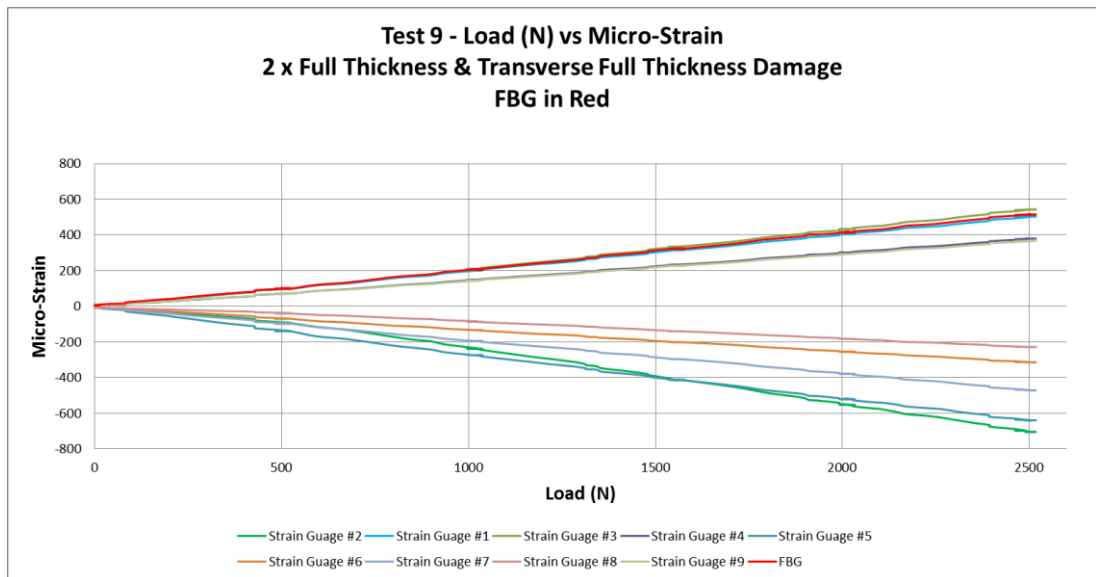


Figure 192. Test 9 – Load & strain gauge / FBG comparison plot.

The linear FBG line in the following plot indicates a close correlation between the FBG and strain gauge #7, located in the number one position and being the closest FBG replicating strain gauge. As in Test 4 thru 8 this correlation has continued with the application of increased simulated battlefield damage to a 3 x full thickness hole level of damage.

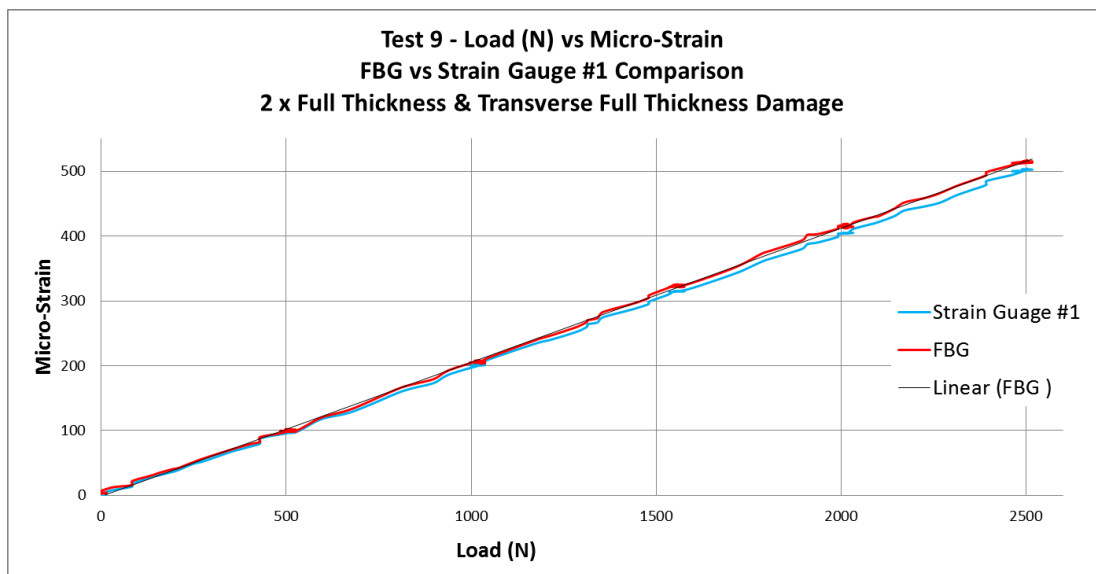


Figure 193. Test 9 - FBG and strain gauge #1 comparison.

The following FBG plots present a tensile sensing condition.

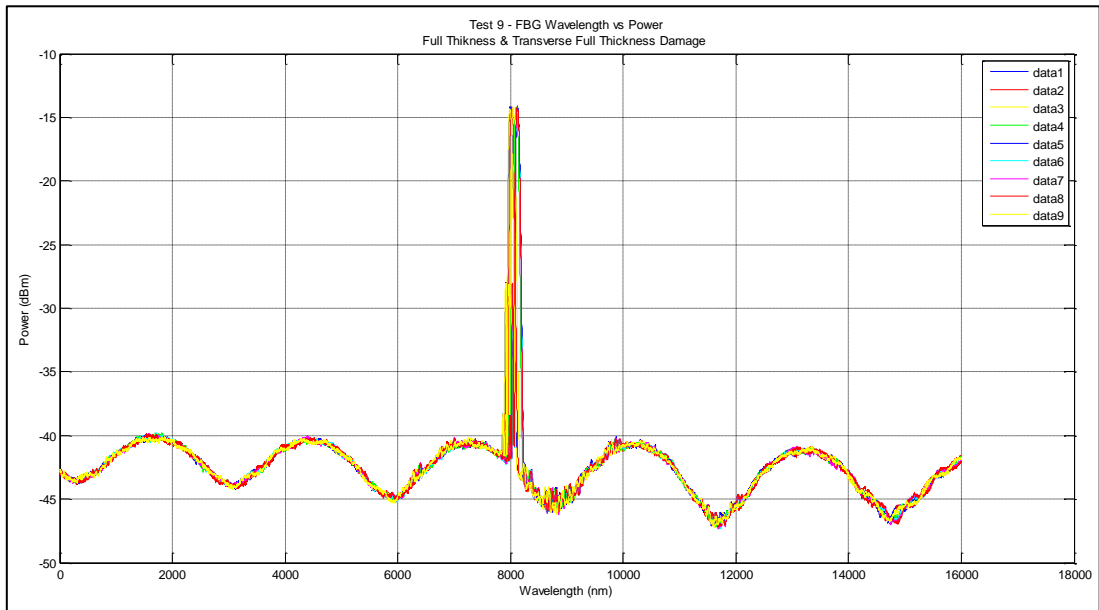


Figure 194. Test 9 - FBG wavelength vs power complete plot.

The following FBG plot depicts a peak shift from left to right indicating a tensile strain sensed by the FBG.

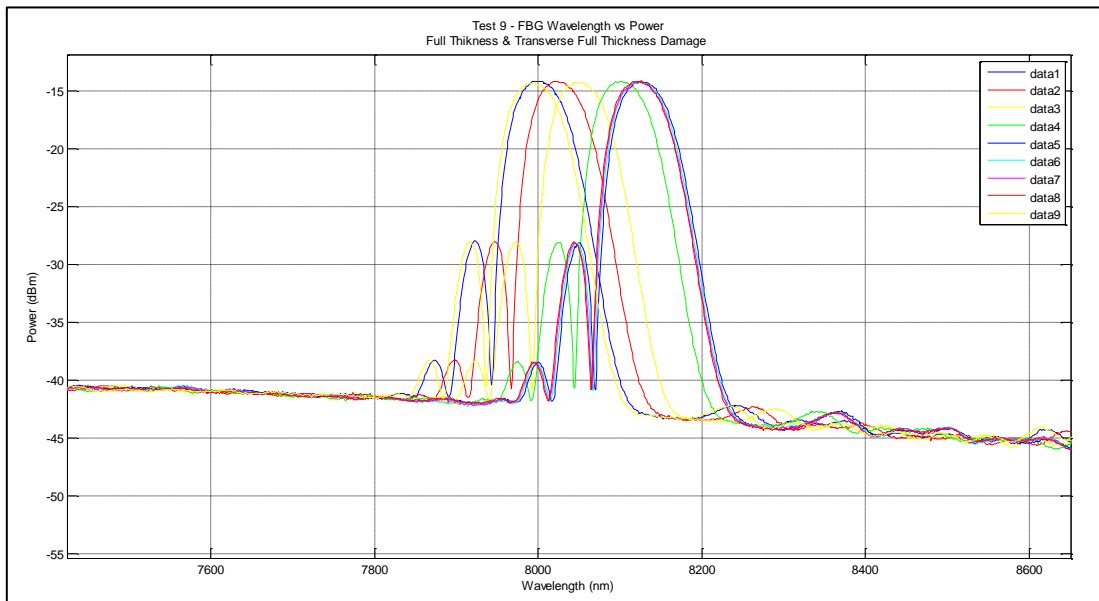


Figure 195. Test 9 - FBG wavelength vs power reduced scale plot.

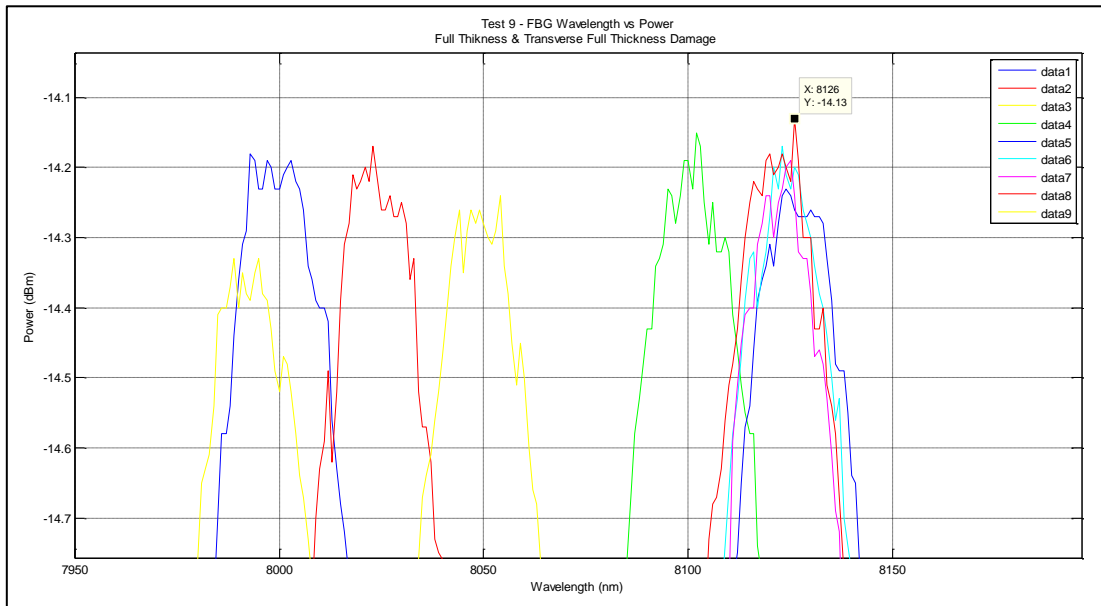


Figure 196. Test 9 - FBG wavelength vs power peak with chirping.

Test 9 Summary Table

The following table is a summary of the data collected during Test 9. Of particular interest is the comparison between the FBG and strain gauge at position #1 (SG #1); however, it must be remembered that they are located approximately 40.0mm apart in an axial orientation.

Table 56. Test 9 - data summary table.

Sensor Type / Location	Max. Load (N)	Max. Deflection (mm)	Max. Micro-Strain ($\mu\epsilon$)
FBG	2518.0	68.81	516.92
SG #1			504.07
SG #2			-705.31
SG #3			542.33
SG #4			379.59
SG #5			-638.23
SG #6			-313.84
SG #7			-470.51
SG #8			-229.78
SG #9			366.13

Table 56 details several micro-strains readings as a negative value which is indicative of a compressive strain, whilst a positive return is a tensile strain.

Conclusions

The fifth dedicated damage data acquisition test detailed a close comparison between the FBG and strain gauges, in particular, strain gauge #1 with both sensing tensile strain. This indicates that it is reasonable to expect that an FBG applied in each of the strain gauge locations would perform and return commensurate data as that provided by the strain gauge system when simulated battlefield damage of 3 x full thickness penetration depth holes are in-place.